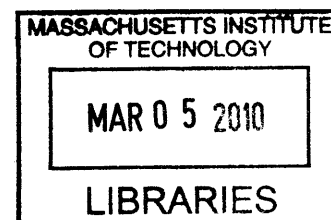


Tumor Vasculature and Microenvironment during Progression and Treatment: Insights from Optical Microscopy

by

Ryan M. Lanning

B.S. Biology
B.S. Chemistry
University of California – Irvine
(2000)



Submitted to the Harvard-MIT Division of Health Sciences and Technology
In Partial fulfillment of the Requirements
For the Degree of

DOCTOR OF PHILOSOPHY IN MEDICAL ENGINEERING
at the
MASSACHUSETTS INSTITUTE OF TECHNOLOGY

ARCHIVES

September 2009

~~February 2010~~

© 2009 Ryan M. Lanning
All Rights Reserved

The author hereby grants to MIT permission to reproduce and to distribute publicly paper and electronic copies of this thesis in whole or in part.

Signature of Author: _____

Harvard-M.I.T. Division of Health Sciences and Technology
June 9, 2009

Certified by: _____

Rakesh K. Jain, Ph.D.
Andrew Werk Cook Professor of Tumor Biology
Harvard Medical School/ Massachusetts General Hospital
Thesis Supervisor

Accepted by: _____

Ram Sasisekharan, PhD
Edward Hood Taplin Professor of Health Sciences & Technology and Biological Engineering
Director, Harvard-M.I.T. Division of Health Sciences and Technology

To my wife, Gina
without whom none of this would have been possible
and to my parents,
who fostered my zest for learning

Tumor Vasculature and Microenvironment during Progression and Treatment: Insights from Optical Microscopy

Ryan M. Lanning

Submitted to the Harvard/MIT Division of Health Sciences and Technology on June 9, 2009 in
Partial Fulfillment of the Requirements for the degree of Doctor of Philosophy in Medical
Engineering

ABSTRACT:

In addition to cancer cells, solid tumors consist of a variety of cell types and tissues defining a complex microenvironment that influences disease progression and response to therapy. To fully characterize and probe the tumor microenvironment, new tools are needed to quantitatively assess microanatomical and physiological changes during tumor growth and treatment. Particularly important, is the metabolic microenvironment defined in tumors by hypoxia (low pO_2) and acidity (low pH). These parameters have been shown to influence response to radiation therapy and chemotherapy. However, very little is known about spatio-temporal changes in pO_2 and pH during tumor progression and therapy. By modifying the technique of intravital multiphoton microscopy (MPM) to perform phosphorescence quenching microscopy, I developed a non-invasive method to quantify oxygen tension (pO_2) in living tissue at high three-dimensional resolution. To probe functional changes in the metabolic microenvironment, I measured *in vivo* pO_2 during tumor growth and antiangiogenic (vascular targeted) treatment in preclinical tumor models.

Nanotechnology is rapidly emerging as an important source of biocompatible tools that may shape the future of medical practice. Fluorescent semiconductor nanocrystals (NCs), also known as quantum dots, are a powerful tool for biological imaging, cellular targeting and molecular sensing. I adapted novel fluorescence resonance energy transfer (FRET) –based nanocrystal (NC) biosensors for use with MPM to qualitatively measure *in vivo* extracellular pH in tumors at high-resolution.

While intravital multiphoton microscopy demonstrates utility and adaptability in the study of cancer and response to therapy, the requisite high numerical aperture and exogenous contrast agents result in a limited capacity to investigate substantial tissue volumes or probe dynamic changes repeatedly over prolonged periods. By applying optical frequency domain imaging (OFDI) as an intravital microscopic tool, the technical limitations of multiphoton microscopy can be circumvented providing unprecedented access to previously unexplored, critically important aspects of tumor biology. Using entirely intrinsic mechanisms of contrast within murine tumor models, OFDI is able to simultaneously, rapidly, and repeatedly probe the microvasculature, lymphatic vessels, and tissue microstructure and composition over large volumes. Using OFDI-based techniques, measurements of tumor angiogenesis, lymphangiogenesis, tissue viability and both vascular and cellular responses to therapy were demonstrated, thereby highlighting the potential of OFDI to facilitate the exploration of pathophysiological processes and the evaluation of treatment strategies.

Thesis Supervisor: Rakesh K. Jain, Ph.D.
Andrew Werk Cook Professor of Tumor Biology, HMS, MGH

CONTENTS

Table Contents

DEDICATION.....	3
ABSTRACT.....	5
I. Original Contributions.....	22
II. INTRODUCTION AND SPECIFIC AIMS.....	26
II.1 INTRODUCTION AND MOTIVATION:.....	27
II.2 METABOLIC MICROENVIRONMENT	27
II.3 VASCULATURE OF THE TUMOR MICROENVIRONMENT.....	28
<i>II.3a Blood and Lymphatic Vasculature: Structure and Function.....</i>	<i>29</i>
<i>II.3b Tumor Angiogenesis.....</i>	<i>30</i>
<i>II.3c Imaging Angiogenesis in the Tumor Microenvironment.....</i>	<i>31</i>
II.4 THE ROLE OF OXYGEN IN SOLID TUMORS.....	33
<i>II.4a Molecular Effects of Tumor Oxygenation.....</i>	<i>34</i>
<i>II.4b Clinical Measurements of Tumor Oxygenation.....</i>	<i>35</i>
<i>II.4c Direct Measurements of pO₂ in the Tumor Microenvironment</i>	<i>36</i>
<i>II.4d Modeling Tumor Oxygenation</i>	<i>39</i>
<i>II.4e pO₂ in the Context of Anti-Cancer Therapy.....</i>	<i>40</i>
II.5 METHODS FOR QUANTITATIVE OXYGEN SENSING <i>IN VIVO</i>:.....	41
<i>II.5a Polarographic Methods:</i>	<i>41</i>
<i>II.5a Hemoglobin Saturation Spectrophotometry:.....</i>	<i>42</i>
<i>II.5b Histology – Molecular and Chemical Markers of Oxygenation Status.....</i>	<i>42</i>
<i>II.5c Phosphorescence Quenching Methods.....</i>	<i>44</i>
<i>II.5d Other Methods for Measuring Oxygen.....</i>	<i>46</i>
II.6 THE ROLE OF PH IN SOLID TUMORS	46
<i>II.6a Etiology of low pH in the metabolic microenvironment of tumors.....</i>	<i>47</i>
<i>II.6b Effect of Tumor pH on Progression</i>	<i>48</i>
<i>II.6c Implications of Tumor pH on Therapy.....</i>	<i>49</i>
II.7 <i>IN VIVO</i> METHODS FOR QUANTITATIVE PH SENSING IN TUMORS.....	49
<i>II.7a Invasive Techniques: Microelectrodes and More.....</i>	<i>50</i>
<i>II.7b Nuclear Magnetic Resonance Imaging and Spectroscopy.....</i>	<i>50</i>
<i>II.7c Optical Imaging of pH.....</i>	<i>51</i>
II.8 ANTIANGIOGENIC THERAPY AND “NORMALIZATION” OF THE TUMOR MICROENVIRONMENT	52
<i>II.8a Antiangiogenic Agents and Their Targets.....</i>	<i>52</i>

CONTENTS

II.8b	Normalization Hypothesis.....	53
II.8c	Trastuzumab as an Antiangiogenic Agent.....	55
II.9	INTRAVITAL MULTIPHOTON MICROSCOPY.....	56
II.9a	Principles of Multiphoton Microscopy.....	56
II.9b	Multiphoton Microscopy in Cancer Biology.....	58
II.10	LUMINESCENT SEMICONDUCTOR NANOCRYSTALS.....	59
II.11	FLUORESCENCE RESONANCE ENERGY TRANSFER AND SENSING.....	61
II.11a	Principles of FRET.....	61
II.11b	Examples of FRET using Fluorescent Nanocrystals.....	63
II.12	OPTICAL COHERENCE TOMOGRAPHY.....	65
II.12a	Principles and Techniques.....	66
II.12b	Application to Tumor Biology.....	67
II.13	SPECIFIC AIMS.....	69
II.13a	HYPOTHESIS 1. Phosphorescence Quenching MPM can provide quantitative pO_2 sensing in tumors.....	70
II.13b	HYPOTHESIS 2. NC-constructs can provide quantitative FRET-based pH sensing in tumors.....	71
II.13c	HYPOTHESIS 3. Optical frequency domain imaging can non-invasively perform three-dimensional microscopy of vascular networks, lymphatics, tissue viability and microanatomy in solid tumors.....	72
II.14	REFERENCES.....	73
III.	MULTIPHOTON PHOSPHORESCENCE QUENCHING MICROSCOPY.....	96
III.1	INTRODUCTION AND MOTIVATION:.....	97
III.2	EXPERIMENTAL DESIGN OF MP-PQM.....	98
III.2a	Time Domain versus Frequency Domain.....	99
III.2b	Experimental Setup.....	101
III.2c	MP-PQM Experiment Protocols.....	105
III.3	MULTIPHOTON EXCITATION OF Pd-PORPHYRIN pO_2 SENSOR.....	107
III.3a	Two-photon Excitation of Pd-porphyrin.....	108
III.3b	Phosphorescence Saturation.....	111
III.4	CALIBRATION OF MP-PQM pO_2 MEASUREMENTS.....	114
III.4a	Calibration Considerations.....	114
III.4b	Calibration Procedures.....	116
III.4c	Two-phase calibration.....	120
III.5	CHARACTERIZATION OF MP-PQM.....	123
III.5a	Photon Counting Bin Size.....	123
III.5b	Excitation Pulse Duration.....	124
III.5c	Phosphorescence Saturation – Practical Effects.....	126

CONTENTS

III.5d	<i>Instrument Response</i>	128
III.5e	<i>Two-photon Excitation Wavelength</i>	129
III.5f	<i>Measurement Resolution – Effects of Phosphor Diffusion and Flow</i>	132
III.5g	<i>Measurement Repeatability in vitro and in vivo</i>	138
III.6	<i>IN VIVO DEMONSTRATION AND APPLICATION</i>	138
III.6a	<i>Perturbation of Tissue Oxygenation</i>	139
III.6b	<i>Oxygenation of Skeletal Muscle – Krogh Tissue Cylinder Model</i>	142
III.7	<i>FURTHER CONSIDERATIONS AND FUTURE OUTLOOK FOR MP-PQM</i>	143
III.8	<i>SUMMARY</i>	147
III.9	<i>ADDITIONAL MATERIALS AND METHODS</i>	147
III.9a	<i>Animal Models</i>	147
III.9b	<i>Preparation of Oxygen Sensor</i>	148
III.10	<i>REFERENCES</i>	149
IV.	<i>IN VIVO HIGH-RESOLUTION THREE-DIMENSIONAL QUANTIFICATION OF PO₂ IN SOLID TUMORS</i>	154
IV.1	<i>INTRODUCTION AND MOTIVATION</i>	155
IV.2	<i>OXYGEN PROFILES IN SOLID TUMORS</i>	156
IV.3	<i>THREE-DIMENSIONAL MAPPING OF TUMOR OXYGENATION</i>	159
IV.3a	<i>Correlation of pO₂ and Vascular Metrics</i>	160
IV.3b	<i>Tumor Oxygen Consumption</i>	164
IV.4	<i>TUMOR OXYGENATION DURING GROWTH AND ACROSS MODELS</i>	167
IV.4a	<i>Tumor Growth: Angiogenesis and Oxygen</i>	167
IV.4b	<i>Tumor Growth: Depth Gradients in Oxygenation</i>	175
IV.5	<i>SPATIAL DISTRIBUTION OF TUMOR VASCULAR NETWORKS INFLUENCE TISSUE OXYGENATION</i>	176
IV.5a	<i>Cylindrical Models of Oxygen Diffusion in Tumors</i>	177
IV.5b	<i>In Vivo Oxygen Diffusion from Normal and Tumor Vascular Geometries</i>	178
IV.6	<i>TUMOR OXYGENATION DURING TARGETED THERAPY</i>	189
IV.6a	<i>Measurement of pO₂ in a Breast Tumor Model during Therapy with Trastuzumab</i>	190
IV.6b	<i>Measurement of pO₂ during VEGF-R2 Blockade</i>	193
IV.7	<i>SUMMARY</i>	197
IV.8	<i>MATERIALS AND METHODS</i>	200
IV.8a	<i>Animal Models</i>	200
IV.8b	<i>MP-PQM</i>	201
IV.8c	<i>Oxygen Tension Mapping Data Analysis</i>	202
IV.8d	<i>Numerical Simulations of Oxygen Profiles and Distributions from In Vivo Measurements</i>	204
IV.8e	<i>Invasion Percolation Model</i>	204

CONTENTS

IV.8f	Targeted Therapies	204
IV.8g	In vitro Trastuzumab Inhibition Assay.....	205
IV.8h	Statistical Analysis	205
IV.9	REFERENCES	206
V.	NANOCRYSTAL CONSTRUCT FRET-BASED PH SENSING IN SOLID TUMORS	213
V.1	INTRODUCTION AND MOTIVATION:	214
V.2	MULTIPHOTON MULTISPECTRAL AND FRIM SYSTEM.....	215
V.3	MULTIPHOTON EXCITATION OF NC-CONSTRUCTS.....	219
V.3a	Semiconductor Nanocrystals as Two-photon Antennas	220
V.3b	Multiphoton Excitation of NC pH Biosensor.....	221
V.4	BIOCOMPATIBILITY OF NC-BIOSENSORS	222
V.5	pH CALIBRATION	227
V.6	IN VIVO DEMONSTRATION OF NC-BIOSENSOR.....	232
V.6a	NC pH biosensors Measure Qualitative Changes in pH due to Glucose Administration.	233
V.6b	NC-biosensors are Unaffected In Vivo by Tissue Optical Properties	239
V.7	SUMMARY	240
V.8	ADDITIONAL MATERIALS AND METHODS.....	240
V.8a	Animal Models	240
V.8b	In vivo Biocompatibility Studies	241
V.8c	In Vitro Calibration Measurements.....	242
V.8d	Ex Vivo Tumor Tissue Calibration.....	242
V.8e	Ex Vivo Calibration in Tumor Cell Slurry	243
V.8f	In Vivo Hyperglycemia Experiments.....	244
V.8g	Statistical Analysis	244
V.9	REFERENCES	245
VI.	THREE-DIMENSIONAL MICROSCOPY OF VASCULAR NETWORKS, LYMPHATICS, CELL VIABILITY AND TISSUE MICROENVIRONMENT IN VIVO USING OPTICAL FREQUENCY DOMAIN IMAGING	248
VI.1	INTRODUCTION AND MOTIVATION:	249
VI.2	NOVEL OFDI INSTRUMENTATION AND METHODS.....	250
VI.3	WIDE-FIELD THREE-DIMENSIONAL ANGIOGRAPHY.....	251
VI.3a	Neoplastic and Normal Microvasculature Across Types and Sites.....	252
VI.3b	Monitoring Angiogenesis	254
VI.3c	OFDI complements MPM in Imaging Tumor Vasculature.....	256
VI.4	MORPHOLOGICAL AND FRACTAL CHARACTERIZATION OF VASCULAR NETWORKS	258

CONTENTS

VI.4a	<i>Vascular Morphology from OFDI Angiograms</i>	258
VI.4b	<i>Three-dimensional Fractal Analysis of Tumor Vasculature</i>	261
VI.5	IMAGING VASCULAR DYNAMICS DURING TUMOR GROWTH AND TREATMENT.....	261
VI.6	CONTRAST-FREE LYMPHANGIOGRAPHY.....	263
VI.7	IMAGING TISSUE VIABILITY.....	265
VI.8	MULTIPARAMETRIC MONITORING OF THERAPEUTIC RESPONSE.....	267
VI.8a	<i>Antiangiogenic Therapy: VEGF-R2 Blockade</i>	268
VI.8b	<i>Cytotoxic Therapy: Diphtheria Toxin</i>	270
VI.9	DISCUSSION.....	273
VI.10	SUMMARY.....	274
VI.11	MATERIALS AND METHODS.....	275
VI.11a	<i>OFDI system</i>	275
VI.11b	<i>OFDI Signal and Image Processing and Quantification</i>	277
VI.11c	<i>Three-Dimensional Tumor Volume and Boundary Calculation</i>	279
VI.11d	<i>Normalized Scattering/Viability</i>	279
VI.11e	<i>Quantification of Viable Fraction</i>	280
VI.11f	<i>Animal models</i>	281
VI.11g	<i>Anti-angiogenic therapy: VEGF-R2 blockade</i>	282
VI.11h	<i>Cytotoxic therapy</i>	282
VI.11i	<i>Prolonged time-lapse imaging</i>	282
VI.11j	<i>Quantitative Angiography</i>	283
VI.11k	<i>Fractal Analysis</i>	285
VI.11l	<i>Visualization</i>	286
VI.11m	<i>Quantitative Lymphangiography</i>	286
VI.11n	<i>Multiphoton microscopy and registration</i>	287
VI.11o	<i>Statistical analysis</i>	288
VI.12	REFERENCES.....	288
VII.	CONCLUDING STATEMENTS AND FUTURE DIRECTIONS	292
VII.1	INTRODUCTION:.....	293
VII.2	OPTIMIZING AND ADVANCING MP-PQM.....	295
VII.3	NEW NC-BIOSENSOR CONSTRUCTS AND DESIGNS.....	296
VII.4	FUTURE DIRECTIONS OF OFDI IN CANCER BIOLOGY.....	299
VII.5	CONCLUDING STATEMENTS.....	304
VII.6	REFERENCES.....	305

CONTENTS

ACKNOWLEDGEMENTS.....307
CURRICULUM VITAE.....311

CONTENTS

List of Figures

FIGURE II-1 INTRAVITAL OPTICAL MICROSCOPY OF MURINE WINDOW CHAMBER MODELS.-----	32
FIGURE II-2 QUENCHING OF PHOSPHORESCENCE BY MOLECULAR OXYGEN.-----	43
FIGURE II-3 PRINCIPLES OF MULTIPHOTON EXCITATION.-----	56
FIGURE II-4 FLUORESCENT SEMICONDUCTOR NANOCRYSTALS: PROPERTIES AND <i>IN VIVO</i> IMAGING.-----	59
FIGURE II-5 FRET-BASED SENSING USING SEMICONDUCTOR NANOCRYSTALS.-----	63
FIGURE II-6 FRET-BASED NC BIOSENSOR FOR PH IN THE PHYSIOLOGICAL RANGE FOUND IN TUMORS. ---	64
FIGURE II-7 BASIC PRINCIPLES OF OPTICAL COHERENCE TOMOGRAPHY.-----	68
FIGURE III-1 METHODS TO MEASURE LUMINESCENT LIFETIME.-----	99
FIGURE III-2 MULTIPHOTON PHOSPHORESCENCE QUENCHING MICROSCOPY SETUP.-----	103
FIGURE III-3 CUSTOM USER INTERFACE FOR MP-PQM EXPERIMENTS.-----	105
FIGURE III-4 MP-PQM EXPERIMENTAL PROTOCOLS FOR <i>IN VIVO</i> MEASUREMENTS.-----	106
FIGURE III-5 TWO-PHOTON EXCITATION OF PD-PORPHYRIN PHOSPHORESCENT OXYGEN SENSOR.-----	108
FIGURE III-6 <i>IN VIVO</i> TWO-PHOTON EXCITATION OF PD-PORPHYRIN OXYGEN SENSOR.-----	109
FIGURE III-7 SINGLE- AND TWO-PHOTON ACTION CROSS-SECTIONS FOR PD-PORPHYRIN SOLUBLE OXYGEN SENSOR. -----	110
FIGURE III-8 RECIRCULATING SEALED CALIBRATION SYSTEM EMPLOYING A FIBER OXYGENATOR.-----	116
FIGURE III-9 MP-PQM CALIBRATION OF OXYPHOR R2: IN THE ABSENCE (A) AND PRESENCE (B) OF VARYING BSA CONCENTRATIONS.-----	118
FIGURE III-10 SCHLENK LINE FREEZE-PUMP-THAW METHOD.-----	119
FIGURE III-11 MP-PQM DISECERNS TWO SPECIES OF PHOSPHOR IN THE PRESENCE OF ALBUMIN.-----	121
FIGURE III-12 CALIBRATION OF THE FREE (LEFT) AND ALBUMIN BOUND (RIGHT) PHOSPHOR SPECIES USING MP- PQM.-----	123
FIGURE III-13 EFFECT OF PHOTON COUNTING BIN SIZE ON MEASURED LIFETIME.-----	124
FIGURE III-14 EFFECT OF EXCITATION PULSE DURATION ON MEASURED PHOSPHORESCENCE LIFETIME FOR BOTH 0% (A) AND 5% (B) BSA.-----	125
FIGURE III-15 PHOSPHORESCENCE SATURATION DURING THE EXCITATION PULSE OF MP-PQM AT DIFFERENT OXYGEN TENSION.-----	127
FIGURE III-16 EXCITATION LASER MP-PQM PULSE INCIDENT ON THE SAMPLE.-----	129
FIGURE III-17 CHANGE IN PHOSPHORESCENCE LIFETIME DUE TO TWO-PHOTON EXCITATION WAVELENGTH. -----	130
FIGURE III-18 DIFFUSION OF OXYGEN CENTER FROM CENTER OF FOCAL VOLUME FOR DIFFERENT OXYGEN TENSIONS.-----	133

CONTENTS

FIGURE III-19 THREE-DIMENSIONAL CONCENTRATION PROBABILITY PROFILES DETERMINE THE VOLUME RESOLUTION OF MP-PQM.-----	135
FIGURE III-20 MEASUREMENT VOLUME FOR MP-PQM.-----	136
FIGURE III-21 VOLUME RESOLUTION DISPLACEMENT DURING INTRAVASCULAR MP-PQM MEASUREMENTS IN UNIDIRECTIONAL FLOWS.-----	137
FIGURE III-22 MP-PQM MEASUREMENT ERROR.-----	138
FIGURE III-23 HYPEROXIA IN NORMAL MURINE SKIN QUANTIFIED BY MP-PQM.-----	140
FIGURE III-24 MURINE SKELETAL MUSCLE OXYGENATION.-----	141
FIGURE III-25 DORSAL SKINFOLD CHAMBER IMPLANTED ON A SCID MOUSE.-----	148
FIGURE IV-1 VASCULAR OXYGEN PROFILES FROM SIMILARLY SIZED VESSELS IN TUMORS AND NORMAL TISSUE.-----	157
FIGURE IV-2 NANOVASCULAR SURGERY USING MULTIPHOTON MICROSCOPY.-----	158
FIGURE IV-3 THREE-DIMENSIONAL MAPPING OF TUMOR OXYGENATION USING MP-PQM.-----	159
FIGURE IV-4 CORRELATION OF PO_2 WITH VASCULAR METRICS.-----	162
FIGURE IV-5 TUMOR OXYGEN PROFILES AND CONSUMPTION.-----	164
FIGURE IV-6 ANGIOGENESIS DURING TUMOR GROWTH.-----	168
FIGURE IV-7 COMPARISON OF TUMOR VASCULAR NETWORKS AT DAY 0 (<i>TOP</i>) AND 9 (<i>BOTTOM</i>).-----	170
FIGURE IV-8 DEPTH GRADIENTS IN PO_2 DURING TUMOR GROWTH.-----	175
FIGURE IV-9 CYLINDRICAL GEOMETRY FOR DESCRIBING DIFFUSIVE PROCESSES.-----	177
FIGURE IV-10 NORMAL AND TUMOR TISSUE VASCULAR NETWORKS DESCRIBED BY NUMBER OF TISSUE VOXELS AT A GIVEN DISTANCE FROM A VESSEL.-----	179
FIGURE IV-11 MODELING THE DIFFUSION OF A SMALL MOLECULE IN AN ARBITRARILY DEFINED GEOMETRY USING $n\delta$.-----	180
FIGURE IV-12 FINITE VOLUME METHOD TO NUMERICALLY CALCULATE CONCENTRATION PROFILES FOR THE GENERALIZED SOLUTION TO THE DIFFUSION FROM AN ARBITRARY VASCULAR NETWORK.-----	182
FIGURE IV-13 NUMERICAL SIMULATIONS USING THE FINITE VOLUME METHOD TO DETERMINE STEADY STATE OXYGEN CONCENTRATION PROFILES FOR GENERALIZED FUNCTIONS OF $n(\delta)$.-----	184
FIGURE IV-14 <i>IN VIVO</i> PO_2 PROFILES FOR NORMAL AND NEOPLASTIC TISSUE DETERMINED FROM MP-PQM MEASUREMENTS.-----	185
FIGURE IV-15 <i>IN VIVO</i> OXYGEN TENSION PROBABILITY DISTRIBUTIONS.-----	186
FIGURE IV-16 NUMERICAL CALCULATION OF OXYGEN PROFILES AND ASSOCIATED OXYGEN PROBABILITY DISTRIBUTIONS FROM <i>IN VIVO</i> MEASUREMENTS OF $n(\delta)$.-----	187
FIGURE IV-17 INVASION PERCOLATION NETWORKS REVEAL LARGE AVASCULAR REGIONS AND DEFINE $n(\delta)$.-----	188
FIGURE IV-18 BREAST TUMOR RESPONSE TO HERCEPTIN.-----	190

CONTENTS

FIGURE IV-19 IN VITRO HER2 ASSAY OF MDA-MB-361HK IN COMPARISON TO OTHER CELL LINES.-----	191
FIGURE IV-20 MURINE MAMMARY CARCINOMA (MCAIV) RESPONSE TO VEGF-R2 BLOCKADE.-----	192
FIGURE IV-21 HUMAN COLORECTAL ADENOCARCINOMA XENOGRAFT (LS174T) RESPONSE TO VEGF-R2 BLOCKADE. -----	194
FIGURE IV-22 ORTHOTOPIC MURINE MAMMARY ADENOCARCINOMA (EO771) RESPONSE TO VEGF-R2 BLOCKADE. -----	195
FIGURE IV-23 PRUNING OF THE VASCULAR NETWORK IN AN EO771 TUMOR BY VEGF-R2 BLOCKADE WITH DC101. -----	197
FIGURE V-1 TWO-PHOTON EXCITATION OF BCECF.-----	214
FIGURE V-2 SETUP FOR RATIOMETRIC PH MEASUREMENTS USING MULTIPHOTON MICROSCOPY.-----	216
FIGURE V-3 RATIOMETRIC IMAGING OF NC-BIOSENSOR CONSTRUCTS WITH MULTIPHOTON MICROSCOPY. -----	217
FIGURE V-4 PMT RESPONSE OVER TIME FOR RATIOMETRIC IMAGING WITH NCS.-----	218
FIGURE V-5 TWO PHOTON EXCITATION OF NC-CXR CONSTRUCT: DEMONSTRATION OF A TWO-PHOTON ANTENNA. -----	219
FIGURE V-6 NORMALIZED TWO-PHOTON ACTION CROSS-SECTIONS FOR AN NC-SNARF PH BIOSENSOR COMPARED TO ITS FREE COMPONENTS. -----	222
FIGURE V-7 NC-CONSTRUCT <i>IN VIVO</i> BIOCOMPATIBILITY AFTER INTRAVENOUS INJECTION. -----	223
FIGURE V-8 <i>IN VIVO</i> EXTRAVASATION OF DHLA-PEG NANOCRYSTAL CONSTRUCTS FROM THE TUMOR VASCULATURE. -----	224
FIGURE V-9 <i>IN VIVO</i> DISTRIBUTION OF NC-CXR CONSTRUCTS FUNCTIONALIZED WITH VARIOUS BIOCOMPATIBLE LIGANDS.-----	225
FIGURE V-10 MULTIPHOTON RATIOMETRIC SPECTRAL CALIBRATION OF AN NC-SNARF PH BIOSENSOR IN PBS. -----	227
FIGURE V-11 CALIBRATION OF NC-SNARF PH BIOSENSOR IN PHOSPHATE BUFFERED SALINE WITH 4% BOVINE SERUM ALBUMIN.-----	228
FIGURE V-12 CALIBRATION USING MULTIPHOTON FRIM.-----	229
FIGURE V-13 <i>EX VIVO</i> MP-FRIM CALIBRATION OF NC-BIOSENSOR.-----	230
FIGURE V-14 COMPARISON OF PH CALIBRATIONS WITH THE NC PH BIOSENSOR USING MP-FRIM IN BOTH SOLUTION AND <i>EX VIVO</i> TUMOR TISSUE. -----	231
FIGURE V-15 METABOLIC ACIDOSIS DUE TO INTRAMUSCULAR ANESTHETICS.-----	233
FIGURE V-16 ACIDOSIS OF THE TUMOR MICROENVIRONMENT DUE TO HYPERGLYCEMIA.-----	235
FIGURE V-17 <i>IN VIVO</i> PH SENSING DURING HYPERGLYCEMIA USING METHOXY-PEG NC-BIOSENSORS. --	236
FIGURE V-18 MP-FRIM RATIOMETRIC IMAGES WITH THE TUMOR VASCULATURE IMAGED BY MPM. ---	238

CONTENTS

FIGURE V-19 NC-CXR CONTROL CONSTRUCT DEMONSTRATES NO RATIOMETRIC CHANGE WITH PH ALTERATION BY GLUCOSE ADMINISTRATION.-----	239
FIGURE V-20 DIFFERENCES IN TISSUE SCATTERING WITH DEPTH FOR THE NC AND SNARF EMISSION CHANNELS OVER THE COURSE OF A HYPERGLYCEMIA EXPERIMENT.-----	243
FIGURE VI-1 PRINCIPLES OF <i>IN VIVO</i> MULTIPARAMETRIC IMAGING WITH OPTICAL FREQUENCY DOMAIN IMAGING (OFDI).-----	251
FIGURE VI-2 OFDI ANGIOGRAPHY ACROSS TUMOR TYPES AND SITES.-----	252
FIGURE VI-3 OFDI ANGIOGRAPHY OF NORMAL TISSUES.-----	253
FIGURE VI-4 IMAGING ACROSS TISSUE MICROENVIRONMENTS REVEALS STRIKINGLY DIFFERENT VASCULAR NETWORKS.-----	254
FIGURE VI-5 ANGIOGENESIS IN A MURINE MAMMARY CARCINOMA MODEL.-----	255
FIGURE VI-6 COMPARISON OF MULTIPHOTON AND OFDI ANGIOGRAPHY.-----	256
FIGURE VI-7 VASCULAR TRACING AND STRUCTURAL CORRELATION.-----	257
FIGURE VI-8 DETERMINATION OF TUMOR BOUNDARIES AND VOLUME IN THREE-DIMENSIONAL SPACE.-----	259
FIGURE VI-9 FRACTAL CHARACTERIZATION OF TUMOR VASCULAR NETWORKS IMAGED BY OFDI ANGIOGRAPHY.-----	260
FIGURE VI-10 VASCULAR DYNAMICS OF FIELDS AND TIME INTERVALS NOT ACCESSIBLE WITH TRADITIONAL APPROACHES.-----	262
FIGURE VI-11 CONTRAST-FREE LYMPHANGIOGRAPHY USING OFDI.-----	263
FIGURE VI-12 LONGITUDINAL TRACKING OF LYMPHATICS USING OFDI.-----	265
FIGURE VI-13 IMAGING TISSUE VIABILITY.-----	266
FIGURE VI-14 ANTIANGIOGENIC RESPONSE TO VEGF-R2 BLOCKADE IMAGED BY OFDI.-----	267
FIGURE VI-15 THERAPEUTIC RESPONSE TO VEGFR-2 BLOCKADE CHARACTERIZED BY OFDI.-----	269
FIGURE VI-16 DC101 TREATMENT RESTRAINS INTRATUMORAL VASCULAR GROWTH NEAR TUMOR MARGIN.-----	270
FIGURE VI-17 DIRECTED CYTOTOXIC THERAPY AND MULTIPARAMETRIC ANALYSIS BY OFDI.-----	271
FIGURE VI-18 QUANTIFICATION OF THE RESPONSE OF AN LS174T TUMOR IMPLANTED IN THE DORSAL SKINFOLD CHAMBER TO A SINGLE DIPHTHERIA TOXIN ADMINISTRATION.-----	272
FIGURE VI-19 OFDI INSTRUMENTATION.-----	275
FIGURE VI-20 SIGNAL PROCESSING ALGORITHMS AND QUANTITATIVE ANALYSIS.-----	277
FIGURE VI-21 METHOD FOR DETERMINING VIABLE/NECROTIC FRACTIONS WITH OFDI.-----	280
FIGURE VII-1 NANOCRYSTAL BIOSENSOR FOR OXYGEN.-----	297
FIGURE VII-2 <i>IN VIVO</i> IMAGING OF NC-IMMUNOCONSTRUCTS, FIBROBLAST-LIKE STROMAL CELLS, AND COLLAGEN MATRIX IN A SARCOMA TUMOR MODEL.-----	298
FIGURE VII-3 ANGLE-RESOLVED OFDI OF NORMAL MURINE SKIN IN THE DSC.-----	301

CONTENTS

FIGURE VII-4 HIGHER DOPPLER BACKGROUND SIGNAL OBSERVED IN A HUMAN GLIOBLASTOMA XENOGRAFT.

----- 302

FIGURE VII-5 *IN VIVO* MICROARCHITECTURE AND PERFUSION OF MURINE MAMMARY DUCTS IMAGED BY OFDI.

----- 303

List of Tables

TABLE III-1: STERN-VOLMER QUENCHING CONSTANTS DETERMINED BY LINEAR REGRESSION FOR SINGLE EXPONENTIAL DECAY.....	118
TABLE III-2: OXYPHOR R2 CALIBRATED LIFETIME IN ANOXIC CONDITIONS (τ_0).....	120
TABLE IV-1: CORRELATION OF PO ₂ WITH VESSEL DIAMETER (D) OR INTERSTITIAL DISTANCE (R) ACROSS MULTIPLE TUMORS.....	160
TABLE IV-2 CORRELATION OF PO ₂ WITH VESSEL DIAMETER (D) AND INTERSTITIAL DISTANCE (R) IN NORMAL TISSUES.....	161
TABLE IV-3: MEAN OXYGEN CONSUMPTION ACROSS TUMOR TYPES.....	165
TABLE IV-4: COMPARISON OF MEAN TUMOR OXYGENATION (MMHG).....	167
TABLE IV-5: COMPARISON OF MEAN VASCULAR RADIUS (μ M).....	169
TABLE IV-6: COMPARISON OF VASCULAR VOLUME FRACTION.....	169
TABLE IV-7: HYPOXIC FRACTION DURING TUMOR GROWTH.....	171
TABLE IV-8: DISTANCE (μ M) FROM HYPOXIC REGIONS TO CLOSEST VESSEL.....	172
TABLE IV-9: CORRELATION OF VASCULAR METRICS WITH TUMOR OXYGENATION AND HYPOXIC FRACTION OVER TIME.....	173
TABLE V-1: SUMMARY OF NC CONSTRUCT RESULTS <i>IN VITRO</i> AND <i>IN VIVO</i>	226

CONTENTS

List of Abbreviations

μm	micron (1×10^{-6} meters)
AOM	<u>A</u> cousto- <u>o</u> ptic <u>m</u> odulator
APD	<u>A</u> valanche <u>P</u> hotodiode
AR	<u>A</u> nti- <u>R</u> eflective
b/w-	<u>b</u> y <u>w</u> eight
BCECF	2',7'- <u>b</u> is-(2- <u>c</u> arboxy <u>e</u> thyl)-5-(and-6)- <u>c</u> arboxy <u>f</u> luorescein
BSA	<u>B</u> ovine <u>S</u> erum <u>A</u> lbumin
CA IX	<u>C</u> arbonic <u>A</u> nhydrase 9
CdSe	Cadmium-Selenide
CFD	<u>C</u> umulative <u>F</u> requency <u>D</u> istribution
CXR	<u>C</u> arboxy- <u>X</u> - <u>R</u> hodamine
CW	<u>C</u> ranial <u>W</u> indow
DHLA	<u>D</u> ihydro <u>l</u> ipoic <u>A</u> cid
DSC	<u>D</u> orsal <u>S</u> kinfold <u>C</u> hamber
EO771	Murine mammary carcinoma
EOM	<u>E</u> lectro- <u>o</u> ptic <u>m</u> odulator
FITC	<u>F</u> luorescein <u>I</u> so <u>t</u> hiocyanate
FOV	<u>F</u> ield <u>o</u> f <u>V</u> iew
FRAP	<u>F</u> luorescence <u>R</u> ecovery <u>a</u> fter <u>P</u> hotobleaching

CONTENTS

FRET	<u>F</u> luorescence (or <u>F</u> örster) <u>R</u> esonance <u>E</u> nergy <u>T</u> ransfer
FRIM	<u>F</u> luorescence <u>R</u> atiometric <u>I</u> maging
Fs	<u>f</u> emto <u>s</u> econd
FWHM	<u>F</u> ull- <u>w</u> idth <u>h</u> alf <u>m</u> aximum
GaAs	<u>G</u> allium <u>A</u> rsenide
GDD	<u>G</u> roup <u>D</u> elay <u>D</u> ispersion
GFP	<u>G</u> reen <u>F</u> luorescent <u>P</u> rotein
GLUT1	<u>G</u> lucose <u>T</u> ransporter Type <u>1</u>
GM	<u>G</u> öppert- <u>M</u> ayer : $1 \times 10^{-50} \text{ cm}^4 \text{ s}$
HER2	<u>H</u> uman <u>E</u> pidermal growth factor <u>R</u> eceptor <u>2</u>
HIF-1	<u>H</u> ypoxia <u>I</u> nducible <u>F</u> actor-1
HSTS26T	Human soft-tissue sarcoma
IgG	<u>I</u> mmunoglobulin <u>G</u>
kDa	<u>k</u> ilo <u>D</u> alton: 1×10^3 Daltons
LCTF	<u>L</u> iquid <u>C</u> rystal <u>T</u> unable <u>F</u> ilter
LS174T	Human colorectal adenocarcinoma
MCalV	murine mammary carcinoma
MDA-MB-361HK	Human breast adenocarcinoma
MFP	<u>M</u> ammary <u>F</u> at <u>P</u> ad
MGH	<u>M</u> assachusetts <u>G</u> eneral <u>H</u> ospital

CONTENTS

Mhz	megahertz
MIT	<u>Massachusetts Institute of Technology</u>
mm	<u>millimeter</u>
MP-FRIM	<u>Multiphoton Fluorescence Ratiometric Imaging</u>
MPM	<u>Multiphoton Microscopy</u> (also known as MPLSM – <u>Multiphoton Laser Scanning Microscopy</u>)
MP-PQM	<u>Multiphoton Phosphorescence Quenching Microscopy</u>
MRS	<u>Magnetic Resonance Spectroscopy</u>
MU89	Human melanoma
MVD	<u>Microvascular Density</u>
NA	<u>Numerical Aperture</u>
NADH	<u>Nicotinamide Adenine Dinucleotide (reduced)</u>
NC	<u>Nanocrystal</u>
NF-κB	<u>Nuclear Factor κB</u>
NHS	<u>N-hydroxysulfosuccinimide</u>
NIR	<u>Near Infrared</u>
nm	<u>nanometer</u>
OCT	<u>Optical Coherence Tomography</u>
OFDI	<u>Optical Frequency Domain Imaging</u>
PBS	<u>Phosphate Buffered Saline</u>
Pd	<u>Palladium</u>

CONTENTS

PEG	<u>P</u> oly <u>e</u> thylene <u>G</u> lycol
pHe	<u>e</u> xtracellular pH
PMT	<u>P</u> hoto <u>m</u> ultiplier <u>T</u> ube
PMT	<u>P</u> hoto <u>m</u> ultiplier <u>T</u> ube
pO₂	partial pressure of molecular oxygen (O ₂); a.k.a <u>oxygen tension</u> .
PQM	<u>P</u> hos <u>ph</u> orescence <u>Q</u> u <u>e</u> nching <u>M</u> icroscopy
QE	<u>Q</u> uantum <u>E</u> fficiency
RBC	<u>R</u> ed <u>B</u> lood <u>C</u> ell
ROI	<u>R</u> egion <u>o</u> f <u>I</u> nterest
SCID	<u>S</u> evere <u>C</u> ombined <u>I</u> mmunode <u>f</u> iciency
SE	<u>S</u> tandard <u>E</u> rror
SHG	<u>S</u> econd <u>H</u> armonic <u>G</u> eneration
SNARF-5F	<u>s</u> em <u>i</u> n <u>a</u> phthor <u>h</u> od <u>a</u> fluor- <u>5</u> F 5-(and-6)-carboxylic acid
SNR	<u>S</u> ignal to <u>N</u> oise <u>R</u> atio
STED	<u>S</u> timulated <u>E</u> mission <u>D</u> epletion Microscopy
UV	<u>U</u> ltraviolet
VEGF	<u>V</u> ascular <u>E</u> ndothelial <u>G</u> rowth <u>F</u> actor
WAD	<u>W</u> ide <u>A</u> rea <u>D</u> etection
ZnS	<u>Z</u> inc <u>S</u> ulfide

I. Original Contributions

CHAPTER 1

The microenvironment of solid tumors is complex and heterogeneous consisting of a variety of cell types. The interactions between the components of the tumor microenvironment and pathophysiology are not well understood. This Thesis focuses on studying the metabolic microenvironment and microvasculature, both critical determinants of disease progression and response to therapy. The overall goal is to develop new minimally invasive tools to perform multiparametric analysis of the tumor microenvironment during both tumor growth and response to therapy.

Oxygen is a key player in the metabolic microenvironment of tumors, which is typically characterized by hypoxia. Techniques exist to measure *in vivo* oxygen tension (pO_2), however each method has its intrinsic limitations. No single technique exists to perform high-resolution spatio-temporal quantification of pO_2 in the context of the tumor microenvironment. In this Thesis I develop a method to quantitatively measure oxygen tension by applying the principles of phosphorescence quenching to multiphoton microscopy (MP-PQM; Chapter 3). I demonstrate that MP-PQM is able to measure oxygen in the interstitial space with a resolution as low as $1\mu m^3$ using phosphorescent palladium-porphyrins, previously believed to be unattainable due to transport characteristics of the porphyrin oxygen sensors. The two-photon excitation properties of Pd-porphyrin is fully characterized for the first time including the effects of phosphorescence saturation, an important consideration using mode-locked pulsed laser sources, and the theoretical *in vivo* resolution. Finally, I show that the Krogh tissue cylinder model for oxygen diffusion in skeletal muscle may not be applicable in real-world capillary networks due to the anisotropic arrangement of the muscle fibers.

In the tumor microenvironment, oxygen has been shown to be heterogeneous and many models have been postulated to explain the tumor oxygenation due to the vascular geometry. However, few direct measurements of tumor pO_2 exist with spatial correlation to the tumor vasculature. Secondly, the effect of targeted anti-cancer therapies, such as antiangiogenic agents, on the tumor pO_2 is not well known. Here, I develop a method to map oxygen tension onto the tumor vasculature with high three-

dimensional resolution and deep penetration ($\sim 400\mu\text{m}$) using MP-PQM (Chapter 4). With this technique, I illustrate the differences in oxygen consumption and spatio-temporal profiles in pO_2 across a variety of tumor types. Further, I introduce a model to predict tumor oxygenation and tissue pO_2 profiles using a simple metric describing the microvasculature and associated tissue volumes. The results exhibit good agreement with *in vivo* oxygen measurements using MP-PQM. Finally, the metabolic tumor microenvironment is probed with MP-PQM during either VEGF-R2 blockade or trastuzumab (Herceptin) treatment. Both are treatment protocols translatable to clinical treatments. The results suggest that antiangiogenic therapies should be titrated for a limited dose response to transiently increase pO_2 and therefore the efficacy of radiation therapy and many chemotherapeutics.

A related metabolic parameter to pO_2 is the pH of the tumor microenvironment, which is often found to be acidic. The pH gradients found in tumors across the cancer cell membranes have protective effects against many chemotherapeutics, reducing their cytotoxicity. More understanding is needed about how this parameter changes during tumor progression and therapy so that therapeutic regimens with better prognostic outcome can be designed. To this end, I introduce a novel Förster resonance energy transfer (FRET)-based semiconductor nanocrystal (NC; also known as quantum dots) biosensor, developed in collaboration with investigators from the Bawendi and Nocera labs at MIT, for *in vivo* measurements of pH in tumors (Chapter 5). I show that nanocrystals act as a two-photon antenna, conferring the ideal photophysical properties of the NC to acceptor dyes under excitation in the nonlinear regime with MPM. Through multiple evolutions of NC construct design, a biocompatible pH sensor with limited non-specific interactions is developed and shown to qualitatively measure pH. Finally, the NC-biosensor is demonstrated to perform ratiometric pH measurements during hyperglycemia in the tumor microenvironment and correlate the results with the local tumor vasculature using multiphoton fluorescence ratiometric imaging. Further, I present sensing schemes and evidence of NC-biosensors for other analytes important in

CHAPTER 1

tumor biology as well as the potential for targeting these constructs to the tumor microenvironment(Chapter 7).

While the metabolic microenvironment plays a critical role in tumor progression and therapeutic response, other components of the tumor microenvironment also influence the same parameters. Methods exist to assess each component individually although many are invasive or require administration of exogenous contrast agents. A non-invasive multiparametric imaging method is needed to characterize the tumor microenvironment. In collaboration with investigators in the Wellman Labs, we show that optical frequency domain imaging (OFDI) is capable of simultaneously imaging the tumor vasculature, lymphatics, tissue viability and tumor microanatomy with high-resolution over significant tissue volumes (Chapter 6). Through the development of novel techniques, instrumentation and algorithms, we demonstrate the unique capabilities of OFDI to quantitatively image *in vivo* the microenvironment of model tumors rapidly and persistently over time without requiring exogenous contrast agents. We also show that OFDI can study the multiparametric response to both vascular- and cellular-targeted therapies. The abilities of OFDI for studying tumor biology are impressive and I introduce additional concepts that may potentially permit non-invasive measurement of blood flow velocity, vascular permeability, macromolecular transport, cellular metabolism, edema and spontaneous tumorigenesis (Chapter 7).

The technologies introduced and developed in this Thesis are hopefully only the beginning of a new era in non-invasive multiparametric analysis of the tumor microenvironment. Many unanswered questions about *in vivo* cancer biology and response to treatment remain and additional tools are always needed to find solutions and pose new more directed questions. Each new step in advancing our understanding of the tumor microenvironment may help develop new methods and drugs for treating cancer translatable to the clinic.

II. Introduction and Specific Aims

II.1 Introduction and Motivation:

Solid tumors are complex and heterogeneous tissues consisting of a variety of cell types. The tumor microenvironment can be ascribed to all components outside of the tumor cells themselves. This is a broad definition encompassing the vasculature, stromal cells, extracellular matrix, host tissues and metabolic parameters. All of these biological components have been shown to play a critical role in both tumor progression and treatment¹. *In vivo* heterotypic interactions between the tumor microenvironment and the cancer cells themselves are multifaceted and not well understood. New minimally invasive tools are needed to perform multiparametric analysis of the tumor microenvironment to elucidate these underlying mechanisms.

This Thesis will focus on the development of quantitative *in vivo* imaging tools that probe the tumor microenvironment. In particular, this work focuses on studying the metabolic microenvironment and microvasculature, both important determinants of disease progression and therapeutic response. In this Chapter, I define the metabolic microenvironment and its important implications on tumor growth, metastasis, and therapy. I also describe the anatomical and molecular characteristics of the blood and lymphatic vasculature of solid tumors including consequences of antiangiogenic therapy. The advances and limitations of current techniques for studying both the tumor vasculature and metabolic microenvironment are also described. Finally, I give a brief background of the technologies employed in this Thesis: multiphoton microscopy, fluorescent semiconductor nanocrystals and optical coherence tomography. This Chapter concludes with the specific aims and hypotheses driving the work presented in the following Chapters.

II.2 Metabolic Microenvironment

Hypoxia and low pH are hallmarks of the tumor microenvironment. These physiologic parameters are important determinants of tumor growth, gene expression², metastatic potential³, metabolism, prognosis⁴⁻⁶, and response to therapy^{7,8}. Additionally, these

physiological parameters vary with tumor location in the host and within the same tumor from one day to the next⁹⁻¹². Furthermore, oxygen consumption and increased metabolic waste by cancer and endothelial cells coupled with poor perfusion by abnormal tumor vasculature contribute to the hypoxic and acidic environment of the tumor¹³. Oxygen sensitizes a tissue to radiation¹⁴; therefore, the hypoxic tumor microenvironment effectively shields cancer cells from radiotherapy. Additionally, many chemotherapeutics, such as paclitaxel, are pH sensitive and demonstrate reduced cytotoxic efficacy at the acidic pH's found in solid tumors^{8,15}. Thus, further understanding of the dynamic relationship between pO₂ and pH in the tumor microenvironment during disease progression and treatment is critical to improve response to therapy.

Energy metabolism in tumors is complex and experimental studies have provided contradictory results. *In vitro* studies have demonstrated that the rate of oxygen consumption is dependent on both pO₂ and glucose^{16,17}. The Warburg hypothesis proposes that cancer cell oxidative metabolism is grossly disturbed instead relying on glycolysis¹⁸. However, this concept has been challenged because many cancers demonstrate high levels of oxygen consumption¹⁹⁻²¹. Further, it has long been known that many tumor types demonstrate high levels of respiration (oxidative metabolism) relative to aerobic or anaerobic glycolysis²². High levels of glycolysis increases the concentration of lactic acid in tissue and thus was believed to be the sole source of acidic pH. However, resultant tumor acidity has also been attributed to increased carbon dioxide (CO₂) due to oxidative respiration²³. Interestingly, an *in vivo* study simultaneously measuring pO₂ and pH demonstrated no correlation between the two metabolic indicators²⁴, suggesting that tumor cell metabolism is uncoupled utilizing whatever substrates (oxygen and/or glucose) are available.

II.3 Vasculature of the Tumor Microenvironment

Two types of vasculature, blood and lymphatic, play critical roles in cancer progression and response to treatment. In solid tumors both are abnormal structurally and

functionally contributing to pathophysiology. Intravital microscopy methods have permitted *in situ* visualization of both vascular networks in the tumor microenvironment²⁵⁻³¹. Additional techniques have provided insights into *in vivo* function (or dysfunction) of the tumor microvasculature and their impact on transport, metastasis and treatment^{13,32-38}. It should be noted that cancer is a complex disease and the characteristics of the vascular networks, like the metabolic microenvironment is heterogeneous across tumor types and even within a single tumor.

II.3a BLOOD AND LYMPHATIC VASCULATURE: STRUCTURE AND FUNCTION

Tumor vascular networks are morphologically irregular consisting of dilated and tortuous vessels with ill-defined routes of transport typified by blind ends and loops^{29,39-41}. Flow through the blood vessels is intermittent and heterogeneous with many regions of stasis or flow reversal⁴²⁻⁴⁶. Both the abnormal structure and high hematocrit in tumors influence the variable resistance to fluid flow in the tumor vasculature^{47,48}. Additionally, heterogeneous expression of vascular cell surface markers reduces leukocyte-endothelial cell interactions in the tumor vasculature⁴⁹. The vascular wall in tumors is also found to be immature in cellular makeup leading to high permeability due to the presence of fenestrations in the endothelium, absence of supporting cells, irregular endothelial cell placement, and mosaic structures with interspersed cancer cells⁵⁰⁻⁵³. Finally, solid stress from the surrounding cancer cells over-burdens the vessel structural capacity leading to compression of many vessels in the microenvironment⁵⁴⁻⁵⁷.

The striking characteristic of intratumoral lymphatics is that they do not exist in a functional form^{38,58,59}. The walls of lymphatic vessels are not designed for high pressures and in fact are found in a collapsed state in many normal tissues. Compression from the surrounding cancer cells in a solid tumor inhibits any lymphatic transport. Reduction of the tumor cell burden through cellular-targeted therapy can relieve some of the stress permitting patent lymphatic vessels in the tumor microenvironment⁵⁷. Conversely, the lymphatics at the tumor margin are found to be dilated in many tumors suggesting

lymphatic metastasis must occur by these routes⁶⁰⁻⁶². These lymphatic vessels may be pre-existing or recruited through lymphangiogenesis⁶³.

Structural and functional malformations in both blood and lymphatic tumor-associated vessels promote significant interstitial fluid pressures (IFP) in solid tumors⁶⁴⁻⁶⁶. The combination of increased vascular permeability and lack of functional lymphatics, which reduce tissue fluid volume, leads to increased IFP. Further, both the oncotic and hydrostatic pressure gradients across the tumor vessel wall are severely decreased due to the leakage of macromolecules (protein) and equilibrium between mean vascular pressure and IFP, respectively⁶⁷. These effects in addition to inefficient transport within the vascular networks are physicochemical barriers to drug delivery to the tumor microenvironment^{34,68}.

II.3b TUMOR ANGIOGENESIS

The formation of new vessels to supply a growing tumor is a critical step in disease progression. The requirement of vascular recruitment for tumor growth has been known for some time⁶⁹⁻⁷¹. The limitations of oxygen diffusion in metabolically active tumors place constraints on continued cell proliferation unless new vessels are recruited. This process, termed angiogenesis, typically occurs through sprouting or intussusception⁷² from adjacent normal vessels. Vasculogenesis can also contribute to tumor vessel formation from recruitment of endothelial cell precursors to newly forming vessels⁷³. These processes actively occur in embryogenesis and many normal tissues including during wound healing^{49,74}.

Angiogenesis has proved a predictive indicator of tumor progression and response to therapy in clinical disease^{36,75,76}. The degree of angiogenesis in the primary tumor has been shown to be linked to metastases⁷⁷. In breast cancer in particular, it has been demonstrated that angiogenesis plays a central role in the progression of disease both locally and in metastases⁷⁸. Clinicopathologic studies have also shown that angiogenesis, as determined by microvascular density (MVD), correlate strongly with both the aggressive nature of primary disease and metastatic potential in breast cancer⁷⁹⁻⁸¹.

Angiogenesis in tumors is hypothesized to be caused by an imbalance between pro- and anti-angiogenic factors⁸². The “angiogenic switch”, when the imbalance shifts to pro-angiogenic factors, is widely understood to be a critical step in tumorigenesis⁸³. The angiogenic phenotype is not ascribed to all cells within the tumor, but is often found in a subpopulation that influences vessel formation for the whole tumor¹. A variety of soluble factors have been implicated in promoting angiogenesis, but none more so than the vascular endothelial growth factor (VEGF) family of proteins⁸⁴. VEGF has been shown to be upregulated in both tumor cells and tumor-associated stromal cells^{51,85}. Increasing VEGF expression leads to increased angiogenesis and tumor growth in animal models^{86,87}. Levels of VEGF expression have been positively correlated with poor clinical prognosis in a variety of cancers^{80,88,89}. Other factors such as basic fibroblast growth factor and platelet derived growth factor have been implicated in angiogenesis as well^{90,91}. These angiogenic pathways may be more important in some cancers or as alternative routes of angiogenesis during vascular targeted therapies. Besides directly supporting angiogenesis through growth factors, these cells often induce down-regulation of antiangiogenic factors such as thrombospondin through heterotypic interactions between the cancer cells and stroma⁹².

Lymphangiogenesis is also regulated by the VEGF family of proteins. One isomer of vascular endothelial growth factor (VEGF-C) has been implicated in peripheral lymphatic hyperplasia in solid tumors⁹³. Upregulation of VEGF-C has been shown to increase metastases in animal models³⁷. Expression of VEGF-C and its receptor VEGF-R3 have been associated with the presence of distance metastases and poor prognosis in a number of clinical cancers⁹⁴⁻⁹⁶.

II.3c IMAGING ANGIOGENESIS IN THE TUMOR MICROENVIRONMENT

A number of methods exist to image blood and lymphatic vessels in the tumor microenvironment. Histological techniques permit molecular phenotyping of tissue, but must be performed *ex vivo*. Further, complications exist in drawing conclusions from histological samples for both angiogenesis and lymphangiogenesis. Microvascular

density (MVD) is typically the metric used to characterize tumor angiogenesis. However, the link between this parameter and what occurs *in vivo* is questioned in the literature⁹⁷. In histology of lymphatic vessels, the commonly used molecular marker of lymphatic endothelial cells (LYVE-1) has been shown non-specific as it can be expressed on other cells types⁹⁸. Non-invasive imaging methods such as magnetic resonance imaging⁹⁹, micro-computed tomography¹⁰⁰ and positron emission tomography¹⁰¹ have progressed significantly in their ability to assess angiogenesis and vascular function¹⁰². However, the minimum resolution of these techniques is in the 50-100 μm range. Further, the results of the various techniques used with MRI have proved to be indirect measures of angiogenesis and vascular function with much debate in the literature on qualitative meaning^{103,104}.

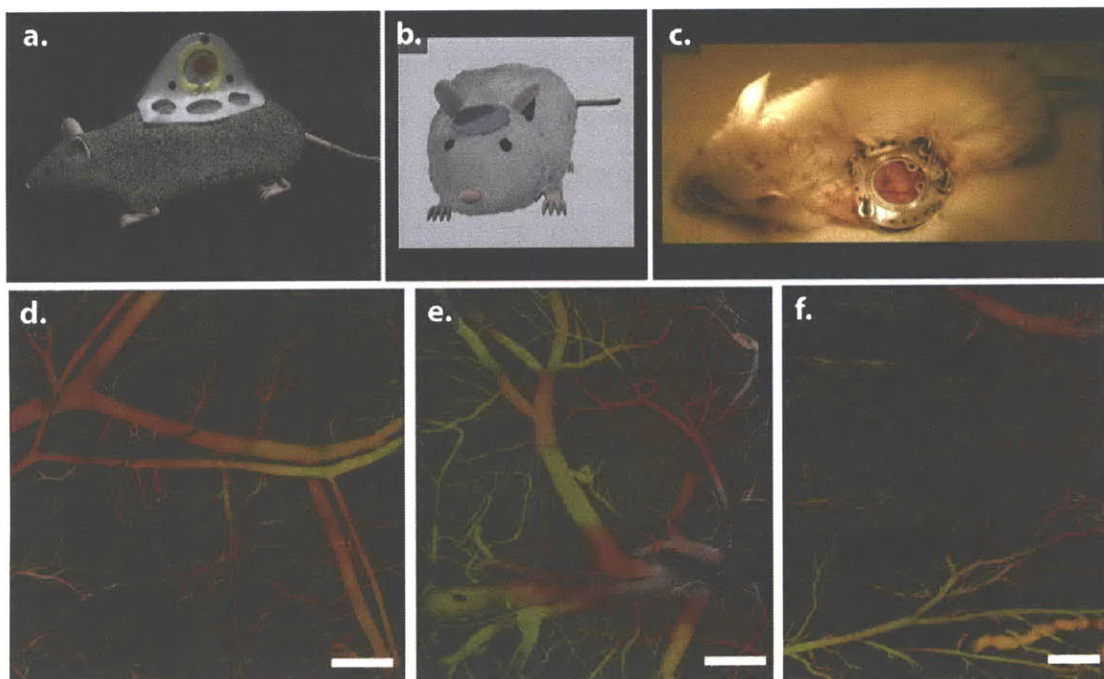


Figure II-1 Intravital optical microscopy of murine window chamber models. (a) Dorsal skinfold chamber model (DSC). (b) Cranial window model (CW). (c) Mammary fat pad chamber. (d) Normal vascular networks in the dorsal skin of a SCID mouse taken in a DSC (a). Both capillary networks and larger arteries and arterioles are seen paired with veins. (e) Vasculature in a murine brain from a CW (b). The large venous sinuses are visible as well as the convolute cortical capillaries. (f) Vasculature in the mammary fat pad of a female SCID mouse bearing a MFP chamber (c). Upon closer inspection the optical distortion effects of the adipocytes can be seen. The lower right of the image also contains a mammary duct containing fluorescent contrast. All images are mosaic colorized depth projection from MPM angiography. Mouse model animations courtesy of L.L. Munn. Scale bars - 500 μm .

Intravital microscopy has proved a useful tool in understanding both angiogenesis and lymphangiogenesis in the tumor microenvironment¹⁰⁵. This term is ascribed to a variety of optical techniques that employ non- or minimally invasive methods to image *in vivo* vascular networks. The resolution of intravital microscopy ranges from less than one micron for multiphoton microscopy (MPM) to 10 microns for wide-field epifluorescence or transillumination microscopy. With modified techniques, functional parameters can also be quantified or assessed with intravital microscopy. Many of these methods will be discussed in greater detail below.

Coupling intravital microscopy with animal models generally requires special tissue preparations to provide access to the tumor. *In situ* preparations using tumors grown subcutaneously in regions of thin epidermis such as the murine ear, tail or foot can be used although light penetration is limited. Acute preparations such as extirpation of the abdominal mesentery¹⁰⁶ or surgical exposure of subcutaneous tumors through a skin flap provide direct access, but also disturb the microenvironment and have limited repeatability. Chronic window chamber preparations provide relatively long-term non-invasive access to the tumor vasculature microenvironment²⁶ (**Figure II-1**). In this Thesis, nearly all imaging was performed in murine tumor models bearing dorsal skinfold chambers (DSC), mammary fat pad chambers (MFP), and cranial windows (CW).

II.4 The Role of Oxygen in Solid Tumors

Hypoxia, or low oxygen in the tumor microenvironment has been known for some time to be an important indicator of progression and response to therapy. However, only in the last two decades have the various techniques to measure oxygen become readily available in both the laboratory and clinic. This has permitted clinicians to study the prognostic significance of tumor oxygenation and laboratory investigators to study the sources and potential implications in the tumor microenvironment. Three areas of focus have arisen from these studies. The first is the tumor cell selection and genetic alterations influenced by hypoxia¹⁰⁷. The second involves the pathophysiological origination of these oxygen fluctuations and their implication in disease progression and

treatment¹⁰⁸⁻¹¹¹. Lastly, the complex effect of certain treatments on the tumor oxygenation and the role this may play in rationally scheduling combined therapies is a major focus of translational research^{10,82,112-116}. Regarding oxygen tension in the tumor microenvironment, this thesis will focus on the latter two avenues.

II.4a MOLECULAR EFFECTS OF TUMOR OXYGENATION

The major molecular target identified in modulating cancer cell response to hypoxia is hypoxia inducible factor α (HIF-1 α). This protein is constitutively expressed, but typically undergoes degradation in normoxic environments. When not degraded, HIF-1 α acts as a transcription factor regulating many cellular responses to hypoxia such as growth factors², angiogenesis¹¹⁷, metabolism (increasing glycolysis and decreasing pH)¹¹⁸, apoptotic pathways¹¹⁹ and metastatic potential¹²⁰. The regulatory pathways controlled by HIF-1 pathway are very complex and their effects on tumor growth can be contradictory. Typically the effects of HIF-1 α are enhanced by oncogenes or mutations in tumor suppressors that may interrupt some of the pathways that inhibit tumor growth¹.

Expression of HIF-1 α has served as a prognostic marker for unfavorable outcome in many cancers¹²¹⁻¹²³. Therefore, HIF-1 would appear to be a good target of therapy in tumors. Unfortunately direct inhibitors of HIF-1 α are still under investigation and the result of inhibition is difficult to realize due to its complex regulation in the cell^{124,125}. Investigations have therefore also focused on other regulatory downstream or upstream elements in the HIF pathway^{126,127}. The majority of studies have focused on three major targets of HIF-1 α . The first is a glucose transporter involved in glycolysis - GLUT1. Increased expression of this gene in tumors has been indicative of increased or deregulated glycolysis¹²⁸. The second is CAIX, a carbonic anhydrase that regulates cell pH and is an isozyme found only associated with cancer¹²⁹. Finally, HIF-1 α has been shown to directly upregulate vascular endothelial growth factor (VEGF) and other angiogenic promoters^{107,117}. In neoplasia, the VEGF family of proteins is correlated with angiogenesis, vessel permeability, tumor growth and clinical outcome⁴⁹. Using both

GLUT1 and CAIX as molecular markers, hypoxic regions of the tumor can be specifically determined in some cancer models¹³⁰, however results in clinical cancers are mixed¹³¹. Similarly, *in vivo* VEGF expression has been shown to be regulated by oxygen gradients rather than absolute levels of hypoxia^{132,133}.

II.4b CLINICAL MEASUREMENTS OF TUMOR OXYGENATION

Hypoxia has been demonstrated to be a negative prognostic indicator for both disease progression and therapeutic response in a variety of tumors in the clinical setting. Using polarographic electrode methods, oxygen tension was measured in metastatic squamous cell carcinoma patients prior to radiotherapy. Tumors with complete response exhibited mean pO₂ around 21mmHg, while non-responding tumors had hypoxic mean values around 5mmHg¹³⁴. Studies using Eppendorf needle measurements in cervical cancer patients found the level of hypoxia (< 10mmHg) to predict survival for advanced disease¹³⁵. However, this prognostic significance has never been observed with histological assessment of hypoxia¹³⁶. This is likely due to the fact that only viable cells can be stained with the bioreductive markers for hypoxia eliminating any necrotic regions from the hypoxic determination. This discrepancy between pO₂ electrode and histological measurements has been demonstrated in animal models¹³⁷. Hypoxia has been shown to be a significant prognostic indicator of disease progression regardless of stage in head and neck cancers¹³⁸. Interestingly, direct measurements of hypoxia have not been demonstrated as a significant indicator of disease progression¹³⁹. However, indirect measurements of genes, such as HIF and CA-IX, have shown strong correlation with disease progression in many different types of breast cancer^{140,141}.

Brain cancers have proved challenging to directly study tumor oxygenation given their anatomical location. However, some limited studies have been carried out using both polarographic and histological methods. While the histological grade of glioma patients was prognostic of survival, intra-operatively measured median tumor oxygenation was not¹⁴². Further confounding results, hypoxic fractions determined by EF5 did prove a

negative indicator of survival, but did not correlate with direct measurements of pO_2 ^{137,143,144}.

The challenge in quantifying oxygenation in the clinical setting, such as brain tumors, has led to the development of additional non-invasive imaging methods. These have been briefly mentioned in the previous section. Technologies such as (18)F-FMISO positron emission tomography¹⁴⁵ and BOLD-MRI¹⁴⁶ prove promising for clinical evaluation of tumor oxygenation¹⁴⁷. However, non-invasive clinical imaging modalities have only, thus far, proven prognostic in animal models¹⁴⁸. Therefore, most studies focusing on the direct measurement of oxygen in the tumor microenvironment and its pathophysiological significance have been performed in preclinical models.

II.4c DIRECT MEASUREMENTS OF PO_2 IN THE TUMOR MICROENVIRONMENT

The sources of hypoxia in tumors are three-fold. One is chronic due to the heterogeneous, abnormal and tortuous tumor vascular networks creating regions of tissue $>70\mu\text{m}$ from a vessel¹⁴⁹. Due to limitations on the diffusion of oxygen, large regions of avascular tumor tissue are often found to be hypoxic. The second is acute hypoxia due to transient fluctuations in vascular perfusion¹⁵⁰. Finally, hypoxia due to decreased hematocrit, or oxygen carrying capacity, due to anemic paraneoplastic syndromes¹⁵¹ or shunting in the tumor vascular network¹⁵². The multiple determinants of tumor oxygenation suggest a very complex relationship between the vasculature, tumor cells, and metabolic microenvironment.

Using non-invasive optical measurements of pO_2 such as PQM, many studies have provided direct assessment of oxygenation in multiple tumor types and preclinical models. Much of this work has focused pO_2 in the intravascular compartment in tumors. Multiple studies have demonstrated that mean intravascular oxygen tension is lower than that found in normal tissue¹⁵³⁻¹⁵⁶. Specifically, across tumors, vascular pO_2 has been found to both correlate with perfusion¹⁵⁷ and not^{24,150}. The effect of hyperoxia on tumor vascular oxygenation has likewise produced conflicting results in the literature. Dewhirst *et al* found that the pO_2 increase with carbogen (95% O_2 and 5% CO_2) inhalation in rats

was only transient¹⁵³, while others found a constant level up to 15mmHg higher^{155,158}. Surprisingly, the transient increase in pO₂ was found not to be accompanied by vasomotor activity in the tumor vasculature. Increased pO₂ induced by hyperoxia has also been shown to be stable in subcutaneous tumors by fiber optic oxygen probes¹⁵⁹.

Importantly, anesthetics have also been found to perturb tumor oxygenation; indicating an important consideration when performing pO₂ measurements. Ketamine/xylazine mixtures have been found to decrease mean tumor oxygen tension by 10-15mmHg compared to awake animals¹⁵⁵. Pentobarbital anesthesia has been shown to induce changes in blood gases likely due to fluctuations in the depth of anesthesia over time¹⁶⁰. By far the best anesthetic appears to be isoflurane which induces a transient (~20min) decrease in pO₂ before stabilizing^{157,159}.

While some of these studies have been performed in subcutaneously implanted tumors many have utilized the optically accessible window chamber models for rats¹⁶¹ and mice⁶⁴. These have permitted unique access to quantify macroscale spatio-temporal properties of tumor models. The difference in intravascular oxygen tension across different regions of the microenvironment has been observed to decrease towards the tumor center¹⁵⁶. Normal vessels adjacent to the tumor were found to be ~70mmHg, while those in the tumor margin were ~25mmHg and near the core close to 12mmHg. Further, these same investigators have shown decreasing longitudinal gradients in vascular pO₂ exist from the fascial surface of the chamber (skin capillary bed) to the tumor surface^{162,163}. However, a significant difference between the two surfaces was not found in mean pO₂, but only in the 10th and 25th percentiles of the oxygen distributions, i.e. number of hypoxic measurements. These effects may be an artifact of the model as other investigators have not observed such steep gradients between surfaces²⁴. Evidence of this is suggested by the fact that the microvascular density (MVD) is significantly different between the two regions. Nonetheless, decreasing oxygen tension towards the core of a tumor would not be unexpected. Even many decades ago, histology of human lung tumors revealed a viable margin and necrotic core¹⁶⁴.

Increasing hypoxia has been further confirmed in the lab as evidenced from *in vitro* tumor spheroid experiments¹⁶⁵.

Less commonly reported in the literature are interstitial measurements of pO_2 correlated with the microvasculature. A debate exists regarding the tumor compartment probed by pO_2 measurements with PQM. The large anionic charge and binding to albumin of the water soluble phosphor have lead some to suggest that pO_2 measurements are dominated by the intravascular space^{157,158}. Others highlight the permeable and leaky tumor vasculature as a source of oxygen sensor extravasation into the interstitium. Even in normal tissue, interstitial measurements of pO_2 have been successfully performed^{166,167}. This is likely due to the exchange of albumin between the vascular and interstitial spaces¹⁶⁸.

Noninvasive measurements of tumor oxygenation in the interstitial space have been performed in colorectal adenocarcinoma xenotransplants in the dorsal skinfold chamber of SCID mice. A number of interesting findings have resulted from these studies. The pO_2 in well vascularized regions was found to be equivalent to that in normal tissue and drop only a maximum of 5mmHg away from a vessel in the region¹⁵⁵. In less vascularized regions (vessel spaces > 200 μ m) heterogeneous shapes in the interstitial oxygen profiled were found as well as hypoxic and anoxic pO_2 at distances 70-80 μ m and 150-200 μ m away from the vessel wall, respectively^{24,155}. Further, no correlation was found between blood velocity or vessel diameter. In fact, intravascular measurements revealed perfused vessels with hypoxic pO_2 values (<5mmHg). Investigators following the mean tumor pO_2 during growth found the values decreasing with time²⁴. Given the depth limitations (~50 μ m) of the PQM due to tissue absorption and scattering of the excitation light, this may be due to the hypoxic tumor surface effect observed by others¹⁶³. Many of the results found using PQM have been confirmed in other studies in the chamber models employing oxygen microelectrodes. These studies demonstrated the differential of pO_2 across regions of the vascular network¹⁵⁶ and also realized an inverse correlation of pO_2 with vascular distance¹⁵⁰.

Recent studies have focused on temporal fluctuations in tumor pO_2 and their impact on hypoxia. Microelectrode measurements in the tumor interstitium have demonstrated instability in median pO_2 due to alterations in red blood cell (RBC) flux even at distances around the diffusion limit of oxygen in the model ($140\mu m$)¹⁵⁰. On a macroscopic scale, up to 50% of the presumed intravascular pO_2 has been shown to dynamically change $>5\text{mmHg}$ over 10s of minutes¹⁶⁹. The pathophysiologic source of these perturbations are likely traced to changes in vascular flow⁴⁵ and provide evidence of episodic hypoxia¹⁷⁰. Acute hypoxia induced by such fluctuations may have a profound effect on the selection of malignant cell populations^{171,172}. Such changes due to transient hypoxia have been shown to increase lymphatic metastases in mice¹⁷³.

II.4d MODELING TUMOR OXYGENATION

Coupling characteristics of the tumor vascular network with direct oxygen measurements has permitted the application of mathematic models to describe the metabolic microenvironment of the tumor. The simplest model employs cylindrical geometry, originally proposed by Krogh¹⁷⁴. Applied in a semi one-dimensional geometry to intravascular pO_2 measurements in the tumor, the Krogh cylinder model suggests hypoxia at distances $>140\mu m$ from a vessel and in the tumor center¹⁵⁶. Of course this is dependent on both the blood velocity in the source vessels and tissue oxygen consumption (QO_2). Interestingly, the rate of oxygen delivery to the tumor is not independent of oxygen consumption. Early *in vivo* experiments demonstrated that tumor tissue oxygen consumption varied with changes in blood oxygen concentration and perfusion¹⁷⁵.

More advanced models have taken into account vascular geometry in both two- and three-dimensional networks. Generally, the heterogeneous structure of the tumor vasculature is a significant factor in reducing the thresholds (oxygen consumption and distances to nearest vessel) required to reach hypoxia¹⁷⁶. Similar diffusion based models using exogenous staining of *in vivo* hypoxia and MVD reveal hypoxic regions even in the presence of vessels, although the oxygen tension within these vessels is very low¹⁵⁴.

Other models have included additional metabolic factors related to oxygen. Combining the diffusion-reaction relationships of oxygen with glucose transport reveals that reducing oxygen consumption or decreasing the intervessel distance can eliminate hypoxia in tumor vascular networks¹⁷⁷. More complex models that account for metabolic changes dependent on the local concentration of oxygen reveal gradients in glycolytic factors¹⁷⁸. The gradients imply that regions of hypoxia can alter the metabolism of entire macroscopic regions of the tumor. Many of these models have focused on the formation of chronic hypoxia. However, mathematical simulations have suggested that the same structural and functional vascular parameters that define chronic hypoxia also characterize acute hypoxic events, particularly vascular geometry (distance to nearest vessel)¹⁷⁹.

II.4e PO₂ IN THE CONTEXT OF ANTI-CANCER THERAPY

Beyond the challenges of delivering drugs to tumors³⁴, cancer therapies can both be influenced by and affect tumor oxygenation. It is well known that oxygen is a sensitizer for radiation therapy¹⁴. However, the efficacy of many chemotherapeutics are subject to the level of oxygen in the tumor microenvironment. The activity of bioreductive drugs and alkylating agents are increased in hypoxic environments^{180,181}. Increased bioreduction in low oxygen is the basis of hypoxic histological stains such as pimonidazole and EF-5. In fact, many investigators have proposed clever drug designs to take advantage of hypoxia creating pro-drugs that are activated through bioreduction^{182,183}. Other agents demonstrate reduced cytotoxicity in low oxygenated tumors, particularly those, like radiation, that create free radicals to damage tissue^{180,184}. Many cytotoxic agents rely on proliferating cells to induce cellular damage. Tumor cells have been shown to decrease metabolic rates and become senescent in hypoxic environments², thus evading some chemotherapeutics¹⁸⁵. Further, hypoxia can select for therapeutic resistance and more malignant phenotypes^{107,172}.

II.5 Methods for Quantitative Oxygen Sensing *In Vivo*:

There are a number of methods that permit *in vivo* measurement of oxygen. However, some are indirect measurements of oxygen concentration, while others are invasive or require histological examination. It is important to note whether a method measures oxygen tension (pO_2), which is related to the oxygen concentration ($[O_2]$) through the specific solubility in a given medium, or a related, but independent measure such as oxygen saturation (S_{O_2}) or a molecular marker responsive to a given range. Many of the methodologies presented here have been reviewed in detail by others¹⁸⁶⁻¹⁸⁸.

II.5a POLAROGRAPHIC METHODS:

Polarographic microelectrodes have long been considered the “gold-standard” in biological measurements of oxygen. These microelectrodes, often termed Clark-type microelectrodes, quantify dissolved oxygen through modulation in the electrical current due to reduction of molecular oxygen to water at the platinum cathode¹⁸⁹. Due to the electrochemical reaction, oxygen electrodes consume oxygen within the small catchment volume surrounding the cathode. Further, the electrodes require maintenance of equilibrium, a stable immediate microenvironment, for accurate measurements. This is often obtained by allowing stabilization after application and utilizing a recessed and coated electrode¹⁹⁰. Advancements in electrode design have minimized their catchment volume ($\sim 1 \mu\text{m}$) and significantly reduced oxygen consumption¹⁸⁸. However, biological application of the electrode is an invasive procedure requiring mechanoreceptors for proper application, perturbs the local microenvironment due to the occlusion of tissue and is not typically repeatable. Further, microelectrodes are less sensitive at low pO_2 values ($<10\text{mmHg}$)¹⁹¹. A comprehensive study across a number of laboratory sites examining both clinical and pre-clinical measurements of pO_2 using Eppendorf electrodes demonstrated significant variability even in the same tumor models¹⁹². However, given the sensitivity, minimal probed volume and significant resolution ($0.01\text{-}1 \mu\text{M } [O_2]$), the microelectrode is often used as a reference in the development of other techniques¹⁸⁷.

II.5a HEMOGLOBIN SATURATION SPECTROPHOTOMETRY:

The optical absorbance of hemoglobin changes with the binding of oxygen. Using at least two wavelengths of light it is possible to determine the fraction of oxyhemoglobin and therefore the oxygen saturation^{193,194}. This method has been applied both in optical microscopy in pre-clinical models and near-infrared spectroscopy of humans¹⁹⁵. Because the signal depends on hemoglobin concentration, the oxygen saturation values correspond only to the intravascular component of the tissue. Current studies are mixed on the ability to differentiate the contribution of myoglobin from hemoglobin, which would provide oxygen saturation of the muscular compartment as well^{196,197}. While these methods are optically-based and non-invasive, the relation of oxygen saturation to pO₂ is complex. To convert measurements to quantitative oxygen concentrations, knowledge of the oxy-hemoglobin dissociation curve and local carbon dioxide and pH required. Further, even in microscopic implementations, the volume sampled is larger than polarographic methods¹⁸⁷.

II.5b HISTOLOGY – MOLECULAR AND CHEMICAL MARKERS OF OXYGENATION STATUS

Given both the radiobiological significance of oxygen¹⁴ and the potentially prognostic indicator of oxygen levels in tumors², concerted efforts have been made to develop histological techniques for assessing oxygen content. While these methods are invasive, either performed on biopsies or post-mortem, they do provide insight into hypoxic fractions and molecular profiling. The most common histological markers of hypoxia are the nitroimidazoles: pimonidazole¹⁹⁸ and EF5¹⁹⁹. Under hypoxic conditions, these compounds are metabolized by cells *in vivo* leading to reactive anionic species that form adducts with intracellular macromolecules. Identification is performed by using antibodies against these adducts. Both compounds have been utilized in the clinical setting to assess tumor hypoxia^{143,200}, and have also demonstrated staining in normal tissues with physiological hypoxia²⁰¹. Because adduct formation is dependent on cellular metabolism, necrotic regions must be excluded from histological assessment. This fact may also explain the discrepancy with other methods where low pO₂ measurements are

not always correlated with staining¹³⁷. Recently, 18F-fluoromisonidazole compounds have been used for non-invasive imaging of tumor hypoxia in the clinical setting using positron emission tomography^{202,203}.

In the past decade, additional endogenous molecular markers of hypoxia have been investigated as immunohistochemical markers. These include the hypoxia inducible factor 1 (HIF-1) and its target genes CA9 (of the carbonic anhydrase family) and the membrane glucose transporter GLUT-1^{204,205}. However, these molecules are also regulated by factors other than hypoxia making them indiscriminate markers oxygen status¹³¹.

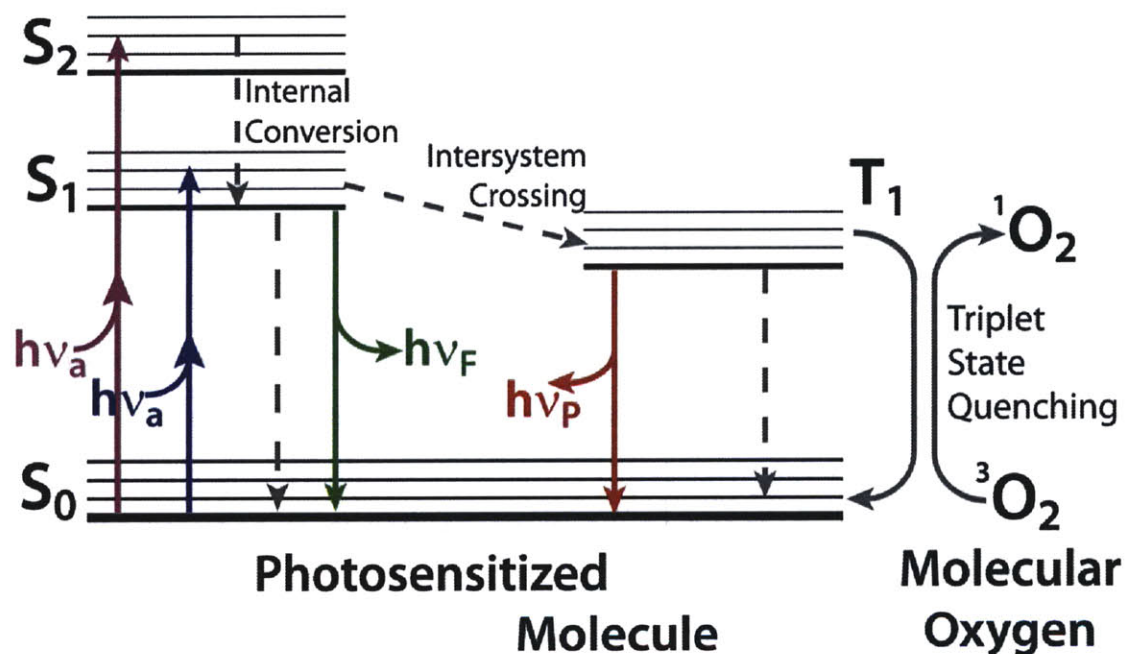


Figure II-2 Quenching of phosphorescence by molecular oxygen. The Jablonski diagram illustrates the electronic energy levels of a luminescent molecule. Single photon absorption is shown for two excited singlet electronic states (violet and blue). Phosphorescent molecules undergo intersystem crossing to the triplet state. The excited electron in the triplet state shares the same spin orientation as the ground state preventing simple relaxation to the ground singlet state. This "forbidden" transition increases the lifetime of the photosensitized molecule so that relaxation and photon emission occur over a longer time scale. For a group of excited molecules, this emission is termed phosphorescence to differentiate its longer lifetime (milliseconds to days) and origin from the triplet state from fluorescence (nanoseconds). Molecular oxygen, which is paramagnetic and already in a triplet state, can "quench" phosphorescence by promoting intersystem crossing through collisional non-radiative decay.

II.5c PHOSPHORESCENCE QUENCHING METHODS

The effect of oxygen on the quantum yield of luminescence has been known for quite some time²⁰⁶. Further, it was rapidly realized that these changes in luminescence intensity could be used to quantify the amount of oxygen present²⁰⁷. For a population of luminescent molecules, the quantum yield and therefore intensity is directly proportional to the lifetime of the excited state prior to relaxation to the ground state and release of a photon. Paramagnetic molecular oxygen can quench most luminescent molecules by inducing intersystem crossing from the singlet excited state to a *dark* state that is either long lived eventually experiencing non-radiative decay to the ground state or chemically modified²⁰⁸. A subset of luminescent molecules undergo spontaneous intersystem crossing to the triplet state after excitation experiencing a longer radiative rate of decay, phosphorescence, due to the spin-forbidden transition to the ground state. Molecular oxygen can quench the long lived phosphorescence (microseconds to days) through collisions with the excited triplet state molecule inducing non-radiative decay (**Figure II-2**).

For most luminescent quenching reactions, collisional quenching by molecular oxygen is well described by the Stern-Volmer relationship²⁰⁸, shown in Eq. (II.1)

$$\frac{I_0}{I} = \frac{\tau_0}{\tau} = 1 + k_q\tau_0[\text{O}_2] = 1 + K_{SV}[\text{O}_2] \quad (\text{II.1})$$

The ratio of the emission intensity in the absence, I_0 , and presence, I , of oxygen is related to the concentration of oxygen through the Stern-Volmer constant, K_{SV} , where k_q is a diffusion limited second order rate constant²⁰⁹:

$$k_q = 4r\pi RDN_A/10^3 \quad (\text{II.2})$$

Here, D is the sum of the diffusion constants for the phosphorescent sensor and oxygen, R is the radius of interaction and r is the quenching efficiency, usually 1. The Stern-Volmer relationship can easily be derived by considering the luminescent quantum efficiency of the sensor in the absence and presence of oxygen,

CHAPTER 2

$$I_0 \propto \Phi = \frac{k_p}{k_p + k_{nr}} \quad (\text{II.3})$$

$$I \propto \Phi = \frac{k_p}{k_p + k_{nr} + k_q[\text{O}_2]} \quad (\text{II.4})$$

where k_p and k_{nr} are first order decay rates for emissive and non-radiative processes, respectively. By taking the ratio of I_0 to I and substituting for the definition of the lifetime in the absence of quencher, $\tau_0 = 1/(k_p + k_{nr})$, the Stern-Volmer relationship [Eq. (II.1)] is obtained for a dynamic quenching process. A similar result is obtained if the ratio of the luminescent lifetimes is used instead. The Stern-Volmer relationship is non-linear for some compounds depending on the oxygen concentration^{210,211}.

Probes for oxygen sensing by quenched luminescence utilized constructs based on palladium(II) or platinum(II) porphyrin moieties, ruthenium (II) compounds, or osmium (II)¹⁸⁶. The quenched fluorescence of ruthenium(II) is utilized in many fiber optic sensors such as the OxyLite™ system²¹² and the FOXY™ system²¹³. Fiber optic sensors have been applied in both industrial and biological settings. However, similar to the polarographic electrodes, inserting a fiber optic probe into tissue perturbs the environment. Osmium probes are in development²¹⁴; however the long wavelength emission (> 700nm) makes their use difficult.

By far the most commonly used optical oxygen sensors are the metalloporphyrins. Their long lifetime (10-100s μ s) and large quenching constant, k_q , makes them very sensitive to low oxygen states^{187,188,215}. Palladium metalloporphyrins are widely used for biological sensing and many water soluble and biocompatible forms have been developed²¹⁵⁻²¹⁹. The platinum metalloporphyrins have shorter lifetimes²²⁰, unless bound in a polymer²²¹, making them less useful as soluble probes. The soluble palladium porphyrins have been applied in a variety of experimental imaging setups including fluorescence lifetime microscopy^{24,155,167,222,223} and frequency domain lifetime instruments²²⁴

II.5d OTHER METHODS FOR MEASURING OXYGEN

In addition to the optical methods for determining oxygen status, other relatively non-invasive methods exist and have been applied in both animal models and the clinical setting. The relative merits and limitations have been reviewed in detail elsewhere^{187,225}. A number of methods have been developed utilizing nuclear magnetic resonance (NMR) techniques. The spin relaxation rate of ¹⁹F nuclei in perfluorocarbons directly injected into the site of interest is sensitive to the oxygen tension²²⁶. In magnetic resonance spectroscopy, endogenous molecular metabolites that are related to oxygen status of the tissue can be non-invasively quantified²²⁷. Further, specific pulse sequences in magnetic resonance imaging are sensitive to paramagnetic deoxyhemoglobin in the blood (BOLD-MRI) allowing non-invasive assessment of vascular oxygenation²²⁸. All of these nuclear magnetic resonance techniques are beholden to the minimum resolution of the instrumentation ($\sim 100 \mu\text{m}^3$) and measure oxygen status (or related parameters) over minutes. A related technique to NMR is electron paramagnetic resonance (EPR), which measures the broadening of the hydrogen electron spin spectral linewidths of an administered spin probe²²⁹. The width of these lines is related to the collision rate of molecular oxygen with the spin probe. EPR oxymetry is less sensitive to low pO_2 tissue values than phosphorescent methods¹⁸⁷. However, the technique has rapidly progressed towards clinical applications²³⁰.

II.6 The Role of pH in Solid Tumors

Similar to oxygenation, solid tumor pH plays a significant role in tumor progression and response to therapy. It is well known that the tumor microenvironment is typically found to be acidic^{8,231-234}. The extracellular pH (pHe) in tumors ranges from $\sim 6.3-7$, while by comparison in normal tissue pH is maintained by homeostatic mechanism around neutral (7.3-7.4)^{231,235}. In discussing tumor pH, it is important to distinguish between the extracellular and intracellular compartments. The *in vivo* intracellular pH (pHi) of cancer cells is often found to be alkaline relative to normal tissue (7.12 – 7.65 versus 6.99 – 7.20)²³⁵. There are three major areas of research regarding the pH of the tumor

microenvironment. The first is the origination of low microenvironment pH and the associated transcellular gradient. The second is the effect of pH on tumor progression including direct effects on cellular genes. Finally, the implications of tumor pH on therapy have been a major focus in the cancer field for decades.

II.6a ETIOLOGY OF LOW pH IN THE METABOLIC MICROENVIRONMENT OF TUMORS

The cause of acidic pH and the transmembrane gradient in tumors has been long debated. Hypoxia has been shown to increase glycolysis a process known as the Pasteur effect²³⁶. The regulation of glycolysis by hypoxia is directed through the HIF-1 pathway²³⁷. However, many tumors do not exhibit the Pasteur effect suggesting acidosis is caused by other mechanisms. The Warburg hypothesis postulates that acidosis is due to a metabolic disturbance of cancer cells promoting glycolysis even in aerobic environments^{18,20,238}. Highlighting the complex nature of tumor metabolism, it has been demonstrated that inhibiting glycolysis does not prevent acidification of pH¹¹⁸. In fact, carbon dioxide in addition to lactate has been identified as a significant source of tumor acidity^{23,232}. Instead it is likely that tumors metabolize whatever substances are present utilizing multiple metabolic reactions including glutaminolysis and the pentose phosphate pathway. Demonstrably, administration of glucose does increase glycolysis and lower pH in the tumor microenvironment^{231,239,240}. Of course not all of the pH changes are due to glycolytic metabolism as a bolus of glucose also enacts hemodynamic effects^{241,242}. Of particular interest in tumors is how both the transmembrane and interstitial vascular pH gradients are established.

It has been well established that a pH drop exists across the cellular membrane of cancer cells in tumors^{235,243-246}. It is now understood that this gradient exists due to active transport processes occurring in tumor cells. The Na⁺/H⁺ exchanger (NEH1) and H⁺/lactate cotransporter (monocarboxylate transporter, MCT) acidify the tumor microenvironment by forcing protons into the extracellular space^{247,248}. Intracellular alkalinization drives both cancer cell proliferation and glycolysis²⁴⁹. Further supporting this mechanism is the fact that proton pump inhibitors abolish the transmembrane pH

gradient²⁵⁰. These mechanisms protect the cancer cells from the clastogenicity of the acidic microenvironment^{251,252} and have profound implications for therapy.

In addition to transmembrane gradients, tumors display decreasing pH from the vascular wall inward and across the tumor as a whole. In many experimentally studies tumors, vascular gradients have been measured^{24,70,234,253,254}. The pH drop along these gradients ranges from 0.1-0.5 units. Gradients have also been found to exist at the periphery of solid tumors²⁵⁵. These gradients are possibly formed by two different mechanisms. Poor perfusion and transport of metabolic products from the tumor due to the tortuous and inefficient vasculature decrease tumor pO_2 within the interstitium²⁵⁶. Second, hydrogen ion diffusion along concentration gradients to the tumor periphery creates a pH drop across the tumor²⁵⁵. The transport of hydrogen ions is likely carried with buffers allowing such gradients to be modeled²⁵⁷. It should be noted that while interstitial pH gradients do exist in tumors, they are in no way universal. pHe has been found to be heterogeneous within a tumor²⁵⁸, across tumor types²⁵⁹ and even in patients with similar cancers²³⁴.

II.6b EFFECT OF TUMOR PH ON PROGRESSION

The pH of the tumor microenvironment has been shown to promote aggressive phenotypes. Tumors with increased glycolysis and lactate production demonstrate increased metastasis in both animal models^{257,260-262} and patients^{263,264}. These results have led investigators to propose the acid-mediated tumor invasion hypothesis^{255,265}. The proposed mechanism for invasion is multistep. The endogenous mechanisms of the cancer cells decrease pHe which induces normal cell death through p53-mediated apoptosis^{266,267}. By upregulating both VEGF^{133,268} and interleukin-8²⁶⁹, low pH promotes angiogenesis increasing tumorigenicity. The acidic microenvironment also indirectly promotes degradation of the extracellular matrix²⁷⁰⁻²⁷². Finally, low pH reduces immune screening of the tumor in the microenvironment²⁷³. Interestingly, a recent study treating preclinical animal models with sodium bicarbonate, which raised pHe, showed a

reduction in spontaneous metastasis²⁷⁴. The activity of the Na⁺/H⁺ exchanger has been associated with metastatic phenotype²⁴⁸.

II.6c IMPLICATIONS OF TUMOR pH ON THERAPY

Analogous to pO₂, the pH of the tumor microenvironment exhibits a spectrum of effects on different cancer treatments. The main culprit in controlling the cytotoxicity of certain therapeutics is the transmembrane gradient. The interstitial gradients also affect treatment, but more by spatial heterogeneities in the response of groups of cells to therapeutic agents. Chemotherapeutics that are weak bases like anthracyclines, Vinka alkaloids and misonidazole are unable to penetrate the cell membrane to induce damage^{8,244,275}. Increasing *in vivo* pHe through the administration of bicarbonate has demonstrated increased cytotoxicity of these agents²⁷⁶. Conversely, the transmembrane pH gradient increases the cytotoxicity of weak acids²⁷⁷. Drugs that utilize the existing gradient by modifying pHi are under active investigation^{8,278}. Interestingly, low pH has also been shown to confer resistance to radiation therapy²⁷⁹⁻²⁸¹.

A unique approach to treating solid tumors has employed hyperthermia. Coupling hyperthermia with hyperglycemia, which reduces pHe eliminates or reverses the transmembrane pH gradient^{279,282,283}. Presumably, this occurs through a lowering of pHi and blockage of the hydrogen ion transporters²⁸⁴. However, in light of recent understanding regarding the effect of low pH on the malignant phenotype, combined hyperthermia and hyperglycemia may not be advisable.

II.7 *In Vivo* Methods for Quantitative pH Sensing in Tumors

A variety of techniques exist for measuring hydrogen ion concentration (pH) in cells and tumors. Similar to quantification of oxygen, these methods vary in their level of invasiveness. Some also permit collection of additional parameters to assess pH in association with other physiological or anatomical features. In discussing the quantification of pH, it is important to note what *in vivo* compartment is contributing to the measured value. The procedures employed can either measure only pHe or pHi,

although use of multiple probes or applications can simultaneously detect both. Another difference between techniques that can influence measured values is the spatial resolution and depth limits of the pH measurements.

II.7a INVASIVE TECHNIQUES: MICROELECTRODES AND MORE

One of the older methods for *in vivo* quantification of pH is the application of microelectrodes sensitive to hydrogen ions (H^+). Analogous to the polarographic method for pO_2 sensing, pH microelectrodes are invasive and measure pH in the catchment volume, which varies depending on the probe. Much has also been made about potential artifacts in the pH values due to disturbance of the tissue acid/base balance through insertion and consumption²³⁵. Measurements with microelectrodes have been performed both in patients²³⁴ and animal models^{8,254,285}. These investigators found intratumor pH gradients ranging in pH drops from 0.1 – 0.5 across the tumor. The implantable Guillino micropore chamber has also been employed to measure pH and other metabolites in the tumor microenvironment²³². However, the technique lacks any spatially localized information. Finally, recent work has focused on the development of fiber optic probes that do not consume hydrogen ions²⁸⁶⁻²⁸⁸. These measurement tools employ changes in the emission or excitation of pH sensitive dyes placed in permeable membranes at the tip of the probe. While such probes may not consume the analyte, they do mechanically disturb the tumor microenvironment.

II.7b NUCLEAR MAGNETIC RESONANCE IMAGING AND SPECTROSCOPY

Intrinsic nuclei and those introduced by exogenous probes are sensitive to the pH of the local environment. The spin relaxation of the stable isotope of inorganic phosphorous (^{31}P) is sensitive to the local pH²⁸⁹. Changes in pH induce a chemical shift in the ^{31}P resonance that can be calibrated for using the Henderson-Hasselbach equation. The endogenous signal from ^{31}P arises from the intracellular compartment allowing for differentiation from extracellular pH in tumors²⁴³. In tumor xenografts, the technique has demonstrated that pH decreases during tumor growth²⁹⁰. The amount of endogenous ^{31}P is small limiting the signal to noise of pH measurements. Exogenous

probes labeled with ^{31}P provide greater signal to noise ratios and highlight the extracellular compartment^{245,291}. The *in vivo* spatial resolution of ^{31}P magnetic resonance spectroscopy (MRS) is around 4mm³²⁹².

Similar to ^{31}P nuclear magnetic resonance measurements, the most common stable isotope of fluorine (^{19}F) is also sensitive to pH. Fluorinated exogenous probes have been developed for ^{19}F MRS that permit simultaneous measurement of both pHi and pHe quantifying the transmembrane gradient^{246,293}. Probes employing the ^1H hydrogen nucleus have been found to be the most sensitive to pH. Intrinsic ^1H resonances cannot be employed due to interference from other endogenous metabolites and water²³⁵. Due to higher sensitivity, ^1H MRS uses shorter times (20 minutes) and smaller voxel sizes ($\sim 2\text{mm}^3$)²⁹⁴. The use of ^1H MRS also allows for correlation of vascular parameters with MRI²⁹⁵ and with other metabolites like choline and lactate²⁹⁶. Gadolinium complexes that are pH-sensitive have also been developed for use at the higher spatial imaging resolution of MRI ($\sim 100\mu\text{m}$)²⁴⁵. Other imaging techniques, such as positron emission tomography, have also demonstrated potential for noninvasive measurements of pH²⁹⁷.

II.7c OPTICAL IMAGING OF PH

Numerous fluorescent dye molecules exist that have absorption or emission properties that are sensitive to local pH. The two most common dyes used *in vivo* are BCECF (2',7'-bis-(2-carboxyethyl)-5-(and-6)-carboxyfluorescein)²⁹⁸ and SNARF-5F²⁹⁹, which are based on fluorescein derivatives. BCECF is often employed as a excitation ratiometric dye given that its absorption spectrum changes with pH^{300,301}. The pKa of the dye is in the relevant physiological range ~ 6.98 . SNARF-5F is also used as a ratiometric dye, though typically through the ration of its emission. However, the dye is both excitation and emission sensitive with a pKa near neutral (7.3 – 7.4)²⁹⁹. Both dyes are available as cell permeable compounds for measurement of pHi.

pH sensitive dyes have been used to measure tumor pHe using fluorescence ratiometric imaging (FRIM) in a number of studies. Early studies in tumor tissue demonstrated that FRIM measurements correlated well with pH as determined by microelectrodes³⁰². The

use of FRIM allows relatively high-resolution measurements of pH compared to other techniques and correlation with the tumor vasculature. These studies have shown that the pH is spatially modulated with respect to the vasculature. pH correlates strongly both with distance from the vessel wall and vascular density^{24,231,253}. However, no correlation of pH with blood flow or local oxygenation was demonstrated in tumors²⁴. While FRIM is the most common application of these dyes, their fluorescent lifetime is also sensitive to pH³⁰³ and has been utilized to measure pH³⁰⁴. These optical techniques may provide descent spatial resolution, however axial resolution and depth penetration (~50 μ m) is limited.

II.8 Antiangiogenic Therapy and “Normalization” of the Tumor Microenvironment

II.8a ANTIANGIOGENIC AGENTS AND THEIR TARGETS

Anti-angiogenic therapy, a vascular targeted agent that blocks the formation and maintenance of new vessels, was originally conceived as a way to starve a tumor of its blood supply^{305,306}. Angiostatin, a 38kDa plasminogen fragment produced naturally including by some tumors, was discovered by Judah Folkman and shown to reduced metastases³⁰⁷ and induce tumor dormancy³⁰⁸. The same group also identified another endogenous inhibitor of angiogenesis produced from a fragment of Collagen XVIII termed endostatin³⁰⁹. While these peptide fragments have demonstrated success in animal models, clinical trials with endogenous antiangiogenic compounds have only recently begun^{310,311}.

Instead major focus has been on targeting the vascular endothelial growth pathway. Work in animal models has demonstrated that blockade of VEGF-Receptor 2 (VEGF-R2) inhibits angiogenesis and delay tumor growth³¹². A humanized antibody to soluble VEGF, bevacizumab (Avastin), has been approved by the Federal Drug Administration for treatment of colorectal cancer and advanced lung cancer³¹³. Recent work has expanded the field of antiangiogenic therapy to include broad spectrum and small molecule

tyrosine kinase inhibitors that target multiple VEGF and other growth factor receptors^{314,315}. However, in the last decade, results in both the laboratory and clinic have suggested a more complex role for antiangiogenic agents in cancer therapy.

II.8b NORMALIZATION HYPOTHESIS

The concept of using antiangiogenic therapy to alter disease progression by starving the tumor of its blood supply has been challenged by both laboratory and clinical results. Phase I and II clinical trials using the contemporary anti-angiogenic agent bevacizumab have reported varied results with either no evidence of improvement in progression of disease or only a partial response in some patients^{11,114,314,316,317}. Even in relatively well controlled xenograft animal models, antiangiogenic therapy has produced mixed results. Early studies administering a single antiangiogenic agent demonstrated initial tumor growth arrest and vascular regression only to be followed by a second stage of angiogenesis and tumor relapse^{49,312,318-320}. These results combined with variable clinical effects have led to the idea that antiangiogenic therapy needs to be rationally scheduled and may work better in combination with other therapies^{11,115,321}. Particularly important is the dynamic effects antiangiogenic agents have on the metabolic microenvironment of solid tumors.

It is well known that oxygen sensitizes a tissue to radiation¹⁴; therefore one would expect anti angiogenic agents and radiation to be antagonizing factors. Surprisingly, a variety of antiangiogenic agents including angiostatin³²² and blockage of the vascular endothelial growth factor pathway^{323,324,325} have demonstrated increased therapeutic efficacy when combined with radiation therapy in animal models. A recent study employing a xenograft model of glioblastoma and using *in vivo* microscopy has demonstrated a vascular “normalization window” during which radiation increased the tumor growth delay compared to administration before or after³²⁶. Immunohistochemical analysis also showed decreased hypoxia during the window. Further, measurements of tumor microenvironmental pO₂ during antiangiogenic therapy have revealed a period of increased mean oxygen tension^{318,327,328}.

The acidic microenvironment is also susceptible to changes induced by antiangiogenic therapy. Certain antiangiogenic agents have been shown to reduce the cancer cell transmembrane gradient³²⁹. This gradient, coupled with poor transport properties of the tumor vasculature present significant barriers to chemotherapeutics³³⁰. Reducing the intracellular pH and thus the gradient with the acidic microenvironment enhances the cytotoxic effects of many weak-acid drugs³³¹. Animal studies have shown improved efficacy of cytotoxic therapy when administered with antiangiogenic therapy^{332,333}.

Clinical trials have provided even further support to a beneficial effect of antiangiogenic therapy in combination with other treatments. Anti-VEGF treatments have demonstrated synergistic results when combined with standard chemotherapeutics in colorectal¹¹⁶ and potentially other clinical cancers¹¹⁵. A number of mechanisms have been proposed for the improved response of radiation therapy and chemotherapeutics in combination with antiangiogenics³³⁴ including augmented anti-vascular effects³³⁵, increased tumor cell repopulation, and vascular “normalization”.

As first presented by my thesis advisor Dr. Rakesh Jain, the “normalization” hypothesis proposes that the immature and inefficient blood vessels of the tumor are selectively pruned through antiangiogenic therapy by initiating apoptosis of excess endothelial cells, decreasing vessel diameter, vascular density and permeability¹³. These microscopic changes leave the remaining vasculature with a “normal-like” appearance and may enhance function. The “normalization” of tumor vasculature by antiangiogenic therapy has profound implications on combined treatment. The less tortuous and lower resistance vessels may be able to better transport therapeutic agents to the tumor and remove metabolic waste increasing tumor pH. Additionally, higher tissue perfusion in the tumor could mean increased pO₂, enhancing the effects of radiation therapy. However, other therapeutic agents or radiation treatments must be applied when the vasculature is optimally “normalized” to have the greatest effect. If therapy scheduling or dosing is suboptimal, there could be antagonism between cytotoxic and antiangiogenic therapies or decreased delivery of other therapeutic agents.

II.8c TRASTUZUMAB AS AN ANTIANGIOGENIC AGENT

Other targeted anti-cancer therapies may also down-regulate angiogenic molecules through indirect mechanisms. Recently, in an *in vivo* xenograft model of breast cancer, trastuzumab (Herceptin) was shown to “normalize” and induce regression of tumor vasculature and decrease a number of angiogenic factors³³⁶. Trastuzumab, a monoclonal antibody against HER2/neu, is currently used for the treatment of advanced metastatic breast cancer. As a whole, the clinical results of breast cancer treatment using trastuzumab have been mixed. Only a subset of HER2/neu over-expressing breast cancer patients have responded to treatment with others showing no effect with either monotherapy or in combination with therapeutic agents^{337,338}. Administration of trastuzumab to HER2-positive breast cancer cell lines *in vitro* has been promising, demonstrating decreased growth rate³³⁹ and increased radiosensitivity³⁴⁰. In addition to promoting vascular normalization, inhibiting HER2/neu may enhance combinatorial therapies through other pathways.

HER2/neu is a proto-oncogene product that was shown to be amplified or over-expressed in 10 to 34% of breast cancers and has been associated with poor prognosis and resistance to chemotherapy in both primary and metastatic disease³⁴¹. The amplification of the gene encoding HER2/neu, c-erbB-2, or activation of the receptor by heregulin leads to increased HIF-1 α ³⁴² and VEGF³⁴³ expression. At the cellular level, the molecular pathways modulated by HIF-1 α increase glycolysis, alter genetic expression, enhance metastatic potential and induce radiation resistance^{2,118}. In the clinic, increased angiogenesis and hypoxia have been demonstrated for HER2-positive primary tumors³⁴⁴. The increased hypoxia in HER2/neu over-expressing breast cancer suggests that its presence may induce resistance to radiotherapy. It has recently been shown that HER2/neu amplification protects breast cancer cells against radiotherapy by enhancing the activity of NF- κ B, a protein stress factor that blocks apoptosis in response to oxidative stress induced by ionizing radiation³⁴⁰. Therefore, targeting the HER2/neu

receptor with trastuzumab may enhance radiotherapy by potentially diminishing the hypoxic cell population that may be resistant.

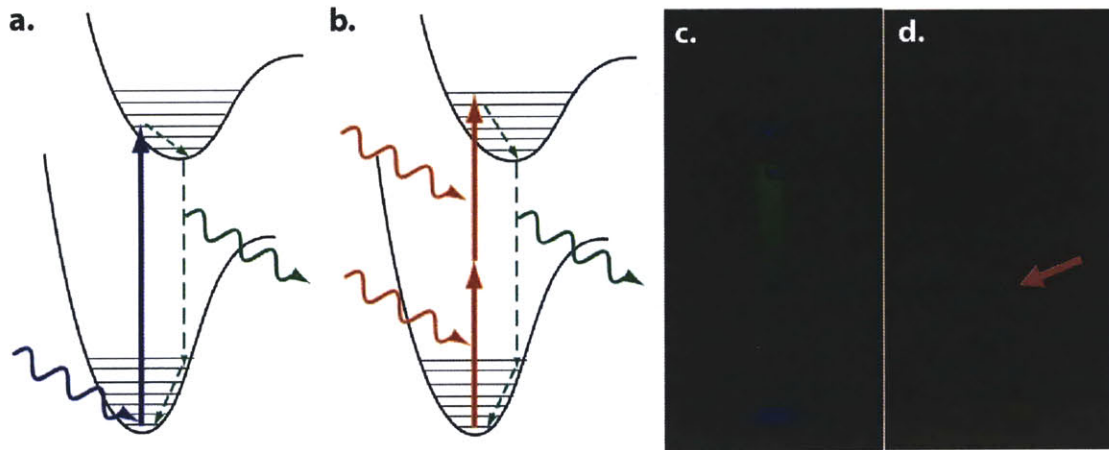


Figure II-3 Principles of multiphoton excitation. (a) Single photon and (b) two-photon excitation from the ground state of a molecular fluorophore. (c) Hourglass shape of fluorescent emission during single photon excitation of fluorescein. (d) Under two-photon excitation of the same sample using the same objective lens, fluorescence is only observed to occur from the focal volume (red arrow).

II.9 Intravital Multiphoton Microscopy

In the past 15 years, a novel form of optical microscopy utilizing ultrafast lasers and high numerical aperture lasers has become a critical tool in the study of *in vivo* biological properties. This technique, multiphoton microscopy, provides non-invasive optical imaging with significant depth penetration at high three-dimensional resolution^{25,345,346}. The intrinsic properties of multiphoton excitation allow MPLSM to image fluorescently labeled structures in tissue with a three-dimensional resolution of ~1 micron up to depths of 450-600 microns, depending upon the tissue type.

II.9a PRINCIPLES OF MULTIPHOTON MICROSCOPY

The principle of multiphoton absorption in molecules, specifically two-photon was originally devised by Maria Goeppert-Mayer in 1931³⁴⁷. Ordinarily, fluorescent molecules are promoted to their excited molecular state with absorption of a single photon of light of an approximate energy equivalent to the separation between the ground and excited states (**Figure II-3a**). In two or multiphoton excitation, two or more

photons of light are simultaneously absorbed by a molecule to reach the excited state (**Figure II-3b**). Once excited, the process of fluorescent emission is independent of the excitation mode³⁴⁶. The excitation probability of molecules by a non-linear process through multiphoton absorption was found to be extremely small at ordinary light intensities. It was not until the advent of high power light sources such as the maser and laser that two-photon absorption and excitation of fluorescence could be experimentally observed³⁴⁸. However, at the light intensities utilized to perform non-linear excitation of fluorescence, damage to biological tissue would be significant. In the early 1990s, the introduction of the ultrafast pulsed laser near-infrared laser sources revolutionized the application of multiphoton excitation to fluorescence microscopy.

By adapting the technique of confocal microscopy, which employed a galvanometer scanning mechanism to spatially image a sample, Denk *et al* were able to perform two-photon imaging of biological samples using an ultrafast laser source³⁴⁵. In confocal microscopy, pinhole detection is required in order to reject fluorescent emission from out of plane excitation for optical sectioning³⁴⁹. This constraint coupled with visible excitation wavelengths limits both the signal to noise and depth penetration of confocal microscopy in biological samples. In MPM, fluorescent emission exhibits a quadratic dependence on incident intensity significantly reducing the probability of excitation outside the focal volume (**Figure II-3c,d**).

$$I_{fl} \propto I^2 \quad (\text{II.5})$$

Therefore, fluorescence only occurs from the focal volume defined by the optics and the emission can be detected in non-descanned fashion without a pinhole. Since excitation occurs only in the focal volume, any potentially damaging processes like photobleaching or thermal effects are limited spatially^{350,351}. This is unlike single photon excitation, which occurs throughout the sample even though fluorescent emission may only be collected from one depth focus. Further, the use of near-infrared excitation light (700-1020nm) populates a region of the electromagnetic spectrum at which absorption in biological materials by water, hemoglobin, adipose tissue and other chromophores is at

a minimum³⁴⁹. This permits deeper imaging in biological samples than confocal microscopy. However, it should be noted that optical resolution scales with wavelength. Therefore radial resolution is slightly higher in confocal microscopy than MPM. In most literature, including this Thesis, the term “multiphoton” microscopy or excitation nearly always refers to two-photon excitation. Three-photon and higher orders of excitation have been observed in certain biological molecules like serotonin³⁵² and DNA labels, like DAPI³⁵³, that absorb in the ultraviolet range. While these processes exist, they are often not applied *in vivo*.

II.9b MULTIPHOTON MICROSCOPY IN CANCER BIOLOGY

Intravital imaging of tumors was first introduced by the Steele Laboratory in collaboration with the So Lab at MIT²⁹. Application of MPM to transgenic mouse models demonstrated quantitative imaging of endogenous molecular reporters, tumor vasculature and blood flow²⁵. Second harmonic generation, a nonlinear optical process that occurs due to a different photophysical process than multiphoton excitation, can also be performed in tumors using MPM instrumentation. Coupling MPM and second harmonic imaging permits imaging of type I collagen in the context of the tumor microenvironment³⁵⁴. Dynamic changes in the extracellular matrix due to compounds that induce degradation^{355,356} or as a result of cellular interaction with the collagen fibers³⁵⁷ can be observed in tumors. Modifications in the technique of MPM allow the study of molecular transport in the tumor microenvironment through either fluorescence correlation³⁵⁸ or fluorescence recovery after photobleaching^{359,360} techniques.

The simple theory behind multiphoton microscopy allows for implementation in a variety of experimental designs. The compounds that are used for imaging can be quite versatile, permitting the use of some that respond to tissue physiology. This allows for simultaneous imaging and physiological monitoring of tissue. In the study of neoplasia, MPM provides many possibilities for studying pathophysiology.

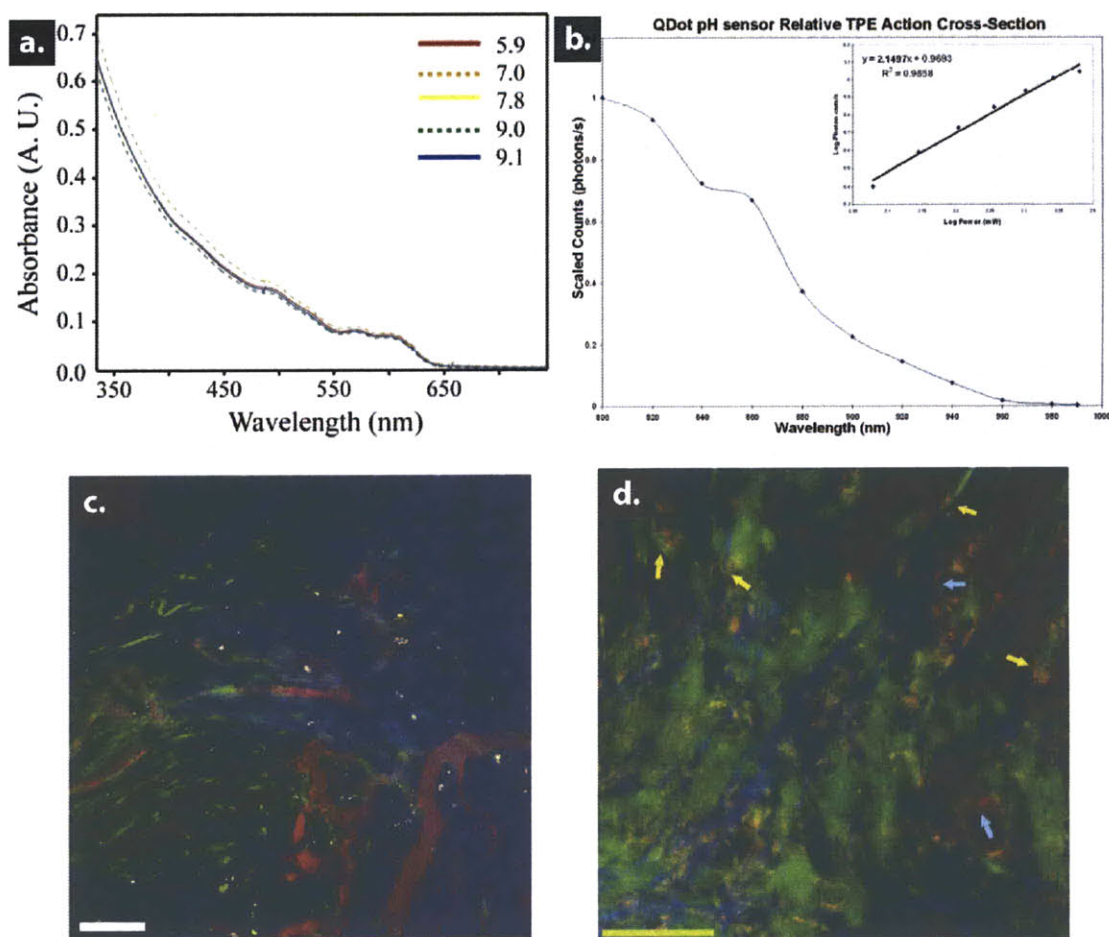


Figure II-4 Fluorescent semiconductor nanocrystals: properties and *in vivo* imaging. (a) NC absorption unaffected by pH at physiological extremes. (b) NCs possess broad two-photon excitation cross-sections. *Inset:* Quadratic dependence of NC excitation with ultrafast NIR lasers. (c) *In vivo* angiography in a murine tumor model with red NCs. Scale bar - 100 μ m (d) NC-immunoconstructs (orange) labeling integrin- β 1 in a VEGF-GFP mouse. Stromal cells (green). SHG from collagen (blue). Scale bar - 150 μ m.

II.10 Luminescent Semiconductor Nanocrystals

Nanotechnology is rapidly emerging as an important source of biocompatible tools that may shape the future of medical practice. Fluorescent semiconductor nanocrystals (NC)³⁶¹, also known as quantum dots, can provide the basic scaffolding for constructing such tools. The intrinsic properties of NCs including high quantum yield, photostability, tunable narrow emission peak, and broad excitation, has made them increasingly attractive for biological imaging^{362,363}. The photophysical properties of NCs are relatively insensitive to the local microenvironment (**Figure II-4a**). The ability to modify surface

coatings of NCs without affecting the photophysical characteristics of the NC core permits control of the way NCs interact with and respond to their environment. NCs are increasingly used in biological research as fluorescent tracers in microscopy^{364,365} (**Figure II-4c**), imaging molecular targets³⁶⁶, cell tracking^{363,367}, and sensing³⁶⁸. Further, NCs have proven reliable fluorescent markers for *in vivo* multiphoton microscopy because of an unparalleled two-photon excitation cross-section^{369,370} (**Figure II-4b**). Recently, NCs have been exploited to study drug delivery and tumor pathophysiology^{366,367,370} (**Figure II-4d**).

Fluorescent nanocrystals consist of a spherical inorganic core (2-10 nm diameter) typically made of CdSe obtained by colloidal synthesis. The core is the source of the optical signal which is defined by its size. Excitons - excited electrons bound to the positively charged holes remaining in the valence band of a semiconductor material – undergo quantum confinement when the size of the NC core approaches the distance between the electron and hole^{371,372}. As the dimensions of the NC core become increasingly smaller than the exciton, the band gap of the material increases. Increasing band gaps lead to higher energy photons, thus smaller NCs emit at shorter wavelengths³⁷³. The existence of higher molecular-like states in quantum confinement confers the broad absorption spectra observed with NCs³⁷⁴. An additional inorganic coating, usually ZnS, creates a protective shell that reduces non-fluorescing relaxation pathways of the exciton, thus increasing quantum yield. These core-shell NCs also are more robust to chemical degradation and photobleaching^{375,376}. Other core materials (InP and InAs) not utilizing heavy metals, which are biologically toxic, are under investigation^{377,378}. However, *in vivo* toxicity has not been observed in murine studies even with repeated exposure over extended periods^{364,379-382}.

For biological applications, inorganic NCs need to be solubilized and passivated to minimize interactions with biological molecules. Chapter 5 will address this issue in detail for the development of an ideal NC biosensor that penetrates tumor tissue without binding. Surface coatings that contain polyethylene glycol (PEG) chains generally have improved retention times in circulation after intravenous injection^{362,383-}

³⁸⁷. However, the terminal charge of the PEGs is critical in refining interactions and transport in tissue, particularly the tumor microenvironment³⁸⁸⁻³⁹¹. The biocompatible surface coating is the major contributor to the hydrodynamic radius of the NC an important consideration when considering delivery and transport in the tumor microenvironment^{68,392-394}. The biocompatible surface coating also serves as a scaffold for conjugating molecules for targeting and, as will be discussed, sensing.

II.11 Fluorescence Resonance Energy Transfer and Sensing

Conventional ratiometric sensors for pH exhibit either different emissive or absorptive properties subject to the hydrogen ion concentration. Therefore, two states exist in these pH indicators, which if resolvable make them internally calibrated sensors. Both BCECF and SNARF are examples of two-state ratiometric sensors^{299,300}. While these probes are reliable in single photon excitation epifluorescence microscopy, the ability to resolve the two states is impossible in multiphoton microscopy. The innovation of a ratiometric sensor based on fluorescence resonance energy transfer (FRET) between an NC coupled with a pH sensitive dye resolves these issues (**Error! Reference source not found.**). The construct should assume the excitation properties of the NC, which exhibits a large two-photon absorption cross-section with a broad excitation range^{369,370}. This scheme permits the selection of almost any analyte sensitive dye molecule as excitation will occur through the NC.

II.11a PRINCIPLES OF FRET

The process of FRET involves the non-radiative transfer of energy from a fluorescent donor molecule to an acceptor. The process was first described in 1948 by Theodor Förster³⁹⁵, hence FRET is sometimes referred to as Förster resonance energy transfer. Energy transfer typically occurs from a lower wavelength emitting donor over a short distance (20-60Å) and is due to a dipole-dipole interaction of the donor and acceptor molecules²⁰⁸. The rate of energy transfer (k_T) is inversely proportional to the sixth

power of the donor-acceptor separation distance (r^6) and directly related to the spectral overlap of the donor emission and acceptor absorption (J).

$$k_T(r) = k_D \frac{\kappa^2}{r^6} \left(\frac{9000(\ln 10)}{128 \pi^5 N n^4} \right) J \quad (\text{II.1})$$

Here k_D is the radiative emission rate of the donor in free solution defined by the emission lifetime (τ_D) and quantum yield (ϕ_D).

$$k_D = \frac{\phi_D}{\tau_D}. \quad (\text{II.2})$$

κ^2 describes the orientation of the dipoles, which in the case of randomly oriented dipoles is considered to be $\frac{2}{3}$ ³⁴⁹. This has proved successful in other FRET-based NC-protein sensors³⁹⁶. N is Avogadro's number and n is the index of refraction of the aqueous medium (1.4). The overlap integral is defined by the normalized fluorescence emission spectrum of the donor ($F_D(\lambda)$) in nm or cm and the excitation wavelength dependent extinction coefficient of the acceptor ($\epsilon_A(\lambda)$) in units of $\text{M}^{-1}\text{cm}^{-1}$.

$$J = \int_0^\infty F_D(\lambda) \epsilon_A(\lambda) \lambda^4 d\lambda \quad (\text{II.3})$$

The resonance energy transfer relationship is typically not defined as in Eq. (II.1), but instead it is written in terms of the Forster distance (R_0). This is the distance at which the FRET rate is equivalent to the donor fluorescent emission rate: τ_D^{-1} .

$$R_0^6 = \kappa^2 \left(\frac{9000(\ln 10)}{128 \pi^5 N n^4} \right) J \quad (\text{II.4})$$

The energy transfer efficiency (E) is fraction of photons absorbed by the donor that are transferred to the acceptor. This can be defined by the rates of these two processes assuming that loss occurs only through radiative and non-radiative decay by the donor.

$$E = \frac{k_T}{k_T + \tau_D^{-1}} = \frac{R_0^6}{R_0^6 + r^6} \quad (\text{II.5})$$

The FRET efficiency is typically determined by measuring the fluorescence lifetime of the donor in the presence and absence of bound acceptor.

$$E = 1 - \frac{\tau_{DA}}{\tau_D} \quad (\text{II.6})$$

If a number of acceptor molecules are present that can interact equally with the donor, then the transfer efficiency increases with each additional acceptor. In the case of FRET using NCs, more than one donor molecule is often attached to the NC due to its larger size (6-12nm). In this case transfer efficiency is defined as follows³⁹⁶,

$$E = \frac{mR_0^6}{mR_0^6 + r^6} \quad (\text{II.7})$$

where m is the number of bound acceptor molecules.

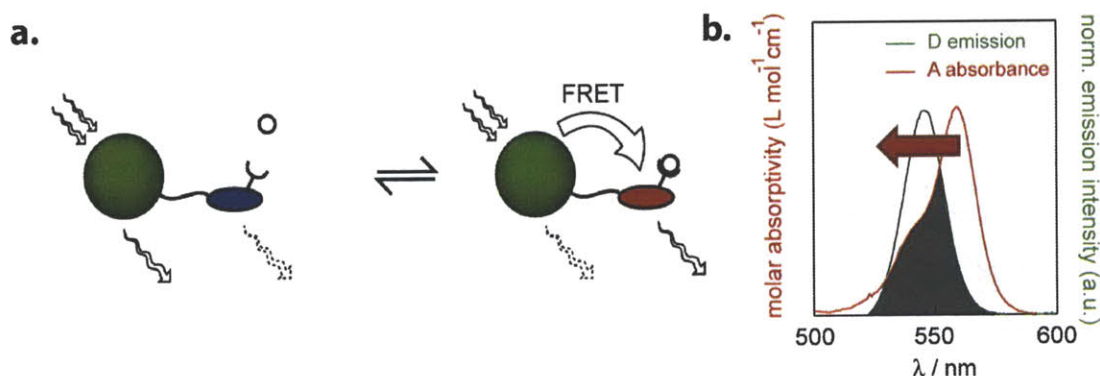


Figure II-5 FRET-based sensing using semiconductor nanocrystals. (a). In the absence of analyte most emission occurs from the NC. When analyte binds, the extinction coefficient of the sensitive dye shifts - altering the FRET efficiency. (b). In the case of the pH biosensor, the efficiency increases with increasing pH: decreasing NC fluorescence and increasing dye emission. In a two-photon absorption of the NC is shown.

II.11b EXAMPLES OF FRET USING FLUORESCENT NANOCRYSTALS

Besides the configuration presented in Figure II-5a, fluorescent nanocrystal sensors have been proposed and demonstrated in a variety of schemes. The most common NCs utilized in FRET arrangements are based on Cadmium-Selenide cores (CdSe). The work presented in this thesis focuses entirely on this type of NC. CdSe NC energy transfer relationships were first observed between NCs of different diameters in solids³⁹⁷. The

broad absorption spectrum of NCs and relatively short fluorescent lifetime of many organic fluorophores typically prevents the use of NCs as FRET acceptors in other situations³⁹⁸. A study using water soluble NCs bound to maltose binding proteins with different organic fluorophores attached demonstrated through a series of experiments many of the photophysical and FRET properties of NCs as energy transfer donors³⁹⁶.

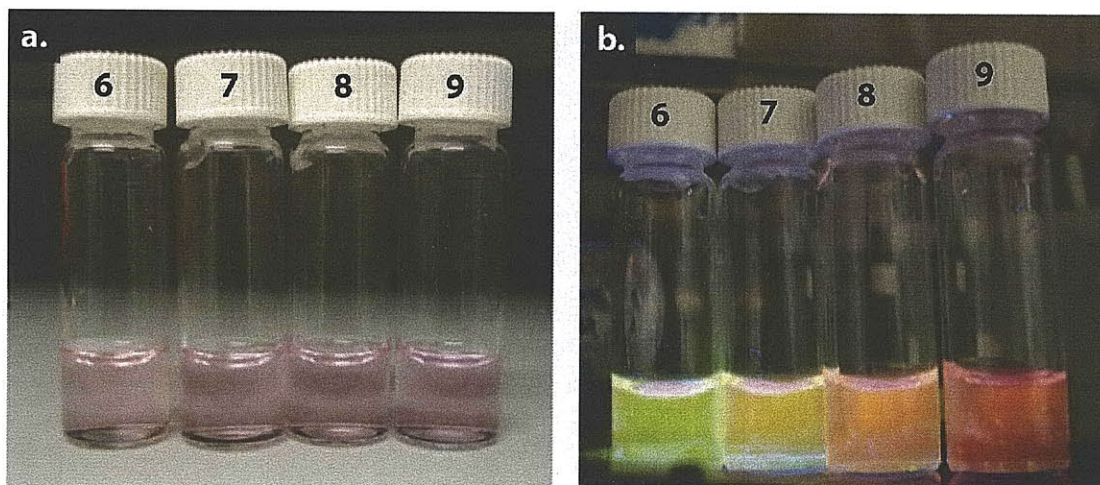


Figure II-6 FRET-based NC biosensor for pH in the physiological range found in tumors. (a) NC biosensor without excitation of the NC at pH 6-9. (b) Under ultraviolet illumination the difference in fluorescent emission is striking. *Photos courtesy of Dr. R. Somers.*

The use of NCs in FRET-based chemical and biological sensors has been thoroughly reviewed elsewhere³⁹⁸. Biological processes that modify the FRET distance between NCs and a fluorophore have been used to detect DNA replication³⁹⁹, DNA cleavage⁴⁰⁰ and the interaction between *in vitro* protein complexes⁴⁰¹. Displacement of a quencher attached to an NC by a molecule of interest has been used to sense both maltose³⁶⁸ and TNT⁴⁰². Determination of ion concentrations has been performed using NC to NC FRET through analyte promoted NC aggregation³⁹⁸. The above NC sensing protocols can be very accurate to low concentrations of analyte; however the probe is consumed during the process making sensing irreversible. Coupling the NC directly to chromophores or fluorophores with an absorption spectrum dependent on the concentration of an analyte creates a reversible probe (Figure II-5Error! Reference source not found.b). Conjugating a pH sensitive chromophore to an NC permitted reversible sensing of pH

through the changes in NC emission due to modulation of the FRET efficiency. However, calibration and *in vivo* sensing in this setting is difficult due to the single emission unless fluorescence lifetime measurements are performed⁴⁰³. A ratiometric pH probe based on conjugation of an NC with a pH-sensitive fluorophore demonstrated internally referenced pH sensing due to the presence of two detectable emissions and maintenance of an isosbestic point⁴⁰⁴.

In summary, linking a NC to an environmentally sensitive fluorescent dye in which there is a donor-acceptor FRET relationship allows for ratiometric spectral comparison (via modulation of energy transfer or dye emission lifetime/intensity) dependent upon analyte concentration. With judicious dye selection, so that there is limited direct excitation, a reversible internally calibrated ratiometric biosensor is possible due to the photostability and environmental insensitivity of the NC. The entire construct inherits the broad excitation spectrum and large two-photon excitation cross-section of the NC – highly desirable attributes for use *in vivo* with MPM. The pH sensor developed in this Thesis (**Figure II-6**) employs this design for a ratiometric pH probe for use with multiphoton FRIM.

II.12 Optical Coherence Tomography

Image contrast in coherent microscopy like optical coherence tomography (OCT) is derived from the dependence of optical scattering on endogenous tissue structure and function rather than from fluorescent labels as in MPM. These differences in technique allow OCT systems to circumvent some of the limitations of MPM. Because the beam focus is not used to select specific depths, OCT alleviates the requirement for high numerical aperture optics, thereby simplifying wide-field imaging. Furthermore, OCT can image at longer wavelengths where penetration depth in tissue is improved to several millimeters, and can image frequently over prolonged periods without concern for accumulation of fluorescent tracer. However, methods for effectively characterizing biological parameters of tumor microenvironment and structure through optical scattering are lacking in OCT

II.12a PRINCIPLES AND TECHNIQUES

Optical coherence tomography⁴⁰⁵ (OCT) is an alternative approach for *in vivo* microscopy. OCT uses the delay of light reflected from tissue, i.e., the “time of flight”, to image across depth, analogous to ultrasonography. Classically, OCT is performed in the time-domain using an interferometer which measures the cross-correlation of a sample and reference beam from the same light source (**Figure II-7**). The time delay of the light along the reference path determines the imaging depth, while the amplitude of the interference pattern represents the intensity of the reflected (backscattered) light not randomly scattered in the sample. Low coherence light sources, which contain a number of optical frequencies, are employed in OCT due to the small coherence length. The coherence length, or distance over which interference can occur, defines the axial (depth) resolution of the OCT system. Significant resolution down to 1 μ m is achievable with ultrafast mode-locked laser sources due to the short coherence length, although imaging depth is limited due to the NIR wavelengths (~800nm) of the sources⁴⁰⁶⁻⁴⁰⁸. Most OCT systems use infrared light around 1300nm, which allow depth penetration up to a few millimeters due to lower scattering in biological tissues^{409,410}. Radial resolution is set by the beam focusing lens and spatial sampling density of beam scanning or sample translation. Because OCT uses interferometric techniques to determine the amplitude and time delays of the reflected signal very low light intensities can be detected.

In time-domain OCT, depth scanning is performed through translation of the reference arm to adjust the time delay of the system. This method limits the imaging speed of the system due to mechanical translation for depth. An alternative approach is to perform OCT in the frequency domain, whereby depth is encoded as a function of wavelength⁴¹¹. This approach eliminates the need to scan the reference beam, significantly speeding up the imaging time. Frequency-domain OCT also improves the detection sensitivity by several orders of magnitude because all depth information is obtain simultaneously rather than only within the coherence length of the light source as in time-domain

methods⁴¹²⁻⁴¹⁴. Frequency-domain can be performed by 1) using a spectrometer at the detector to obtain the cross-correlation interference signal as a function of wavelength, a technique known as “spectral radar”⁴¹⁵ and spectral-domain OCT; or 2) using a wavelength-swept broadband laser source⁴¹⁶ known as optical frequency domain imaging (OFDI). In this Thesis, OFDI will be used for all coherent microscopy studies.

OCT instrumentation and methodology can be adapted to probe a number of parameters in biological tissue. At a basic level, the image contrast in OCT is derived from optical scattering in the tissue which is both a source of signal and noise – termed speckle⁴¹⁷. Tissue scattering in OCT allows differentiation of anatomical boundaries and pathological features. Measurement of *in vivo* tissue birefringence using polarization sensitive OCT has been shown to identify collagen and other fibrillar proteins as well as vascular smooth muscle^{418,419}. Spectroscopic OCT, which measures the wavelength dependence of the backscattered light, has demonstrated sensitivity to discriminate scattering particles of various sizes^{420,421}. Finally, phase-resolved OCT or Doppler OCT can be used to detect movement of scatters such as fluid flow in vessels⁴²².

II.12b APPLICATION TO TUMOR BIOLOGY

OCT has been applied to cancer imaging mainly as a histological technique for assessing tumor size and boundaries. A number of studies in animal models and clinically relevant dermatological cancers have demonstrated tumors generally have a high scattering signature in OCT relative to normal tissue⁴²³⁻⁴²⁷. The scattering difference between tumor and surrounding normal tissues is due to the increased nuclear to cytoplasm ratio⁴²⁸. Given the increased reflectance observed between tissue boundaries, OCT has also been used to study changes in the layers of the epithelium during tumorigenesis⁴²⁹. Application of high-resolution OCT to *ex vivo* clinical samples has demonstrated good correlation of microanatomical structures like calcifications, cysts, enlarged nuclei and blood vessels with histology⁴³⁰. Histological changes observed in tumor grading may also be detectable with OCT^{431,432}. Heterogeneous scattering patterns have also been observed in tumor tissue, although investigations into the underlying mechanisms are

lacking^{424,432}. In model tumor spheroids, high scattering regions in the core have been attributed to necrotic tissue^{433,434}. It has additionally been suggested that OCT may be qualitatively sensitive to edema as reflected in low scattering regions⁴²⁹.

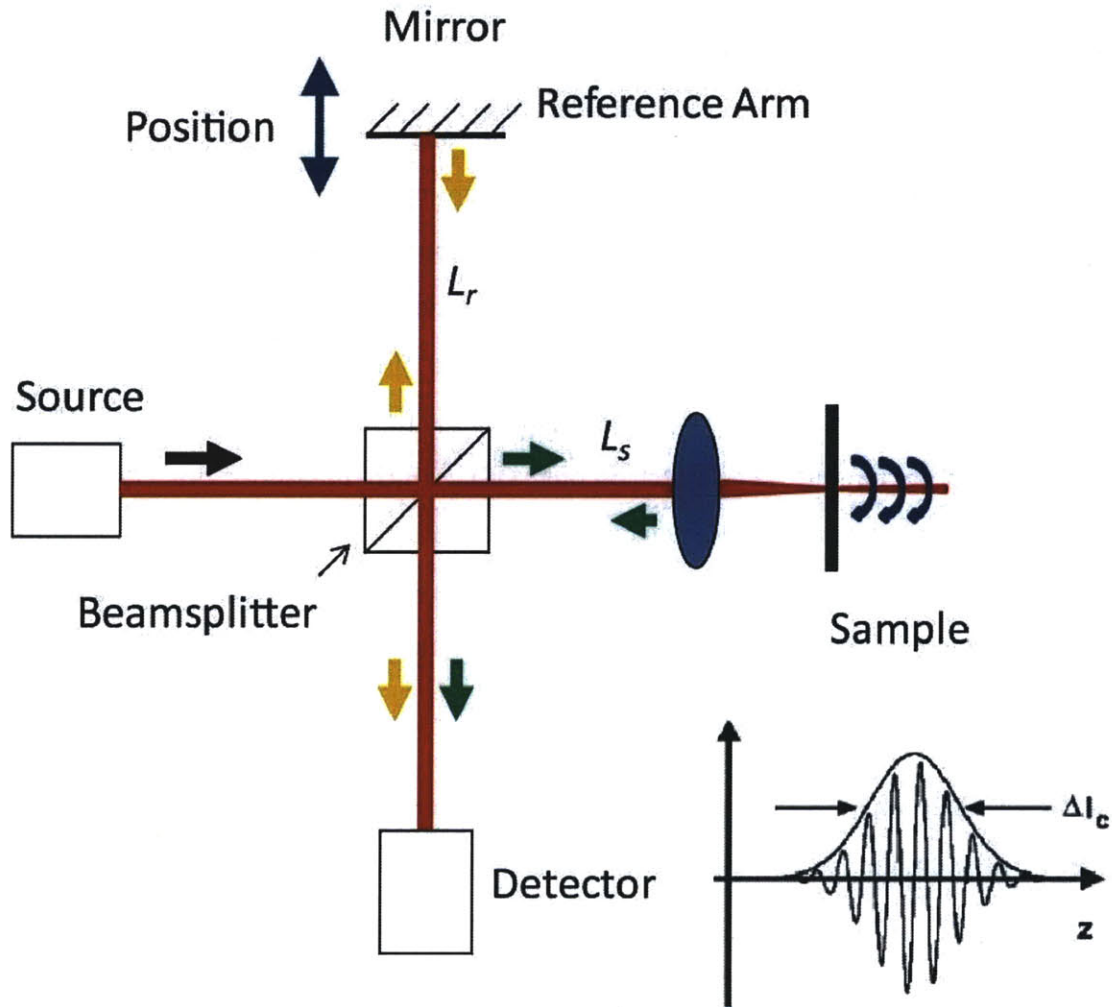


Figure II-7 Basic principles of optical coherence tomography. Light from a coherent source is split into a sample and reference arm. After interacting with the scattering sample, the sample and reference arms are recombined on a detector forming an interference pattern (*inset*).

Doppler OCT techniques have also been applied in both animal and human tumors to assess vascular function. Some investigators have provided quantitative measures of flow, but in most cases changes in perfusion are monitored. The effects of both vascular disrupting agents and photodynamic therapy on vascular perfusion have been studied in animal models^{435,436}. To date, three-dimensional morphological parameters of tumor

vascular have not been presented in the literature, although simple reconstructions of superficial large vessels have been demonstrated⁴³⁷. However, Doppler OCT has been used to measure cross-sectional areas and diameters of perfused vessels according to the phase modulation signal⁴³⁸. In these studies, the measurements are limited to vessels around 100 μ m and severely influenced by “shadowing”⁴³⁷ due to increased backscatter from the blood. Doppler OCT techniques have also been adapted to endoscopic instrumentation for applications in the human gastrointestinal tract with preliminary results suggesting *in vivo* perfusion studies may be possible⁴³⁹.

II.13 Specific Aims

Understanding the role of the tumor microenvironment in the progression of disease and response to therapy will lead to better therapeutic regimens and clinical outcome. Particularly important in the microenvironment are the physiological parameters of oxygen tension (pO_2) and pH. These variables have been shown to directly or indirectly impact response to radiation therapy (pO_2) and chemotherapy (pO_2 and pH)^{7,8}. By modifying the technique of multiphoton microscopy^{25,345} to perform phosphorescence quenching microscopy⁴⁴⁰, I will develop a non-invasive method to quantify pO_2 in living tissue at high-resolution. I will adapt novel fluorescence resonance energy transfer-based nanocrystal (NC) biosensors⁴⁰⁴ for use with MPM to quantify pH in living tissue at high-resolution. I will measure pO_2 and pH *in vivo* during tumor growth and antiangiogenic treatment with the VEGFR-2 blocking antibody DC101 in orthotopic and ectopic tumor models. While MPM demonstrates utility and adaptability in the study of cancer and response to therapy, new techniques are needed to non-invasively study pre-clinical tumor models and assess cell viability. To this end, I will apply Optical Frequency Domain Imaging⁴¹⁶ to study solid tumors over wide fields with microscopic resolution.

II.13a HYPOTHESIS 1. PHOSPHORESCENCE QUENCHING MPM CAN PROVIDE QUANTITATIVE PO₂ SENSING IN TUMORS.

Anti-angiogenic therapy has been shown to alter the tumor vasculature morphology and function, paradoxically improving the efficacy of chemotherapy and radiation treatment. Recently, trastuzumab was demonstrated to modify the tumor vasculature in a manner analogous to many vascular targeted anti-angiogenic agents³³⁶. The structural morphology and functional characteristics of vessels in tumors dictates oxygen and nutrient delivery to the cells. This directly impacts efficacy of both radiotherapy and chemotherapy. Therefore, I expect that an understanding of the dynamic changes in pO₂ during therapy with trastuzumab or DC101 will help schedule more efficacious combined therapeutic regimens for the treatment of solid tumors³¹⁵.

Aim 1a. Adapt phosphorescence quenching microscopy to the technique of MPM and measure pO₂ *in vitro* and *in vivo*.

By modifying the technique of MPM, I will adapt the principles of phosphorescence quenching microscopy (PQM) to the nonlinear optical regime. I will select, characterize and optimize porphyrin-based oxygen sensors for use *in vivo* with MPM. Calibration will be obtained *in vitro* in a closed system for the range of physiologically relevant dissolved pO₂ using MPM. *In vivo* measurements of oxygen tension will be assessed using MPM in transparent window mouse models. Proof of principle for the technique will be demonstrated by confirming the Krogh tissue cylinder model¹⁷⁴ in skeletal muscle fibers in mice.

Aim 1b. Measure changes in pO₂ during tumor growth.

Using solid tumors grown in dorsal skin-fold chamber, mammary fat pad, and cranial window mouse models, pO₂ will be quantified during tumor progression. Measurements will be made both in the interstitial and intravascular spaces of the tumor microenvironment.

CHAPTER 2

Aim 1c. Measure changes in pO_2 during anti-angiogenic therapy with DC101 in solid tumors.

I will perform high-resolution multiphoton phosphorescence quenching microscopy in both a human colorectal adenocarcinoma model (LS174T) and murine mammary carcinoma (MCalV) implanted ectopically in the DSC during administration of DC101. Further, I will assess tumor microenvironmental pO_2 in orthotopic murine mammary carcinoma (EO771) in response to anti-angiogenic therapy by DC101. Morphology of the tumor vasculature will also be assessed by MPM angiography and correlated with pO_2 measurements.

Aim 1d. Measure changes in pO_2 in breast cancer tumors during monotherapy with trastuzumab.

Fluctuations in the intravascular and interstitial pO_2 due to trastuzumab will be measured with PQM using MPM in HER2-positive mammary tumors in the MFP transparent window chamber mouse model. Morphology of the tumor vasculature will also be assessed by MPM angiography and correlated with pO_2 measurements. These results will help identify potential treatment windows during which vascular function may be altered by trastuzumab.

II.13b HYPOTHESIS 2. NC-CONSTRUCTS CAN PROVIDE QUANTITATIVE FRET-BASED PH SENSING IN TUMORS.

Aim 2a. Measure pH *in vitro* and *in vivo* using a NC-biosensor for pH and MPM.

I will optimize the *in vivo* use of FRET-based NC-biosensors with MPM by determining construct stability, minimal particle size, biological pKa, and maximally detectable fluorescence emission and sensitivity. Calibration will be conducted *in vitro* and *in vivo* tumor tissue for the range of physiologically relevant pH. *In vivo* measurements of pH will be assessed using MPM in transparent window mouse models.

Aim 2b. Measure changes in pH during hyperglycemia.

CHAPTER 2

Using transparent window mouse models, I will measure dynamic changes in pH during experimentally induced hyperglycemia. The pH sensitive FRET signal from the NC-biosensor will be monitored by MPM in the interstitium and correlated with the tumor vasculature.

II.13c HYPOTHESIS 3. OPTICAL FREQUENCY DOMAIN IMAGING CAN NON-INVASIVELY PERFORM THREE-DIMENSIONAL MICROSCOPY OF VASCULAR NETWORKS, LYMPHATICS, TISSUE VIABILITY AND MICROANATOMY IN SOLID TUMORS.

High resolution, intravital multiphoton microscopy has provided powerful mechanistic insights into tumor biology. However, the requisite high numerical aperture and exogenous contrast agents result in a limited capacity to investigate substantial tissue volumes or to probe dynamic changes repeatedly over prolonged periods. By using coherent optical principles distinct from multiphoton microscopy, optical frequency domain imaging circumvents these limitations and may provide an unprecedented ability to probe critically important aspects of tumor biology.

Aim 3a. Perform non-invasive, high-resolution, wide-field angiography of tumor vascular networks without the administration of exogenous contrast using OFDI.

By applying Doppler principles, OFDI can detect vasculature through contrast derived from the intrinsic fluid motion within the vessels. I will demonstrate the ability of OFDI to monitor vascular morphology and geometry frequently and over prolonged timescales in solid tumors. Further, I will characterize the performance of OFDI angiography through direct comparison with multiphoton microscopy.

Aim 3b. Perform contrast-free functional lymphangiography using OFDI.

By taking advantage of the optical scattering differences between functional lymphatic vessels and the surrounding tissue, OFDI can map lymphatic networks without the use of exogenous dyes. I will show that OFDI lymphangiography supersedes standard methods by providing an ability to map lymphatic networks over larger regions and more frequent timepoints.

Aim 3c. Characterize *in vivo* tissue viability using OFDI.

Based on differences in tissue reflectance, OFDI can differentiate necrotic/apoptotic regions from viable tissue. I will show that OFDI can monitor tissue viability during tumor progression and demonstrate that the spatial distribution of viable tissue can be correlated with the distance to the vascular network.

Aim 3d. Assess multiparametric responses of both vascular-targeted and cellular-targeted therapies using OFDI.

To demonstrate the utility of OFDI as a tool to monitor anti-cancer therapy, I will perform multiparametric imaging of tumors during either antiangiogenic therapy by DC101 or direct targeting of tumor cells through the use of diphtheria toxin.

II.14 References

1. Weinberg, R.A. *The biology of cancer*, (Garland Science, New York, 2007).
2. Harris, A.L. Hypoxia—a key regulatory factor in tumour growth. *Nat Rev Cancer* **2**, 38-47 (2002).
3. Rofstad, E.K. Microenvironment-induced cancer metastasis. *Int J Radiat Biol* **76**, 589-605 (2000).
4. Evans, S.M. & Koch, C.J. Prognostic significance of tumor oxygenation in humans. *Cancer Lett* **195**, 1-16 (2003).
5. Koukourakis, M.I., *et al.* Enhanced expression of SPARC/osteonectin in the tumor-associated stroma of non-small cell lung cancer is correlated with markers of hypoxia/acidity and with poor prognosis of patients. *Cancer Res* **63**, 5376-5380 (2003).
6. Weinmann, M., Belka, C. & Plasswilm, L. Tumour hypoxia: impact on biology, prognosis and treatment of solid malignant tumours. *Onkologie* **27**, 83-90 (2004).
7. Brown, J.M. Tumor microenvironment and the response to anticancer therapy. *Cancer Biol Ther* **1**, 453-458 (2002).
8. Tannock, I.F. & Rotin, D. Acid pH in tumors and its potential for therapeutic exploitation. *Cancer Res* **49**, 4373-4384 (1989).
9. Boudreau, N. & Myers, C. Breast cancer-induced angiogenesis: multiple mechanisms and the role of the microenvironment. *Breast Cancer Res* **5**, 140-146 (2003).
10. Jain, R.K. Normalization of tumor vasculature: an emerging concept in antiangiogenic therapy. *Science* **307**, 58-62 (2005).
11. Jain, R.K. Antiangiogenic therapy for cancer: current and emerging concepts. *Oncology (Williston Park)* **19**, 7-16 (2005).

12. Monsky, W.L., *et al.* Role of host microenvironment in angiogenesis and microvascular functions in human breast cancer xenografts: mammary fat pad versus cranial tumors. *Clin Cancer Res* **8**, 1008-1013 (2002).
13. Jain, R.K. Normalizing tumor vasculature with anti-angiogenic therapy: a new paradigm for combination therapy. *Nat Med* **7**, 987-989 (2001).
14. Gray, L.H., Conger, A.D., Ebert, M., Hornsey, S. & Scott, O.C. The concentration of oxygen dissolved in tissues at the time of irradiation as a factor in radiotherapy. *Br J Radiol* **26**, 638-648 (1953).
15. Vukovic, V. & Tannock, I.F. Influence of low pH on cytotoxicity of paclitaxel, mitoxantrone and topotecan. *Br J Cancer* **75**, 1167-1172 (1997).
16. Freyer, J.P. & Sutherland, R.M. Regulation of growth saturation and development of necrosis in EMT6/Ro multicellular spheroids by the glucose and oxygen supply. *Cancer Res* **46**, 3504-3512 (1986).
17. Hlatky, L., Sachs, R.K. & Alpen, E.L. Joint oxygen-glucose deprivation as the cause of necrosis in a tumor analog. *J Cell Physiol* **134**, 167-178 (1988).
18. Warburg, O. On the origin of cancer cells. *Science* **123**, 309-314 (1956).
19. Burk, D. & Schade, A.L. On respiratory impairment in cancer cells. *Science* **124**, 270-272 (1956).
20. Warburg, O. On respiratory impairment in cancer cells. *Science* **124**, 269-270 (1956).
21. Weinhouse, S. On respiratory impairment in cancer cells. *Science* **124**, 267-269 (1956).
22. Crabtree, H.G. Observations on the carbohydrate metabolism of tumours. *Biochem J* **23**, 536-545 (1929).
23. Helmlinger, G., Sckell, A., Dellian, M., Forbes, N.S. & Jain, R.K. Acid production in glycolysis-impaired tumors provides new insights into tumor metabolism. *Clin Cancer Res* **8**, 1284-1291 (2002).
24. Helmlinger, G., Yuan, F., Dellian, M. & Jain, R.K. Interstitial pH and pO₂ gradients in solid tumors in vivo: high-resolution measurements reveal a lack of correlation. *Nat Med* **3**, 177-182 (1997).
25. Brown, E.B., *et al.* In vivo measurement of gene expression, angiogenesis and physiological function in tumors using multiphoton laser scanning microscopy. *Nat Med* **7**, 864-868 (2001).
26. Jain, R.K., Munn, L. L., and Fukumura, D. Transparent window models and intravital microscopy. in *Tumor models in cancer research* (ed. Teicher, B.A.) pp. 647-671 (Humana Press, Totowa, N.J., 2002).
27. Jain, R.K., Brown, E.B., Munn, L.L. & Fukumura, D. Intravital microscopy of normal and diseased tissues in the mouse. in *Live cell imaging : a laboratory manual* (eds. Goldman, R.D. & Spector, D.L.) pp 435-466 (Cold Spring Harbor Laboratory Press, Cold Spring Harbor, N.Y., 2005).
28. Jain, R.K., Munn, L.L. & Fukumura, D. Dissecting tumour pathophysiology using intravital microscopy. *Nat Rev Cancer* **2**, 266-276 (2002).
29. Padera, T.P., Stoll, B.R., So, P.T. & Jain, R.K. Conventional and high-speed intravital multiphoton laser scanning microscopy of microvasculature, lymphatics, and leukocyte-endothelial interactions. *Mol Imaging* **1**, 9-15 (2002).
30. Barrett, T., Choyke, P.L. & Kobayashi, H. Imaging of the lymphatic system: new horizons. *Contrast Media Mol Imaging* **1**, 230-245 (2006).
31. Clement, O. & Luciani, A. Imaging the lymphatic system: possibilities and clinical applications. *Eur Radiol* **14**, 1498-1507 (2004).

CHAPTER 2

32. Hashizume, H., *et al.* Openings between defective endothelial cells explain tumor vessel leakiness. *Am J Pathol* **156**, 1363-1380 (2000).
33. Jain, R.K. Transport of molecules across tumor vasculature. *Cancer Metastasis Rev* **6**, 559-593 (1987).
34. Jain, R.K. Delivery of molecular medicine to solid tumors. *Science* **271**, 1079-1080 (1996).
35. Kashiwagi, S., *et al.* NO mediates mural cell recruitment and vessel morphogenesis in murine melanomas and tissue-engineered blood vessels. *J Clin Invest* **115**, 1816-1827 (2005).
36. Folkman, J. Role of angiogenesis in tumor growth and metastasis. *Semin Oncol* **29**, 15-18 (2002).
37. Hoshida, T., *et al.* Imaging Steps of Lymphatic Metastasis Reveals That Vascular Endothelial Growth Factor-C Increases Metastasis by Increasing Delivery of Cancer Cells to Lymph Nodes: Therapeutic Implications. *Cancer Res* **66**, 8065-8075 (2006).
38. Padera, T.P., *et al.* Lymphatic metastasis in the absence of functional intratumor lymphatics. *Science* **296**, 1883-1886 (2002).
39. Less, J.R., Skalak, T.C., Sevick, E.M. & Jain, R.K. Microvascular architecture in a mammary carcinoma: branching patterns and vessel dimensions. *Cancer Res* **51**, 265-273 (1991).
40. Peters, W., Teixeira, M., Intaglietta, M. & Gross, J.F. Microcirculatory studies in rat mammary carcinoma. I. Transparent chamber method, development of microvasculature, and pressures in tumor vessels. *J Natl Cancer Inst* **65**, 631-642 (1980).
41. Vakoc, B.J., *et al.* Three-dimensional microscopy of the tumor microenvironment in vivo using optical frequency domain imaging. *Nature Medicine* **Accepted**(2009).
42. Chaplin, D.J. & Hill, S.A. Temporal heterogeneity in microregional erythrocyte flux in experimental solid tumours. *Br J Cancer* **71**, 1210-1213 (1995).
43. Chaplin, D.J., Olive, P.L. & Durand, R.E. Intermittent blood flow in a murine tumor: radiobiological effects. *Cancer Res* **47**, 597-601 (1987).
44. Eskey, C.J., Koretsky, A.P., Domach, M.M. & Jain, R.K. 2H-nuclear magnetic resonance imaging of tumor blood flow: spatial and temporal heterogeneity in a tissue-isolated mammary adenocarcinoma. *Cancer Res* **52**, 6010-6019 (1992).
45. Intaglietta, M., Myers, R.R., Gross, J.F. & Reinhold, H.S. Dynamics of microvascular flow in implanted mouse mammary tumours. *Bibl Anat*, 273-276 (1977).
46. Jain, R.K. Determinants of tumor blood flow: a review. *Cancer Res* **48**, 2641-2658 (1988).
47. Sevick, E.M. & Jain, R.K. Geometric resistance to blood flow in solid tumors perfused ex vivo: effects of tumor size and perfusion pressure. *Cancer Res* **49**, 3506-3512 (1989).
48. Sevick, E.M. & Jain, R.K. Effect of red blood cell rigidity on tumor blood flow: increase in viscous resistance during hyperglycemia. *Cancer Res* **51**, 2727-2730 (1991).
49. Carmeliet, P. & Jain, R.K. Angiogenesis in cancer and other diseases. *Nature* **407**, 249-257 (2000).
50. Gerlowski, L.E. & Jain, R.K. Microvascular permeability of normal and neoplastic tissues. *Microvasc Res* **31**, 288-305 (1986).
51. Jain, R.K. Molecular regulation of vessel maturation. *Nature Medicine* **9**, 685-693 (2003).
52. Yuan, F., Leunig, M., Berk, D.A. & Jain, R.K. Microvascular permeability of albumin, vascular surface area, and vascular volume measured in human adenocarcinoma LS174T using dorsal chamber in SCID mice. *Microvasc Res* **45**, 269-289 (1993).
53. Yuan, F., *et al.* Vascular permeability and microcirculation of gliomas and mammary carcinomas transplanted in rat and mouse cranial windows. *Cancer Res* **54**, 4564-4568 (1994).

CHAPTER 2

54. Araujo, R.P. & McElwain, D.L. New insights into vascular collapse and growth dynamics in solid tumors. *J Theor Biol* **228**, 335-346 (2004).
55. Galie, M., *et al.* Tumor vessel compression hinders perfusion of ultrasonographic contrast agents. *Neoplasia* **7**, 528-536 (2005).
56. Griffon-Etienne, G., Boucher, Y., Brekken, C., Suit, H.D. & Jain, R.K. Taxane-induced apoptosis decompresses blood vessels and lowers interstitial fluid pressure in solid tumors: clinical implications. *Cancer Res* **59**, 3776-3782 (1999).
57. Padera, T.P., *et al.* Cancer cells compress intratumour vessels. *Nature* **427**, 695 (2004).
58. Jain, R.K. & Fenton, B.T. Intratumoral lymphatic vessels: a case of mistaken identity or malfunction? *J Natl Cancer Inst* **94**, 417-421 (2002).
59. Pepper, M.S. Lymphangiogenesis and tumor metastasis: myth or reality? *Clin Cancer Res* **7**, 462-468 (2001).
60. Asano, S., Cho, H., Sonoda, Y. & Sagami, S. [Dilation changes of lymphatic vessels observed around cutaneous tumors]. *Nippon Hifuka Gakkai Zasshi* **93**, 1329-1335 (1983).
61. Isaka, N., Padera, T.P., Hagendoorn, J., Fukumura, D. & Jain, R.K. Peritumor lymphatics induced by vascular endothelial growth factor-C exhibit abnormal function. *Cancer Research* **64**, 4400-4404 (2004).
62. Leu, A.J., Berk, D.A., Lymboussaki, A., Alitalo, K. & Jain, R.K. Absence of functional lymphatics within a murine sarcoma: a molecular and functional evaluation. *Cancer Res* **60**, 4324-4327 (2000).
63. Ji, R.C. Lymphatic endothelial cells, tumor lymphangiogenesis and metastasis: New insights into intratumoral and peritumoral lymphatics. *Cancer Metastasis Rev* **25**, 677-694 (2006).
64. Leunig, M., *et al.* Angiogenesis, microvascular architecture, microhemodynamics, and interstitial fluid pressure during early growth of human adenocarcinoma LS174T in SCID mice. *Cancer Res* **52**, 6553-6560 (1992).
65. Boucher, Y., Salehi, H., Witwer, B., Harsh, G.R.t. & Jain, R.K. Interstitial fluid pressure in intracranial tumours in patients and in rodents. *Br J Cancer* **75**, 829-836 (1997).
66. Milosevic, M., Fyles, A., Hedley, D. & Hill, R. The human tumor microenvironment: invasive (needle) measurement of oxygen and interstitial fluid pressure. *Semin Radiat Oncol* **14**, 249-258 (2004).
67. Tong, R.T., *et al.* Vascular normalization by vascular endothelial growth factor receptor 2 blockade induces a pressure gradient across the vasculature and improves drug penetration in tumors. *Cancer Res* **64**, 3731-3736 (2004).
68. Jain, R.K. Delivery of molecular and cellular medicine to solid tumors. *Adv Drug Deliv Rev* **46**, 149-168 (2001).
69. Ausprunk, D.H., Knighton, D.R. & Folkman, J. Vascularization of normal and neoplastic tissues grafted to the chick chorioallantois. Role of host and preexisting graft blood vessels. *Am J Pathol* **79**, 597-618 (1975).
70. Gimbrone, M.A., Jr., Leapman, S.B., Cotran, R.S. & Folkman, J. Tumor dormancy in vivo by prevention of neovascularization. *J Exp Med* **136**, 261-276 (1972).
71. Gullino, P.M. Angiogenesis and oncogenesis. *J Natl Cancer Inst* **61**, 639-643 (1978).
72. Patan, S., Munn, L.L. & Jain, R.K. Intussusceptive microvascular growth in a human colon adenocarcinoma xenograft: a novel mechanism of tumor angiogenesis. *Microvasc Res* **51**, 260-272 (1996).
73. Semenza, G.L. Vasculogenesis, angiogenesis, and arteriogenesis: mechanisms of blood vessel formation and remodeling. *J Cell Biochem* **102**, 840-847 (2007).

74. Carmeliet, P. Angiogenesis in life, disease and medicine. *Nature* **438**, 932-936 (2005).
75. Fox, S.B., Gasparini, G. & Harris, A.L. Angiogenesis: pathological, prognostic, and growth-factor pathways and their link to trial design and anticancer drugs. *Lancet Oncol* **2**, 278-289 (2001).
76. Toi, M., Bando, H. & Kuroi, K. The predictive value of angiogenesis for adjuvant therapy in breast cancer. *Breast Cancer* **7**, 311-314 (2000).
77. Kirsch, M., Schackert, G. & Black, P.M. Metastasis and angiogenesis. *Cancer Treat Res* **117**, 285-304 (2004).
78. Schneider, B.P. & Miller, K.D. Angiogenesis of breast cancer. *J Clin Oncol* **23**, 1782-1790 (2005).
79. Guidi, A.J., Fischer, L., Harris, J.R. & Schnitt, S.J. Microvessel density and distribution in ductal carcinoma in situ of the breast. *J Natl Cancer Inst* **86**, 614-619 (1994).
80. Guidi, A.J., et al. Vascular permeability factor (vascular endothelial growth factor) expression and angiogenesis in patients with ductal carcinoma in situ of the breast. *Cancer* **80**, 1945-1953 (1997).
81. Weidner, N., Semple, J.P., Welch, W.R. & Folkman, J. Tumor angiogenesis and metastasis--correlation in invasive breast carcinoma. *N Engl J Med* **324**, 1-8 (1991).
82. Jain, R.K. Taming Vessels to Treat Cancer. *Scientific American* **298**, 56-63 (2008).
83. Ribatti, D., Nico, B., Crivellato, E., Roccaro, A.M. & Vacca, A. The history of the angiogenic switch concept. *Leukemia* **21**, 44-52 (2007).
84. Ferrara, N. Vascular endothelial growth factor: molecular and biological aspects. *Curr Top Microbiol Immunol* **237**, 1-30 (1999).
85. Fukumura, D., et al. Tumor induction of VEGF promoter activity in stromal cells. *Cell* **94**, 715-725 (1998).
86. Larcher, F., Murillas, R., Bolontrade, M., Conti, C.J. & Jorcano, J.L. VEGF/VPF overexpression in skin of transgenic mice induces angiogenesis, vascular hyperpermeability and accelerated tumor development. *Oncogene* **17**, 303-311 (1998).
87. Jain, R.K. Tumor angiogenesis and accessibility: role of vascular endothelial growth factor. *Semin Oncol* **29**, 3-9 (2002).
88. Han, H., et al. Vascular endothelial growth factor expression in stage I non-small cell lung cancer correlates with neoangiogenesis and a poor prognosis. *Ann Surg Oncol* **8**, 72-79 (2001).
89. Maeda, K., et al. Expression of p53 and vascular endothelial growth factor associated with tumor angiogenesis and prognosis in gastric cancer. *Oncology* **55**, 594-599 (1998).
90. Xu, L., Tong, R., Cochran, D.M. & Jain, R.K. Blocking platelet-derived growth factor-D/platelet-derived growth factor receptor beta signaling inhibits human renal cell carcinoma progression in an orthotopic mouse model. *Cancer Res* **65**, 5711-5719 (2005).
91. Dellian, M., Witwer, B.P., Salehi, H.A., Yuan, F. & Jain, R.K. Quantitation and physiological characterization of angiogenic vessels in mice: effect of basic fibroblast growth factor, vascular endothelial growth factor/vascular permeability factor, and host microenvironment. *Am J Pathol* **149**, 59-71 (1996).
92. Watnick, R.S., Cheng, Y.N., Rangarajan, A., Ince, T.A. & Weinberg, R.A. Ras modulates Myc activity to repress thrombospondin-1 expression and increase tumor angiogenesis. *Cancer Cell* **3**, 219-231 (2003).
93. Jeltsch, M., et al. Hyperplasia of lymphatic vessels in VEGF-C transgenic mice. *Science* **276**, 1423-1425 (1997).

94. Sugiura, T., *et al.* VEGF-C and VEGF-D expression is correlated with lymphatic vessel density and lymph node metastasis in oral squamous cell carcinoma: Implications for use as a prognostic marker. *Int J Oncol* **34**, 673-680 (2009).
95. Alabi, A.A., Suppiah, A., Madden, L.A., Monson, J.R. & Greenman, J. Preoperative serum levels of serum VEGF-C is associated with distant metastasis in colorectal cancer patients. *Int J Colorectal Dis* **24**, 269-274 (2009).
96. Gu, Y., Qi, X. & Guo, S. Lymphangiogenesis induced by VEGF-C and VEGF-D promotes metastasis and a poor outcome in breast carcinoma: a retrospective study of 61 cases. *Clin Exp Metastasis* **25**, 717-725 (2008).
97. Hlatky, L., Hahnfeldt, P. & Folkman, J. Clinical application of antiangiogenic therapy: microvessel density, what it does and doesn't tell us. *J Natl Cancer Inst* **94**, 883-893 (2002).
98. Mouta Carreira, C., *et al.* LYVE-1 is not restricted to the lymph vessels: expression in normal liver blood sinusoids and down-regulation in human liver cancer and cirrhosis. *Cancer Res* **61**, 8079-8084 (2001).
99. Degani, H., Chetrit-Dadiani, M., Bogin, L. & Furman-Haran, E. Magnetic resonance imaging of tumor vasculature. *Thromb Haemost* **89**, 25-33 (2003).
100. Badea, C.T., Hedlund, L.W., De Lin, M., Boslego Mackel, J.F. & Johnson, G.A. Tumor imaging in small animals with a combined micro-CT/micro-DSA system using iodinated conventional and blood pool contrast agents. *Contrast Media Mol Imaging* **1**, 153-164 (2006).
101. Willmann, J.K., *et al.* Targeted microbubbles for imaging tumor angiogenesis: assessment of whole-body biodistribution with dynamic micro-PET in mice. *Radiology* **249**, 212-219 (2008).
102. Gerstner, E.R., Sorensen, A.G., Jain, R.K. & Batchelor, T.T. Advances in neuroimaging techniques for the evaluation of tumor growth, vascular permeability, and angiogenesis in gliomas. *Curr Opin Neurol* **21**, 728-735 (2008).
103. Baudelet, C., Cron, G.O. & Gallez, B. Determination of the maturity and functionality of tumor vasculature by MRI: correlation between BOLD-MRI and DCE-MRI using P792 in experimental fibrosarcoma tumors. *Magn Reson Med* **56**, 1041-1049 (2006).
104. Haider, M.A., *et al.* Correlations between dynamic contrast-enhanced magnetic resonance imaging-derived measures of tumor microvasculature and interstitial fluid pressure in patients with cervical cancer. *J Magn Reson Imaging* **25**, 153-159 (2007).
105. Fukumura, D. & Jain, R.K. Imaging angiogenesis and the microenvironment. *APMIS* **116**, 695-715 (2008).
106. Intaglietta, M., Tompkins, W.R. & Richardson, D.R. Velocity measurements in the microvasculature of the cat omentum by on-line method. *Microvasc Res* **2**, 462-473 (1970).
107. Bristow, R.G. & Hill, R.P. Hypoxia and metabolism. Hypoxia, DNA repair and genetic instability. *Nat Rev Cancer* **8**, 180-192 (2008).
108. Dewhirst, M.W., *et al.* Review of methods used to study oxygen transport at the microcirculatory level. *Int J Cancer* **90**, 237-255 (2000).
109. Gillies, R.J., Schornack, P.A., Secomb, T.W. & Raghunand, N. Causes and effects of heterogeneous perfusion in tumors. *Neoplasia* **1**, 197-207 (1999).
110. Moeller, B.J., *et al.* The relationship between hypoxia and angiogenesis. *Semin Radiat Oncol* **14**, 215-221 (2004).

CHAPTER 2

111. Moeller, B.J., Richardson, R.A. & Dewhirst, M.W. Hypoxia and radiotherapy: opportunities for improved outcomes in cancer treatment. *Cancer Metastasis Rev* **26**, 241-248 (2007).
112. Brown, J.M. & Wilson, W.R. Exploiting tumour hypoxia in cancer treatment. *Nat Rev Cancer* **4**, 437-447 (2004).
113. Dewhirst, M.W., Cao, Y. & Moeller, B. Cycling hypoxia and free radicals regulate angiogenesis and radiotherapy response. *Nat Rev Cancer* **8**, 425-437 (2008).
114. Duda, D.G., Batchelor, T.T., Willett, C.G. & Jain, R.K. VEGF-targeted cancer therapy strategies: current progress, hurdles and future prospects. *Trends Mol Med* **13**, 223-230 (2007).
115. Duda, D.G., Jain, R.K. & Willett, C.G. Antiangiogenics: the potential role of integrating this novel treatment modality with chemoradiation for solid cancers. *J Clin Oncol* **25**, 4033-4042 (2007).
116. Willett, C.G., *et al.* Complete pathological response to bevacizumab and chemoradiation in advanced rectal cancer. *Nat Clin Pract Oncol* **4**, 316-321 (2007).
117. Semenza, G.L. Regulation of mammalian O₂ homeostasis by hypoxia-inducible factor 1. *Annu Rev Cell Dev Biol* **15**, 551-578 (1999).
118. Gatenby, R.A. & Gillies, R.J. Why do cancers have high aerobic glycolysis? *Nat Rev Cancer* **4**, 891-899 (2004).
119. Greijer, A.E. & van der Wall, E. The role of hypoxia inducible factor 1 (HIF-1) in hypoxia induced apoptosis. *J Clin Pathol* **57**, 1009-1014 (2004).
120. Sullivan, R. & Graham, C.H. Hypoxia-driven selection of the metastatic phenotype. *Cancer Metastasis Rev* **26**, 319-331 (2007).
121. Daponte, A., *et al.* Prognostic significance of Hypoxia-Inducible Factor 1 alpha(HIF-1 alpha) expression in serous ovarian cancer: an immunohistochemical study. *BMC Cancer* **8**, 335 (2008).
122. Enatsu, S., *et al.* Expression of hypoxia-inducible factor-1 alpha and its prognostic significance in small-sized adenocarcinomas of the lung. *Eur J Cardiothorac Surg* **29**, 891-895 (2006).
123. Gruber, G., *et al.* Hypoxia-inducible factor 1 alpha in high-risk breast cancer: an independent prognostic parameter? *Breast Cancer Res* **6**, R191-198 (2004).
124. Chan, D.A., Krieg, A.J., Turcotte, S. & Giaccia, A.J. HIF gene expression in cancer therapy. *Methods Enzymol* **435**, 323-345 (2007).
125. Patiar, S. & Harris, A.L. Role of hypoxia-inducible factor-1alpha as a cancer therapy target. *Endocr Relat Cancer* **13 Suppl 1**, S61-75 (2006).
126. Melillo, G. Targeting hypoxia cell signaling for cancer therapy. *Cancer Metastasis Rev* **26**, 341-352 (2007).
127. Rankin, E.B. & Giaccia, A.J. The role of hypoxia-inducible factors in tumorigenesis. *Cell Death Differ* **15**, 678-685 (2008).
128. Macheda, M.L., Rogers, S. & Best, J.D. Molecular and cellular regulation of glucose transporter (GLUT) proteins in cancer. *J Cell Physiol* **202**, 654-662 (2005).
129. Pastorekova, S., Zatovicova, M. & Pastorek, J. Cancer-associated carbonic anhydrases and their inhibition. *Curr Pharm Des* **14**, 685-698 (2008).
130. He, F., *et al.* Noninvasive molecular imaging of hypoxia in human xenografts: comparing hypoxia-induced gene expression with endogenous and exogenous hypoxia markers. *Cancer Res* **68**, 8597-8606 (2008).
131. Mayer, A., Hockel, M. & Vaupel, P. Endogenous hypoxia markers: case not proven! *Adv Exp Med Biol* **614**, 127-136 (2008).

CHAPTER 2

132. Raleigh, J.A., *et al.* Hypoxia and vascular endothelial growth factor expression in human squamous cell carcinomas using pimonidazole as a hypoxia marker. *Cancer Res* **58**, 3765-3768 (1998).
133. Fukumura, D., *et al.* Hypoxia and acidosis independently up-regulate vascular endothelial growth factor transcription in brain tumors in vivo. *Cancer Res* **61**, 6020-6024 (2001).
134. Gatenby, R.A., *et al.* Oxygen distribution in squamous cell carcinoma metastases and its relationship to outcome of radiation therapy. *Int J Radiat Oncol Biol Phys* **14**, 831-838 (1988).
135. Hockel, M., *et al.* Intratumoral pO₂ predicts survival in advanced cancer of the uterine cervix. *Radiother Oncol* **26**, 45-50 (1993).
136. Nordsmark, M., *et al.* The prognostic value of pimonidazole and tumour pO₂ in human cervix carcinomas after radiation therapy: a prospective international multi-center study. *Radiother Oncol* **80**, 123-131 (2006).
137. Evans, S.M., *et al.* Comparative measurements of hypoxia in human brain tumors using needle electrodes and EF5 binding. *Cancer Res* **64**, 1886-1892 (2004).
138. Nordsmark, M., *et al.* Prognostic value of tumor oxygenation in 397 head and neck tumors after primary radiation therapy. An international multi-center study. *Radiother Oncol* **77**, 18-24 (2005).
139. Chaudary, N. & Hill, R.P. Hypoxia and metastasis in breast cancer. *Breast Dis* **26**, 55-64 (2006).
140. Bos, R., *et al.* Levels of hypoxia-inducible factor-1alpha independently predict prognosis in patients with lymph node negative breast carcinoma. *Cancer* **97**, 1573-1581 (2003).
141. Vleugel, M.M., *et al.* Differential prognostic impact of hypoxia induced and diffuse HIF-1alpha expression in invasive breast cancer. *J Clin Pathol* **58**, 172-177 (2005).
142. Lally, B.E., *et al.* The interactions of polarographic measurements of oxygen tension and histological grade in human glioma. *Cancer J* **12**, 461-466 (2006).
143. Evans, S.M., *et al.* Imaging and analytical methods as applied to the evaluation of vasculature and hypoxia in human brain tumors. *Radiat Res* **170**, 677-690 (2008).
144. Evans, S.M., *et al.* Hypoxia is important in the biology and aggression of human glial brain tumors. *Clin Cancer Res* **10**, 8177-8184 (2004).
145. Chen, W. & Silverman, D.H. Advances in evaluation of primary brain tumors. *Semin Nucl Med* **38**, 240-250 (2008).
146. Yetkin, F.Z. & Mendelsohn, D. Hypoxia imaging in brain tumors. *Neuroimaging Clin N Am* **12**, 537-552 (2002).
147. Menon, C. & Fraker, D.L. Tumor oxygenation status as a prognostic marker. *Cancer Lett* **221**, 225-235 (2005).
148. Rodrigues, L.M., Howe, F.A., Griffiths, J.R. & Robinson, S.P. Tumor R2* is a prognostic indicator of acute radiotherapeutic response in rodent tumors. *J Magn Reson Imaging* **19**, 482-488 (2004).
149. Vaupel, P. & Mayer, A. Hypoxia in cancer: significance and impact on clinical outcome. *Cancer Metastasis Rev* **26**, 225-239 (2007).
150. Lanzen, J., *et al.* Direct demonstration of instabilities in oxygen concentrations within the extravascular compartment of an experimental tumor. *Cancer Res* **66**, 2219-2223 (2006).
151. Cotran, R.S., Kumar, V., Collins, T. & Robbins, S.L. *Robbins pathologic basis of disease*, (Saunders, Philadelphia, 1999).

CHAPTER 2

152. Vaupel, P. Tumor microenvironmental physiology and its implications for radiation oncology. *Semin Radiat Oncol* **14**, 198-206 (2004).
153. Dewhirst, M.W., *et al.* Arteriolar oxygenation in tumour and subcutaneous arterioles: effects of inspired air oxygen content. *Br J Cancer Suppl* **27**, S241-246 (1996).
154. Pogue, B.W., Paulsen, K.D., O'Hara, J.A., Wilmot, C.M. & Swartz, H.M. Estimation of oxygen distribution in RIF-1 tumors by diffusion model-based interpretation of pimonidazole hypoxia and eppendorf measurements. *Radiat Res* **155**, 15-25 (2001).
155. Torres Filho, I.P., Leunig, M., Yuan, F., Intaglietta, M. & Jain, R.K. Noninvasive measurement of microvascular and interstitial oxygen profiles in a human tumor in SCID mice. *Proc Natl Acad Sci U S A* **91**, 2081-2085 (1994).
156. Dewhirst, M.W., *et al.* Perivascular oxygen tensions in a transplantable mammary tumor growing in a dorsal flap window chamber. *Radiat Res* **130**, 171-182 (1992).
157. Ziemer, L.S., Lee, W.M., Vinogradov, S.A., Sehgal, C. & Wilson, D.F. Oxygen distribution in murine tumors: characterization using oxygen-dependent quenching of phosphorescence. *J Appl Physiol* **98**, 1503-1510 (2005).
158. Cerniglia, G.J., Wilson, D.F., Pawlowski, M., Vinogradov, S. & Biaglow, J. Intravascular oxygen distribution in subcutaneous 9L tumors and radiation sensitivity. *J Appl Physiol* **82**, 1939-1945 (1997).
159. Wen, B., Urano, M., O'Donoghue, J.A. & Ling, C.C. Measurements of partial oxygen pressure pO₂ using the OxyLite system in R3327-AT tumors under isoflurane anesthesia. *Radiat Res* **166**, 512-518 (2006).
160. Matsuda, Y., *et al.* Comparison of newly developed inhalation anesthesia system and intraperitoneal anesthesia on the hemodynamic state in mice. *Biol Pharm Bull* **30**, 1716-1720 (2007).
161. Papenfuss, H.D., Gross, J.F., Intaglietta, M. & Treese, F.A. A transparent access chamber for the rat dorsal skin fold. *Microvasc Res* **18**, 311-318 (1979).
162. Wilson, D.F., *et al.* Oxygen distributions within R3230Ac tumors growing in dorsal flap window chambers in rats. *Adv Exp Med Biol* **454**, 603-609 (1998).
163. Dewhirst, M.W., *et al.* Quantification of longitudinal tissue pO₂ gradients in window chamber tumours: impact on tumour hypoxia. *Br J Cancer* **79**, 1717-1722 (1999).
164. Thomlinson, R.H. & Gray, L.H. The histological structure of some human lung cancers and the possible implications for radiotherapy. *Br J Cancer* **9**, 539-549 (1955).
165. Nichols, M.G. & Foster, T.H. Oxygen diffusion and reaction kinetics in the photodynamic therapy of multicell tumour spheroids. *Phys Med Biol* **39**, 2161-2181 (1994).
166. Yaegashi, K., Itoh, T., Kosaka, T., Fukushima, H. & Morimoto, T. Diffusivity of oxygen in microvascular beds as determined from PO₂ distribution maps. *Am J Physiol* **270**, H1390-1397 (1996).
167. Tsai, A.G., *et al.* Microvascular and tissue oxygen gradients in the rat mesentery. *Proc Natl Acad Sci U S A* **95**, 6590-6595 (1998).
168. Staub, N.C. & Taylor, A.E. *Edema*, (Raven Press, New York, 1984).
169. Cardenas-Navia, L.I., *et al.* The pervasive presence of fluctuating oxygenation in tumors. *Cancer Res* **68**, 5812-5819 (2008).
170. Brown, J.M. Evidence for acutely hypoxic cells in mouse tumours, and a possible mechanism of reoxygenation. *Br J Radiol* **52**, 650-656 (1979).
171. Reynolds, T.Y., Rockwell, S. & Glazer, P.M. Genetic instability induced by the tumor microenvironment. *Cancer Res* **56**, 5754-5757 (1996).
172. Graeber, T.G., *et al.* Hypoxia-mediated selection of cells with diminished apoptotic potential in solid tumours. *Nature* **379**, 88-91 (1996).

CHAPTER 2

173. Cairns, R.A. & Hill, R.P. Acute hypoxia enhances spontaneous lymph node metastasis in an orthotopic murine model of human cervical carcinoma. *Cancer Res* **64**, 2054-2061 (2004).
174. Krogh, A. The number and distribution of capillaries in muscles with calculations of the oxygen pressure head necessary for supplying the tissue. *J Physiol* **52**, 409-415 (1919).
175. Gullino, P.M., Grantham, F.H. & Courtney, A.H. Utilization of oxygen by transplanted tumors in vivo. *Cancer Res* **27**, 1020-1030 (1967).
176. Secomb, T.W., Hsu, R., Dewhirst, M.W., Klitzman, B. & Gross, J.F. Analysis of oxygen transport to tumor tissue by microvascular networks. *Int J Radiat Oncol Biol Phys* **25**, 481-489 (1993).
177. Kirkpatrick, J.P., Brizel, D.M. & Dewhirst, M.W. A mathematical model of tumor oxygen and glucose mass transport and metabolism with complex reaction kinetics. *Radiat Res* **159**, 336-344 (2003).
178. Walenta, S., *et al.* Tissue gradients of energy metabolites mirror oxygen tension gradients in a rat mammary carcinoma model. *Int J Radiat Oncol Biol Phys* **51**, 840-848 (2001).
179. Dasu, A., Toma-Dasu, I. & Karlsson, M. Theoretical simulation of tumour oxygenation and results from acute and chronic hypoxia. *Phys Med Biol* **48**, 2829-2842 (2003).
180. Skarsgard, L.D., Skwarchuk, M.W., Vinczan, A., Kristl, J. & Chaplin, D.J. The cytotoxicity of melphalan and its relationship to pH, hypoxia and drug uptake. *Anticancer Res* **15**, 219-223 (1995).
181. Chaplin, D.J. & Acker, B. The effect of hydralazine on the tumor cytotoxicity of the hypoxic cell cytotoxin RSU-1069: evidence for therapeutic gain. *Int J Radiat Oncol Biol Phys* **13**, 579-585 (1987).
182. Ahn, G.O. & Brown, M. Targeting tumors with hypoxia-activated cytotoxins. *Front Biosci* **12**, 3483-3501 (2007).
183. Brown, J.M. & Giaccia, A.J. The unique physiology of solid tumors: opportunities (and problems) for cancer therapy. *Cancer Res* **58**, 1408-1416 (1998).
184. Brown, J.M. Tumor hypoxia in cancer therapy. *Methods Enzymol* **435**, 297-321 (2007).
185. Cosse, J.P. & Michiels, C. Tumour hypoxia affects the responsiveness of cancer cells to chemotherapy and promotes cancer progression. *Anticancer Agents Med Chem* **8**, 790-797 (2008).
186. Papkovsky, D.B. Methods in optical oxygen sensing: protocols and critical analyses. *Methods Enzymol* **381**, 715-735 (2004).
187. Swartz, H.M. & Dunn, J.F. Measurements of oxygen in tissues: overview and perspectives on methods. *Adv Exp Med Biol* **530**, 1-12 (2003).
188. Tsai, A.G., Johnson, P.C. & Intaglietta, M. Oxygen gradients in the microcirculation. *Physiol Rev* **83**, 933-963 (2003).
189. Clark, L.C., Jr., Wolf, R., Granger, D. & Taylor, Z. Continuous recording of blood oxygen tensions by polarography. *J Appl Physiol* **6**, 189-193 (1953).
190. Whalen, W.J., Riley, J. & Nair, P. A microelectrode for measuring intracellular PO₂. *J Appl Physiol* **23**, 798-801 (1967).
191. Kallinowski, F., Zander, R., Hoeckel, M. & Vaupel, P. Tumor tissue oxygenation as evaluated by computerized-pO₂-histography. *Int J Radiat Oncol Biol Phys* **19**, 953-961 (1990).
192. Nozue, M., *et al.* Interlaboratory variation in oxygen tension measurement by Eppendorf "Histograph" and comparison with hypoxic marker. *J Surg Oncol* **66**, 30-38 (1997).

CHAPTER 2

193. Pittman, R.N. & Duling, B.R. Measurement of percent oxyhemoglobin in the microvasculature. *J Appl Physiol* **38**, 321-327 (1975).
194. Pittman, R.N. & Duling, B.R. A new method for the measurement of percent oxyhemoglobin. *J Appl Physiol* **38**, 315-320 (1975).
195. Mancini, D.M., *et al.* Validation of near-infrared spectroscopy in humans. *J Appl Physiol* **77**, 2740-2747 (1994).
196. Arakaki, L.S., Burns, D.H. & Kushmerick, M.J. Accurate myoglobin oxygen saturation by optical spectroscopy measured in blood-perfused rat muscle. *Appl Spectrosc* **61**, 978-985 (2007).
197. Lee, J., *et al.* Broadband diffuse optical spectroscopy measurement of hemoglobin concentration during hypovolemia in rabbits. *Physiol Meas* **27**, 757-767 (2006).
198. Raleigh, J.A., Franko, A.J., Koch, C.J. & Born, J.L. Binding of misonidazole to hypoxic cells in monolayer and spheroid culture: evidence that a side-chain label is bound as efficiently as a ring label. *Br J Cancer* **51**, 229-235 (1985).
199. Lord, E.M., Harwell, L. & Koch, C.J. Detection of hypoxic cells by monoclonal antibody recognizing 2-nitroimidazole adducts. *Cancer Res* **53**, 5721-5726 (1993).
200. Ljungkvist, A.S., Bussink, J., Kaanders, J.H. & van der Kogel, A.J. Dynamics of tumor hypoxia measured with bioreductive hypoxic cell markers. *Radiat Res* **167**, 127-145 (2007).
201. Arteel, G.E., Thurman, R.G., Yates, J.M. & Raleigh, J.A. Evidence that hypoxia markers detect oxygen gradients in liver: pimonidazole and retrograde perfusion of rat liver. *Br J Cancer* **72**, 889-895 (1995).
202. Bruehlmeier, M., Roelcke, U., Schubiger, P.A. & Ametamey, S.M. Assessment of hypoxia and perfusion in human brain tumors using PET with ¹⁸F-fluoromisonidazole and ¹⁵O-H₂O. *J Nucl Med* **45**, 1851-1859 (2004).
203. Nordmark, M., *et al.* Measurements of hypoxia using pimonidazole and polarographic oxygen-sensitive electrodes in human cervix carcinomas. *Radiother Oncol* **67**, 35-44 (2003).
204. Olive, P.L. & Aquino-Parsons, C. Measurement of tumor hypoxia using single-cell methods. *Semin Radiat Oncol* **14**, 241-248 (2004).
205. Russell, J., *et al.* Immunohistochemical detection of changes in tumor hypoxia. *Int J Radiat Oncol Biol Phys* **73**, 1177-1186 (2009).
206. Kautsky, H. & Hirsch, A. Wechselwirkung zwischen angeregten Farbstoff-Molekülen und Sauerstoff "Reciprocal effect between lively coloring material molecules and oxygen". *Berichte der deutschen chemischen Gesellschaft (A and B Series)* **64**, 2677-2683 (1931).
207. Kautsky, H. & Muller, G.O. Changes of luminescence produced by oxygen. Detection of traces of oxygen. *Zeitschrift fur Naturforschung A (Astrophysik, Physik und Physikalische Chemie)* **2a**, 167-172 (1947).
208. Lakowicz, J.R. *Principles of fluorescence spectroscopy*, (Kluwer Academic/Plenum, New York, 1999).
209. Lo, L.W., Koch, C.J. & Wilson, D.F. Calibration of oxygen-dependent quenching of the phosphorescence of Pd-meso-tetra (4-carboxyphenyl) porphine: a phosphor with general application for measuring oxygen concentration in biological systems. *Anal Biochem* **236**, 153-160 (1996).
210. Eftink, M.R. & Ghiron, C.A. Exposure of tryptophanyl residues in proteins. Quantitative determination by fluorescence quenching studies. *Biochemistry* **15**, 672-680 (1976).
211. Hartmann, P.L., M.J.P.; Lippitsch, M.E. Response characteristics of luminescent oxygen sensors. *Sensors and Actuators B* **B29**, 251-257 (1995).

212. Griffiths, J.R. & Robinson, S.P. The OxyLite: a fibre-optic oxygen sensor. *Br J Radiol* **72**, 627-630 (1999).
213. Krihak, M.K.S., M.R. . Highly sensitive, all solid state fibre optic oxygen sensor based on the sol-gel coating technique. *Electronics Letters* **32**, 240-242 (1996).
214. McLaurin, E.M.G., A.B.; Bawendi, M.G.; Nocera, D.G. Two-Photon Absorbing Nanocrystal Sensors for Ratiometric Detection of Oxygen. *JACS* (2009).
215. Vanderkooi, J.M., Maniara, G., Green, T.J. & Wilson, D.F. An optical method for measurement of dioxygen concentration based upon quenching of phosphorescence. *J Biol Chem* **262**, 5476-5482 (1987).
216. Dunphy, I., Vinogradov, S.A. & Wilson, D.F. Oxyphor R2 and G2: phosphors for measuring oxygen by oxygen-dependent quenching of phosphorescence. *Anal Biochem* **310**, 191-198 (2002).
217. Rumsey, W.L., Vanderkooi, J.M. & Wilson, D.F. Imaging of phosphorescence: a novel method for measuring oxygen distribution in perfused tissue. *Science* **241**, 1649-1651 (1988).
218. Vinogradov, S.A. & Wilson, D.F. "Dendritic" porphyrins. New protected phosphors for oxygen measurements in vivo. *Adv Exp Med Biol* **428**, 657-662 (1997).
219. Wilson, D.F. Oxygen dependent quenching of phosphorescence: a perspective. *Adv Exp Med Biol* **317**, 195-201 (1992).
220. O'Donovan, C.H., James; Yashunski, Dmitri; Papkovsky, Dmitri B. Phosphorescent oxygen-sensitive materials for biological applications. *Journal of Materials Chemistry* **15**, 2946-2951 (2005).
221. Soini, A.E., Seveus, L., Meltola, N.J., Papkovsky, D.B. & Soini, E. Phosphorescent metalloporphyrins as labels in time-resolved luminescence microscopy: effect of mounting on emission intensity. *Microsc Res Tech* **58**, 125-131 (2002).
222. Shonat, R.D.R., Keith N.; Johnson, Paul C. Phosphorescence quenching and the microcirculation: An automated, multipoint oxygen tension measuring instrument. *Review of Scientific Instruments* **66**, 5075-5084 (1995).
223. Torres Filho, I.P. & Intaglietta, M. Microvessel PO₂ measurements by phosphorescence decay method. *Am J Physiol* **265**, H1434-1438 (1993).
224. Vinogradov, S.A.F.-S., M.A.; Dugan, B.W.; Wilson, D.F. Frequency domain instrument for measuring phosphorescence lifetime distributions in heterogeneous samples. *Review of Scientific Instruments* **72**, 3396-3406 (2001).
225. Swartz, H.M. & Dunn, J. The difficulties in comparing in vivo oxygen measurements: turning the problems into virtues. *Adv Exp Med Biol* **566**, 295-301 (2005).
226. Mason, R.P., Rodbumrung, W. & Antich, P.P. Hexafluorobenzene: a sensitive ¹⁹F NMR indicator of tumor oxygenation. *NMR Biomed* **9**, 125-134 (1996).
227. He, Q., *et al.* Magnetic resonance spectroscopic imaging of tumor metabolic markers for cancer diagnosis, metabolic phenotyping, and characterization of tumor microenvironment. *Dis Markers* **19**, 69-94 (2003).
228. Ogawa, S., Lee, T.M., Kay, A.R. & Tank, D.W. Brain magnetic resonance imaging with contrast dependent on blood oxygenation. *Proc Natl Acad Sci U S A* **87**, 9868-9872 (1990).
229. Halpern, H.J., *et al.* Oxymetry deep in tissues with low-frequency electron paramagnetic resonance. *Proc Natl Acad Sci U S A* **91**, 13047-13051 (1994).
230. Swartz, H.M., *et al.* Clinical applications of EPR: overview and perspectives. *NMR Biomed* **17**, 335-351 (2004).

231. Dellian, M., Helmlinger, G., Yuan, F. & Jain, R.K. Fluorescence ratio imaging of interstitial pH in solid tumours: effect of glucose on spatial and temporal gradients. *Br J Cancer* **74**, 1206-1215 (1996).
232. Gullino, P.M., Grantham, F.H., Smith, S.H. & Haggerty, A.C. Modifications of the acid-base status of the internal milieu of tumors. *J Natl Cancer Inst* **34**, 857-869 (1965).
233. Martin, G.R. & Jain, R.K. Noninvasive measurement of interstitial pH profiles in normal and neoplastic tissue using fluorescence ratio imaging microscopy. *Cancer Res* **54**, 5670-5674 (1994).
234. Wike-Hooley, J.L., Haveman, J. & Reinhold, H.S. The relevance of tumour pH to the treatment of malignant disease. *Radiother Oncol* **2**, 343-366 (1984).
235. Gillies, R.J., Raghunand, N., Karczmar, G.S. & Bhujwala, Z.M. MRI of the tumor microenvironment. *J Magn Reson Imaging* **16**, 430-450 (2002).
236. Griffiths, J.R. Causes and consequences of hypoxia and acidity in tumour microenvironments. *Bioessays* **23**, 295-296 (2001).
237. Seagroves, T.N., et al. Transcription factor HIF-1 is a necessary mediator of the pasteur effect in mammalian cells. *Mol Cell Biol* **21**, 3436-3444 (2001).
238. Racker, E. & Spector, M. Warburg effect revisited: merger of biochemistry and molecular biology. *Science* **213**, 303-307 (1981).
239. Jain, R.K., Shah, S.A. & Finney, P.L. Continuous noninvasive monitoring of pH and temperature in rat Walker 256 carcinoma during normoglycemia and hyperglycemia. *J Natl Cancer Inst* **73**, 429-436 (1984).
240. Jahde, E. & Rajewsky, M.F. Tumor-selective modification of cellular microenvironment in vivo: effect of glucose infusion on the pH in normal and malignant rat tissues. *Cancer Res* **42**, 1505-1512 (1982).
241. Sevick, E.M. & Jain, R.K. Blood flow and venous pH of tissue-isolated Walker 256 carcinoma during hyperglycemia. *Cancer Res* **48**, 1201-1207 (1988).
242. DiPette, D.J., Ward-Hartley, K.A. & Jain, R.K. Effect of glucose on systemic hemodynamics and blood flow rate in normal and tumor tissues in rats. *Cancer Res* **46**, 6299-6304 (1986).
243. Evelhoch, J.L., Sapareto, S.A., Jick, D.E. & Ackerman, J.J. In vivo metabolic effects of hyperglycemia in murine radiation-induced fibrosarcoma: a ³¹P NMR investigation. *Proc Natl Acad Sci U S A* **81**, 6496-6500 (1984).
244. Raghunand, N., et al. Plasmalemmal pH-gradients in drug-sensitive and drug-resistant MCF-7 human breast carcinoma xenografts measured by ³¹P magnetic resonance spectroscopy. *Biochem Pharmacol* **57**, 309-312 (1999).
245. Raghunand, N. Tissue pH measurement by magnetic resonance spectroscopy and imaging. *Methods Mol Med* **124**, 347-364 (2006).
246. Mason, R.P. Transmembrane pH gradients in vivo: measurements using fluorinated vitamin B6 derivatives. *Curr Med Chem* **6**, 481-499 (1999).
247. Montcourrier, P., Silver, I., Farnoud, R., Bird, I. & Rochefort, H. Breast cancer cells have a high capacity to acidify extracellular milieu by a dual mechanism. *Clin Exp Metastasis* **15**, 382-392 (1997).
248. Cardone, R.A., Casavola, V. & Reshkin, S.J. The role of disturbed pH dynamics and the Na⁺/H⁺ exchanger in metastasis. *Nat Rev Cancer* **5**, 786-795 (2005).
249. Reshkin, S.J., et al. Na⁺/H⁺ exchanger-dependent intracellular alkalinization is an early event in malignant transformation and plays an essential role in the development of subsequent transformation-associated phenotypes. *FASEB J* **14**, 2185-2197 (2000).

250. De Milito, A. & Fais, S. Tumor acidity, chemoresistance and proton pump inhibitors. *Future Oncol* **1**, 779-786 (2005).
251. Morita, T., Nagaki, T., Fukuda, I. & Okumura, K. Clastogenicity of low pH to various cultured mammalian cells. *Mutat Res* **268**, 297-305 (1992).
252. Morita, T. Low pH leads to sister-chromatid exchanges and chromosomal aberrations, and its clastogenicity is S-dependent. *Mutat Res* **334**, 301-308 (1995).
253. Martin, G.R. & Jain, R.K. Fluorescence ratio imaging measurement of pH gradients: calibration and application in normal and tumor tissues. *Microvasc Res* **46**, 216-230 (1993).
254. Kallinowski, F., *et al.* Blood flow, metabolism, cellular microenvironment, and growth rate of human tumor xenografts. *Cancer Res* **49**, 3759-3764 (1989).
255. Gatenby, R.A., Gawlinski, E.T., Gmitro, A.F., Kaylor, B. & Gillies, R.J. Acid-mediated tumor invasion: a multidisciplinary study. *Cancer Res* **66**, 5216-5223 (2006).
256. Jain, R.K. Therapeutic implications of tumor physiology. *Curr Opin Oncol* **3**, 1105-1108 (1991).
257. Schornack, P.A. & Gillies, R.J. Contributions of cell metabolism and H⁺ diffusion to the acidic pH of tumors. *Neoplasia* **5**, 135-145 (2003).
258. Vaupel, P.W., Frinak, S. & Bicher, H.I. Heterogeneous oxygen partial pressure and pH distribution in C3H mouse mammary adenocarcinoma. *Cancer Res* **41**, 2008-2013 (1981).
259. Garcia-Martin, M.L., *et al.* Mapping extracellular pH in rat brain gliomas in vivo by 1H magnetic resonance spectroscopic imaging: comparison with maps of metabolites. *Cancer Res* **61**, 6524-6531 (2001).
260. Rofstad, E.K., Mathiesen, B., Kindem, K. & Galappathi, K. Acidic extracellular pH promotes experimental metastasis of human melanoma cells in athymic nude mice. *Cancer Res* **66**, 6699-6707 (2006).
261. Martinez-Zaguilan, R., *et al.* Acidic pH enhances the invasive behavior of human melanoma cells. *Clin Exp Metastasis* **14**, 176-186 (1996).
262. Schlappack, O.K., Zimmermann, A. & Hill, R.P. Glucose starvation and acidosis: effect on experimental metastatic potential, DNA content and MTX resistance of murine tumour cells. *Br J Cancer* **64**, 663-670 (1991).
263. Walenta, S., *et al.* Correlation of high lactate levels in head and neck tumors with incidence of metastasis. *Am J Pathol* **150**, 409-415 (1997).
264. Schwickert, G., Walenta, S., Sundfor, K., Rofstad, E.K. & Mueller-Klieser, W. Correlation of high lactate levels in human cervical cancer with incidence of metastasis. *Cancer Res* **55**, 4757-4759 (1995).
265. Gatenby, R.A. & Gillies, R.J. A microenvironmental model of carcinogenesis. *Nat Rev Cancer* **8**, 56-61 (2008).
266. Park, H.J., Lyons, J.C., Ohtsubo, T. & Song, C.W. Acidic environment causes apoptosis by increasing caspase activity. *Br J Cancer* **80**, 1892-1897 (1999).
267. Williams, A.C., Collard, T.J. & Paraskeva, C. An acidic environment leads to p53 dependent induction of apoptosis in human adenoma and carcinoma cell lines: implications for clonal selection during colorectal carcinogenesis. *Oncogene* **18**, 3199-3204 (1999).
268. Shi, Q., *et al.* Regulation of vascular endothelial growth factor expression by acidosis in human cancer cells. *Oncogene* **20**, 3751-3756 (2001).

CHAPTER 2

269. Shi, Q., *et al.* Constitutive and inducible interleukin 8 expression by hypoxia and acidosis renders human pancreatic cancer cells more tumorigenic and metastatic. *Clin Cancer Res* **5**, 3711-3721 (1999).
270. Cuvier, C., Jang, A. & Hill, R.P. Exposure to hypoxia, glucose starvation and acidosis: effect on invasive capacity of murine tumor cells and correlation with cathepsin (L + B) secretion. *Clin Exp Metastasis* **15**, 19-25 (1997).
271. Glunde, K., *et al.* Extracellular acidification alters lysosomal trafficking in human breast cancer cells. *Neoplasia* **5**, 533-545 (2003).
272. Rozhin, J., Sameni, M., Ziegler, G. & Sloane, B.F. Pericellular pH affects distribution and secretion of cathepsin B in malignant cells. *Cancer Res* **54**, 6517-6525 (1994).
273. Lardner, A. The effects of extracellular pH on immune function. *J Leukoc Biol* **69**, 522-530 (2001).
274. Robey, I.F., *et al.* Bicarbonate increases tumor pH and inhibits spontaneous metastases. *Cancer Res* **69**, 2260-2268 (2009).
275. Holden, S.A., Teicher, B.A. & Herman, T.S. Effect of environmental conditions (pH, oxygenation, and temperature) on misonidazole cytotoxicity and radiosensitization in vitro and in vivo in FSaIIc fibrosarcoma. *Int J Radiat Oncol Biol Phys* **20**, 1031-1038 (1991).
276. Raghunand, N., Mahoney, B., van Sluis, R., Baggett, B. & Gillies, R.J. Acute metabolic alkalosis enhances response of C3H mouse mammary tumors to the weak base mitoxantrone. *Neoplasia* **3**, 227-235 (2001).
277. Kozin, S.V., Shkarin, P. & Gerweck, L.E. The cell transmembrane pH gradient in tumors enhances cytotoxicity of specific weak acid chemotherapeutics. *Cancer Res* **61**, 4740-4743 (2001).
278. Gerweck, L.E. & Seetharaman, K. Cellular pH gradient in tumor versus normal tissue: potential exploitation for the treatment of cancer. *Cancer Res* **56**, 1194-1198 (1996).
279. Ohtsubo, T., *et al.* Acidic environment modifies heat- or radiation-induced apoptosis in human maxillary cancer cells. *Int J Radiat Oncol Biol Phys* **49**, 1391-1398 (2001).
280. Freeman, M.L. & Sierra, E. An acidic extracellular environment reduces the fixation of radiation damage. *Radiat Res* **97**, 154-161 (1984).
281. Holahan, E.V., Stuart, P.K. & Dewey, W.C. Enhancement of survival of CHO cells by acidic pH after x irradiation. *Radiat Res* **89**, 433-435 (1982).
282. Chu, G.L. & Dewey, W.C. The role of low intracellular or extracellular pH in sensitization to hyperthermia. *Radiat Res* **114**, 154-167 (1988).
283. Jayasundar, R., Honess, D., Hall, L.D. & Bleehen, N.M. Simultaneous evaluation of the effects of RF hyperthermia on the intra- and extracellular tumor pH. *Magn Reson Med* **43**, 1-8 (2000).
284. Kitai, R., *et al.* Sensitization to hyperthermia by intracellular acidification of C6 glioma cells. *J Neurooncol* **39**, 197-203 (1998).
285. Volk, T., Jahde, E., Fortmeyer, H.P., Glusenkamp, K.H. & Rajewsky, M.F. pH in human tumour xenografts: effect of intravenous administration of glucose. *Br J Cancer* **68**, 492-500 (1993).
286. Wolthuis, R., McCrae, D., Saaski, E., Hartl, J. & Mitchell, G. Development of a medical fiber-optic pH sensor based on optical absorption. *IEEE Trans Biomed Eng* **39**, 531-537 (1992).
287. Goldstein, S.R., Peterson, J.I. & Fitzgerald, R.V. A miniature fiber optic pH sensor for physiological use. *J Biomech Eng* **102**, 141-146 (1980).

288. Xu, Z., Rollins, A., Alcalá, R. & Marchant, R.E. A novel fiber-optic pH sensor incorporating carboxy SNAFL-2 and fluorescent wavelength-ratiometric detection. *J Biomed Mater Res* **39**, 9-15 (1998).
289. Stubbs, M., *et al.* An assessment of ³¹P MRS as a method of measuring pH in rat tumours. *NMR Biomed* **5**, 351-359 (1992).
290. Evanochko, W.T., *et al.* In vivo ³¹P NMR study of the metabolism of murine mammary 16/C adenocarcinoma and its response to chemotherapy, x-radiation, and hyperthermia. *Proc Natl Acad Sci U S A* **80**, 334-338 (1983).
291. Gillies, R.J., Liu, Z. & Bhujwalla, Z. ³¹P-MRS measurements of extracellular pH of tumors using 3-aminopropylphosphonate. *Am J Physiol* **267**, C195-203 (1994).
292. Ojugo, A.S., *et al.* Measurement of the extracellular pH of solid tumours in mice by magnetic resonance spectroscopy: a comparison of exogenous (¹⁹F) and (³¹P) probes. *NMR Biomed* **12**, 495-504 (1999).
293. Mehta, V.D., *et al.* 6-Fluoropyridoxol: a novel probe of cellular pH using ¹⁹F NMR spectroscopy. *FEBS Lett* **349**, 234-238 (1994).
294. van Sluis, R., *et al.* In vivo imaging of extracellular pH using ¹H MRSI. *Magn Reson Med* **41**, 743-750 (1999).
295. Bhujwalla, Z.M., *et al.* Combined vascular and extracellular pH imaging of solid tumors. *NMR Biomed* **15**, 114-119 (2002).
296. Provent, P., *et al.* Serial in vivo spectroscopic nuclear magnetic resonance imaging of lactate and extracellular pH in rat gliomas shows redistribution of protons away from sites of glycolysis. *Cancer Res* **67**, 7638-7645 (2007).
297. Kearfott, K.J., Junck, L. & Rottenberg, D.A. C-11 dimethylxazolidinedione (DMO): biodistribution, radiation absorbed dose, and potential for PET measurement of regional brain pH: concise communication. *J Nucl Med* **24**, 805-811 (1983).
298. Rink, T.J., Tsien, R.Y. & Pozzan, T. Cytoplasmic pH and free Mg²⁺ in lymphocytes. *J Cell Biol* **95**, 189-196 (1982).
299. Liu, J., Diwu, Z. & Leung, W.Y. Synthesis and photophysical properties of new fluorinated benzo[c]xanthene dyes as intracellular pH indicators. *Bioorg Med Chem Lett* **11**, 2903-2905 (2001).
300. Bright, G.R., Fisher, G.W., Rogowska, J. & Taylor, D.L. Fluorescence ratio imaging microscopy: temporal and spatial measurements of cytoplasmic pH. *J Cell Biol* **104**, 1019-1033 (1987).
301. Kaneko, K., Guth, P.H. & Kaunitz, J.D. In vivo measurement of rat gastric surface cell intracellular pH. *Am J Physiol* **261**, G548-552 (1991).
302. Mordon, S., Devoisselle, J.M. & Maunoury, V. In vivo pH measurement and imaging of tumor tissue using a pH-sensitive fluorescent probe (5,6-carboxyfluorescein): instrumental and experimental studies. *Photochem Photobiol* **60**, 274-279 (1994).
303. Szmanski, H. & Lakowicz, J.R. Optical measurements of pH using fluorescence lifetimes and phase-modulation fluorometry. *Anal Chem* **65**, 1668-1674 (1993).
304. Hanson, K.M., *et al.* Two-photon fluorescence lifetime imaging of the skin stratum corneum pH gradient. *Biophys J* **83**, 1682-1690 (2002).
305. Folkman, J. Fighting cancer by attacking its blood supply. *Sci Am* **275**, 150-154 (1996).
306. Sato, T.N. A new approach to fighting cancer? *Proc Natl Acad Sci U S A* **95**, 5843-5844 (1998).
307. O'Reilly, M.S., *et al.* Angiostatin: a novel angiogenesis inhibitor that mediates the suppression of metastases by a Lewis lung carcinoma. *Cell* **79**, 315-328 (1994).

CHAPTER 2

308. O'Reilly, M.S., Holmgren, L., Chen, C. & Folkman, J. Angiostatin induces and sustains dormancy of human primary tumors in mice. *Nat Med* **2**, 689-692 (1996).
309. O'Reilly, M.S., *et al.* Endostatin: an endogenous inhibitor of angiogenesis and tumor growth. *Cell* **88**, 277-285 (1997).
310. Folkman, J. Endogenous angiogenesis inhibitors. *APMIS* **112**, 496-507 (2004).
311. Folkman, J. Antiangiogenesis in cancer therapy--endostatin and its mechanisms of action. *Exp Cell Res* **312**, 594-607 (2006).
312. Prewett, M., *et al.* Antivascular endothelial growth factor receptor (fetal liver kinase 1) monoclonal antibody inhibits tumor angiogenesis and growth of several mouse and human tumors. *Cancer Res* **59**, 5209-5218 (1999).
313. Ferrara, N., Hillan, K.J., Gerber, H.P. & Novotny, W. Discovery and development of bevacizumab, an anti-VEGF antibody for treating cancer. *Nat Rev Drug Discov* **3**, 391-400 (2004).
314. Jain, R.K. Lessons from multidisciplinary translational trials on anti-angiogenic therapy of cancer. *Nat Rev Cancer* **8**, 309-316 (2008).
315. Jain, R.K., Duda, D.G., Clark, J.W. & Loeffler, J.S. Lessons from phase III clinical trials on anti-VEGF therapy for cancer. *Nat Clin Pract Oncol* **3**, 24-40 (2006).
316. Miller, K.D., *et al.* Randomized phase III trial of capecitabine compared with bevacizumab plus capecitabine in patients with previously treated metastatic breast cancer. *J Clin Oncol* **23**, 792-799 (2005).
317. Ramaswamy, B. & Shapiro, C.L. Phase II trial of bevacizumab in combination with docetaxel in women with advanced breast cancer. *Clin Breast Cancer* **4**, 292-294 (2003).
318. Hansen-Algenstaedt, N., *et al.* Tumor oxygenation in hormone-dependent tumors during vascular endothelial growth factor receptor-2 blockade, hormone ablation, and chemotherapy. *Cancer Res* **60**, 4556-4560 (2000).
319. Yuan, F., *et al.* Time-dependent vascular regression and permeability changes in established human tumor xenografts induced by an anti-vascular endothelial growth factor/vascular permeability factor antibody. *Proc Natl Acad Sci U S A* **93**, 14765-14770 (1996).
320. Jain, R.K., *et al.* Endothelial cell death, angiogenesis, and microvascular function after castration in an androgen-dependent tumor: role of vascular endothelial growth factor. *Proc Natl Acad Sci U S A* **95**, 10820-10825 (1998).
321. Kerbel, R. & Folkman, J. Clinical translation of angiogenesis inhibitors. *Nat Rev Cancer* **2**, 727-739 (2002).
322. Mauceri, H.J., *et al.* Combined effects of angiostatin and ionizing radiation in antitumor therapy. *Nature* **394**, 287-291 (1998).
323. Gorski, D.H., *et al.* Blockage of the vascular endothelial growth factor stress response increases the antitumor effects of ionizing radiation. *Cancer Res* **59**, 3374-3378 (1999).
324. Kozin, S.V., *et al.* Vascular endothelial growth factor receptor-2-blocking antibody potentiates radiation-induced long-term control of human tumor xenografts. *Cancer Res* **61**, 39-44 (2001).
325. Lee, C.G., *et al.* Anti-Vascular endothelial growth factor treatment augments tumor radiation response under normoxic or hypoxic conditions. *Cancer Res* **60**, 5565-5570 (2000).
326. Winkler, F., *et al.* Kinetics of vascular normalization by VEGFR2 blockade governs brain tumor response to radiation: role of oxygenation, angiopoietin-1, and matrix metalloproteinases. *Cancer Cell* **6**, 553-563 (2004).

CHAPTER 2

327. Dings, R.P., *et al.* Scheduling of radiation with angiogenesis inhibitors anginex and Avastin improves therapeutic outcome via vessel normalization. *Clin Cancer Res* **13**, 3395-3402 (2007).
328. Ansiaux, R., *et al.* Mechanism of reoxygenation after antiangiogenic therapy using SU5416 and its importance for guiding combined antitumor therapy. *Cancer Res* **66**, 9698-9704 (2006).
329. Orive, G., Reshkin, S.J., Harguindey, S. & Pedraz, J.L. Hydrogen ion dynamics and the Na⁺/H⁺ exchanger in cancer angiogenesis and antiangiogenesis. *Br J Cancer* **89**, 1395-1399 (2003).
330. Tredan, O., Galmarini, C.M., Patel, K. & Tannock, I.F. Drug resistance and the solid tumor microenvironment. *J Natl Cancer Inst* **99**, 1441-1454 (2007).
331. Wong, P., Lee, C. & Tannock, I.F. Reduction of intracellular pH as a strategy to enhance the pH-dependent cytotoxic effects of melphalan for human breast cancer cells. *Clin Cancer Res* **11**, 3553-3557 (2005).
332. Teicher, B.A., *et al.* Influence of an anti-angiogenic treatment on 9L gliosarcoma: oxygenation and response to cytotoxic therapy. *Int J Cancer* **61**, 732-737 (1995).
333. Dickson, P.V., *et al.* Bevacizumab-induced transient remodeling of the vasculature in neuroblastoma xenografts results in improved delivery and efficacy of systemically administered chemotherapy. *Clin Cancer Res* **13**, 3942-3950 (2007).
334. Kerbel, R.S. Antiangiogenic therapy: a universal chemosensitization strategy for cancer? *Science* **312**, 1171-1175 (2006).
335. Blagosklonny, M.V. How Avastin potentiates chemotherapeutic drugs: action and reaction in antiangiogenic therapy. *Cancer Biol Ther* **4**, 1307-1310 (2005).
336. Izumi, Y., Xu, L., di Tomaso, E., Fukumura, D. & Jain, R.K. Tumour biology: herceptin acts as an anti-angiogenic cocktail. *Nature* **416**, 279-280 (2002).
337. Baselga, J. Herceptin alone or in combination with chemotherapy in the treatment of HER2-positive metastatic breast cancer: pivotal trials. *Oncology* **61 Suppl 2**, 14-21 (2001).
338. Vogel, C.L., *et al.* Efficacy and safety of trastuzumab as a single agent in first-line treatment of HER2-overexpressing metastatic breast cancer. *J Clin Oncol* **20**, 719-726 (2002).
339. Kauraniemi, P., *et al.* Effects of Herceptin treatment on global gene expression patterns in HER2-amplified and nonamplified breast cancer cell lines. *Oncogene* **23**, 1010-1013 (2004).
340. Guo, G., *et al.* Expression of ErbB2 enhances radiation-induced NF-kappaB activation. *Oncogene* **23**, 535-545 (2004).
341. Ross, J.S. & Fletcher, J.A. The HER-2/neu oncogene: prognostic factor, predictive factor and target for therapy. *Semin Cancer Biol* **9**, 125-138 (1999).
342. Laughner, E., Taghavi, P., Chiles, K., Mahon, P.C. & Semenza, G.L. HER2 (neu) signaling increases the rate of hypoxia-inducible factor 1alpha (HIF-1alpha) synthesis: novel mechanism for HIF-1-mediated vascular endothelial growth factor expression. *Mol Cell Biol* **21**, 3995-4004 (2001).
343. Bagheri-Yarmand, R., Vadlamudi, R.K., Wang, R.A., Mendelsohn, J. & Kumar, R. Vascular endothelial growth factor up-regulation via p21-activated kinase-1 signaling regulates heregulin-beta1-mediated angiogenesis. *J Biol Chem* **275**, 39451-39457 (2000).
344. Blackwell, K.L., *et al.* HER-2 gene amplification correlates with higher levels of angiogenesis and lower levels of hypoxia in primary breast tumors. *Clin Cancer Res* **10**, 4083-4088 (2004).

CHAPTER 2

345. Denk, W., Strickler, J.H. & Webb, W.W. Two-photon laser scanning fluorescence microscopy. *Science* **248**, 73-76 (1990).
346. Zipfel, W.R., Williams, R.M. & Webb, W.W. Nonlinear magic: multiphoton microscopy in the biosciences. *Nat Biotechnol* **21**, 1369-1377 (2003).
347. Göppert-Mayer, M. Über Elementarakte mit zwei Quantensprüngen. *Annalen der Physik* **401**, 273-294 (1931).
348. Kaiser, W. & Garrett, C.G.B. Two-Photon Excitation in CaF₂: Eu²⁺. *Physical Review Letters* **7**, 229 (1961).
349. Pawley, J.B. *Handbook of biological confocal microscopy*, (Springer, New York, NY, 2006).
350. Patterson, G.H. & Piston, D.W. Photobleaching in two-photon excitation microscopy. *Biophys J* **78**, 2159-2162 (2000).
351. Galbraith, J.A. & Terasaki, M. Controlled damage in thick specimens by multiphoton excitation. *Mol Biol Cell* **14**, 1808-1817 (2003).
352. Maiti, S., Shear, J.B., Williams, R.M., Zipfel, W.R. & Webb, W.W. Measuring serotonin distribution in live cells with three-photon excitation. *Science* **275**, 530-532 (1997).
353. Lakowicz, J.R., *et al.* Time-resolved fluorescence spectroscopy and imaging of DNA labeled with DAPI and Hoechst 33342 using three-photon excitation. *Biophys J* **72**, 567-578 (1997).
354. Zipfel, W.R., *et al.* Live tissue intrinsic emission microscopy using multiphoton-excited native fluorescence and second harmonic generation. *Proc Natl Acad Sci U S A* **100**, 7075-7080 (2003).
355. Brown, E., *et al.* Dynamic imaging of collagen and its modulation in tumors in vivo using second-harmonic generation. *Nat Med* **9**, 796-800 (2003).
356. McKee, T.D., *et al.* Degradation of fibrillar collagen in a human melanoma xenograft improves the efficacy of an oncolytic herpes simplex virus vector. *Cancer Res* **66**, 2509-2513 (2006).
357. Perentes, J.Y., *et al.* In vivo imaging of extracellular matrix remodeling by tumor-associated fibroblasts. *Nat Methods* **6**, 143-145 (2009).
358. Alexandrakis, G., *et al.* Two-photon fluorescence correlation microscopy reveals the two-phase nature of transport in tumors. *Nat Med* **10**, 203-207 (2004).
359. Brown, E.B., Wu, E.S., Zipfel, W. & Webb, W.W. Measurement of molecular diffusion in solution by multiphoton fluorescence photobleaching recovery. *Biophys J* **77**, 2837-2849 (1999).
360. Chauhan, V.P., *et al.* Multiscale measurements distinguish cellular and interstitial hindrances to diffusion in vivo. *Biophys J* **97**, In Press (2009).
361. Empedocles, S.A., Norris, D.J. & Bawendi, M.G. Photoluminescence Spectroscopy of Single CdSe Nanocrystallite Quantum Dots. *Phys Rev Lett* **77**, 3873-3876 (1996).
362. Medintz, I.L., Uyeda, H.T., Goldman, E.R. & Mattoussi, H. Quantum dot bioconjugates for imaging, labelling and sensing. *Nat Mater* **4**, 435-446 (2005).
363. Michalet, X., *et al.* Quantum dots for live cells, in vivo imaging, and diagnostics. *Science* **307**, 538-544 (2005).
364. Dubertret, B., *et al.* In vivo imaging of quantum dots encapsulated in phospholipid micelles. *Science* **298**, 1759-1762 (2002).
365. Jain, R.K. & Stroh, M. Zooming in and out with quantum dots. *Nat Biotechnol* **22**, 959-960 (2004).
366. Wu, X., *et al.* Immunofluorescent labeling of cancer marker Her2 and other cellular targets with semiconductor quantum dots. *Nat Biotechnol* **21**, 41-46 (2003).

367. Gao, X., Cui, Y., Levenson, R.M., Chung, L.W. & Nie, S. In vivo cancer targeting and imaging with semiconductor quantum dots. *Nat Biotechnol* **22**, 969-976 (2004).
368. Medintz, I.L., *et al.* Self-assembled nanoscale biosensors based on quantum dot FRET donors. *Nat Mater* **2**, 630-638 (2003).
369. Larson, D.R., *et al.* Water-soluble quantum dots for multiphoton fluorescence imaging in vivo. *Science* **300**, 1434-1436 (2003).
370. Stroh, M., *et al.* Quantum dots spectrally distinguish multiple species within the tumor milieu in vivo. *Nat Med* **11**, 678-682 (2005).
371. Brus, L.E. A simple model for the ionization potential, electron affinity, and aqueous redox potentials of small semiconductor crystallites. *The Journal of Chemical Physics* **79**, 5566-5571 (1983).
372. Crommie, M.F., Lutz, C.P. & Eigler, D.M. Confinement of Electrons to Quantum Corrals on a Metal Surface. *Science* **262**, 218-220 (1993).
373. Murray, C.B., Norris, D.J. & Bawendi, M.G. Synthesis and characterization of nearly monodisperse CdE (E = sulfur, selenium, tellurium) semiconductor nanocrystallites. *Journal of the American Chemical Society* **115**, 8706-8715 (1993).
374. Leatherdale, C.A., Woo, W.K., Mikulec, F.V. & Bawendi, M.G. On the Absorption Cross Section of CdSe Nanocrystal Quantum Dots. *The Journal of Physical Chemistry B* **106**, 7619-7622 (2002).
375. Dabbousi, B.O., *et al.* (CdSe)ZnS Core - Shell quantum dots: Synthesis and Characterization of a size series of highly luminescent nanocrystallites. *J phys Chem B* **101**, 9463-9475 (1997).
376. Hines, M.A. & Guyot-Sionnest, P. Synthesis and Characterization of Strongly Luminescing ZnS-Capped CdSe Nanocrystals. *The Journal of Physical Chemistry* **100**, 468-471 (1996).
377. Kim, S.W., *et al.* Engineering InAs(x)P(1-x)/InP/ZnSe III-V alloyed core/shell quantum dots for the near-infrared. *J Am Chem Soc* **127**, 10526-10532 (2005).
378. Zimmer, J.P., *et al.* Size series of small indium arsenide-zinc selenide core-shell nanocrystals and their application to in vivo imaging. *J Am Chem Soc* **128**, 2526-2527 (2006).
379. Ballou, B., Lagerholm, B.C., Ernst, L.A., Bruchez, M.P. & Waggoner, A.S. Noninvasive imaging of quantum dots in mice. *Bioconjug Chem* **15**, 79-86 (2004).
380. Hardman, R. A toxicologic review of quantum dots: toxicity depends on physicochemical and environmental factors. *Environ Health Perspect* **114**, 165-172 (2006).
381. Jaiswal, J.K., Mattoussi, H., Mauro, J.M. & Simon, S.M. Long-term multiple color imaging of live cells using quantum dot bioconjugates. *Nat Biotechnol* **21**, 47-51 (2003).
382. Lidke, D.S., *et al.* Quantum dot ligands provide new insights into erbB/HER receptor-mediated signal transduction. *Nat Biotechnol* **22**, 198-203 (2004).
383. Riegler, J. & Nann, T. Application of luminescent nanocrystals as labels for biological molecules. *Anal Bioanal Chem* **379**, 913-919 (2004).
384. Allen, T.M. Ligand-targeted therapeutics in anticancer therapy. *Nat Rev Cancer* **2**, 750-763 (2002).
385. Duncan, R. The dawning era of polymer therapeutics. *Nat Rev Drug Discov* **2**, 347-360 (2003).
386. Ferrari, M. Cancer nanotechnology: opportunities and challenges. *Nat Rev Cancer* **5**, 161-171 (2005).
387. Langer, R. Drug delivery and targeting. *Nature* **392**, 5-10 (1998).

388. Campbell, R.B., *et al.* Cationic charge determines the distribution of liposomes between the vascular and extravascular compartments of tumors. *Cancer Res* **62**, 6831-6836 (2002).
389. Dellian, M., Yuan, F., Trubetskoy, V.S., Torchilin, V.P. & Jain, R.K. Vascular permeability in a human tumour xenograft: molecular charge dependence. *Br J Cancer* **82**, 1513-1518 (2000).
390. Hamblin, M.R., Rajadhyaksha, M., Momma, T., Soukos, N.S. & Hasan, T. In vivo fluorescence imaging of the transport of charged chlorin e6 conjugates in a rat orthotopic prostate tumour. *Br J Cancer* **81**, 261-268 (1999).
391. Thurston, G., *et al.* Cationic liposomes target angiogenic endothelial cells in tumors and chronic inflammation in mice. *J Clin Invest* **101**, 1401-1413 (1998).
392. Jain, R.K. Transport of molecules in the tumor interstitium: a review. *Cancer Res* **47**, 3039-3051 (1987).
393. Jain, R.K. Barriers to drug delivery in solid tumors. *Sci Am* **271**, 58-65 (1994).
394. Jain, R.K. The next frontier of molecular medicine: delivery of therapeutics. *Nat Med* **4**, 655-657 (1998).
395. Forster, T. Intermolecular energy migration and fluorescence. *Ann. Phys.* **2**, 55-75 (1948).
396. Clapp, A.R., *et al.* Fluorescence resonance energy transfer between quantum dot donors and dye-labeled protein acceptors. *J Am Chem Soc* **126**, 301-310 (2004).
397. Kagan, C.R., Murray, C.B., Nirmal, M. & Bawendi, M.G. Electronic energy transfer in CdSe quantum dot solids. *Phys Rev Lett* **76**, 1517-1520 (1996).
398. Somers, R.C., Bawendi, M.G. & Nocera, D.G. CdSe nanocrystal based chem-/bio- sensors. *Chem Soc Rev* **36**, 579-591 (2007).
399. Patolsky, F., *et al.* Lighting-up the dynamics of telomerization and DNA replication by CdSe-ZnS quantum dots. *J Am Chem Soc* **125**, 13918-13919 (2003).
400. Gill, R., Willner, I., Shweky, I. & Banin, U. Fluorescence resonance energy transfer in CdSe/ZnS-DNA conjugates: probing hybridization and DNA cleavage. *J Phys Chem B* **109**, 23715-23719 (2005).
401. Bakalova, R., Zhelev, Z., Ohba, H. & Baba, Y. Quantum dot-based western blot technology for ultrasensitive detection of tracer proteins. *J Am Chem Soc* **127**, 9328-9329 (2005).
402. Goldman, E.R.M., I.L.; Whitley, J.L.; Hayhurst, A.; Clapp, A.R.; Uyeda, H.T.; Deschamps, J.R.; Lassman, M.E.; Mattoussi, H. A hybrid quantum dot-antibody fragment fluorescence resonance energy transfer-based TNT sensor. *J Am Chem Soc* **127**, 6744-6751 (2005).
403. Tomasulo, M., Yildiz, I. & Raymo, F.M. pH-sensitive quantum dots. *J Phys Chem B* **110**, 3853-3855 (2006).
404. Snee, P.T., *et al.* A ratiometric CdSe/ZnS nanocrystal pH sensor. *J Am Chem Soc* **128**, 13320-13321 (2006).
405. Huang, D., *et al.* Optical coherence tomography. *Science* **254**, 1178 (1991).
406. Bouma, B., *et al.* High-resolution optical coherence tomographic imaging using a mode-locked ti:Al₂O₃ laser source. *Opt Lett* **20**, 1486-1488 (1995).
407. Drexler, W., *et al.* Ultrahigh-resolution ophthalmic optical coherence tomography. *Nat Med* **7**, 502-507 (2001).
408. Povazay, B., *et al.* Submicrometer axial resolution optical coherence tomography. *Opt Lett* **27**, 1800-1802 (2002).

409. Fujimoto, J.G., *et al.* Optical biopsy and imaging using optical coherence tomography. *Nat Med* **1**, 970-972 (1995).
410. Schmitt, J.M., Knuttel, A., Yadlowsky, M. & Eckhaus, M.A. Optical-coherence tomography of a dense tissue: statistics of attenuation and backscattering. *Phys Med Biol* **39**, 1705-1720 (1994).
411. Bouma, B.E., Yun, S.H., Vakoc, B.J., Suter, M.J. & Tearney, G.J. Fourier-domain optical coherence tomography: recent advances toward clinical utility. *Curr Opin Biotechnol* **20**, 111-118 (2009).
412. Choma, M., Sarunic, M., Yang, C. & Izatt, J. Sensitivity advantage of swept source and Fourier domain optical coherence tomography. *Opt Express* **11**, 2183-2189 (2003).
413. de Boer, J.F., *et al.* Improved signal-to-noise ratio in spectral-domain compared with time-domain optical coherence tomography. *Opt Lett* **28**, 2067-2069 (2003).
414. Yun, S.H., *et al.* Comprehensive volumetric optical microscopy in vivo. *Nature Medicine* **12**, 1429-1433 (2006).
415. Hausler, G. & Lindner, M.W. "Coherence radar" and 'spectral radar'—new tools for dermatological diagnosis. *J Biomed Opt* **3**, 21-31 (1998).
416. Yun, S.H., Tearney, G.J., de Boer, J.F., Iftimia, N. & Bouma, B.E. High-speed optical frequency-domain imaging. *Optics Express* **11**, 2953-2963 (2003).
417. Schmitt, J.M., Xiang, S.H. & Yung, K.M. Speckle in optical coherence tomography. *J Biomed Opt* **4**, 95-105 (1999).
418. Nadkarni, S.K., *et al.* Measurement of collagen and smooth muscle cell content in atherosclerotic plaques using polarization-sensitive optical coherence tomography. *J Am Coll Cardiol* **49**, 1474-1481 (2007).
419. Oh, W.Y., *et al.* High-speed polarization sensitive optical frequency domain imaging with frequency multiplexing. *Opt Express* **16**, 1096-1103 (2008).
420. Desjardins, A.E., Vakoc, B.J., Tearney, G.J. & Bouma, B.E. Backscattering spectroscopic contrast with angle-resolved optical coherence tomography. *Opt Lett* **32**, 3158-3160 (2007).
421. Morgner, U., *et al.* Spectroscopic optical coherence tomography. *Opt Lett* **25**, 111-113 (2000).
422. Chen, Z.P., Milner, T.E., Dave, D. & Nelson, J.S. Optical Doppler tomographic imaging of fluid flow velocity in highly scattering media. *Optics Letters* **22**, 64-66 (1997).
423. Gambichler, T., *et al.* Characterization of benign and malignant melanocytic skin lesions using optical coherence tomography in vivo. *J Am Acad Dermatol* **57**, 629-637 (2007).
424. Zysk, A.M. & Boppart, S.A. Computational methods for analysis of human breast tumor tissue in optical coherence tomography images. *J Biomed Opt* **11**, 054015 (2006).
425. Olmedo, J.M., Warschaw, K.E., Schmitt, J.M. & Swanson, D.L. Correlation of thickness of basal cell carcinoma by optical coherence tomography in vivo and routine histologic findings: a pilot study. *Dermatol Surg* **33**, 421-425; discussion 425-426 (2007).
426. Boppart, S.A., Brezinski, M.E., Pitris, C. & Fujimoto, J.G. Optical coherence tomography for neurosurgical imaging of human intracortical melanoma. *Neurosurgery* **43**, 834-841 (1998).
427. Bohringer, H.J., *et al.* Time-domain and spectral-domain optical coherence tomography in the analysis of brain tumor tissue. *Lasers Surg Med* **38**, 588-597 (2006).
428. Boppart, S.A., Luo, W., Marks, D.L. & Singletary, K.W. Optical coherence tomography: feasibility for basic research and image-guided surgery of breast cancer. *Breast Cancer Res Treat* **84**, 85-97 (2004).

CHAPTER 2

429. Pan, Y., *et al.* Detection of tumorigenesis in rat bladders with optical coherence tomography. *Med Phys* **28**, 2432-2440 (2001).
430. Bizheva, K., *et al.* Imaging ex vivo healthy and pathological human brain tissue with ultra-high-resolution optical coherence tomography. *J Biomed Opt* **10**, 11006 (2005).
431. D'Amico, A.V., Weinstein, M., Li, X., Richie, J.P. & Fujimoto, J. Optical coherence tomography as a method for identifying benign and malignant microscopic structures in the prostate gland. *Urology* **55**, 783-787 (2000).
432. Wang, Z.G., *et al.* Optical coherence tomography for noninvasive diagnosis of epithelial cancers. *Conf Proc IEEE Eng Med Biol Soc* **1**, 129-132 (2006).
433. Yu, P., *et al.* Holographic optical coherence imaging of rat osteogenic sarcoma tumor spheroids. *Appl Opt* **43**, 4862-4873 (2004).
434. Sharma, M., Verma, Y., Rao, K.D., Nair, R. & Gupta, P.K. Imaging growth dynamics of tumour spheroids using optical coherence tomography. *Biotechnology Letters* **29**, 273-278 (2007).
435. Aalders, M.C., *et al.* Doppler optical coherence tomography to monitor the effect of photodynamic therapy on tissue morphology and perfusion. *J Biomed Opt* **11**, 044011 (2006).
436. Skliarenko, J.V., *et al.* Effects of the vascular disrupting agent ZD6126 on interstitial fluid pressure and cell survival in tumors. *Cancer Res* **66**, 2074-2080 (2006).
437. Zhao, Y., *et al.* Three-dimensional reconstruction of in vivo blood vessels in human skin using phase-resolved optical Doppler tomography. *IEEE Journal of Selected Topics in Quantum Electronics* **7**, 931-935 (2001).
438. Li, H., *et al.* Feasibility of interstitial Doppler optical coherence tomography for in vivo detection of microvascular changes during photodynamic therapy. *Lasers Surg Med* **38**, 754-761 (2006).
439. Yang, V.X., *et al.* Endoscopic Doppler optical coherence tomography in the human GI tract: initial experience. *Gastrointest Endosc* **61**, 879-890 (2005).
440. Smith, L.M., Golub, A.S. & Pittman, R.N. Interstitial PO(2) determination by phosphorescence quenching microscopy. *Microcirculation* **9**, 389-395 (2002).

III. Multiphoton Phosphorescence Quenching Microscopy

Parts of this chapter will be published:

Lanning RL, Brown EB, Padera TP, Fukumura D, and Jain RK

Manuscript in Preparation

III.1 Introduction and Motivation:

Non-invasive methods for quantitatively probing the tissue microenvironment *in vivo* from normal to disease states, including cancer, are needed. Particularly important is the metabolic microenvironment, which influences normal processes such as embryogenesis, inflammation, and maintenance of bone marrow cell lineages¹⁻⁴. However, it is often perturbed in pathophysiological disorders ranging from atherosclerosis⁵ to cancer^{6,7}. Alterations in these metabolic parameters can serve both as an early indicator of disease in Alzheimer's⁸ and response to anticancer therapy^{5,8,9}. Oxygen plays a key role in the metabolic microenvironment; promoting stem cell development¹, modifying tumor progression, modulating metastasis¹⁰⁻¹² and moderating response to therapy¹³. Interestingly, the effects of oxygen depend on the concentration, which varies greatly in both normal and disease processes. Further, the oxygen gradient in the tissue microenvironment does not always necessarily correlate with supply from the vasculature, particularly in disorders such as cancer where vascular architecture is abnormal. Therefore, an ideal tool for quantifying oxygen concentration would enable high-resolution three-dimensional measurements at significant depths in the context of the surrounding tissue microenvironment.

The quenching of phosphorescence by molecular oxygen provides an optical method for measuring oxygen tension (pO_2). Since the biological application of this technique was first introduced by Vanderkooi and co-workers¹⁴, phosphorescence quenching microscopy (PQM) has been utilized to measure both vascular and interstitial pO_2 gradients *in vivo*¹⁵⁻¹⁷. Unfortunately, these techniques offer decent lateral spatial resolution, but limited tissue penetration ($\sim 50 \mu\text{m}$) and no depth resolution. In the past decade, a novel form of optical microscopy has been developed utilizing ultrafast lasers. This technique, multiphoton microscopy (MPM), provides non-invasive optical imaging with significant depth penetration at high three-dimensional resolution^{18,19}. The intrinsic properties of multiphoton excitation allow MPM to image fluorescently labeled structures in tissue with a three-dimensional resolution of $\sim 1 \mu\text{m}$ up to depths of 450-

600 μm , depending upon the tissue type. The simple theory behind multiphoton microscopy allows for implementation in a variety of experimental designs. The compounds that are used for imaging can be quite versatile, permitting the use of some that respond to tissue physiology. This allows for simultaneous imaging and physiological monitoring of tissue.

This Chapter introduces the technique of multiphoton phosphorescence quenching microscopy (MP-PQM) developed for routine *in vivo* use in a variety of biological models. The methods of phosphorescence quenching microscopy will be described in context of luminescent lifetime measurements. The principles of multiphoton microscopy will be briefly discussed; highlighting considerations in the use of phosphorescent luminophores. The development, design, characterization and implementation of MP-PQM will then be presented. Finally, some brief physiological studies utilizing MP-PQM will be illustrated. Measurement of oxygen in the tumor microenvironment is reserved for Chapter 4.

III.2 Experimental Design of MP-PQM

Multiphoton microscopy provides the capability of imaging deep in biological tissues with an intrinsically defined three-dimensional excitation focus of femtoliter volume limiting out of plane photobleaching¹⁹⁻²¹. Further, the use of near-infrared excitation (700-1000nm) which is within the “optical window” of biological tissue²² allows deep tissue penetration (up to 1mm depending on tissue type)²³. Details of the relative merits and photophysical processes underlining multiphoton excitation have been described in the Introduction. This section describes the decisions and development of MP-PQM for use with phosphorescent metalloporphyrins.

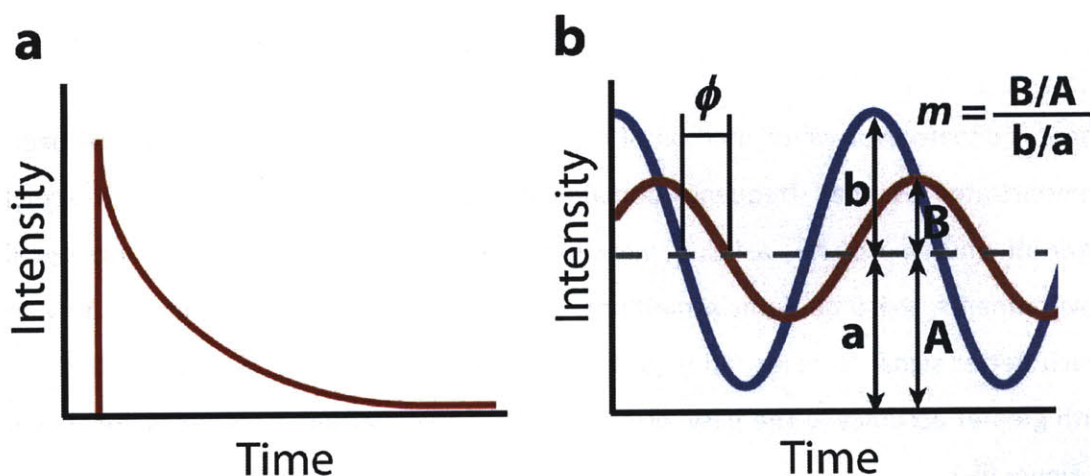


Figure III-1 Methods to measure luminescent lifetime. (a). In the time domain, lifetime is directly measured from the exponential decay after an excitation pulse. (b). In the frequency domain, lifetime is determined from both the phase delay, ϕ , and modulation, m .

III.2a TIME DOMAIN VERSUS FREQUENCY DOMAIN

There are two techniques for measuring the luminescent lifetime of a molecule which are related through the Fourier transform. The time domain, or impulse method, can be technically difficult for short lifetimes or complex decays, but it directly outputs the emission decay²⁴. Simply, in the time-domain a pulse of excitation light much shorter than the luminescence lifetime is used and the decay of emission is measured from the end of the pulse. The decay is typically fit to a single or multiple exponential decay depending if the sample is heterogeneous or not.

$$I(t) = I_0 e^{-t/\tau} \quad I(t) = \sum_i A_i e^{-t/\tau_i} \quad \text{III.1}$$

The second technique is the frequency domain or phase-modulation method whereby luminescence is excited by intensity-modulated light²⁴. The excitation is modulated at a frequency comparable to the inverse of the lifetime ($\omega \propto 2\pi \times \tau^{-1}$) with delayed luminescence responding with the same frequency but phase-shifted (ϕ) and reduced in modulation (m). The lifetime can then be determined from the following relationships.

$$\tan \phi = \omega\tau \quad m = \frac{1}{\sqrt{1 + \omega^2\tau^2}} \quad \text{III.2}$$

There is debate over which method of lifetime measurement is better. What has been demonstrated is that frequency-domain measurements are ideal in high signal environments and possess a faster measurement duty cycle²⁵. However, in low signal environments, the time-domain methods, particularly single-photon counting, provide much better signal to noise ratios (SNR) and have been shown to determine lifetimes with greater accuracy²⁶. The basic principles of the two measurement types are shown in Figure III-1.

The application of time-domain luminescence imaging has been performed in multiphoton microscopy in a variety of ways. The three most common are: 1) pulse-picking with time-gating²⁷ [Eq. III.3], 2) time-correlated single photon-counting²⁸ triggered by each selected pulse or 2) the streak-camera method which measures spatial temporal intensities along a single line scan (x, t) and creates a lifetime image (x, y, τ) by fitting exponential decays [Eq. III.1] to each temporal component²⁹.

$$\tau = \frac{\Delta T}{\ln(I_A/I_B)} \quad \text{III.3}$$

Here in Eq. III.3, the calculation of lifetime is given for time-gating with two gates (A, B) with an interval of ΔT separating them.

Frequency-domain lifetime measurements have been effectively performed to measure luminescent lifetimes *in vitro*³⁰, but to date no studies have been successfully demonstrated in animals larger than *C. elegans*²⁵. Further, in larger animal models, such as mice, the amount of luminescent probe will likely be very low, except in the vasculature, limiting SNR for frequency domain techniques. As will be shown, this is particularly the case for Pd-porphyrins which have a low two-photon absorption cross-section³¹. In addition, this limits the ability to provide appropriate modulation to the excitation signal to excite the porphyrins probe at all times.

III.2b EXPERIMENTAL SETUP

To perform MP-PQM, I chose to use the single photon counting technique triggered by the selection of pulses from the excitation source. While the time to collect measurements is increased in the time domain, it permits the integration of signal to improve SNR, a critical factor for *in vivo* measurements. Additionally, the analysis of the lifetime decay is straightforward and simple enough to include fitting to multiple components. Additionally, online analysis of the lifetimes permitted real-time display of the oxygen tension.

To adapt the technique of multiphoton microscopy to PQM, the rate of porphyrin sensor excitation must be taken into account. The lifetime of the sensor, τ_S , is much greater than the ~ 100 femtosecond pulses from the excitation laser source, τ_L . However, the repetition rate, f , of the laser is much faster than the decay of phosphorescence. For multiphoton excitation, the commonly used Ti:Sapphire laser has a repetition rate of ~ 80 Mhz. This limits the time between pulses to only 12.5ns, much shorter than the lifetime of Pd-porphyrin in the presence of oxygen (10 - 700 μ s). To overcome this obstacle and modulate the excitation of the porphyrin at a rate greater than its decay, I chose to use an electro-optic modulator.

Electro-optic modulators (EOM) have been successfully applied to multiphoton microscopy to perform fluorescence recovery after photobleaching (FRAP)³². In the case of lifetime measurements, no monitoring power is required, only a brief excitation pulse is used. Another group has employed an acousto-optic modulator (AOM) for temporal gating in lifetime measurements³³. Acousto-optic modulators typically have better extinction ratios than EOMs. However, because the emission is dependent on the quadratic (or higher) excitation of light in multiphoton microscopy, the contribution of extinction phase is minimal. Two characteristics of AOMs prompted my selection of an EOM: 1) AOMs are slower at switching than electro-optic modulators; 2) group delay dispersion (GDD) is also higher than EOMs, increasing the femtosecond pulse duration

and reducing multiphoton excitation³⁴. GDD can be corrected, but with additional often complex optics³⁵.

The MP-PQM system incorporates a KD*P Pockels cell (Model: 350-50; Conoptics, Inc., Danbury, CT) EOM and accompanying amplifier/driver as the temporal gate for pulse selection. The duty cycle (excitation pulse width \times repetition rate) of the Pockels Cell was operated in the range of 0.1-0.6%. This equates to excitation pulse durations of approximately 1.28 to 15.36 μ s for rates of \sim 680 to 360 Hz, respectively. These repetition rates allowed even the longest decays to be recorded, while permitting biological recovery of the sample between excitation pulses. Excitation pulses shorter than 1.28 μ s in solution (1mg/ml) or \sim 5.12 μ s *in vivo* did not produce any observable phosphorescence.

The voltage to the EOM was modulated by custom-built electronics; amplifying and switching the triggering pulses from a digital delay generator (DG535, SRS, Sunnyvale, CA). The experimental square wave trigger pulse originating from the DG535 defined the repetition rate; while a second delayed square wave pulse defined the excitation pulse. The voltage and hence laser power of the excitation pulse was adjusted by custom pulse conditioning electronics. As mentioned, the excitation pulses ranged from 1.28 to 15.36 μ s in duration indicating that sample excitation was performed by a train of femtosecond Ti:Sapphire laser pulses ranging in number from \sim 100 to 1230. These durations were still shorter than the experimental lifetimes of the phosphorescent porphyrins oxygen sensor. Using an oscilloscope (Model: TDS-3052, Tektronix, Beaverton, OR) and photodiode at the rejection site of the EOM, the applied voltage and optical response were monitored.

To perform photon counting, I used a multichannel scaler (SR430, SRS, Sunnyvale, CA) to histogram the counts with bin sizes ranging from 1.28 to 10.24 μ s depending on the experimental protocol. Typically, the number of bins was maintained at 1K (1024). However, for long decays the bin number was increased to 3K depending on the bin size. The number of records accumulated by the multichannel scaler was adjusted for

each bin size to keep the integration time equivalent across an experiment. The integration time was usually maintained at 6.5s for *in vivo* and ~3s for *in vitro* measurements.

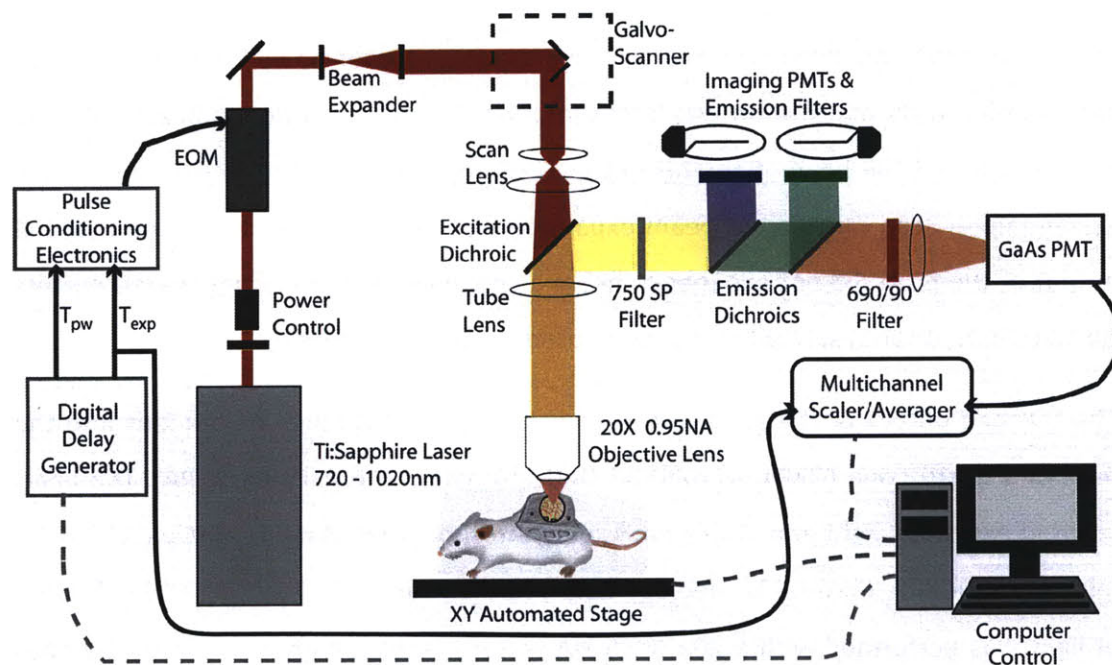


Figure III-2 Multiphoton Phosphorescence Quenching Microscopy Setup. Modification to the MPM instrumentation permitted time-domain measurements of phosphorescent lifetime for real-time oxygen quantification. T_{pw} – temporal duration of the excitation pulse width. T_{exp} – duration of the experimental triggering time, *i.e.* one single pulse and photon counting record. Arrows indicate direction of communication. Dashed grey lines to the computer control were 2-way.

Phosphorescent emission (~690nm) of the Pd-porphyrin was detected by a GaAs photomultiplier tube (PMT; H7421-50, Hamamatsu, Inc., Bridgewater, NJ) for the majority of experiments. This detector has a quantum efficiency (QE) of ~10% around 700nm. To enhance detection, I employed a silicon avalanche photodiode detector (APD; SPCM-AQR-12-FC, PerkinElmer, Fremont, CA) with a QE of 70% at 700nm. In non-turbid media, the collection efficiency (CE) of the setup with the APD was ~8× better than the GaAs PMT. However, *in vivo* measurements in highly scattering thick tissues revealed a lower CE for the APD.

The components for MP-PQM were incorporated into a custom-modified multiphoton microscope based on the Fluoview 300 laser scanner (Olympus FV300, Optical Analysis,

CHAPTER 3

Center Valley, PA). A broadband (710-1020nm) Ti:Sapphire femtosecond laser (MaiTai HP, Spectraphysics, Mountain View, CA) was used as the excitation source. The output of the laser was adjusted using a zero-order half-wave plate (10RP52-2, Newport Corp., Irvine, CA) and Glan-Laser polarizer (10GL08AR.16, Newport Corp., Irvine, CA). During phosphorescence quenching microscopy, the maximum laser power was permitted to pass and intensity modulation was performed by the electro-optic modulator. Due to magnification of the beam diameter in the EOM and the limited reflective area of the galvanometer scan mirrors, no beam expansion was needed. I did determine that the output of the EOM did not experience beam divergence over 5m. Silver coated mirrors (PF10-03-P01, Thorlabs, Newton, NJ) were used for all beam steering.

The scanned output of the galvanometers was collimated through a scan lens into the back of a microscope (Olympus BX61WI Optical Analysis, Center Valley, PA). The near-infrared excitation light and visible emission were separated using a short-pass dichroic mirror (720DCXPR, Chroma Technology Corp., Rockingham, VT). Focusing and collection of light was performed with a 20 \times , 0.95 NA water immersion objective lens (Olympus XLUMPlanFI, Optical Analysis, Center Valley, PA). Given the short spectral separation between the long emission of the phosphorescent sensors (~690nm) and the excitation laser wavelengths, a short-pass (<750nm) AR-coated filter was used in the detector path (750SP-2P, Chroma Technology Corp., Rockingham, VT) to limit background counts from the laser. A 690/90 bandpass filter (690/90M, Chroma Technology Corp., Rockingham, VT) and focusing lens were used in front of the GaAs PMT to collect phosphorescent emission. The complete experimental setup is illustrated in Figure III-2.

Lifetime measurements were performed by a stationary beam and not in scanning mode. Typically, the excitation beam was parked in the center of the field of view (FOV) and the intensity was modulated by the EOM. Different points in the sample were measured by scanning the sample with an automated mechanical XY stage (H101; Prior Scientific, Rockland, MA). Axial depth was adjusted using the automated focusing apparatus built into the microscope and the accompanying Fluoview software (Olympus,

Optical Analysis, Center Valley, PA). For point measurements in a single FOV (intravascular), the stationary beam was manually positioned using the software.

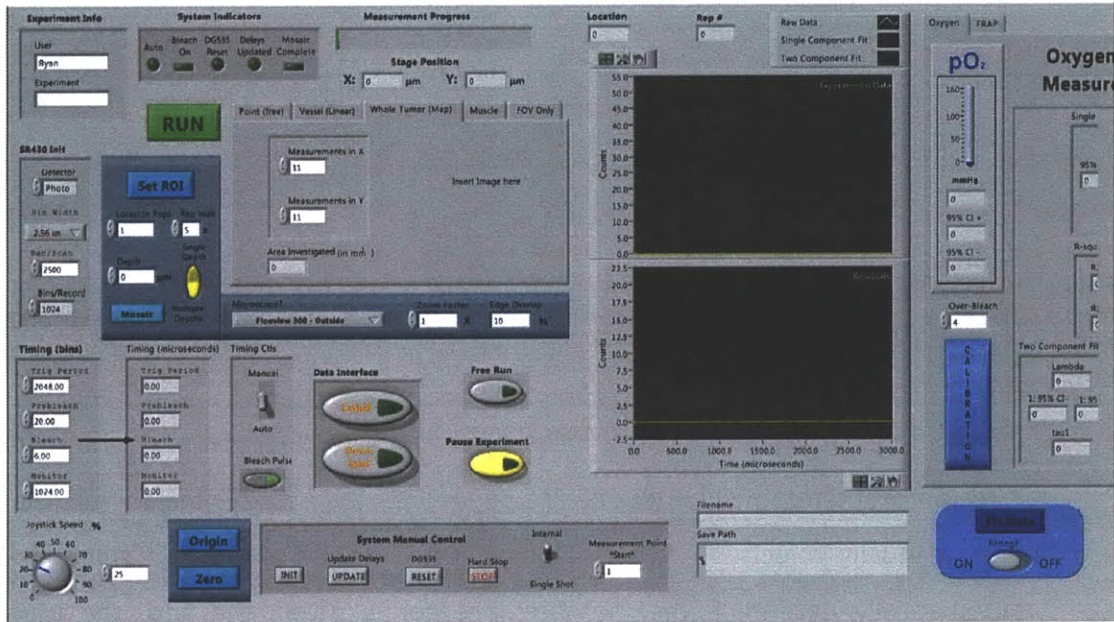


Figure III-3 Custom user interface for MP-PQM experiments. Programming performed in LabView environment.

III.2c MP-PQM EXPERIMENT PROTOCOLS

The MP-PQM instrumentation was automated and controlled by a custom-built user interface (Figure III-3) created in the LabView programming language (National Instruments, Austin, TX). This interface automated five different experiment protocols for collecting oxygenation data.

1. Single Point Measurement – ideal for quantifying oxygen within the vasculature. Allows the user to select points and collect data from each point. Beam positioning is performed manually.
2. Vessel profiles – performs a series of linear measurements with spacing defined by the user. Allows the user to measure oxygen profiles from single vessels by defining the imaging angle in the focal plane that perpendicularly bisects the vessel (**Figure III-4a**). Beam positioning is automated.

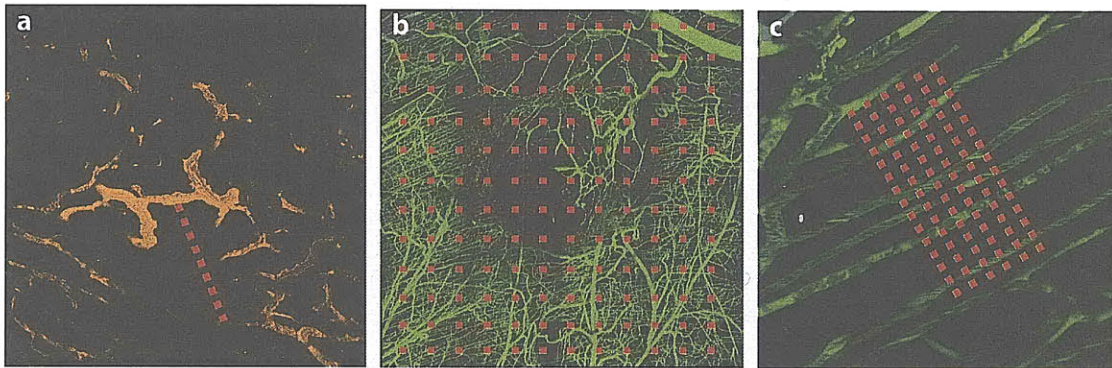


Figure III-4 MP-PQM experimental protocols for *in vivo* measurements. (a). Vessel profile measurement from a single tumor (HT1080) vessel. (b) Oxygen tension map of an entire tumor (Mu89) at a single depth. Image is a depth projection. (c) Krogh cylinder measurements in the capillary network of skeletal muscle tissue. Image is a depth projection.

3. **Oxygen Tension Maps** – performs measurements in a rectangular grid pattern in a region of interest (ROI) and grid size defined by the user (**Figure III-4b**). The user manually selects an ROI in the sample using the motorized stage. To automatically determine the measurement points within the grid, the user specifies the number of grid points in the X and Y direction. For a 12×12 grid, the measurement time is approximately 16 minutes (144 points). The oxygen tension map is collected in a raster pattern. To measure at different depths, the user manually focuses to the specified depth and inputs it into the interface. Defining an ROI also permits the user to image the sample with the multiphoton microscope in a raster pattern with mosaic tiling determined by the FOV size.
4. **Muscle (Krogh Cylinder Measurements)** – Quantifies oxygen in regularly spaced capillary networks typically found in skeletal muscle. This mode is typically used for performing three-dimensional measurements of the Krogh tissue cylinder. Analogous to the vessel profile measurements, the user defines the imaging angle in the focal plane that lies perpendicular to the capillary network with respect to the vertical axis. A series of grid measurements at different depths are performed with spacing defined by the user (**Figure III-4c**).

5. FOV Oxygen Tension Map – Similar to the oxygen tension map, except a user-defined ROI is not required. A raster grid pattern of measurements is made within the confines of the objective field of view.

In all experimental protocols, the oxygen tension is calculated in real-time using Stern-Volmer (see Chapter I) calibration values for the sensor. Single and two-component exponential fitting [Eq. III.4] to the phosphorescent decay is performed within the LabView environment by code written in MatLab (MathWorks, Natick, MA). Two different fitting algorithms are utilized. One performs an unconstrained nonlinear optimization to find the decay constants and amplitudes that minimize the residuals. The second performs a constrained nonlinear least squares fit (Levenberg-Marquardt algorithm) to the raw data to find the same parameters. The difference in fit values is less than 5% between the two methods. However, the unconstrained minimization procedure fits data with low SNR much better than the Levenberg-Marquardt algorithm. The importance of the single and two-component fitting of the lifetime data will be discussed in the Calibration section.

$$I = Ae^{-t/\tau} + C \quad I = Ae^{-t/\tau_1} + Be^{-t/\tau_2} + C \quad \text{III.4}$$

III.3 Multiphoton Excitation of Pd-Porphyrin pO₂ Sensor

The initial challenge in developing multiphoton phosphorescence quenching microscopy was characterizing the multiphoton excitation properties of the oxygen sensor. The porphyrin molecule used for all studies was a Pd-meso-tetra-(4-carboxyphenyl)porphyrin dendrimer (OxyphorR2, Oxygen Enterprises, Ltd., Philadelphia, PA). For experiments, both the ideal excitation wavelength and evidence of multiphoton excitation (MPE), or two-photon excitation in this case, at that wavelength needed to be determined. Further, the phosphorescence lifetime is always much greater than the timing between femtosecond laser pulses, so the effects of excitation saturation needed to be explored. Employing equations describing phosphorescence saturation under pulsed illumination, I show that saturation was not obtained during typical experiments.

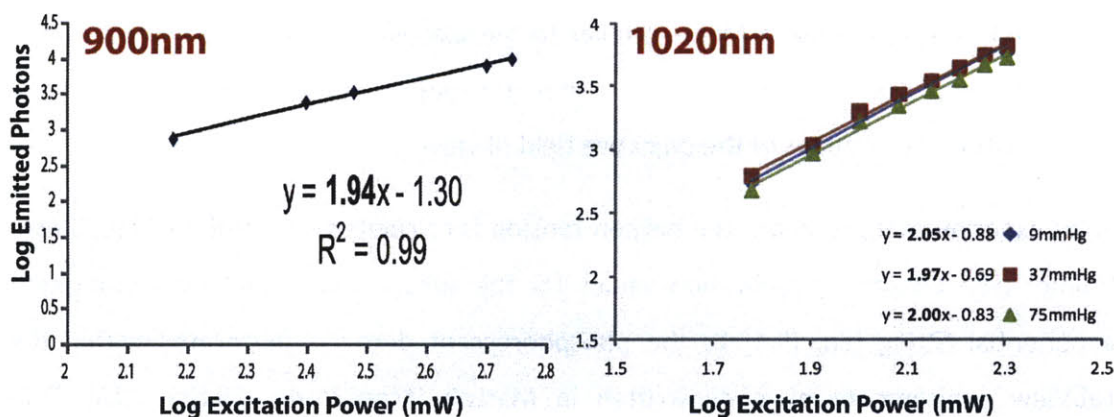


Figure III-5 Two-photon excitation of Pd-porphyrin phosphorescent oxygen sensor. The nonlinear behavior of the phosphorescence with excitation power is observed for both 900 and 1020nm excitation in these logarithmic plots.

III.3a TWO-PHOTON EXCITATION OF PD-PORPHYRIN

It has been previously demonstrated that the two-photon absorption cross-section of the tetraphenylporphyrin free base is very low compared to typical fluorophores³¹. Literature values of only 1-6 Goppert-Meyer (GM, $10^{-50} \text{ cm}^4 \text{ s}^{-1} \text{ photons}^{-1} \text{ molecule}^{-1}$) were reported. For *in vivo* measurements, particularly in the interstitial space, low concentration of sensor further diminishes the phosphorescent yield. The low yield requires the accumulation of a series of pulses in the time-domain to improve SNR (III.2).

In two-photon excitation of luminescence, the emitted intensity should be proportional to the square of the excitation intensity: $I_p \propto I_{ex}^2$ ¹⁹. To determine if the excitation of the phosphorescent sensor occurred by a two-photon process, I measured the phosphorescent emission with different excitation laser powers. Measurements were performed in anoxic (0% pO₂) phosphate buffered solutions (PBS) at pH 7.4 and 37 °C. The phosphorescent lifetime was fit from the point immediately after the excitation pulse to determine the average background counts within each photon counting bin, C in Eq. III.4. The background count was then subtracted from the signal within each bin. To obtain total emission counts, the signal was then summed from immediately after the excitation pulse to the end of the measurement period. Alternatively, an estimate of

total photon counts can be obtained by integrating the single exponential decay [Eq. III.1] to infinity: $I_0\tau$. The excitation of phosphorescence was found to be a two-photon process for excitation at both 900 and 1020nm (**Figure III-5**). *In vivo* two-photon excitation ($n \sim 1.84$) was also confirmed for intravascular measurements at 900nm (**Figure III-6**). Further, the *in vivo* measurements were performed in the presence of the MPM angiographic marker fluorescein isothiocyanate (FITC) – dextran 2M MW. Because the photon counts were determined from lifetime measurements, this experiment illustrated that FITC-Dextran2M does not affect MPE or lifetime of the pO_2 sensor.

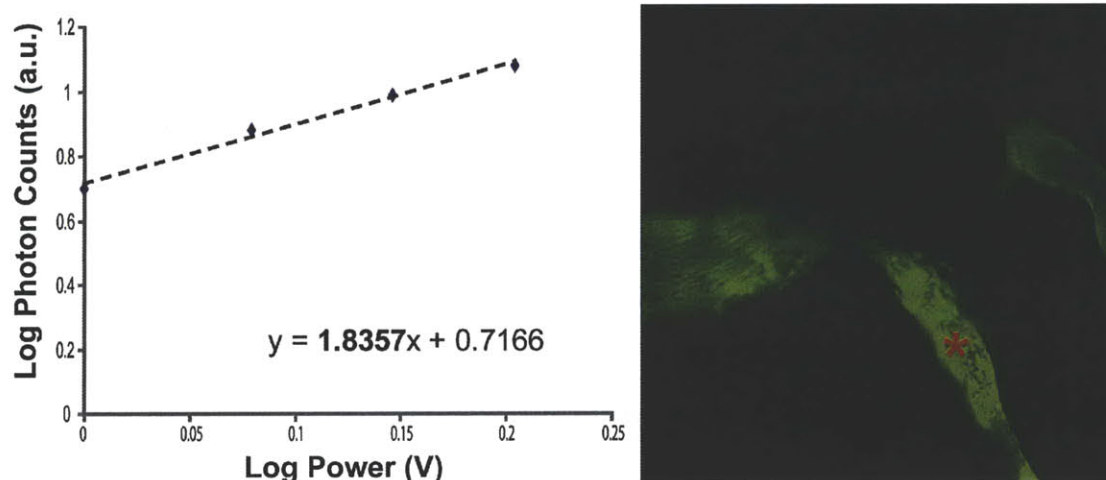


Figure III-6 *In vivo* two-photon excitation of Pd-porphyrin oxygen sensor. Nonlinear excitation of OxyphorR2 sensor in the vasculature of a tumor (*left*). A series of time-domain lifetime measurements were performed in the center (*) of a perfused tumor vessel (*right*). Green – fluorescein isothiocyanate – dextran 2M MW used for MPM angiography.

To determine the two-photon excitation spectrum (action cross-section) for the Pd-porphyrin oxygen sensor, I measured the photon counts after time-domain pulsed excitation analogous to the nonlinear power spectrum. The excitation spectrum for MPM was obtained from 780-1020nm keeping the total power at the sample constant. Slight fluctuations in the true action cross-section would occur due to differences in photon energy, i.e. the number of photons incident on the sample, for the longer wavelengths. However, this contribution should be minimal to the shape of the spectrum. For comparison, the single-photon excitation spectrum was obtained using a spectrophotometer (Beckman Instruments Inc., Fullerton, CA) with continuous

illumination from the visible to near infrared (400-1000nm). The single- and two-photon excitation spectrums both share similar shapes (**Figure III-7**), although the two-photon spectrum is slightly broader and blue-shifted due to different parity-selection rules between the two excitation processes²¹. The quantum yield of phosphorescence is $\sim 10\%$ ^{36,37} and should be the same for two-photon excitation since luminescence emission does not change with nonlinear excitation processes³⁸.

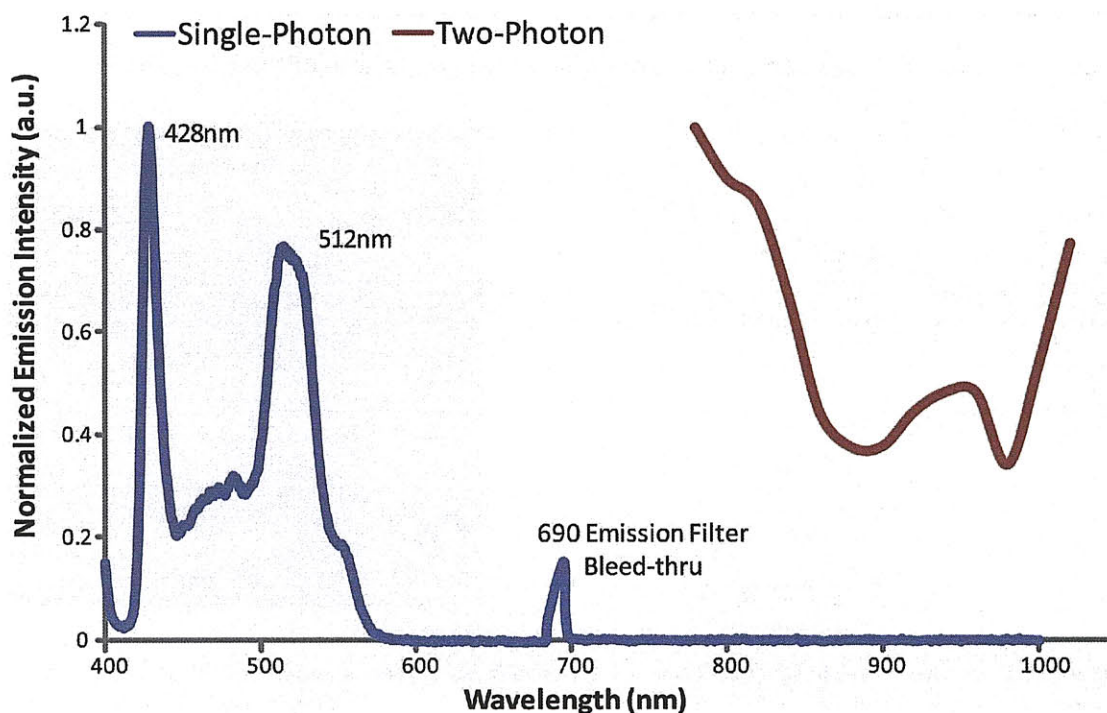


Figure III-7 Single- and Two-photon action cross-sections for Pd-porphyrin soluble oxygen sensor. The notable features of single-photon excitation spectrum are visible in the two-photon action cross-section. The single photon excitation spectrum also shows no absorption/emission in the wavelength range used for two-photon imaging (780-1000nm). The lone peak at 690nm is due to excitation light at the same wavelength as the emission band-pass filter in the spectrophotometer.

As can be seen in Figure III-7, there are two possible choices for excitation of the oxygen sensor: ~ 800 or ~ 1020 nm. I selected to use 1020nm for the following reasons:

1. Although absorption of water is around $5\times$ less at 1020nm than 800nm³⁴, more biological molecules, such as NADH, have much higher two-photon absorption at

800 than 1000nm³⁹. Further, studies have shown increased cellular damage at wavelengths ~800nm than those above 980nm³⁴.

2. The excitation light at 1020nm is less scattered than 800nm light due to the inverse dependence of scattering on the fourth-power of the wavelength. According to the principles of Rayleigh scattering, 800nm is 2.6× more scattering than 1020nm. This should improve excitation deeper in tissue at powers lower than would be needed for 800nm.
3. Excitation light at 800nm is very close to the phosphorescence emission, which extends to 780nm. Therefore it is difficult to separate the laser light from the emitted photons, particularly when using highly sensitive detectors to the near-infrared light range.

III.3b PHOSPHORESCENCE SATURATION

The luminescence of a molecule is a function of its excitation intensity. However, this relationship is not linear at all excitation intensities. As incident illumination is increased, the ground state of the luminescent molecule is depleted and the excited state(s) populated. The photophysical properties of a molecule, defined by its electronic excited states (**Figure II-2**) and their lifetimes (rate constants), and its initial concentration limit the maximum emission intensity. This can be summarized in a simple equation:

$$\frac{N_g}{N_{Tot}} \propto k_i I_{ex} \quad \text{III.5}$$

where N_g is the number of molecules in the ground state, N_{Tot} is the total number of molecules, k_i represents all rate constants defining the molecular states, and I_{ex} is the excitation intensity. Precise equations of state for common fluorescent molecules like fluorescein under continuous wave illumination have been worked out in detail by others⁴⁰. These derivations take into account all possible pathways for excited molecules including triplet states and photobleaching (irreversible loss of fluorescence). The saturation of luminescence can be used to determine many photophysical constants including the absorption cross-section, molecular state lifetimes, quantum yields and

luminescent lifetimes. Interestingly, fluorescence saturation experiments have been proposed as a possible use to characterize complex organic compounds⁴¹.

For fluorescent compounds, ignoring any triplet state contribution, the steady state fluorescence emission under single photon illumination is (adapted from³⁴):

$$Q_f k_f N_1 = \frac{\alpha Q_f k_f}{\alpha + k_f} \quad \text{III.6}$$

Here, Q_f is the quantum efficiency of fluorescence, k_f is the fluorescence decay rate, α is the excitation rate (σI), and N_1 is the number of molecules in the excited singlet state. Eq III.6 illustrates that after an initial linear increase in the fluorescence with excitation intensity, the fluorescence emission slowly plateaus.

Phosphorescence saturation has been investigated since the 1940s, starting with G.N. Lewis⁴². The saturation properties of phosphorescence, due to its long-lived nature, have allowed the investigation of many interesting photophysical properties such as paramagnetism⁴². Under continuous illumination by a light source (laser), a phosphorescent molecule would reach steady-state saturation in a time defined by:

$$\left((k_{20} + Q_{ISC} \frac{\alpha k_{10}}{\alpha + k_{10}}) \right)^{-1} \quad \text{III.7}$$

where k_{20} and k_{10} are the decay rates of the triplet and singlet states, respectively. The quantum efficiency of intersystem crossing is given by Q_{ISC} .

I estimated k_{10} for the OxyphorR2 Pd-porphyrin used in this study to be $4.00 \times 10^8 \text{ s}^{-1}$ based on literature values for other porphyrins⁴³. The quantum efficiency of phosphorescence for Oxyphor R2 is reported to be 10%³⁶. To estimate the time constant for continuous wave illumination at 1020nm, but with two-photon absorption, α is given by $\sigma_2 I^2$. The two-photon absorption cross-section for Pd-porphyrins has been reported to be in the range of 1-2GM. Assuming a constant illumination of 1mW (5.1×10^{15} photons s^{-1}) and a maximum phosphorescence lifetime (k_{20}^{-1}) of 650 μs , a time constant of 650 μs is obtained. However, true MPE utilizes a pulsed laser source, which

greatly enhances the excitation power by packing photons into small pulses. The squared power dependence is actually given by the average squared intensity rather than the squared average intensity of continuous wave excitation²¹:

$$\langle I(t)^2 \rangle = \frac{g_p \langle I(t) \rangle^2}{f\tau} \quad \text{III.8}$$

where g_p is a factor that describes the beam shape (0.66 for Gaussian beam), f is the laser repetition rate (~80MHz), and τ is the pulse width (~150fs). Employing Eq III.8 to determine α obtains a steady-state time constant of 25ns.

Three issues must be addressed here regarding saturation determined in this manner. First, the phosphorescence saturation will be dependent on the concentration in the sample. Second, for every one emitted photon, two were introduced for two-photon excitation. Finally, Eq. III.7 does not take into account the temporal characteristic of the laser source during which excitation only occurs within the femtosecond pulse.

Applying the derivation of Xu and Webb³⁸, a rate equation for the population of the ground state for each ensuing pulse can be written:

$$N_0(n+1) = N_{TOT} - [aQ_{ISC}N_0(n) + N_{TOT} - N_0(n)]e^{-1/\tau_2 f} \quad \text{III.9}$$

Here, n denotes the number of pulses, τ_2 is the phosphorescence lifetime, a is excitation probability per pulse and N_{TOT} is the total population or N_0 prior to any pulses ($n = 0$). It is assumed that the intersystem crossing rate is much faster than the repetition rate ($\tau_{ISC} \ll f^{-1}$). Because the excited singlet to ground state transition rate, $k_{10} \sim 2.5\text{ns}$, is less than the pulse separation (~12.5ns), the population of the singlet state can be ignored ($N_{TOT} = N_0(n) + N_2(n)$). Therefore an equation for the triplet state population can be obtained:

$$N_2(n) = N_{TOT} \frac{aQ_{ISC} \left[1 - (1 - aQ_{ISC})^n e^{-n/\tau_2 f} \right]}{e^{1/\tau_2 f} + aQ_{ISC} - 1} \quad \text{III.10}$$

Assuming that there is a 1% probability ($\alpha = 0.01$) that molecules in the focal volume are excited by a single pulse, which is a generous assessment for the MPE of this porphyrin given the small two-photon cross-section, and the number of laser pulses in the range of excitation pulse durations for MP-PQM (205 - 1230), a triplet state fraction ($\frac{N_2(n)}{N_{TOT}}$) from 0.2 to 0.7 is obtained for a phosphorescence lifetime of 650 μ s. These values are below saturation for nearly the longest detectable lifetime of the phosphor. In section III.5a the experimental effect of excitation pulse duration will be fit to this model to define the effect on phosphorescence saturation.

III.4 Calibration of MP-PQM pO₂ Measurements

To quantify oxygen tension using phosphorescence quenching microscopy, the parameters of the Stern-Volmer relationship must be determined. Assuming a linear Stern-Volmer relationship, a minimum of two measurements at known oxygen tension is required. For some phosphorescent porphyrin sensors, it has been reported that the dynamic quenching response was nonlinear⁴⁴. In this case at least 3 calibration measurements are needed and fit to a second order Taylor expansion of the Stern-Volmer relationship.

$$\frac{1}{\tau} = \frac{1}{\tau_0} + k_q[\text{pO}_2] + k'_q[\text{pO}_2]^2 \quad \text{III.11}$$

III.4a CALIBRATION CONSIDERATIONS

Because the absolute concentration of oxygen in tissue depends on Henry's law⁴⁵ [Eq. III.12], for which the coefficient is often unknown and variable *in vivo*, calibrations are performed for the oxygen tension or partial pressure of oxygen (pO₂). Additionally, temperature affects the solubility of oxygen and therefore Henry's constant (derived from van't Hoff Equation, Eq. III.13), so all calibrations should be performed at the temperatures found *in vivo* (32-37°C). Calibrations are performed in PBS, so if actual oxygen concentrations are desired Eqs. III.12 and III.13 can be used.

$$pO_2 = k_H [O_2] \quad \text{III.12}$$

$$k_{H,T} = k_{H,298K} \exp\left(-\frac{\Delta H^\circ}{R} \left[\frac{1}{T} - \frac{1}{T^\circ}\right]\right) \quad \text{III.13}$$

Here, Henry's constant is k_H , ΔH° is the enthalpy change of the solvent (PBS) at standard temperature and pressure, R is the gas constant, and T is the temperature of the sample.

The Pd-meso-tetra(4-carboxyphenyl) porphyrins dendrimer used for oxygen sensing (Oxyphor R2) is susceptible to other parameters in its local environment that should be addressed. Most importantly is the binding of the sensor to albumin or other binding proteins *in vivo*. In general, the lifetime increases and quenching constant decreases with increasing concentrations of albumin^{36,37,46}. Studies have suggested that the effects on Stern-Volmer sensing parameters are saturated at physiological concentrations of albumin^{36,37,46}. However, as will be shown, MP-PQM discerns differences at even higher concentrations of albumin. This prompted me to explore the development of a two-phase or two-component calibration mechanism as presented in the next section.

Additional parameters that may affect k_q and τ_0 are the temperature, pH, and tonicity (ionic strength). The effect of temperature on τ_0 is significant, however it also follows a linear relationship. As temperature increases, the lifetime of the phosphor decreases due to increased molecular collisions and therefore increased quenching. For Oxyphor R2, it has been shown that the quenching constant, k_q , increased by 3% per °C and the lifetime in the absence of oxygen, τ_0 , decreased by 0.7% per degree with increasing temperature³⁶. The pH has been shown to have minimal effect on the calibration constants in the range of extracellular pH (pHe) found *in vivo* in both normal and tumor tissues (6.4 – 7.4)^{36,37}. Similarly, the tonicity showed no effect in the same study. Therefore in considering calibration of the phosphor for *in vivo* measurements, I chose to perform all calibration procedures at 32 or 37 °C and a pH of 7.4 in PBS. If the temperature of the sample under investigation is kept constant within this range of

temperatures, k_q may change by up to 15% and τ_0 by 3.5%. The error in calculated pO_2 is determined by these two parameters can be estimated⁴⁷:

$$\Delta pO_2 = pO_2 \frac{\Delta k_q}{k_q} + \frac{1}{k_q \tau_0} \frac{\Delta \tau_0}{\tau_0} \quad \text{III.14}$$

For pO_2 values measured in tissue (0 to 60mmHg) this gives an error of around 0.15 to 9mmHg. In general, due to homeostasis and proper maintenance of the sample temperature, the error in k_q and τ_0 should be much smaller, typically around 1-2%. Further, the measurement error will also depend on the sample pO_2 since the technique is most sensitive to low pO_2 .

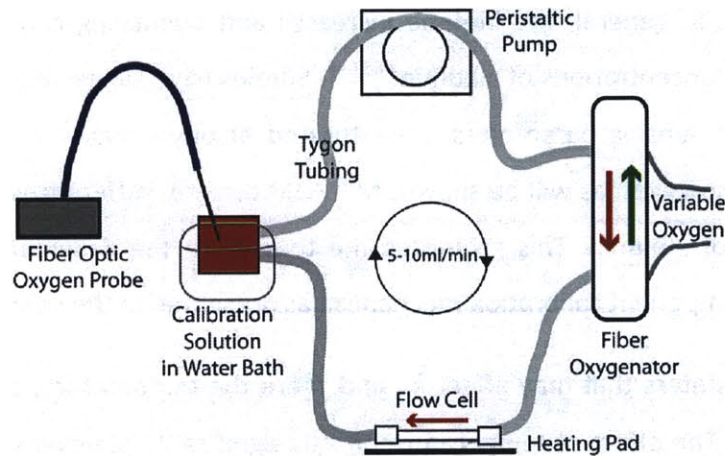


Figure III-8 Recirculating sealed calibration system employing a fiber oxygenator. Diagram of the calibration setup indicating direction of fluid and gas flow and placement of flow cell for MP-PQM. An independent pO_2 measurement is made with an optical fiber ruthenium-based probe.

III.4b CALIBRATION PROCEDURES

The simplest procedure for calibrating the phosphor oxygen sensor is to bubble known mixtures of oxygen and an inert (no dynamic quenching) gas like nitrogen into an aqueous solution of phosphor. Typically, the solutions are allowed to mix for 20-30 minutes which allows the partial pressure of oxygen in the gas mixture to equilibrate with the solution. The calibration samples are then placed in a sealed capillary tube or other optically transparent material that is impermeable to oxygen. This procedure has been successfully employed in a number of studies^{15-17,47,48}, often coupled with an

independent measure of pO_2 . The solutions are either saline (PBS) or plasma from the blood of the experimental animal.

Other methods for calibrating the oxygen sensor take advantage of enzymatic and chemical reactions that consume oxygen. The two most common enzymes and substrates used in the literature are: 1) ascorbate oxidase and ascorbate³⁷ or 2) glucose oxidase (with catalase) and glucose¹⁶. Chemical consumption with sodium dithionite has been successfully used to titrate the amount of soluble oxygen for phosphorescence measurements⁴⁹. In the appropriate environment, all of these oxygen consuming reactions are capable of producing anaerobic solutions.

To perform pO_2 calibration measurements, I developed a sealed recirculating system employing a fiber oxygenator to equilibrate the circulating fluid with gas mixtures of known oxygen concentration balanced with nitrogen (**Figure III-8**). The inclusion of a fiber oxygenator reduced surfactant effects observed with solutions containing albumin. The oxygen tension in the calibration solution was independently measured using a fiber optic ruthenium-based sensor (FOXY, Ocean Optics, Inc., Dunedin, FL). All tubing in the system was impermeable to oxygen (Tygon PVC, McMaster-Carr Supply Co., Robbinsville, NJ). Flow was maintained at $5\text{-}10\text{ ml min}^{-1}$ by using a peristaltic pump (Ismatec 7331-10, Cole-Parmer Instrument Co, Vernon Hills, Illinois). A solution of 1 mg ml^{-1} ($3.6 \times 10^{-4}\text{ M}$) OxyphorR2 in PBS at pH 7.4 was equilibrated with known nitrogen gas mixtures of 0, 1, 2, 5, 10% oxygen (0-80mmHg) using a fiber oxygenator (Hemophan[®] Membrane Fiber Oxygenator, Harvard Apparatus, Holliston, MA). The oxygenator had an 18ml priming volume, so $\sim 50\text{ ml}$ of OxyphorR2 solution was prepared for each calibration. After equilibration with the applied gas mixture, the solution was passed through an oxygen impermeable spectrophotometer flow cell with $500\mu\text{m}$ thick walls (45-Q-2, Starna Cells, Inc., Atascadero, CA). MP-PQM calibration measurements were performed within the flow cell. Both the calibration solution reservoir and flow cell were maintained at 37°C .

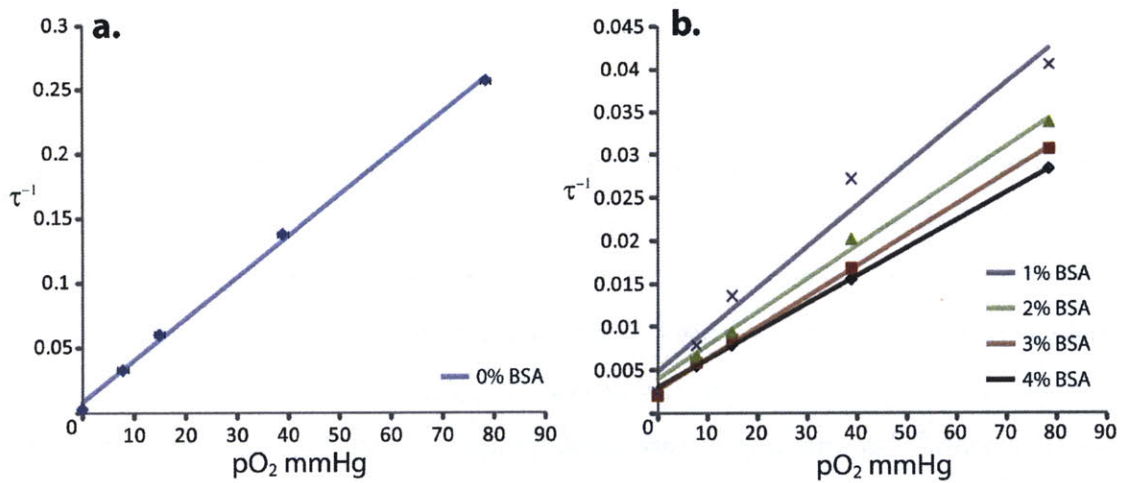


Figure III-9 MP-PQM calibration of Oxyphor R2: in the absence (a) and presence (b) of varying BSA concentrations. Solid lines are linear regression fits to the data to determine the Stern-Volmer constant.

The Stern-Volmer constants (k_q) for Oxyphor R2 solutions containing 0, 1, 2, 3, and 4% by weight bovine serum albumin (BSA, Sigma-Aldrich, Co., St. Louis, MO) were determined using this system (Figure III-9). All measurements were made at 37°C and, if necessary, the pH was adjusted to 7.4. The bin size on the multichannel scaler was set to 2.56 $\mu\text{s}/\text{bin}$ and the pulse duration was 5.12 μs for all measurements. MP-PQM calibration measurements commenced once the measured lifetimes stabilized. This usually took 15-20 minutes after initiating the system. As can be seen from the linear fits, the quenching constant decreases with increasing BSA concentration (Table III-1). At low BSA concentrations (1-2%), the data does not fit as well (increased standard error). However, these concentrations are below physiological levels of albumin and other binding proteins found *in vivo*.

Table III-1: Stern-Volmer Quenching Constants determined by linear regression for single exponential decay.

BSA (% b/w)	k_q ($\text{mmHg}^{-1} \text{s}^{-1}$)	SE	-95% CI	+95% CI
0 %	3205	78	2957	3453
1 %	480	46	332	627
2 %	385	17	310	460
3 %	357	8	333	382
4 %	322	1	317	327

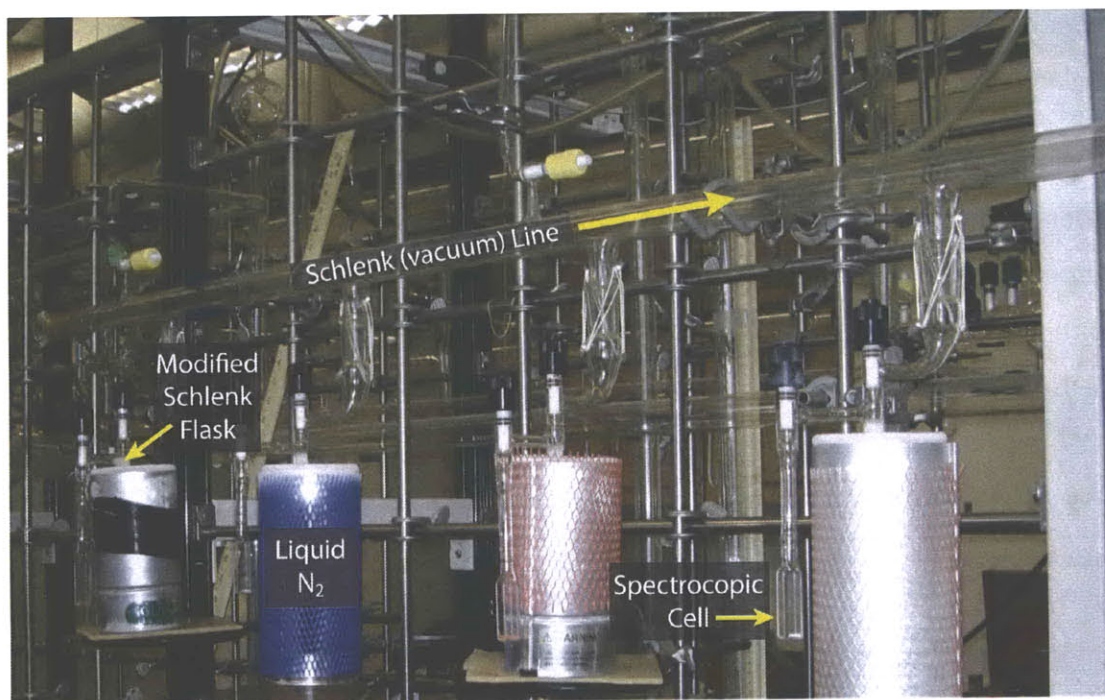


Figure III-10 Schlenk line freeze-pump-thaw method. Samples are shown during the pump process to create deoxygenated solutions

The values of k_q determined by MP-PQM and the recirculating calibration system fit those in the literature very well. The Wilson group, who developed the Oxyphor R2 sensor, reports a quenching constant of $430 \pm 10 \text{ mmHg}^{-1}\text{s}^{-1}$ for 1.5% albumin at 38°C and a pH of 7.4³⁶. In a separate paper, they report a k_q of $410 \text{ mmHg}^{-1}\text{s}^{-1}$ at 2% BSA⁴⁶.

The fiber oxygenator calibration system served well for obtaining quenching constants, but not the anoxic lifetime of the OxyphorR2. Pure deoxygenated solutions are very difficult to obtain, even in closed systems. The method of freeze-pump-thawing yields solutions that are almost entirely anoxic. This method employs flash-freezing of the solution with liquid nitrogen followed by opening the sample to a high vacuum (**Figure III-10**). Once the pressure reaches the baseline value of the vacuum, the sample is closed and the gas is released as the solution is thawed with warm water. The process is repeated until upon reopening of the sample to the vacuum, no change in pressure is observed. Schlenk flasks modified with a quartz 10 mm pathlength cuvette (Starna Cells, Inc., Atascadero, CA) created by James Glass, Inc (Hanover, MA) are used in the process. Over repeated cycles the vapor pressure above the frozen solution is reduced to the

order of 10^{-6} Torr. These low vapor pressures are obtained by an Edwards (West Sussex, England) B34431976 diffusion pump.

Using the vacuum line freeze-pump-thaw method, solutions of Oxyphor R2 containing different amounts of BSA at pH 7.4 were deoxygenated. The anoxic lifetimes were determined using MP-PQM. Using a single exponential fit, it can be seen that τ_0 continues to increase, even at 10% BSA (Table III-1). Unlike single-photon measurements which excite a large volume of phosphor throughout the samples, MP-PQM appears sensitive to unbound (free) phosphor.

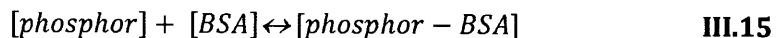
Table III-2: Oxyphor R2 calibrated lifetime in anoxic conditions (τ_0).

BSA % (b/w)	τ_0	SE ⁺	τ_0 Bound*	SE
0%	273.7	0.4		
1%	407.8	1.5	746.2	13.1
3%	483.2	1.4	726.9	7.0
5%	524.7	0.6	723.0	3.7
7%	534.1	1.1	712.3	5.1
10%	584.6	1.5	722.3	7.0

+ - Standard error of at least 10 measurements
 * - τ_0 of bound component determined by fitting to two-component decay with free τ_0 constrained

III.4c TWO-PHASE CALIBRATION

When the calibration solutions were absent of any albumin, single exponential decays [Eq. III.4] fit the data extremely well with evenly distributed residuals. However, in the presence of albumin, the single exponential fits were poor demonstrating residuals that skew at the early timepoints (Figure III-11a). These effects for single-component fitting were also seen in most *in vivo* measurements. This suggested that there may be two or more species contributing to the phosphorescence decay. In the case of the calibration solutions, there were assumed to be only two states for the phosphor molecules: albumin bound and free.



Each of these states contributes to the phosphorescence decay proportional to their concentration. It appears that the high-resolution of the MP-PQM is sensitive to the contributions of the two components.

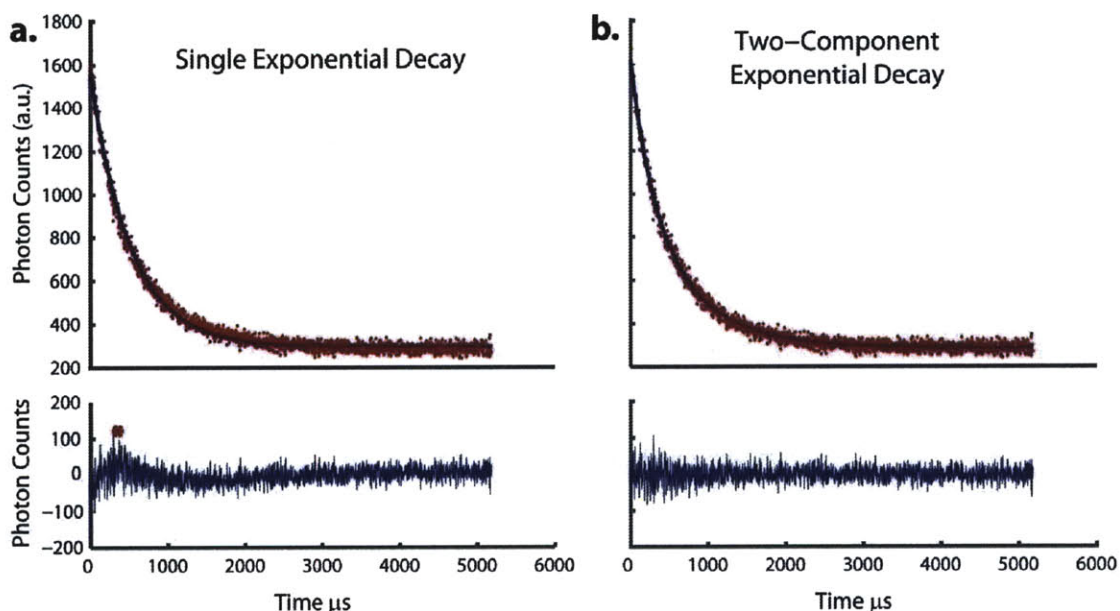


Figure III-11 MP-PQM discerns two species of phosphor in the presence of albumin. At 10% BSA (b/w), fitting to a single exponential (a) results in skewed residuals, particularly at early timepoints (*). By constraining the known lifetime of the soluble free species in a two-component exponential decay, the lifetime of the bound species can be determined. The fit demonstrates evenly distributed residuals (b).

Using the anoxic lifetime determined in the absence of albumin, I fit each of the deoxygenated solutions to a two-component exponential decay model [Eq. III.4] to determine τ_0 of the albumin bound species (Table III-2). The bound lifetime determined for each solution was independent of albumin concentration above 1% (P -value: 0.21). The mean anoxic lifetime was determined to be $726.1 \pm 6.2 \mu\text{s}$. The constrained two-component exponential decay fitting produced evenly distributed residuals at all timepoints (Figure III-11b). Additionally, the fraction of bound and free species could be calculated by determining the emission due to each species using the product of the exponential amplitude and the lifetime for each species.

In order to properly measure $p\text{O}_2$ *in vivo*, the effect of both species on phosphorescence should be taken into account. Therefore, assuming both species follow a linear Stern-

CHAPTER 3

Volmer relationship, I derived an equation to relate the lifetimes of the two species at any pO_2 . At a given oxygen tension the following relation should hold:

$$\frac{1}{k_{q,1}} \left(\frac{1}{\tau_1} - \frac{1}{\tau_{0,1}} \right) = \frac{1}{k_{q,2}} \left(\frac{1}{\tau_2} - \frac{1}{\tau_{0,2}} \right) \quad \text{III.16}$$

where the numbered subscripts denote each of the two species. Solving for the lifetime of the second species gives the same form as the original Stern-Volmer relationship.

$$\frac{1}{\tau_2} = \left[\frac{1}{k_{q,1}} \left(\frac{1}{\tau_1} - \frac{1}{\tau_{0,1}} \right) \right] k_{q,2} + \frac{1}{\tau_{0,2}} \quad \text{III.17}$$

This relationship can now be replaced in Eq. III.4 to fit for a single lifetime.

$$I = Ae^{-t/\tau_1} + Be^{-t \left(\frac{k_{q,2}}{k_{q,1}} \left(\frac{1}{\tau_1} - \frac{1}{\tau_{0,1}} \right) + \frac{1}{\tau_{0,2}} \right)} + C \quad \text{III.18}$$

To apply this equation to phosphorescence decays obtained from samples with unknown pO_2 , the quenching constants and anoxic lifetimes of both species need to be known. To obtain these values, calibration samples containing 0% or 5% BSA at pH 7.4 were prepared using the freeze-pump-thaw method. After obtaining an atmospheric pressure of 2×10^{-6} mmHg within the modified Schlenk flasks, each sample was placed under oxygen pressures ranging from 10-80 mmHg. Phosphorescence lifetimes for the 0% BSA samples were obtained using MP-PQM and fitting to a single exponential decay. MP-PQM measurements were then performed on the 5% BSA samples. The raw data was fit to both the single and two-component exponential decays, constraining one component in the two-component model to the 0% BSA lifetime at that oxygen tension. Linear Stern-Volmer relationships were fit to both the free and bound species to obtain k_q (**Figure III-12**). The quenching constant obtained for the bound species ($285 \text{ mmHg}^{-1} \text{ s}^{-1}$) was lower than that of that obtained from samples containing any concentration of BSA (**Figure III-9**). Using the lifetimes and peak amplitudes to determine the total photons attributed to each species, the bound fraction was determined to be $94.6 \pm 0.3\%$ across all oxygen tensions.

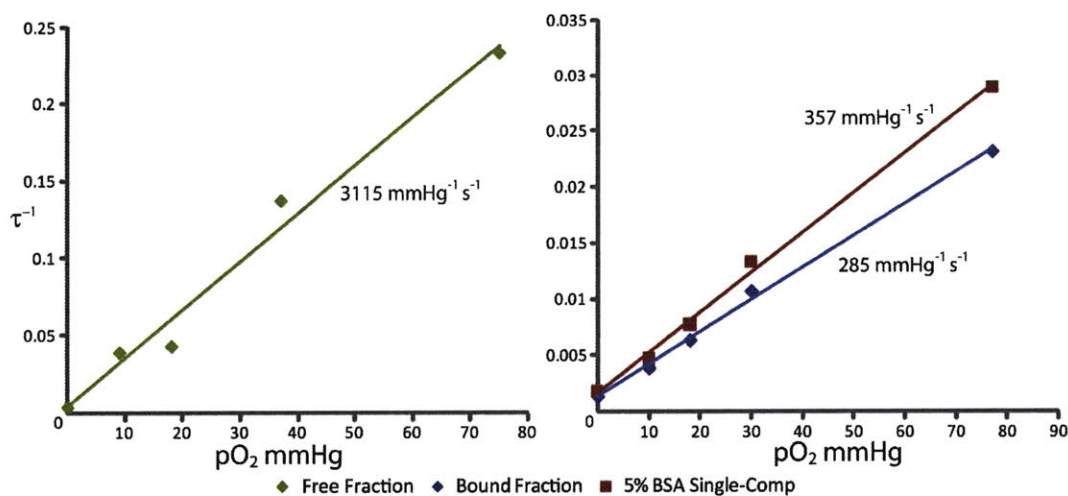


Figure III-12 Calibration of the free (left) and albumin bound (right) phosphor species using MP-PQM. The calibration curve of the single component fit to the 5% BSA solutions is also given for comparison. The Stern-Volmer constant, k_q , is give for each fit.

III.5 Characterization of MP-PQM

The experimental parameters defining time-domain multiphoton phosphorescence quenching microscopy may alter measured pO_2 or the apparent resolution of multiphoton microscopy. The instrument response to parameters such as gating and excitation pulse duration can directly affect the measured phosphorescence lifetime. The excitation wavelength utilized to perform two-photon excitation of the phosphor may also alter lifetime. Phosphorescence saturation or diffusion of phosphor during the measurement may decrease the resolution of oxygen measurements. Further, the repeatability of *in vivo* measurements should be measured to define measurement error. To fully characterize the technique, I quantified the effects of these parameters *in vitro* and in some cases *in vivo* under different oxygen tensions.

III.5a PHOTON COUNTING BIN SIZE

The multichannel scaler counted photons as a function of time by partitioning counts into different histogram bins of a given duration and time from the trigger pulse. In a typical MP-PQM experiment, the bin size should be less than the lifetime in order to acquire an accurate decay. To determine if the size of the photon counting bins correlated with the measured lifetime, I altered the bin size for phosphor solutions

under oxygen tensions ranging from 0 to 75 mmHg and with either 0% or 5% bovine serum albumin. The effect of photon counting statistics (Poisson statistics) was controlled over the experiment by increasing the number of records collected with each smaller bin size to keep total photon counts constant. At all oxygen tensions the measured lifetime was found to be independent by a one-way ANOVA (P -value > 0.05) of all bin sizes less than 50% of the phosphor lifetime for the free species (**Figure III-13**). Further, no statistical difference was found between any pair-wise comparison of bin size ($N = 10$). For the bound component, bin sizes of $0.64 \mu\text{s}$ at the longer and $10.24 \mu\text{s}$ at the shorter lifetimes were found to be statistically different from the rest of the group. For all *in vivo* experiments, bin size was maintained at $2.56 \mu\text{s}$ which showed no effect on lifetime (**Figure III-13b**) and was always much less than the lifetime ($\text{bin size} \ll \tau$).

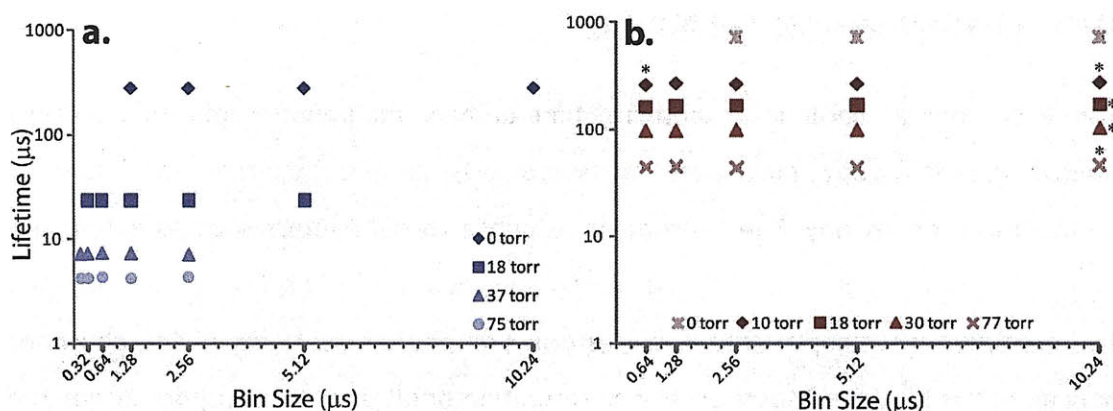


Figure III-13 Effect of photon counting bin size on measured lifetime. (a). At different oxygen tensions and 0% BSA the lifetime of OxyphorR2 was found to be independent of bin size. (b) However, for the bound component, bin sizes on the end of the range demonstrated significant differences from the rest. * - P -value < 0.05

III.5b EXCITATION PULSE DURATION

The technique of multiphoton microscopy is ideally suited for fluorophores with short ($< 4\text{ns}$) lifetimes. The repetition rate of the pulsed femtosecond excitation source is typically around 80MHz. The period of the laser cycle (12ns) allows the decay of fluorescence to occur between pulses without saturating the sample³⁸. However, phosphorescent molecules have much longer lifetimes, so as discussed in the development of the MP-PQM methodology, the duty cycle of the EOM needs to be 0.1-0.6% select only a relatively small portion of pulses.

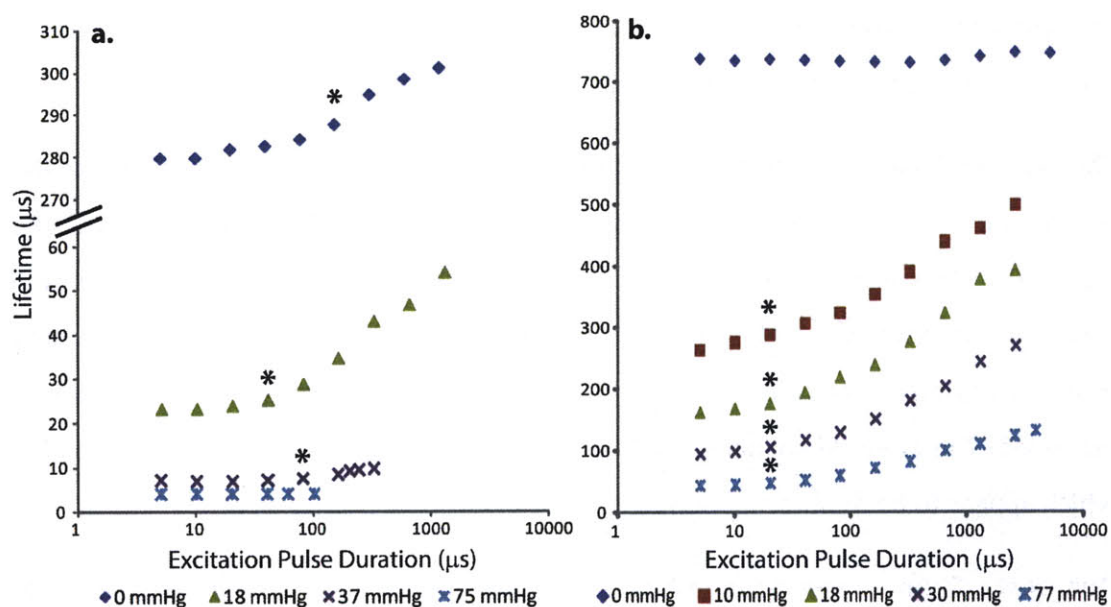


Figure III-14 Effect of excitation pulse duration on measured phosphorescence lifetime for both 0% (a) and 5% (b) BSA. * indicates duration at which all later points are statistically different from the earlier excitation pulse durations.

I determined the effect of the duty cycle by gradually increasing the excitation pulse durations of the electro-optic modulator. The effect of pulse duration on the lifetime was observed for 0% and 5% albumin solutions of Oxyphor R2 at all oxygenation levels used in the calibration (**Figure III-12a**). Interestingly, the measured lifetime tends to increase with pulse durations that are typically longer than the lifetime of the phosphor (**Figure III-14**). With each increase of the excitation pulse duration, more laser pulses are incident on the sample. For the 80MHz Ti:Sapphire laser source, the number of pulses incident on the sample increased from ~ 410 to nearly 160,000. If heating of the sample was occurring, the lifetime would decrease from increased collisional quenching due to the higher average kinetic energy. Even taking into account the exponential decays of numerous subpopulations excited at different times [Eq III.10], the lifetime should still be the same if the local environment is unchanged. However, for nearly every sample studied, the lifetime increased, even at 0 mmHg. One possible explanation for increased lifetime is secondary excitation of the triplet state of the porphyrin to even higher triplet states, thus lengthening the lifetime. This effect has been observed in many luminescent

molecules and particularly affects optical microscopies employing pulsed laser sources, such as stimulated emission depletion microscopy (STED)⁵⁰.

The likely explanation for this finding is that the oxygen within the focal volume of the multiphoton microscope is being consumed by extended periods of quenching with the phosphor. The consumption of oxygen (and potential creation of free radicals) is well known for porphyrins⁴⁴. In this case, it is likely that oxygen within the local environment is decreasing due to consumption; therefore, the apparent phosphorescence lifetime is increased. The effect of changing lifetime is also observed in the exponential decay fits which appear to be multicomponent.

Due to the Stern-Volmer relationship, changes in lifetime have a larger magnitude at higher oxygen tensions. However, the actual percentage change in measured oxygen is less. For example in Figure III-14a, at 37mmHg and 18mmHg, the percentage changes are ~27% versus 50% at the same excitation pulse duration. Any errors due to consumption of oxygen would be increased in areas of lower oxygen tension. The effect of oxygen consumption was less apparent in the more oxygenated samples (75mmHg). Here, more extended pulse durations would be needed to consume enough oxygen to significantly alter the phosphorescence lifetime. For these experiments, which were in a sealed cuvette, measurements immediately following the longer excitation duration measured the appropriate pO_2 . This suggests that the effect of oxygen consumption is only transient, corrected by the diffusion of oxygen from outside the focal volume. *In vivo* this effect may not be observed, especially in hypoxic tissue regions. For this reason, all *in vivo* pulse durations were limited to ~15 μ s or less, well below the region where the lifetime was found to be statistically different.

III.5c PHOSPHORESCENCE SATURATION – PRACTICAL EFFECTS

As discussed in section III.3b, the photophysical properties of the phosphor determine the rates of single ground state depletion and triplet state population. Using a pulsed laser source, such as in MP-PQM, the population fraction of the triplet state is dependent on the number of excitation pulses incident on the sample (n), the fraction

of molecules excited with each laser pulse (a), the repetition rate of the laser source (f) and the lifetime of the triplet state (τ_p). By fitting the phosphorescence emission during excitation pulses of extended duration (Section III.5b) to Eq III.10 in aqueous solutions of OxyphorR2 with known pO_2 ($\propto \tau_p$), the excitation fraction per laser pulse can be found.

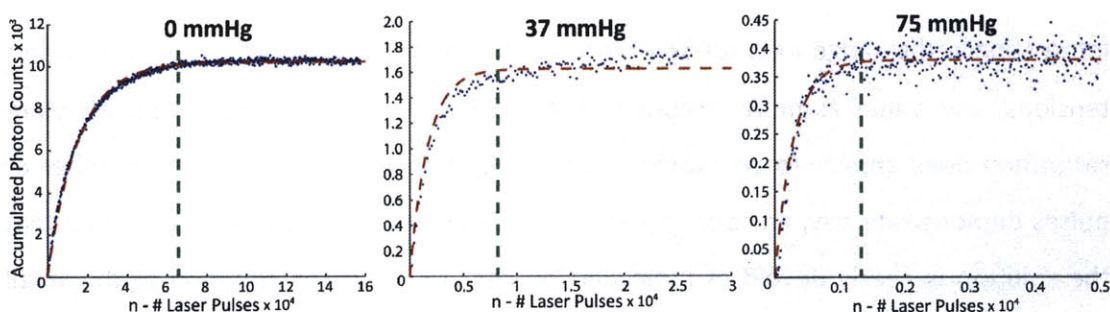


Figure III-15 Phosphorescence saturation during the excitation pulse of MP-PQM at different oxygen tension. Dashed red lines indicate the fit [Eq. III.10]. Dashed green lines indicate the number of incident laser pulses where steady-state saturation is reached for the fits.

I measured phosphorescence saturation of OxyphorR2 under excitation pulses of increased duration at 9, 18, 37, and 75 mmHg. Fitting to the model, I found an excitation fraction per laser pulse (a) of 0.001 – 0.006 depending on the oxygen tension. It is likely that there are a lot of factors affecting a . In fitting Eq. III.10 to real data, the true excitation probability of the phosphor was not taken into account. In reality, a is a combination of the system detection properties (ϕ), two-photon absorption cross-section (σ_2), phosphor concentration (C), beam-shape or second order temporal coherence of the excitation laser (g^2) and excitation power (I_0):

$$a \propto \frac{1}{2} \phi C \sigma_2 g^2 \langle I_0(t) \rangle^2 \quad \text{III.19}$$

Concentration and excitation power were controlled across samples, while the intrinsic properties of the detection system and laser would not change. Therefore it is likely that the range of a is due to changes in the lifetime or quantum yield of the phosphor.

At samples under 0, 37 and 75 mmHg of oxygen, it can be seen that the phosphorescence saturation relation does not fit as well at lower oxygen concentrations (**Figure III-15**). This is due to the consumption of oxygen changing the lifetime of the

phosphor. No more is this apparent than in the tails of the raw data, which do not level off indicating a steady-state, but continue to increase (37mmHg). Only at 75mmHg does steady-state saturation appear to occur. This is likely due to the buffering of oxygen consumption due to the higher concentration, faster rate to saturation because of the shorter lifetime and smaller changes in lifetime due to oxygen consumption. Interestingly, the range of α follows the oxygen tension, suggesting that at the higher tensions, the value is more accurate ($6.2 \pm 3.5 \times 10^{-3}$ at 75 mmHg). Steady-state saturation does appear to be reached at 0mmHg, however, fits at shorter number of pulses demonstrate oxygen consumption. This observation is likely due to the fact that the solution is nearly devoid of molecular oxygen, thus the consumption of the small amount remaining in the focal volume occurs relatively rapidly and steady-state is reached.

Another property can be observed in the fits to the saturation data (**Figure III-15**). The number of pulses required to reach steady-state saturation decreases with increasing oxygen tension due to the decreased quantum yield (dashed green line). For the samples shown (0, 37, and 75 mmHg) the corresponding number of pulses to reach saturation was 65000, 8000, and 1300. Given 12.5 nanoseconds between pulses, the time to saturation (800, 100, and 16 μ s) is about 3 \times the phosphorescent lifetimes for each sample (273, 7.3 and 4.3 μ s). This is greater than that estimated by steady-state continuous excitation [Eq. III.7].

III.5d INSTRUMENT RESPONSE

A difficulty in many time-domain lifetime experiments is the shape of the excitation pulse. Many optical excitation sources have characteristic decay times, often interfering with the measured lifetime. This requires either deconvolution of the excitation pulse from the decay²⁴ or calculating lifetimes with much data removed to reduce the effect of the excitation light³³. The former is often technically difficult, while the latter may give incorrect lifetimes due to the reduced counts and limited data.

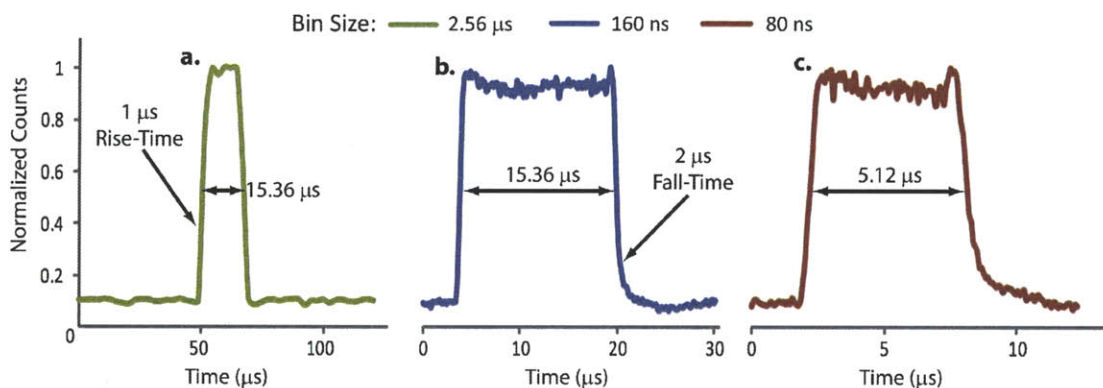


Figure III-16 Excitation laser MP-PQM pulse incident on the sample. (a) Typical *in vivo* experimental pulse at $2.56\mu\text{s}$ bin photon counting. (b) Same pulse as in a, except the collection bins are smaller allowing assessment of the fall-time. (c) A shorter excitation pulse duration.

To characterize MP-PQM, I observed the excitation laser pulse at $15.36\mu\text{s}$ or $5.12\mu\text{s}$ in duration with typical or high resolution photon counting bins (**Figure III-16**). Ordinarily, the 1020nm excitation laser pulse is not observed during the experiment due to the placement of a shortpass filter ($<750\text{nm}$) in the emission path. On all excitation pulses, a rise-time of $1\mu\text{s}$ is observed, which is within the parameters of the electro-optic modulator. The fall-time after the applied voltage is dropped across the EOM is around $2\mu\text{s}$, much less than any experimentally measured decay time *in vivo* (bound species). With shorter excitation pulses ($5.12\mu\text{s}$; **Figure III-16c**), a slight decay is observed after the excitation pulse height has dropped $\sim 10\%$ of the peak. The intensity of this decay is much less than that required to excite the phosphor. Thus, there is likely little interference of the excitation pulse in the measured lifetime.

III.5e TWO-PHOTON EXCITATION WAVELENGTH

Previously, I determined that 1020nm would be the ideal wavelength for *in vivo* excitation of the phosphor. However, no literature exists on the effect of excitation wavelength for TPE on the lifetime of the phosphor. To determine if any change in wavelength occurs, I measured the lifetime at wavelengths ranging from 800 to 1020nm in an anoxic solution of OxyphorR2 (**Figure III-17**). Average excitation power was kept constant, although this means that there still would be more incident photons at

1020nm than 800nm ($\frac{\lambda_2}{\lambda_1}$ per mW or 1.275 in this case). Repeated measurements were collected at each wavelength ($n = 5$).

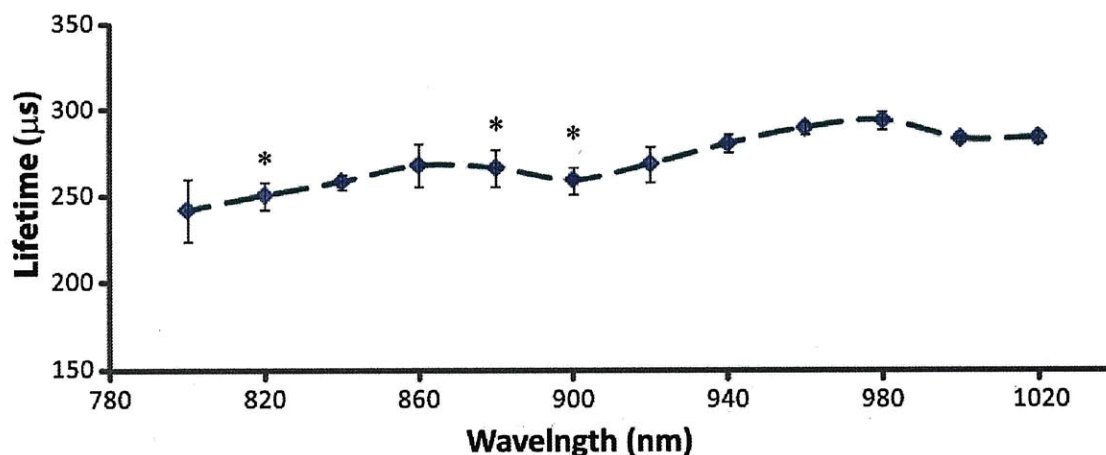


Figure III-17 Change in phosphorescence lifetime due to two-photon excitation wavelength. Errors are given as standard deviation. (*) indicate wavelengths with lifetimes significantly different from 1020nm.

As the excitation wavelength decreases from 1020nm, the lifetime decreases by $\sim 2\mu\text{s}$ every 10nm. This change with wavelength is significant over the tuning range of the Ti:Sapphire laser. The variance in the measurement also increases with decreasing wavelength. This could be due to increased detectable background from the laser, temperature fluctuations, or alterations in the photophysics of the phosphor.

In photon counting, statistical noise typically follows a Poisson distribution³⁴. This means that 63% of the measurements will be between $n \pm \sqrt{n}$. For the measurements here, the statistical noise in the background level increases almost 10-fold from 1020 to 800nm. This is likely a large source of the variance in the exponential fits to the data.

Increased heat due to two-photon absorption of the chromophore has been shown to be negligible for even the highest absorption cross-sections³⁴. However, single photon absorption of near-infrared laser light may increase heating. Of course, the absorption of water is higher at 1020 than 800nm, suggesting that any temperature effects would be reserved for the longer wavelengths. To approximate the temperature increase for a Gaussian laser beam parked for a time t , the following relation can be used for single photon absorption at the focal spot³⁴:

$$T(t) = \frac{\alpha_w \tau_D}{\rho_w c_w} \left(\frac{2P_{avg}}{\pi \omega^2} \right) \ln \left(\frac{t}{\tau_D} + 1 \right) \quad \text{III.20}$$

Here, α_w , ρ_w , and c_w describe the absorption coefficient (0.4 cm^{-1} at 1020nm), mass density (1 g ml^{-1}) and specific heat ($4.2 \text{ J g}^{-1}\text{°C}^{-1}$) of water. P_{avg} and ω are the average excitation power and width of the focal volume, respectively. The characteristic diffusion time of water, τ_D , is given by:

$$\tau_D = \frac{\omega^2}{8k_w} \quad \text{III.21}$$

where k_w is the thermal diffusivity of water ($1.4 \times 10^{-3} \text{ cm}^2\text{s}^{-1}$). The beam waist for 1020nm light and a 0.95 NA objective lens was estimated to be $0.25\mu\text{m}$. The pulse duration for the experiment in Figure III-17 was $5.12 \mu\text{s}$. Substituting all factors into Eq. III.20, a temperature rise of 0.6 °C is estimated for 1020 nm, while at 800nm it is around 0.02 °C . These temperature changes would cause fluctuations of much less than 1% in the lifetime³⁶ and does not explain why 800nm lifetimes are shorter than 1020.

A probable explanation may be stimulated emission of the phosphor from the triplet state. Stimulated emission is a quantum mechanical process whereby a photon induces an electron in an excited state to lose energy through emission of a photon. This contrasts with phosphorescence (or fluorescence), which is a spontaneous, typically thermally regulated, process. The emission from the Oxyphor R2 compound is very broad: peaking around 700nm with a long tail up to 800nm. In theory, if population inversion occurs and the triplet state contains a significant portion of the excited state molecules, which is possible given the discussion in Section III.3b, stimulated emission may occur. Further, the two-photon absorption cross-section of OxyphorR2 is larger around 800nm than at 1020nm suggesting an increased excitation rate populating the triplet state. Stimulated emission of phosphorescence from organic molecules has been demonstrated in the early 1960s⁵¹. Work since then has been in limiting the population of the triplet state to enhance stimulated emission from the singlet state in optical devices such as lasers⁵² or in STED microscopy to limit photobleaching⁵⁰.

III.5f MEASUREMENT RESOLUTION – EFFECTS OF PHOSPHOR DIFFUSION AND FLOW

The oxygen sensor has a relatively long lifetime compared to other fluorophores commonly used in MPM. During phosphorescence emission, the excited molecules can diffuse into and out of the focal volume. An estimate of diffusion distance for a single molecule can be made assuming a three-dimensional random walk.

$$\langle r^2 \rangle = 6Dt \quad \text{III.22}$$

Here the mean square displacement, $\langle r^2 \rangle$, is related to the diffusion coefficient, D , and time. Using this relation, the probability distribution for a particle starting at $r = 0$ can be obtained for given lifetimes of the phosphor (τ).⁵³

$$p(r, \tau) = \frac{1}{8(\pi D \tau)^{3/2}} e^{-r^2/4D\tau} \quad \text{III.23}$$

The diffusion coefficient for the solvated form of OxpyhorR2 was estimated from the Stokes-Einstein relation:

$$D_0 = k_B T / 6\pi\eta R_H \quad \text{III.24}$$

where, Boltzmann's constant, k_B , is $1.3807 \times 10^{-23} \text{ J K}^{-1}$, T is the temperature (310K *in vivo*), and η is the viscosity of water ($6.92 \times 10^{-4} \text{ kg m}^{-1} \text{ s}^{-1}$ at 310K). The hydrodynamic radius, R_H , was estimated from the molecular structure (including dendrimers assuming a solvation shell) to be $55 \times 10^{-10} \text{ m}$. This gives an estimated diffusion coefficient of $5.96 \times 10^{-7} \text{ cm}^2 \text{ s}^{-1}$, which is close to both albumin ($\sim 6.1 \times 10^{-7}$) and hemoglobin ($\sim 6.9 \times 10^{-7}$)⁵³.

Using the Stern-Volmer relation and the calibration constants determined for the bound species, I calculated the probability distributions for a molecule at $r = 0$ for the lifetimes at 0, 45 and 90 mmHg (**Figure III-18a**). Only at very low oxygen tensions do the phosphor molecules near the edge of the focal volume radii for the 0.95NA objective lens used in MP-PQM. In practice, lifetime measurements are performed by collecting the entire decay in the time-domain. This means that the signal will have decayed more

than $\frac{1}{e}$ or 36.7%. Typically, the signal decays below 1% of the peak intensity. Defining the time constant [$t_c = -\tau \ln(0.01)$] for such a signal decay and replacing in Eq. III.23 for τ , new probability distributions are obtained (**Figure III-18b**). For measurements in anoxic environments, around 2% of the molecules from the center of the focal volume are outside the radial $\frac{1}{e^2}$ distances at a time constant equivalent to the phosphor lifetime. This value is even higher (28%) when considering decay to 1% of peak intensity.

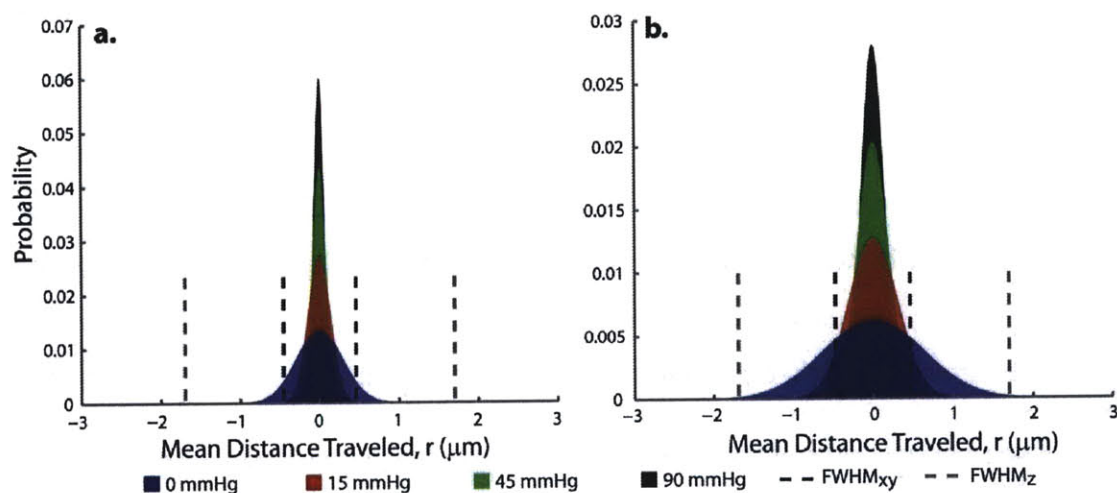


Figure III-18 Diffusion of oxygen center from center of focal volume for different oxygen tensions. Radial diffusion distances for the decay time (a.) and to 1% of peak intensity (b.) are given. The radial (xy) and axial (z) $\frac{1}{e^2}$ distances for the MPM focal volume are noted with dashed lines.

To determine the three-dimensional resolution of the oxygen measurements, the three-dimensional shape of the excited state focal volume and its change over time need to be taken into account. Temporal changes in the focal volume are applied to measure diffusion in multiphoton fluorescence recovery after photobleaching (MP-FRAP). Following the derivation of Brown *et al*³², the relation for the fraction of emitting phosphor molecules was obtained for two-photon excitation:

$$\frac{c(r, z; t)}{c_0} = \sum_{n=0}^{\infty} \frac{-\beta^n \exp \left[-\frac{4nz^2}{\omega_z^2} \frac{1}{1 + (16nDt/\omega_z^2)} - \frac{4nr^2}{\omega_r^2} \frac{1}{1 + (16nDt/\omega_r^2)} \right]}{n! (1 + 16nDt/\omega_z^2)^{1/2} (1 + 16nDt/\omega_r^2)} \quad \text{III.25}$$

The axial (ω_z) and radial (ω_r) $\frac{1}{e^2}$ widths for the three-dimensional focal spot are readily apparent, as well as the diffusion coefficient (D). The parameter β defines the initial rate of excitation [Eq. III.19] over the excitation pulse of the MP-PQM.

$$\frac{1}{2}\phi\sigma_2g^2\langle I_0(0,0)\rangle^2\Delta\tau \quad \text{III.26}$$

Here the detection efficiency (ϕ), two-photon absorption cross-section (σ_2) and second-order temporal anisotropy (g^2) are defined as in Equation III.19. The squared intensity of the stationary beam over the excitation pulse ($\Delta\tau$) determines the total amount of photons incident on the sample.

Assuming an intensity of 50mW at the sample surface and a 15.36 μs excitation pulse duration along with the other relevant constants for the phosphor (used previously) and the focal volume dimensions of a 0.95NA objective, I determined the concentration profiles of previously excited phosphor at 10% of peak phosphorescence (**Figure III-19**).

As can be seen the shape of the concentration probability profile of excited molecules in the three-dimensional excitation volume changes over time. The most dramatic effects are the decrease of concentration in the center of the focal volume, $C(r, z) = C(0, 0)$, as the phosphor diffuses out of the original excitation volume (**Figure III-19**). The volume resolution is higher the more oxygen that is present because quenching occurs over a faster period (τ is shorter). However, even at 100 mmHg the volume containing phosphor at 10% of the decay is nearly two times the original volume (**Figure III-20a**). In anoxic conditions, the effect is even more dramatic, with the volume resolution being nearly 15 times that of the original volume. The actual volumes are on the order of 0.3 to 3 femtoliters for 90 and 0mmHg, respectively. The greatest change due to diffusion occurs in the radial plane visible in the base of the concentration probability profile (**Figure III-20b**). Even at 0 mmHg, the full width half maximum (FWHM) of the probability distributions along either axis (1.04 μm radial and 1.53 μm axial) are smaller than those of other techniques⁵⁴, especially in the z (axial)-direction.

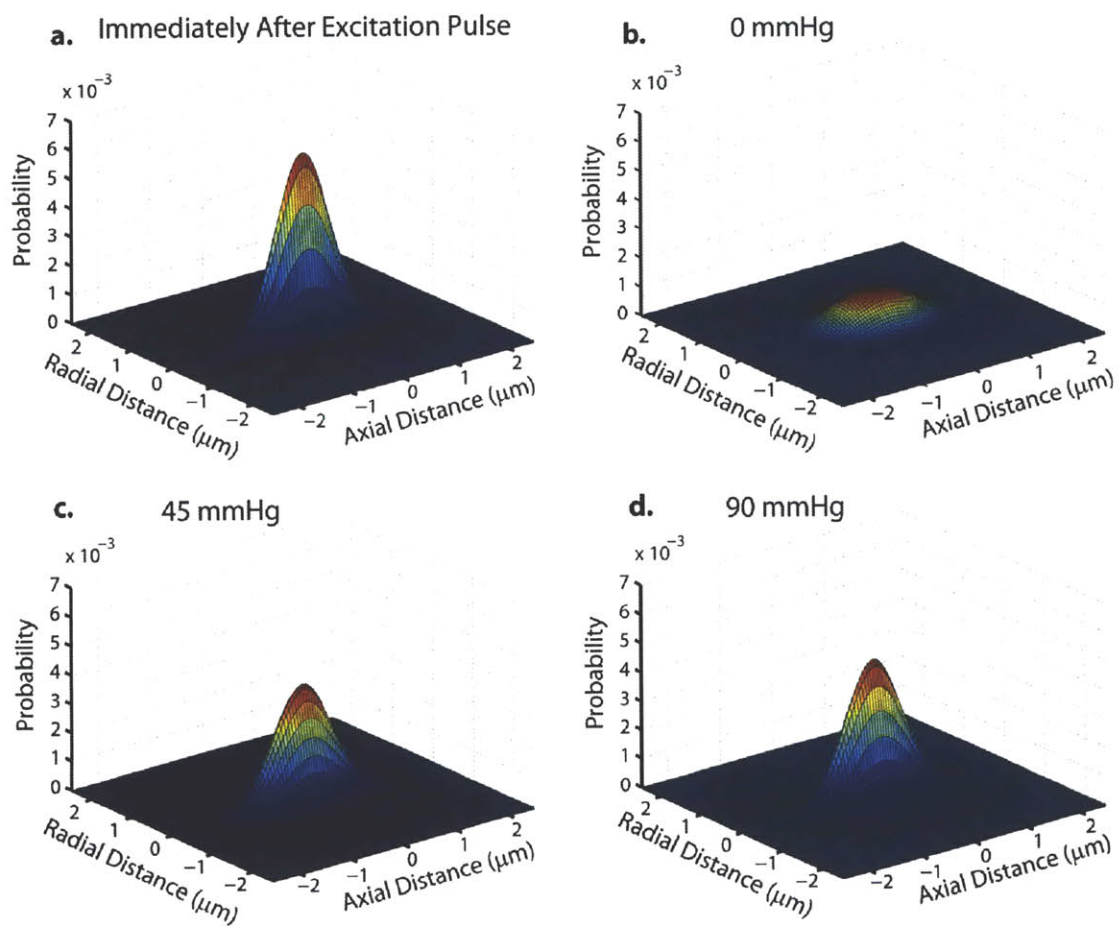


Figure III-19 Three-dimensional concentration probability profiles determine the volume resolution of MP-PQM. (a). The profile immediately after the excitation pulse. **(b).** At 0mmHg the concentration probability has spread out in all directions, enlarging the actual measurement volume. **(c and d).** At higher oxygen tensions, the lifetime of the phosphor is shorter and less diffusion out of the focal volume occurs.

The above probability distributions are useful for estimating the resolution of MP-PQM for diffusion in water. Of course *in vivo* the diffusion constant would potentially be lower than that in water. Further, much of the phosphor is bound to proteins, thus increasing the hydrodynamic radius and slowing the diffusion rate. In the case of intravascular measurements, the blood flow rate will decrease the resolution of the measurement in the direction of flow. In addition to the changes in the volume resolution caused by molecular diffusion during the lifetime of the phosphor (Figure III-19), convection will further displace these volumes.

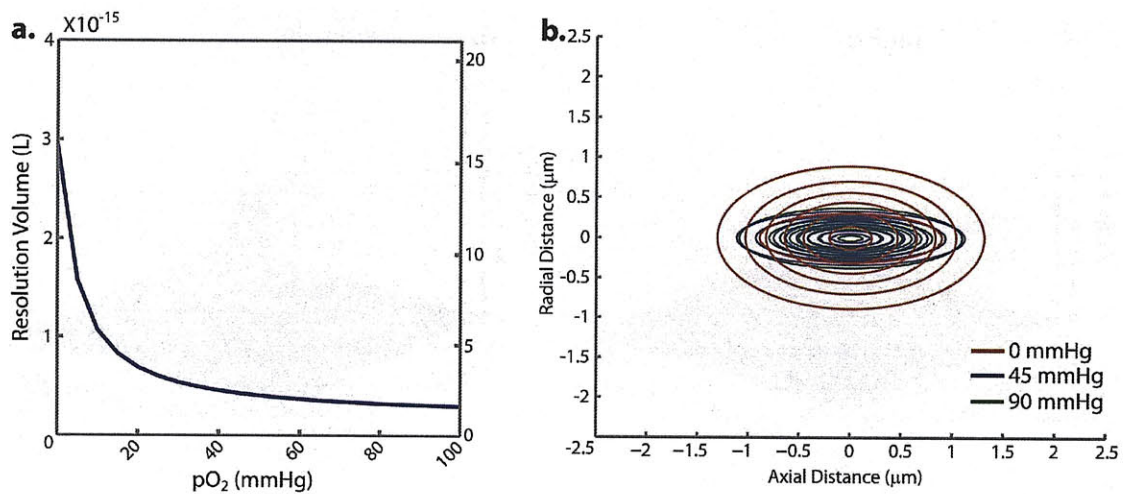


Figure III-20 Measurement volume for MP-PQM. (a). The actual volume of distribution for the phosphor at 10% of the peak intensity immediately after the excitation pulse. (b). Contour plots of the base of the three-dimensional concentration probability profiles illustrating the diffusive spreading for a range of oxygen tensions.

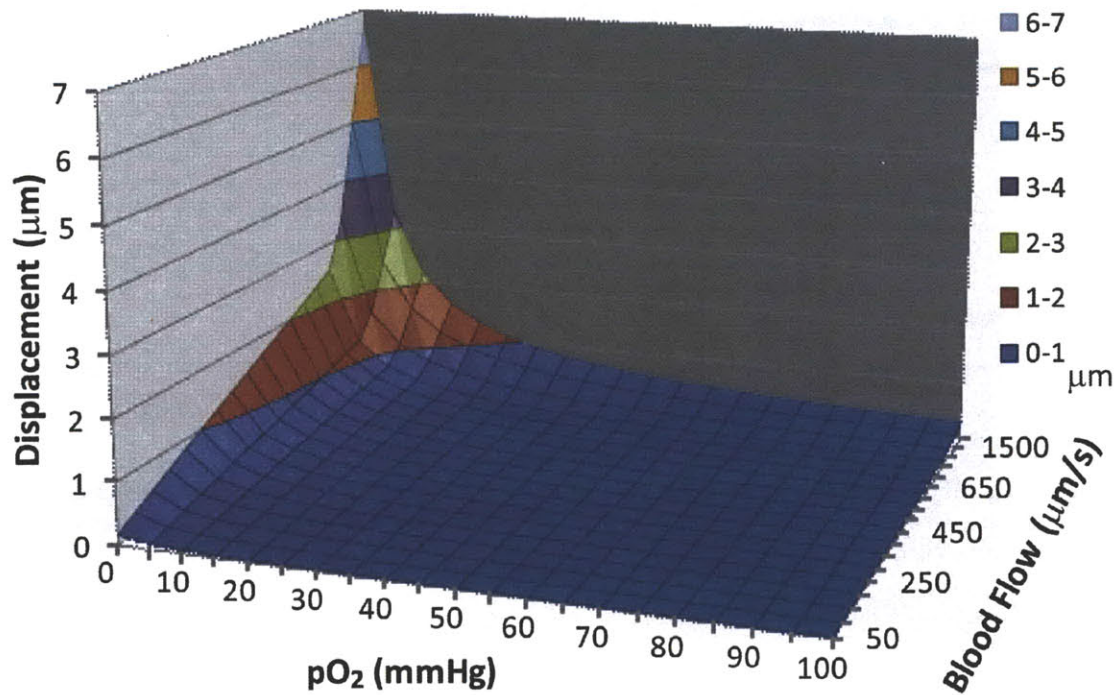


Figure III-21 Volume resolution displacement during intravascular MP-PQM measurements in unidirectional flows. Color gradients indicate increasing displacement with decreasing oxygen tension and increasing blood flow rate.

In normal brain capillaries the blood flow ranges up to 1 mm/s⁵⁵, while in tumors it can be non-existent, although an average of 100–300 μm/s is often observed⁵⁶. Assuming unidirectional flow, I determined the approximate displacement of the resolution volumes in Figure III-19 for flows ranging from 0.05 to 1500 mm/s (**Figure III-21**). At high flow rates, local environments with low oxygenation experience substantial displacement, up to 7 μm. However, at rates found in tumors (~350 μm/s), the displacement is only around 1 μm.

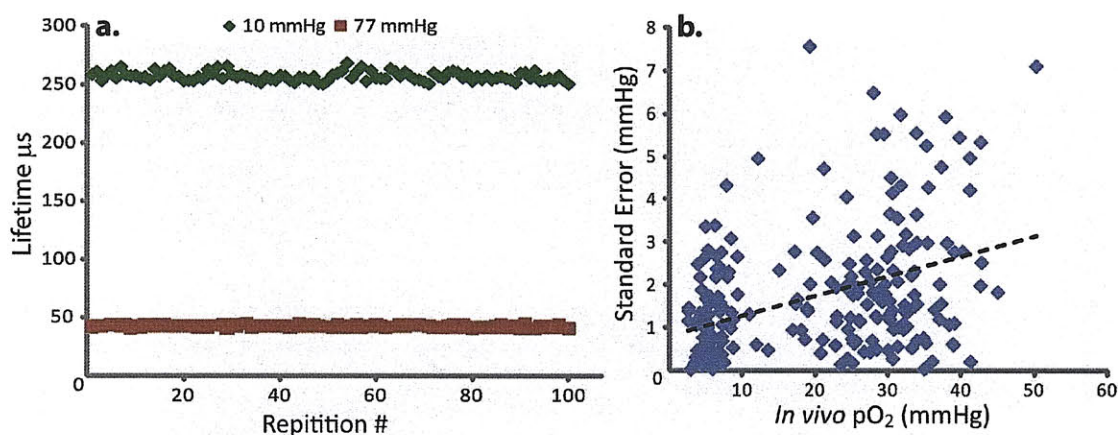


Figure III-22 MP-PQM measurement error. (a). Series of repeated measurements *in vitro* demonstrating no deviation over time. (b). *In vivo* measurements show increasing standard error with higher oxygen tensions. Dashed line - Pearson's correlation of 0.41.

III.5g MEASUREMENT REPEATABILITY IN VITRO AND IN VIVO

In addition to characteristic errors in excitation of the phosphor and effective resolution, intrinsic pO₂ measurements all suffer from a measurement error. To assess the standard error in quantified pO₂ obtained with MP-PQM, I performed either 100 repeated measurements *in vitro* at different oxygen tensions or a series oxygen tension maps *in vivo* taking three measurements at each location. At either high (77mmHg) or low (100mmHg) oxygen tensions, the deviation in the measurement over time is negligible: 42.3 ± 1.0 and 257.3 ± 3.7 mmHg, respectively (Figure III-22a). The standard error at the lower oxygen tension is larger than at higher values; however the actual fluctuation in measured pO₂ is small due to the Stern-Volmer relationship. This is apparent during measurements *in vivo* where the standard error is positively correlated (Pearson's Correlation Coefficient: 0.41) with quantified pO₂ (Figure III-22b). Interestingly, at normoxic oxygen tension, the bound fraction is around 80-90% with little correlation with pO₂ (0.18), while in hypoxic environments it ranges from 40-90% over a very short range (2-10mmHg).

III.6 *In vivo* Demonstration and Application

I further characterized MP-PQM by demonstrating both significant oxygen tension alterations under hyperoxia in normal tissue and mapping oxygen profiles in skeletal muscle of the mouse. Application of the phosphorescence quenching method using Pd-porphyrin sensors in normal tissue has been previously demonstrated in lower resolution epifluorescence microscopy^{47,57,58} or frequency domain measurements by a number of investigators⁵⁹. Many of these measurements have focused on the intravascular space rather than interstitial.

III.6a PERTURBATION OF TISSUE OXYGENATION

Altering the amount of inspired oxygen increases the oxygen saturation of the blood in healthy animals. Interestingly, hyperoxia has been studied as a means of improving the interstitial oxygen tension in a tumor to improve the efficacy of radiotherapy with limited effect^{60,61}. In clinical applications, hyperoxia is usually performed under hyperbaric conditions. In murine skin, increased vascular oxygen under normobaric conditions should improve tissue oxygenation, which would be detectable by MP-PQM.

In male SCID mice bearing dorsal skinfold chambers (DSC) exposing the underlying muscular layers of the dermis, I mapped the oxygen tension under both 21 and 100% inspired oxygen (**Figure III-23**). Measurements at altered fractions of inspired oxygen (FiO_2) were performed over the same location at three different depths in the same animals. The increase in tissue oxygenation was dramatic with tissue around the large arteries and arterioles demonstrating the largest increase in pO_2 (**Figure III-23b,c**). Some regions in the capillary networks do not demonstrate increased oxygen tension in the interstitial space.

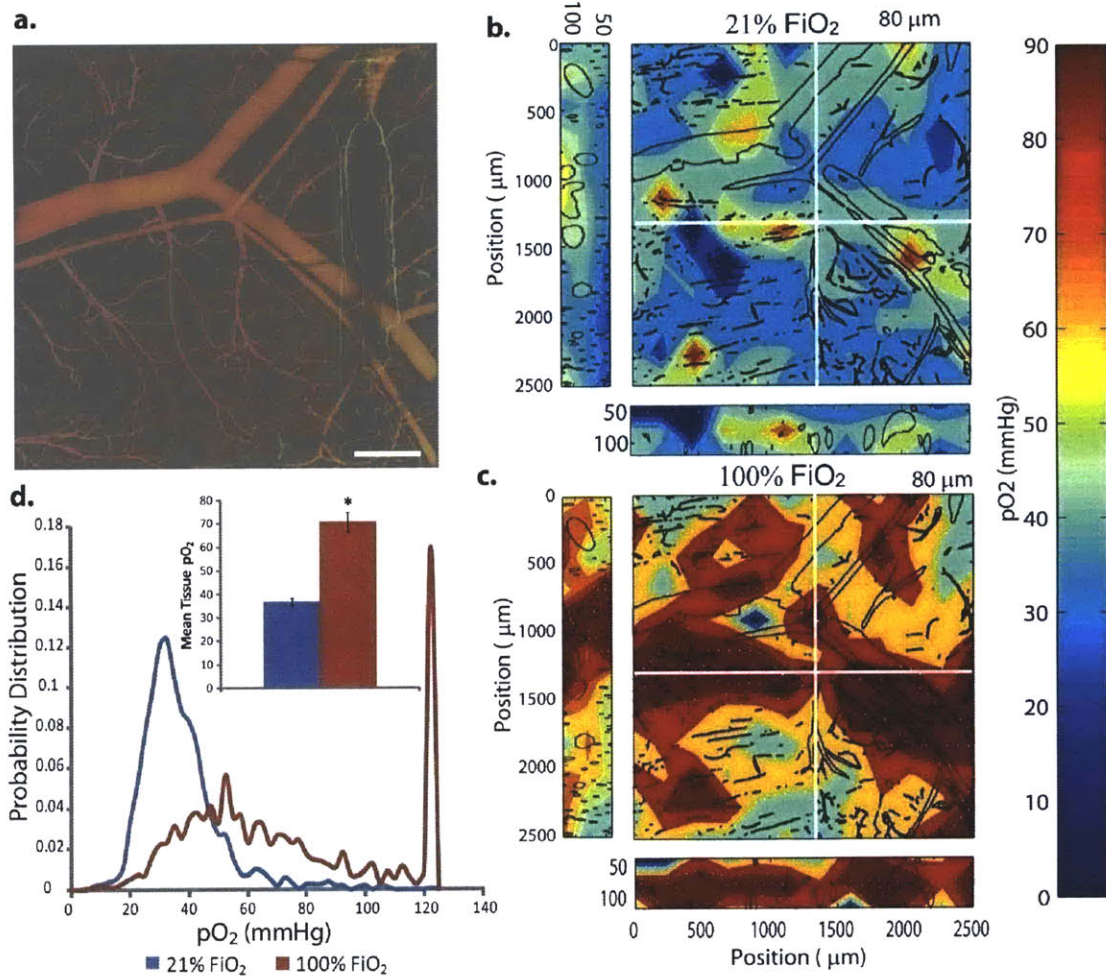


Figure III-23 Hyperoxia in normal murine skin quantified by MP-PQM. (a). Colorized depth projection of normal vasculature. (b). Oxygen tension map at 80µm deep and 21% inspired oxygen. (c). Oxygen tension map at 80µm deep and 100% inspired oxygen. (d). Oxygen tension probability distributions for normal and hyperoxic skin in b and c. *Inset* – mean tissue pO₂ is statistically different between 21 and 100% FiO₂.

The oxygen tension probability distribution under normobaric hyperoxia reveals a shifted mean peak (~32 versus ~52mmHg) and increased variance (**Figure III-23d**). Also visible is a sharp peak at 122mmHg. This is the MP-PQM systems oxygen resolution limit using 2.56µs photon counting bins. Assuming a lifetime on the order of the bin size for the free species, the calculated oxygen tension from the Stern-Volmer relationship and calibration constants is ~122mmHg. Using a smaller counting bin size, maximal detected pO₂ would extend to ~250mmHg for 1.28µs bins. The actual increased oxygen tension in the arteries is probably much higher than 122mmHg. Other investigators have

measured pO_2 levels above 470mmHg under similar conditions in an analogous hamster model⁶². The increased width of the probability distribution under hyperoxic conditions is reflected in the heterogeneity of the oxygen tension map (Figure III-23c). Still the average tissue oxygen tension was significantly higher (P -value $\ll 0.05$) under hyperoxic conditions (Figure III-23d *Inset*).

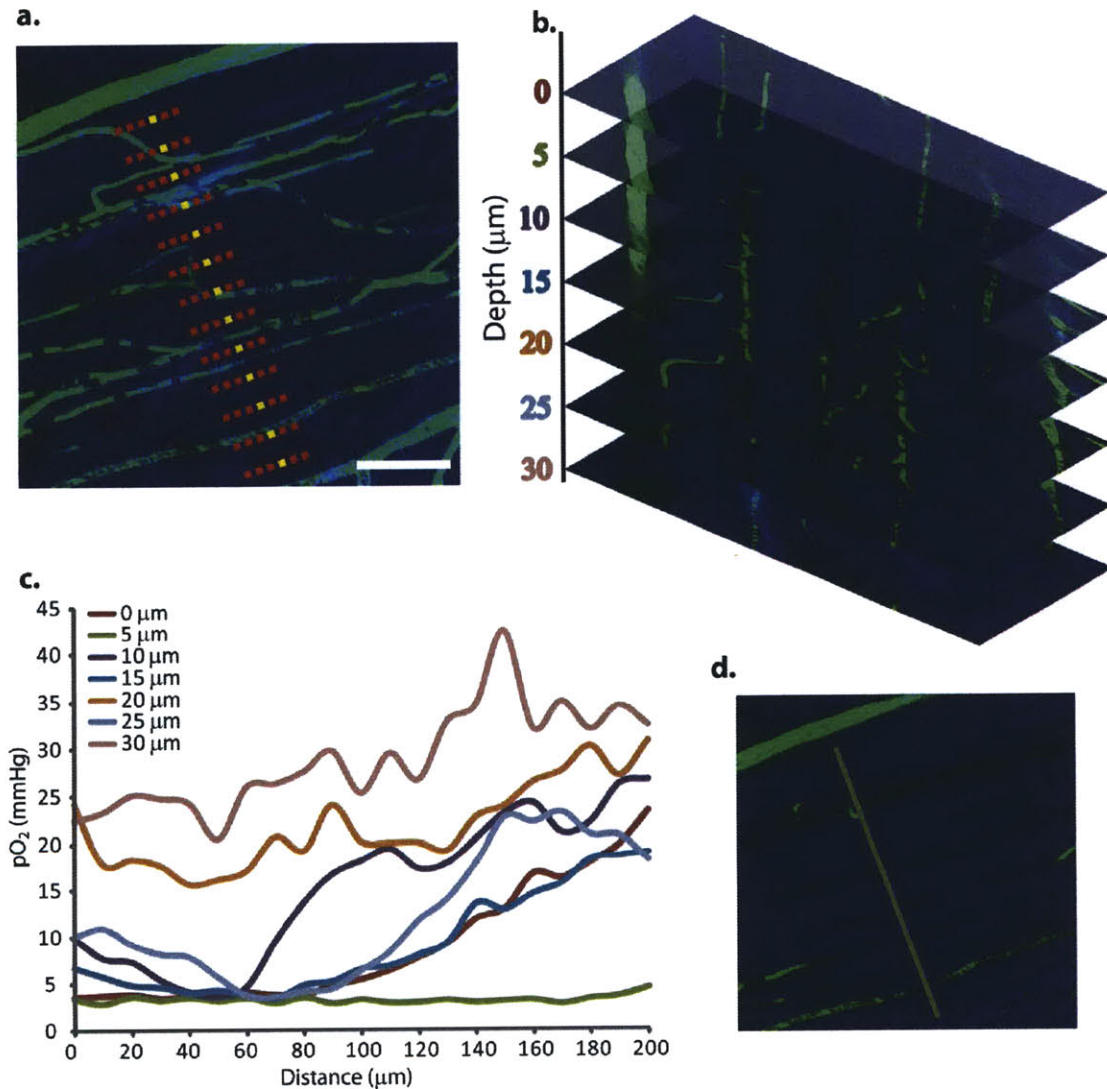


Figure III-24 Murine skeletal muscle oxygenation. (a). Maximum intensity projection of the skin musculature (blue) and associated capillaries (green). The series of planar measurements made at different depths are shown (red). The profiles shown in c are taken from the middle series (yellow). (b) Each individual depth slice where the measurements depicted in a were taken. (c) Oxygen tension profiles along the highlighted line in a (yellow). (d) The profile with the lowest oxygen is outlined on the enface slice showing measurements were taken within the muscle cells. Scale bar - 50 μm .

III.6b OXYGENATION OF SKELETAL MUSCLE – KROGH TISSUE CYLINDER MODEL

In 1919 physiologist August Krogh developed a cylindrical mathematical model for the diffusion of oxygen from capillaries in muscle tissue based on observations of capillary distribution in skeletal muscle^{63,64}. To date, the Krogh tissue cylinder model for oxygen diffusion in three-dimensions has not been experimentally demonstrated by measuring pO₂. This is partially due to inherent complexities in the biological systems studied⁶⁵⁻⁶⁹, but mostly to lack of an appropriate tool for quantifying oxygen tension at significant depths with three-dimensional resolution. Using MP-PQM to measure pO₂ in living tissue addresses these latter difficulties.

I made measurements in the skeletal muscle of the murine skin within the DSC of SCID mice (**Figure III-24a**). Measurements of pO₂ profiles (200µm) were made with 10µm spacing. The skeletal muscle fibers are around 5-10µm, typically surround by capillaries of 4-6µm in diameter, as seen in each depth slice (**Figure III-24b**). Muscle fibers were imaged by second harmonic generation of the myosin thick filaments⁷⁰ in the sarcomeres using MPM. Oxygen tension profiles at each depth (**Figure III-24c**) reveal dramatic differences in oxygenation (4.0 ± 1.0 versus 28.9 ± 5.3mmHg) between measurements within muscle fibers and those outside (**Figure III-24d**). By applying semi-automatic tracing to the MPM vascular images^{71,72}, I was able to measure diameters and distances to each capillary in three dimensions. Using this information with the oxygen measurements, I estimated the values obtained by the Krogh tissue cylinder model⁵³:

$$pO_{2,tissue} = pO_{2,vessel} + \frac{Q_{O_2} R_0^2}{4D_{O_2} S_{O_2}} \left[\left(\frac{r^2 - R_V^2}{R_0^2} \right) - 2 \ln \left(\frac{r}{R_V} \right) \right] \quad \text{III.27}$$

Point measurements of pO₂ were taken in each nearby capillary vessel to determine source levels (pO_{2,vessel}). The average radial distance between capillaries (R₀) within the networks was determined to be ~50µm from the angiographic images. The capillary diameters (2R_V) and radial distance to the vessels (r) from the tissue pO₂ measurements were determined from the vascular tracing. The diffusion rate (D_{O₂}) and solubility (S_{O₂}) of oxygen in tissue was estimated from literature values to be 2.0 × 10⁻⁵

cm^2/s and $2.05 \times 10^{-5} \text{ mlO}_2 \text{ cm}^{-3}\text{mmHg}^{-1}$, respectively. The oxygen consumption vertebrate skeletal muscle ranges from 8.0×10^{-5} to $2.5 \times 10^{-3} \text{ mlO}_2/\text{cm}^3 \text{ s}$ and depends on the blood flow of the associated capillaries⁷³. This is assuming a constant muscle density of 1.06 g/ml^{74} . Distances beyond R_0 for a given capillary and tissue measurement pairing were ignored. This follows the assumption of the Krogh cylinder model that no flux occurs beyond R_0 .

Various values of oxygen consumption within the range for skeletal muscle were used to fit to the Krogh Cylinder model. The sum of the calculated pO_2 values were compared to the MP-PQM measured values at each point. By minimizing the sum of the calculated pO_2 through adjustment of the tissue oxygen consumption (Q_{O_2}), I found a value of $1.65 \times 10^{-4} \text{ mlO}_2 \text{ cm}^{-3}\text{mmHg}^{-1}$, well within the range of that reported in the literature⁷³. However, the standard deviation of the sum was very large due to measurements in regions of different oxygen consumption (muscle fibers versus interstitial space). Additionally, pO_2 measurements inside of the muscle fibers exhibited lower oxygen tension. Interestingly, the measurements inside the muscle fibers also showed less protein bound species than those outside (0.52 ± 0.09 versus 0.86 ± 0.04). This suggests the muscle fibers must be more permeable to the free species. Further, the value of R_0 appears to be anisotropic in three dimensions. Along the XY plane, the separation is around $50\mu\text{m}$, while is much less in the axial dimension in many cases. This likely invalidates the Krogh tissue cylinder model due to overlapping oxygen sources.

III.7 Further Considerations and Future Outlook for MP-PQM

The application of phosphorescence quenching for quantification of pO_2 to multiphoton microscopy provides the ability to probe tissue oxygenation in three-dimensions with high-resolution. I have defined the characteristics and methodology of MP-PQM including techniques for measuring *in vivo* pO_2 . With additional equipment and proper software automation standard MPM in biological laboratories will be easily adaptable to perform oxygen tension measurements using phosphorescent porphyrins.

CHAPTER 3

Through standard techniques, I demonstrated that common porphyrin-based oxygen sensors can be used with nonlinear excitation. However, commercially available porphyrins have small two-photon action cross-sections limiting their efficiency with two-photon excitation. The potential for overcoming the low absorption cross-sections of porphyrins have been recently investigated using Förster resonance energy transfer (FRET)⁷⁵⁻⁷⁷. Through the use of a two-photon absorbing antennae, the phosphorescent yield can be increased. However, none of these probes have been characterized in the context of an *in vivo* environment. Further work in this area should lead to more efficient optical oxygen sensors for MP-PQM.

Given the reduced two-photon action cross-section, I attempted to improve the sensitivity of MPM to porphyrin phosphorescence using detectors with higher quantum efficiencies. Using an avalanche photodiode detector, improved sensitivity was observed for solutions, but not turbid samples or *in vivo* tissue. This was likely due to the fact that the active area of the APD was $\sim 180\mu\text{m}$, while that of standard PMTs are $\geq 8\text{mm}$. In whole area detection (WAD)³⁴ of thick samples, the emitted photons are no longer ballistic, but scattered in an array of angles collected by the objective lens. The ability to focus these scattered photons onto the smaller active area of the APD was greatly diminished in thick tissues. It is possible that descanned detection³⁴ with a pinhole above the confocal limits would permit use of an APD. However, in highly scattering tissues the lower collection efficiency observed with pinhole detection than WAD may offset any possible gain.

A concern regarding luminescent probes with long lifetimes under pulsed excitation is saturation of the excited state. In the case of a phosphorescent molecule, the triplet state may be saturated. Using a commercially available porphyrin sensor, I showed that using the MP-PQM techniques and time-domain methodology proposed in this work, excitation saturation of the triplet state does not occur under standard settings. I did demonstrate at longer impulses in the time-domain, however the time to saturation was longer than theoretically predicted. The longer time to saturation is likely due to the low

fraction of Pd-porphyrin molecules excited per laser pulse (0.006). Therefore, phosphors with improved two-photon absorption cross-sections would reach saturation faster. Any new phosphorescent molecules used with MP-PQM must be assessed for this property to determine the appropriate excitation pulse widths to employ. It should be noted that saturation does not abrogate MPE, but instead alters the shape of the focal volume³⁸ decreasing the three-dimensional resolution of the system. In certain experiments, such as multiphoton fluorescence correlation spectroscopy, the shape of the focal volume can significantly alter the measurement outcome⁷⁸. In the case of MP-PQM, saturation will only probe larger tissue volumes and potentially affect the issues of oxygen measurement resolution reported here.

It was also important to determine the expected *in vivo* pO₂ measurement resolution based on diffusion characteristics of both the sensor and oxygen as well any convective forces that may be present. Generally, I found the resolution scaled nonlinearly with oxygen tension increasing up to volumes of 3 femtoliters in anoxic environments for a 0.95 NA objective lens. At higher pO₂, the resolution is much higher due to the shorter phosphorescent lifetimes limiting the diffusion time. In cases of convection, such as measurements in a perfused and flowing blood vessel, the excited sensors to move with the flow. The distance traveled is dependent on both the fluid velocity and pO₂, with the largest error in measurement spatial resolution occurring in high flows (> 750 μm/s) and low oxygen tensions. Most blood vessel velocities in both normal and neoplastic tissue are below this range. Physiologically, low oxygen tensions will never be found in areas of high flow in normal tissues, abrogating the dramatic effect of convection on the volume resolution. Further, most vessels in tumors that have low flow are also less oxygenated^{15,47}.

I demonstrated the feasibility of MP-PQM in measuring *in vivo* oxygenation of normal tissue in mice including with perturbed FiO₂ and in the skeletal musculature of murine skin. Under normobaric hyperoxia, the oxygen tension was found to increase as expected. However, when correlated with vasculature in three-dimensions, the

response appeared heterogeneous. Further, the probability distribution of oxygen values was also found to have a larger variance than that of tissue under normoxia. It has been previously shown in the skin muscle of mammals that hyperoxia induces vasoconstriction in vessels on the order of capillaries⁷⁹. Studies in the musculature of anesthetized surgical patients have also revealed decreased vascular flow (presumably due to vasoconstriction), although the effect was heterogeneous and led to lower oxygen tensions over time⁸⁰. Therefore, the heterogeneity in the oxygen distribution is likely not due to changes in consumption, but instead a reduction in function capillary density⁶².

In the second *in vivo* experiment, I attempted to apply the Krogh tissue cylinder model to skeletal muscle in murine skin. Overall, I found that the model did not apply well or predict the measured pO_2 values. The capillary networks of the skeletal muscle in the skin possessed regular spacing in two-dimensions (XY plane), but not in three-dimensions. This asymmetry negates a major assumption of the Krogh tissue cylinder model. More interesting was that the oxygen consumption appeared to be heterogeneous throughout the musculature. Even though musculature in the skin is probably not as metabolically active as muscle elsewhere, low oxygen values were measured in some muscle fibers. The low values of pO_2 measured within the muscle fibers can be explained by increased contraction in those particular fiber groups. It has been shown that the oxygen tension within muscle fibers depends on their level of activity⁸¹. Such studies reported oxygen tension values ranging from 25 to 5mmHg in lower metabolically active muscle, in agreement with my results. Other investigators have shown higher values in muscle using other optical techniques^{82,83}. However, these single photon phosphorescence quenching measurements would only measure the average pO_2 in a much larger volume at shallower depths (~ 25-50 μm). Therefore, they may not be able to discern the effects of individual vessels and cells on the oxygen diffusion profile unlike MP-PQM.

III.8 Summary

In this Chapter I have demonstrated the development of quantitative oxygen tension measurements by applying the principles of phosphorescence quenching to multiphoton microscopy. To perform *in vivo* measurements, I created an automated software interface that allows a user to apply different data collection algorithms with real-time oxygen quantification. I developed multiple methods of calibration and showed for the first time that both protein bound and free oxygen sensor species can be differentiated using MP-PQM. This was previously believed to prevent the use of many porphyrin oxygen sensors in the extravascular space⁸³. I fully characterized the technique of MP-PQM including the two-photon excitation of the Pd-porphyrin dendrimer oxygen sensor, effects of phosphorescence saturation, practical application issues in time-domain lifetime imaging, and resolution of the oxygen measurements. *In vivo* application of MP-PQM was demonstrated during conditions of normobaric hyperoxia. Further, I applied the Krogh tissue cylinder model to the capillary networks and muscle fibers in the murine skin. I showed that in three-dimensions, this model may not be applicable for capillary networks in the skin musculature due to the anisotropic arrangement of the muscle fibers. In the next Chapter, I will apply MP-PQM to the study of solid tumor oxygenation during tumor progression and response to targeted therapy.

III.9 Additional Materials and Methods

III.9a ANIMAL MODELS

For oxygen perturbation measurements, dorsal skinfold chambers (DSC) were prepared on male SCID mice using previously described methods⁵⁶. Briefly, the back of the mouse is shaved and depilated. One-half of a pair of symmetrical titanium frames (weight 3.2 g; Workshop, Department of Radiation Oncology, MGH), is implanted on the backside of the extended double layer of skin. The exposed layer of skin is removed in a circular area approximately 15 mm in diameter matching the opening in the chamber faceplate. The remaining skin layer, consisting of epidermis, subcutaneous tissue, and striated muscle,

is covered with the second half of the titanium chamber which contains a glass coverslip (Figure III-25). Following implantation of the chamber, animals are allowed to recover from microsurgery and anesthesia for 48 hours before *in vivo* microscopy studies.



Figure III-25 Dorsal skinfold chamber implanted on a SCID mouse.

To explore the Krogh tissue cylinder model, I developed a transparent window mouse model to non-invasively image skeletal muscle and quantify pO_2 using MP-PQM. A dorsal skinfold chamber is prepared as described above, however, rather than removing all of the skin, a layer of striated skeletal muscle is surgically exposed and cleaned followed by placement of the transparent coverglass. The skeletal muscle fibers and supporting vasculature are imaged by second harmonic generation^{39,84} (SHG) and multiphoton excitation of intravenously injected fluorescein isothiocyanate (FITC) dextran 2M MW (Sigma-Aldrich Co., St. Louis, Mo.), respectively, using MPM. All animal work was approved by the by the MGH Institutional Animal Care and Use Committee.

III.9b PREPARATION OF OXYGEN SENSOR

Palladium meso-tetra(4-carboxyphenyl) porphyrin dendrimer (Oxyphor R2) was obtained from Oxygen Enterprises, Ltd., Philadelphia, PA. For *in vitro* studies Oxyphor R2 was prepared as 1mg/ml (0.36mM) solutions in phosphate buffered saline. Prior to any measurement, the pH was adjusted to 7.4 using either 1M sodium hydroxide or 1M potassium phosphate where appropriate. For *in vivo* measurements, 10mg/ml (3.6mM) solutions of Oxyphor R2 were prepared with mixed 8mg/ml (4 μ M) FITC-Dextran 2M in PBS. The pH was adjusted to 7.4 and the sample filtered (20 μ m) prior to administration.

Samples were administered intravenously (200 μ l) either by tail vein or retro-orbital injection. The dosage of Oxyphor R2 was 100mg/kg.

III.10 References

1. Jones, D.L. & Wagers, A.J. No place like home: anatomy and function of the stem cell niche. *Nat Rev Mol Cell Biol* **9**, 11-21 (2008).
2. Bosco, M.C., *et al.* Monocytes and dendritic cells in a hypoxic environment: Spotlights on chemotaxis and migration. *Immunobiology* **213**, 733-749 (2008).
3. Griffith, L.G. & Swartz, M.A. Capturing complex 3D tissue physiology in vitro. *Nat Rev Mol Cell Biol* **7**, 211-224 (2006).
4. Simon, M.C. & Keith, B. The role of oxygen availability in embryonic development and stem cell function. *Nat Rev Mol Cell Biol* **9**, 285-296 (2008).
5. Stocker, R. & Keane, J.F., Jr. Role of oxidative modifications in atherosclerosis. *Physiol Rev* **84**, 1381-1478 (2004).
6. Laconi, E. The evolving concept of tumor microenvironments. *Bioessays* **29**, 738-744 (2007).
7. Joyce, J.A. & Pollard, J.W. Microenvironmental regulation of metastasis. *Nat Rev Cancer* **9**, 239-252 (2009).
8. Mosconi, L., Pupi, A. & De Leon, M.J. Brain glucose hypometabolism and oxidative stress in preclinical Alzheimer's disease. *Ann N Y Acad Sci* **1147**, 180-195 (2008).
9. Fukumura, D. & Jain, R.K. Tumor microenvironment abnormalities: causes, consequences, and strategies to normalize. *J Cell Biochem* **101**, 937-949 (2007).
10. Chan, D.A. & Giaccia, A.J. Hypoxia, gene expression, and metastasis. *Cancer Metastasis Rev* **26**, 333-339 (2007).
11. Chaudary, N. & Hill, R.P. Hypoxia and metastasis in breast cancer. *Breast Dis* **26**, 55-64 (2006).
12. Hill, R.P., Marie-Egyptienne, D.T. & Hedley, D.W. Cancer stem cells, hypoxia and metastasis. *Semin Radiat Oncol* **19**, 106-111 (2009).
13. Gray, L.H., Conger, A.D., Ebert, M., Hornsey, S. & Scott, O.C. The concentration of oxygen dissolved in tissues at the time of irradiation as a factor in radiotherapy. *Br J Radiol* **26**, 638-648 (1953).
14. Vanderkooi, J.M., Maniara, G., Green, T.J. & Wilson, D.F. An optical method for measurement of dioxygen concentration based upon quenching of phosphorescence. *J Biol Chem* **262**, 5476-5482 (1987).
15. Helmlinger, G., Yuan, F., Dellian, M. & Jain, R.K. Interstitial pH and pO₂ gradients in solid tumors in vivo: high-resolution measurements reveal a lack of correlation. *Nat Med* **3**, 177-182 (1997).
16. Torres Filho, I.P. & Intaglietta, M. Microvessel PO₂ measurements by phosphorescence decay method. *Am J Physiol* **265**, H1434-1438 (1993).
17. Tsai, A.G., *et al.* Microvascular and tissue oxygen gradients in the rat mesentery. *Proc Natl Acad Sci U S A* **95**, 6590-6595 (1998).

18. Brown, E.B., *et al.* In vivo measurement of gene expression, angiogenesis and physiological function in tumors using multiphoton laser scanning microscopy. *Nat Med* **7**, 864-868 (2001).
19. Denk, W., Strickler, J.H. & Webb, W.W. Two-photon laser scanning fluorescence microscopy. *Science* **248**, 73-76 (1990).
20. Helmchen, F. & Denk, W. Deep tissue two-photon microscopy. *Nat Methods* **2**, 932-940 (2005).
21. Zipfel, W.R., Williams, R.M. & Webb, W.W. Nonlinear magic: multiphoton microscopy in the biosciences. *Nat Biotechnol* **21**, 1369-1377 (2003).
22. Xu, C., Zipfel, W., Shear, J.B., Williams, R.M. & Webb, W.W. Multiphoton fluorescence excitation: new spectral windows for biological nonlinear microscopy. *Proc Natl Acad Sci U S A* **93**, 10763-10768 (1996).
23. Centonze, V.E. & White, J.G. Multiphoton excitation provides optical sections from deeper within scattering specimens than confocal imaging. *Biophys J* **75**, 2015-2024 (1998).
24. Lakowicz, J.R. *Principles of fluorescence spectroscopy*, (Kluwer Academic/Plenum, New York, 1999).
25. Gratton, E., Breusegem, S., Sutin, J., Ruan, Q. & Barry, N. Fluorescence lifetime imaging for the two-photon microscope: time-domain and frequency-domain methods. *J Biomed Opt* **8**, 381-390 (2003).
26. McGraw, C.M.K., Gamal; Callis, James B. **Comparison of time and frequency domain methods for luminescence lifetime measurements.** *Journal of Physical Chemistry C* **112**, 8079-8084 (2008).
27. Sytsma J., V.J.M., de Grauw C.J., Gerritsen H.C. Time-gated fluorescence lifetime imaging and microvolume spectroscopy using two-photon excitation. *Journal of Microscopy* **191**, 39-51 (1998).
28. Becker, W., *et al.* Fluorescence lifetime imaging by time-correlated single-photon counting. *Microsc Res Tech* **63**, 58-66 (2004).
29. Krishnan, R.V., Masuda, A., Centonze, V.E. & Herman, B. Quantitative imaging of protein-protein interactions by multiphoton fluorescence lifetime imaging microscopy using a streak camera. *J Biomed Opt* **8**, 362-367 (2003).
30. Pelet, S., *et al.* Frequency domain lifetime and spectral imaging microscopy. *Microsc Res Tech* **69**, 861-874 (2006).
31. Kruk, M.K., Aliaksandr; Drobizhev, Mikhail; Kuzmitsky, Valery; Gael, Vladimir; Rebane, Aleksander. Two-photon absorption of tetraphenylporphyrin free base. *Journal of Luminescence* **105**, 45-55 (2003).
32. Brown, E.B., Wu, E.S., Zipfel, W. & Webb, W.W. Measurement of molecular diffusion in solution by multiphoton fluorescence photobleaching recovery. *Biophys J* **77**, 2837-2849 (1999).
33. Estrada, A.D., Ponticorvo, A., Ford, T.N. & Dunn, A.K. Microvascular oxygen quantification using two-photon microscopy. *Opt Lett* **33**, 1038-1040 (2008).
34. Pawley, J.B. *Handbook of biological confocal microscopy*, (Springer, New York, NY, 2006).
35. Muller, M., Squier, J., Wolleschensky, R., Simon, U. & Brakenhoff, G.J. Dispersion pre-compensation of 15 femtosecond optical pulses for high-numerical-aperture objectives. *J Microsc* **191**, 141-150 (1998).
36. Dunphy, I., Vinogradov, S.A. & Wilson, D.F. Oxyphor R2 and G2: phosphors for measuring oxygen by oxygen-dependent quenching of phosphorescence. *Anal Biochem* **310**, 191-198 (2002).

CHAPTER 3

37. Lo, L.W., Koch, C.J. & Wilson, D.F. Calibration of oxygen-dependent quenching of the phosphorescence of Pd-meso-tetra (4-carboxyphenyl) porphine: a phosphor with general application for measuring oxygen concentration in biological systems. *Anal Biochem* **236**, 153-160 (1996).
38. Lakowicz, J.R. *Topics in fluorescence spectroscopy: Nonlinear and two-photon induced fluorescence.*, (Plenum Press, New York, 1997).
39. Zipfel, W.R., *et al.* Live tissue intrinsic emission microscopy using multiphoton-excited native fluorescence and second harmonic generation. *Proc Natl Acad Sci U S A* **100**, 7075-7080 (2003).
40. G. Zizak, J.B., and J. Winefordner. Rate equation solution for the temporal behavior of a three-level system. *Appl. Opt.* **19**, 3631-3639 (1980).
41. Fadeev, V.V.D., T.A.; Filippova, E.M.; Chubarov, V.V. Source. Saturation spectroscopy as a method for determining the photophysical parameters of complicated organic compounds. *Optics Communications* **166**, 25-33 (1999).
42. Lewis, G.N., Calvin, M., Kasha, M. Photomagnetism, Determination of the Paramagnetic Susceptibility of a Dye in Its Phosphorescent State. *Journal of Chemical Physics* **17**, 804-812 (1949).
43. Baev, A., Rubio-Pons, O., Gel'mukhano, F. & Agren, H. Optical Limiting Properties of Zinc- and Platinum-Based Organometallic Compounds. *The Journal of Physical Chemistry A* **108**, 7406-7416 (2004).
44. Papkovsky, D.B. Methods in optical oxygen sensing: protocols and critical analyses. *Methods Enzymol* **381**, 715-735 (2004).
45. Oxtoby, D.W., Gillis, H.P. & Nachtrieb, N.H. *Principles of modern chemistry*, (Saunders College Pub., Fort Worth, 1999).
46. Lo, L.W., Vinogradov, S.A., Koch, C.J. & Wilson, D.F. A new, water soluble, phosphor for oxygen measurements in vivo. *Adv Exp Med Biol* **428**, 651-656 (1997).
47. Torres Filho, I.P., Leunig, M., Yuan, F., Intaglietta, M. & Jain, R.K. Noninvasive measurement of microvascular and interstitial oxygen profiles in a human tumor in SCID mice. *Proc Natl Acad Sci U S A* **91**, 2081-2085 (1994).
48. Zheng, L., Golub, A.S. & Pittman, R.N. Determination of PO₂ and its heterogeneity in single capillaries. *Am J Physiol* **271**, H365-372 (1996).
49. Tao, Z., Goodisman, J. & Soudi, A.K. Oxygen measurement via phosphorescence: reaction of sodium dithionite with dissolved oxygen. *J Phys Chem A* **112**, 1511-1518 (2008).
50. Donnert, G., *et al.* Macromolecular-scale resolution in biological fluorescence microscopy. *Proc Natl Acad Sci U S A* **103**, 11440-11445 (2006).
51. Morantz, D.J., White, B.G. & Wright, A.J.C. Phosphorescence and Stimulated Emission in Organic Molecules. *The Journal of Chemical Physics* **37**, 2041-2048 (1962).
52. Milonni, P.W. & Eberly, J.H. *Lasers*, (Wiley, New York, 1988).
53. Truskey, G.A., Yuan, F. & Katz, D.F. *Transport phenomena in biological systems*, (Pearson/Prentice Hall, Upper Saddle River, N.J., 2004).
54. Tsai, A.G., Johnson, P.C. & Intaglietta, M. Oxygen gradients in the microcirculation. *Physiol Rev* **83**, 933-963 (2003).
55. Kleinfeld, D., Mitra, P.P., Helmchen, F. & Denk, W. Fluctuations and stimulus-induced changes in blood flow observed in individual capillaries in layers 2 through 4 of rat neocortex. *Proc Natl Acad Sci U S A* **95**, 15741-15746 (1998).

56. Leunig, M., *et al.* Angiogenesis, microvascular architecture, microhemodynamics, and interstitial fluid pressure during early growth of human adenocarcinoma LS174T in SCID mice. *Cancer Res* **52**, 6553-6560 (1992).
57. Vinogradov, S.A., *et al.* Noninvasive imaging of the distribution in oxygen in tissue in vivo using near-infrared phosphors. *Biophys J* **70**, 1609-1617 (1996).
58. Wilson, D.F., *et al.* Oxygen distributions within R3230Ac tumors growing in dorsal flap window chambers in rats. *Adv Exp Med Biol* **454**, 603-609 (1998).
59. Vinogradov, S.A.F.-S., M.A.; Dugan, B.W.; Wilson, D.F. Frequency domain instrument for measuring phosphorescence lifetime distributions in heterogeneous samples. *Review of Scientific Instruments* **72**, 3396-3406 (2001).
60. Churchill-Davidson, I., Sanger, C. & Thomlinson, R.H. Oxygenation in radiotherapy. II. Clinical application. *Br J Radiol* **30**, 406-422 (1957).
61. Suit, H.D. Application of radiobiologic principles to radiation therapy. *Cancer* **22**, 809-815 (1968).
62. Tsai, A.G., Cabrales, P., Winslow, R.M. & Intaglietta, M. Microvascular oxygen distribution in awake hamster window chamber model during hyperoxia. *Am J Physiol Heart Circ Physiol* **285**, H1537-1545 (2003).
63. Krogh, A. The number and distribution of capillaries in muscles with calculations of the oxygen pressure head necessary for supplying the tissue. *J Physiol* **52**, 409-415 (1919).
64. Krogh, A. *The anatomy and physiology of capillaries*, (Hafner Pub. Co., New York,, 1959).
65. Conley, K.E. & Jones, C. Myoglobin content and oxygen diffusion: model analysis of horse and steer muscle. *Am J Physiol* **271**, C2027-2036 (1996).
66. Ellis, C.G., Potter, R.F. & Groom, A.C. The Krogh cylinder geometry is not appropriate for modelling O₂ transport in contracted skeletal muscle. *Adv Exp Med Biol* **159**, 253-268 (1983).
67. Grinberg, O., Novozhilov, B., Grinberg, S., Friedman, B. & Swartz, H.M. Axial oxygen diffusion in the Krogh model: modifications to account for myocardial oxygen tension in isolated perfused rat hearts measured by EPR oximetry. *Adv Exp Med Biol* **566**, 127-134 (2005).
68. Pogue, B.W., Paulsen, K.D., O'Hara, J.A., Wilmot, C.M. & Swartz, H.M. Estimation of oxygen distribution in RIF-1 tumors by diffusion model-based interpretation of pimonidazole hypoxia and eppendorf measurements. *Radiat Res* **155**, 15-25 (2001).
69. Schubert, R.W. & Zhang, X. The equivalent Krogh cylinder and axial oxygen transport. *Adv Exp Med Biol* **411**, 191-202 (1997).
70. Plotnikov, S.V., Millard, A.C., Campagnola, P.J. & Mohler, W.A. Characterization of the myosin-based source for second-harmonic generation from muscle sarcomeres. *Biophys J* **90**, 693-703 (2006).
71. Tyrrell, J.A., *et al.* Robust 3-D modeling of vasculature imagery using superellipsoids. *IEEE Trans Med Imaging* **26**, 223-237 (2007).
72. Tyrrell, J.A., *et al.* A 2-D/3-D model-based method to quantify the complexity of microvasculature imaged by in vivo multiphoton microscopy. *Microvasc Res* **70**, 165-178 (2005).
73. Marsh, R.L. & Ellerby, D.J. Partitioning locomotor energy use among and within muscles. Muscle blood flow as a measure of muscle oxygen consumption. *J Exp Biol* **209**, 2385-2394 (2006).
74. Urbanchek, M.G., Picken, E.B., Kalliainen, L.K. & Kuzon, W.M., Jr. Specific force deficit in skeletal muscles of old rats is partially explained by the existence of denervated muscle fibers. *J Gerontol A Biol Sci Med Sci* **56**, B191-197 (2001).

CHAPTER 3

75. Brinas, R.P., Troxler, T., Hochstrasser, R.M. & Vinogradov, S.A. Phosphorescent oxygen sensor with dendritic protection and two-photon absorbing antenna. *J Am Chem Soc* **127**, 11851-11862 (2005).
76. Finikova, O.S., *et al.* Oxygen microscopy by two-photon-excited phosphorescence. *Chemphyschem* **9**, 1673-1679 (2008).
77. McLaurin, E.M.G., A.B.; Bawendi, M.G.; Nocera, D.G. Two-Photon Absorbing Nanocrystal Sensors for Ratiometric Detection of Oxygen. *JACS* (2009).
78. Berland, K. & Shen, G. Excitation saturation in two-photon fluorescence correlation spectroscopy. *Appl Opt* **42**, 5566-5576 (2003).
79. Bertuglia, S., Colantuoni, A., Coppini, G. & Intaglietta, M. Hypoxia- or hyperoxia-induced changes in arteriolar vasomotion in skeletal muscle microcirculation. *Am J Physiol* **260**, H362-372 (1991).
80. Joachimsson, P.O., *et al.* Adverse effects of hyperoxemia during cardiopulmonary bypass. *J Thorac Cardiovasc Surg* **112**, 812-819 (1996).
81. Kindig, C.A., Howlett, R.A. & Hogan, M.C. Effect of extracellular PO₂ on the fall in intracellular PO₂ in contracting single myocytes. *J Appl Physiol* **94**, 1964-1970 (2003).
82. Poole, D.C., Behnke, B.J., McDonough, P., McAllister, R.M. & Wilson, D.F. Measurement of muscle microvascular oxygen pressures: compartmentalization of phosphorescent probe. *Microcirculation* **11**, 317-326 (2004).
83. Wilson, D.F., *et al.* Oxygen pressures in the interstitial space and their relationship to those in the blood plasma in resting skeletal muscle. *J Appl Physiol* **101**, 1648-1656 (2006).
84. Brown, E., *et al.* Dynamic imaging of collagen and its modulation in tumors in vivo using second-harmonic generation. *Nat Med* **9**, 796-800 (2003).

IV. *In vivo* high-resolution three-dimensional quantification of pO₂ in solid tumors

Parts of this chapter will be published:

Lanning RL, Brown EB, Padera TP, Fukumura D, and Jain RK

Manuscript in Preparation

IV.1 Introduction and Motivation

In solid tumors, the amount of oxygen in the microenvironment plays an important role in progression and response to therapy. Tumors are typically characterized by low oxygen tension, i.e. hypoxia^{1,2}: pO₂ values less than 10-15mmHg in tissue. In the clinic, increased hypoxic fraction has been linked to poor prognosis³⁻⁶. Additional studies have shown a high degree of correlation with hypoxia and metastatic potential⁷⁻¹⁰. In fact, it has been demonstrated that hypoxia promotes the selection of tumor cells with reduced apoptotic potential¹¹. Hypoxia has been shown to independently regulate gene expression including the hypoxia inducible factor (HIF-1 and -2) pathways¹²⁻¹⁴ and the family of angiogenic promoters, vascular endothelial growth factors (VEGF)^{15,16}. Even microscopic tumors once considered too small to be hypoxic, have been shown to have significant hypoxia in some disease states^{17,18}. The degree of hypoxia also directly impacts the formation of the abnormal and irregular tumor vascular networks¹⁹. Recent work indentifying tumor stem cells has also suggested hypoxia may play an important role in maintenance of these cell populations and their gene expression²⁰.

While levels of oxygen in tumors may impact many aspects of tumor progression, one of the most clinically important is response to therapy. It is well known that oxygen sensitizes a tissue to radiation²¹. Therefore, hypoxia in tumors is protective against radiotherapy, particularly if cancer stem cells are immune to such treatments¹⁹. Furthermore, many chemotherapeutics demonstrate reduced cytotoxicity in low oxygen environments²². Initially, it was believed that targeting the tumor vasculature through antiangiogenic therapy would starve the tumor of its blood supply. However, in the last decade, antiangiogenic therapy as a single agent has produced limited success in both animal models and patients^{23,24}. Since oxygen sensitizes a tissue to radiation, one would expect antiangiogenic agents and radiotherapy to be antagonistic. Interestingly, it has been demonstrated that certain antiangiogenic therapies coupled with radiation treatment can produce synergistic results²⁵⁻²⁸. Additionally, antiangiogenic therapy coupled with certain chemotherapeutics has demonstrated increased efficacy in

colorectal and lung cancer patients over either individual treatment^{29,30}. Antiangiogenic therapy may prune the immature and inefficient tumor blood vessels improving perfusion and potentially “normalizing” the metabolic microenvironment including pO_2 ³¹⁻³⁴. A “normalized” tumor microenvironment with increased pO_2 may sensitize the tumor to radiation and maximize cytotoxicity of certain chemotherapeutics.

To realize the full potential of this concept, it is important to gain a deeper understanding of the spatial and temporal changes in tumor pO_2 during disease progression and treatment. Previous techniques for measuring pO_2 *in vivo* were constrained by the significant spatio-temporal heterogeneities found in tumors^{35,36}. These techniques also demonstrated limitations in their tissue penetration, depth resolution, spatial resolution and all lacked true three-dimensional resolution³⁷⁻³⁹. In addition, some methods are invasive and lack the ability to perform measurements in real-time⁴⁰. Multiphoton phosphorescence quenching microscopy (Chapter 3) eliminates many of these constraints, providing a new opportunity to probe the pO_2 of the tumor microenvironment. Therefore, in this Chapter, I will demonstrate the application of MP-PQM to multiple tumor models during progression and treatment.

IV.2 Oxygen Profiles in Solid Tumors

The application of MP-PQM to the measurement of pO_2 in the microenvironment of tumors implanted in window chamber models allows characterization of three-dimensional interstitial oxygen profiles. Up to 400 μ m deep, pO_2 profiles from single vessels in a human melanoma (MU89) xenotransplant in SCID mice were obtained. These were compared to similarly sized vessels (10-20 μ m in diameter) in the skin of mock-transplanted chamber mice (**Figure IV-1**). A distinct separation between the pO_2 level in normal tissue vascular oxygen profiles and those in tumors was readily apparent. The mean intravascular pO_2 (distance = 0 μ m) between normal (49.1 ± 5.5 mmHg) and tumor (19.2 ± 3.4 mmHg) vessels was statistically different (P -value $\ll 0.05$). However, the mean oxygen gradients over the lengths of the profiles were not found to be

different. This suggests that *in vivo* oxygen consumption of the melanoma tumor cells was very similar to that found in normal tissue.

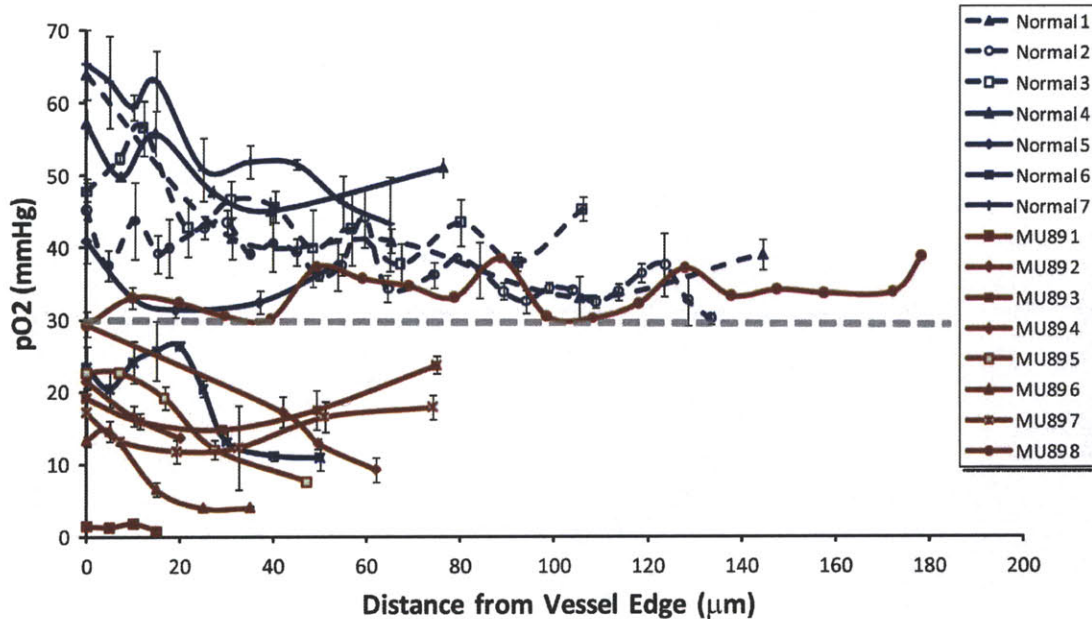


Figure IV-1 Vascular oxygen profiles from similarly sized vessels in tumors and normal tissue. pO_2 profiles from normal murine skin are depicted in blue. Profiles from single vessels in a human melanoma xenograft (MU89) are shown in red. The dashed grey line indicates the separation in oxygen level between normal and neoplastic tissue. The dashed blue profiles in normal tissue were carried out beyond $\sim 80\mu m$ through the use of nanovascular surgery to cauterize nearby vessels.

In melanomas, oxygen profiles longer than $70\mu m$ were readily measurable due to increased intervascular spacing. However, in normal tissues, vessels are spaced relatively close together, often negating any gradient due to oxygen consumption. To obtain such profiles, I performed nanovascular surgery⁴¹⁻⁴³ using the multiphoton excitation laser on vessels nearby the target vessel. Exposure to 1 or 2 high average power (80-100mW) line scans across the diameter of the vessel induced clotting and ceased perfusion beyond the point of claudication (**Figure IV-2**). Using this technique, pO_2 profiles out to $\sim 200\mu m$ were measurable (**Figure IV-1** – dashed blue). Nonetheless, oxygen diffusion from vessels located nearby in three-dimensional space still contributed to a higher oxygen tension than that found in the tumor vascular profiles. This suggests that the vascular architecture in such normal tissues provides better metabolic (pO_2) support for the tissue.

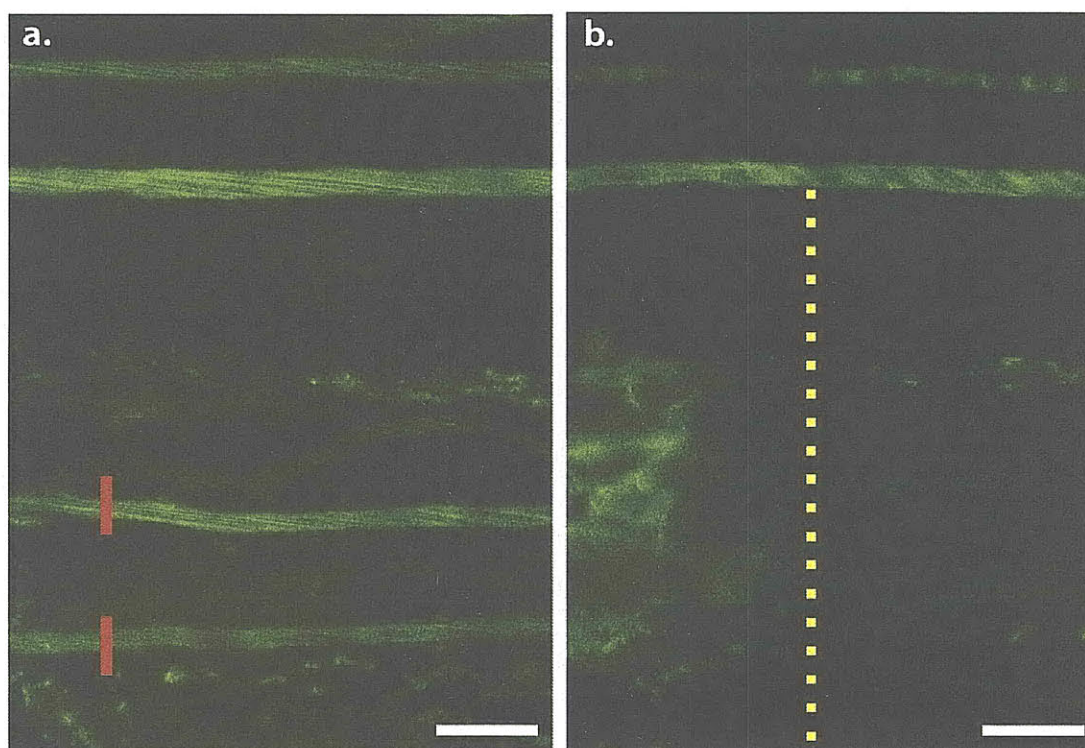


Figure IV-2 Nanovascular surgery using multiphoton microscopy. (a). In order to obtain extended interstitial oxygen profiles in normal murine skin, nearby perfused vessels were cauterized using the multiphoton excitation laser (red). The principles of multiphoton excitation limited the tissue damage to only a small three-dimensional space around the blood vessels. (b) After nanosurgery was performed some extravasated angiographic marker was visible. However, beyond this point perfusion and therefore oxygen delivery was limited permitting longer oxygen profiles to be measured (yellow).

While the measurement of oxygen profiles from single vessels is possible in three-dimensions using MP-PQM, in tumors heterogenous temporal variations in flow limit repeatable measurements. Often times during the collection of a single vascular oxygen profile (5-10minutes), the vessel would undergo transient blockage due to changes in red blood cell flux. This temporarily lowered measured pO_2 in the interstitial space due to cellular consumption and reduced supply of oxygen. Once the blockage was freed, the interstitial space was reoxygenated and pO_2 levels increased. Many other investigators have observed this effect in tumors on both a single vessel and macroscopic scale⁴⁴⁻⁴⁶. Vascular supply fluctuations precluded the use of local vascular oxygen profiles to assess the dynamics of pO_2 in the microenvironment during tumor progression and treatment.

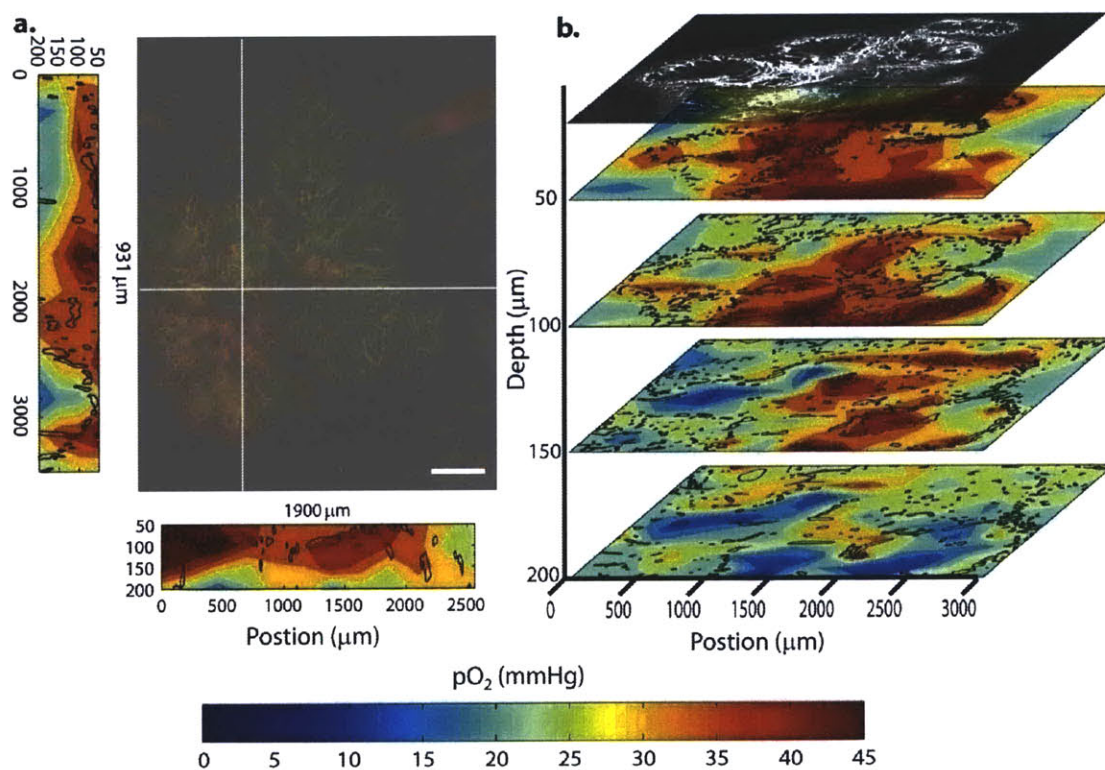


Figure IV-3 Three-dimensional mapping of tumor oxygenation using MP-PQM. (a). Axial cross-sections through the tumor are shown along vertical and horizontal planes. A depth projection of multiphoton angiography of the tumor vascular network is illustrated relative to the cross-section. Color denotes depth (green-red-white). (b). Oxygen tension maps at four different depths within the tumor. The angiographic depth slice at 50 μm is shown for comparison with the oxygen map. Black outlines on the maps indicate the morphometry of the tumor vessels. Scale Bar - 500 μm.

IV.3 Three-dimensional Mapping of Tumor Oxygenation

The technique of MP-PQM allows measurement of pO₂ at single points confined to the three-dimensional excitation volume of the multiphoton microscope. To quantify the oxygenation in the tumor microenvironment in preclinical models and assess the spatial heterogeneity in pO₂, I chose to collect *in vivo* measurements along a grid at multiple depths (**Figure IV-3**). This process reduced the effects of temporal fluctuations in pO₂ observed with single vessel oxygen profiles. Further, it allowed oxygen measurements to be performed with multiphoton angiography. Correlation of the tumor vasculature and pO₂ in three-dimensions throughout the tumor were then possible.

Table IV-1: Correlation of pO₂ with vessel diameter (d) or interstitial distance (r) across multiple tumors. Bold Pearson's correlation coefficients denote significant difference (*P*-value < 0.05) from no correlation (0). *N* - Number of animals in each group.

Day	EO771		MDA-MB-361HK		LS174T		MCAIV-DSC		MCAIV-MFP	
	d	r	d	r	d	r	d	r	d	r
0	-0.003	-0.27	0.069	-0.33	0.014	-0.25	0.18	-0.47	0.066	-0.39
3	-0.046	-0.29	0.029	-0.47	-0.034	-0.42	0.31	-0.39	0.014	-0.34
6	0.045	-0.26	0.047	-0.37	0.022	-0.39	0.22	-0.41	0.036	-0.39
9	-0.14	-0.33	-0.023	-0.31	0.048	-0.61	0.074	-0.39		
	<i>N</i> = 4		<i>N</i> = 8-10		<i>N</i> = 6-10		<i>N</i> = 5-6		<i>N</i> = 2	

IV.3a CORRELATION OF PO₂ AND VASCULAR METRICS

Tumor oxygenation has been shown to depend on the vascular network parameters including geometry and function^{47,48}. *In vivo* interstitial measurements have demonstrated that pO₂ generally decreases with increasing distance from the vessel wall^{35,49}. One of these studies also showed that there is no correlation between tumor vessel diameter and intravascular pO₂. However, all of these measurements have been based on single vascular profiles or limited to intravascular measurements. Any studies that have assessed the global oxygenation of a solid tumor have either relied on mathematical modeling or state that their measurements are intravascular³⁶. No study to date has compared real-time microscopic measurements of pO₂ directly with the tumor vascular network over macroscopic regions.

Using MP-PQM, I was able to obtain oxygen tension maps and high-resolution angiography during the same measurement period. Data was collected over large regions (~16mm²) and up to 350μm in depth across multiple tumor types. pO₂ measurements were collected at single points over a grid spaced at 100-200μm. Vascular metrics, including diameter and length, from the three-dimensional multiphoton angiography were determined using a semi-automatic tracing algorithm⁵⁰. The Euclidean three-dimensional distance ($r^2 = \Delta x^2 + \Delta y^2 + \Delta z^2$) from each measurement point to the closest vessel was determined over the entire oxygen map.

Table IV-2 Correlation of pO₂ with vessel diameter (d) and interstitial distance (r) in normal tissues. Bold Pearson's correlation coefficients denote significant difference (*P*-value < 0.05) from no correlation (0). *N* - Number of animals in each group.

	d	r	<i>N</i>
Skin	0.37	-0.096	4
MFP	0.13	0.067	2
Brain Cortex	0.15	0.014	3

Across all tumor types, a significant negative correlation was found between distance to closest vessel and pO₂ (Table IV-1). The Pearson's correlation coefficients remained relatively constant over 9 days of tumor growth for all tumor types except LS174T. The human colorectal adenocarcinoma (LS174T) implanted in the DSC increased to a maximum correlation of 0.61 by day 9. These correlation were much higher than those found in normal skin, mammary fat pad (MFP) and cortical brain, where the pO₂ was less correlated with distance from nearest vessel (Table IV-2). As will be seen, in normal skin, cortex and mammary fat pad an oxygen gradient from the vessel wall is nearly non-existent in three-dimensions. The difference in vascular network structure is notable between normal MFP tissue and an orthotopic murine mammary carcinoma (EO771; Figure IV-1a and b). Oxygen tension measured at random locations in the EO771 tumor demonstrated a decrease with distance to nearest vessel, while in normal MFP it remained constant (Figure IV-4c).

At first glance, these results may seem counter to previous interstitial *in vivo* pO₂ studies. However, many of those were performed in the stretched rodent abdominal mesentery^{51,52}, which is essentially a two-dimensional tissue. Interstitial oxygen gradients and correlation between oxygen tension and distance have been reported in skeletal muscle⁵³ and cortical brain⁵⁴, which are representative of three-dimensional vascular networks (> 200 μm thick tissues). In muscle, oxygen gradients and therefore a correlation with distance from blood vessel exist due to consumption by the muscle fibers⁵⁵. I demonstrated that such gradients can exist in murine skin skeletal muscle due to increased oxygen consumption in Section III6b. In cortical brain, the authors of the

previous study note that it was very difficult to find locations where gradients existed, suggesting they are limited under normal conditions.

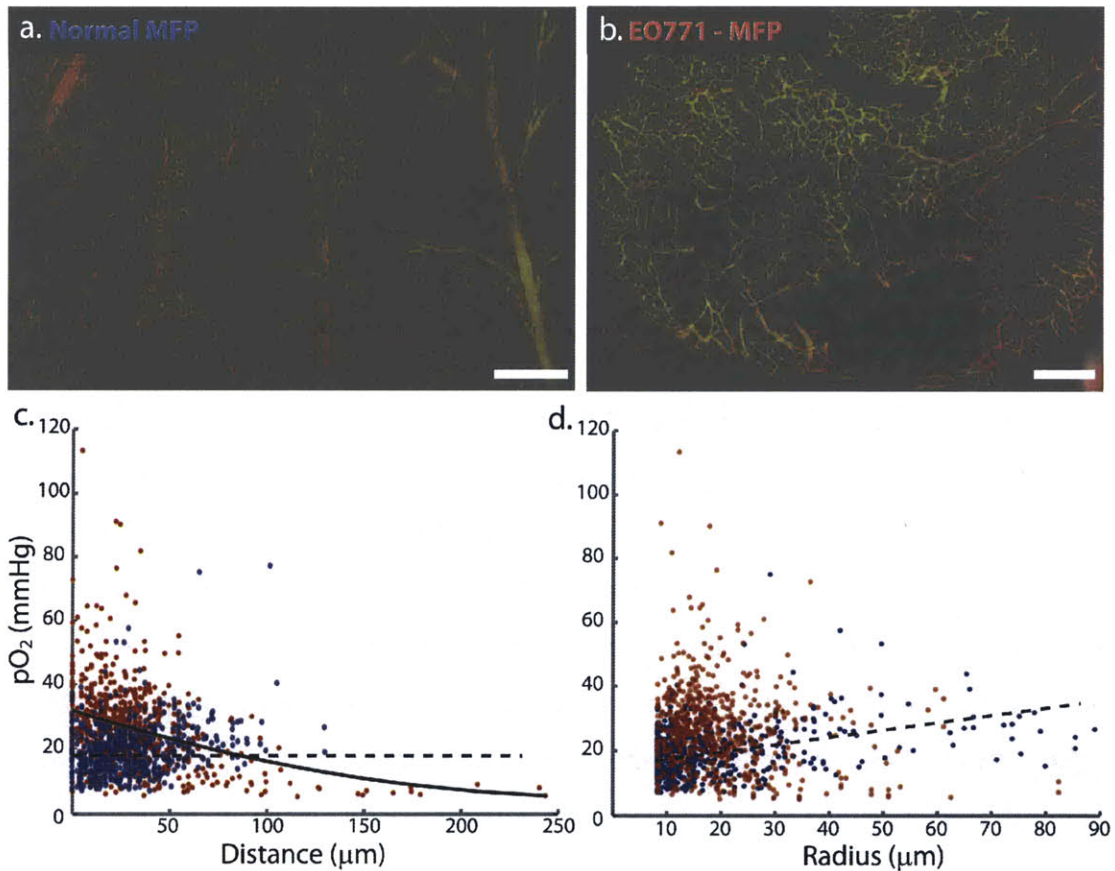


Figure IV-4 Correlation of pO₂ with vascular metrics. (a) Angiographic depth projection of the vasculature in the normal mammary fat pad of a female SCID mouse. (b) Vascular network of an orthotopic murine mammary carcinoma (EO771). (c) Spatial correlation of tumor pO₂. Normal tissue in the MFP shows no correlation with distance to the closest vessel (dashed line). Tumor vascular networks demonstrate a negative correlation with pO₂ and distance to nearest vessel (solid line). (d) Conversely, in normal tissues pO₂ demonstrates a positive correlation with vessel diameter, while measurements in tumors do not display any correlation. c and d: ● - normal ● - tumor. Scale Bars - 500μm.

It is well known that vascular oxygen tension is highly correlated with vessel diameter in both the arterial and venular branches⁵⁶. Phosphorescence quenching microscopy experiments in rodent skin have demonstrated longitudinal pO₂ gradients following the branches of the arterial network – the smaller the vessel diameter, the lower the oxygen⁵⁷. The proposed source of the longitudinal gradients is two-fold. First is that the vascular wall endothelial cells consume oxygen and larger vessels with thicker walls

consume more oxygen^{52,53}. Second, the capillaries are not the sole source of oxygen diffusion to tissue. Instead larger arterioles also supply oxygen to the tissue which have also been shown to play a significant role in the modulation of blood transport to tissue⁵⁶.

Three-dimensional measurements in both the intravascular and interstitial space in murine skin, mammary fat pad and cortex revealed significant correlation of pO_2 with vascular diameter (**Table IV-2**). All normal tissue demonstrated Pearson's coefficients greater than 0.1, however murine skin displayed the largest correlation (0.37). In the neoplastic tissues studied in **Table IV-1**, only MCalV, a murine mammary carcinoma, demonstrated significant correlation of oxygen tension with vessel diameter. All other murine tumor models had non-significant Pearson's correlation coefficients: typically less than 0.05. Supporting these results, previous studies performed in a human colorectal adenocarcinoma xenograft (LS174T) demonstrated no correlation with tumor vessel diameter^{35,49}. In most cases, the heterogeneous structure and morphometry of tumor vascular networks abrogate the normal transport of oxygen to the tissue⁵⁸⁻⁶⁰. The irregular geometry and heterogeneous flow patterns in tumor vasculature uncouple the normal dependence of tissue pO_2 on vascular diameter. The murine mammary carcinoma EO771 demonstrates these effects quite well in comparison to normal murine MFP (**Figure IV-4d**).

The unusual result from the MCalV mammary carcinoma may be explained by the ectopic microenvironment (dorsal skin) providing better oxygen supply or inducing the formation of a more efficient network. Fractal analysis of the tumor vascular network of MCalV in the DSC demonstrated a significant difference from normal skin and increased tortuosity (decreased transport efficiency)⁶¹. This suggests that increased efficiency is not likely the reason for increased correlation. Interestingly, the same tumor type implanted in the mammary fat pad exhibited no correlation with tumor vessel diameter throughout tumor growth (**Table IV-2: MCalV-MFP**). This is further confounded by the fact that both locations exhibit tumors with similar mean diameter vessels (~54 μ m for

DSC and $\sim 68\mu\text{m}$ for MFP) for tumors of equal volume. Therefore differences in the tissue microenvironment and vascular supply must account for the increased correlation in the DSC.

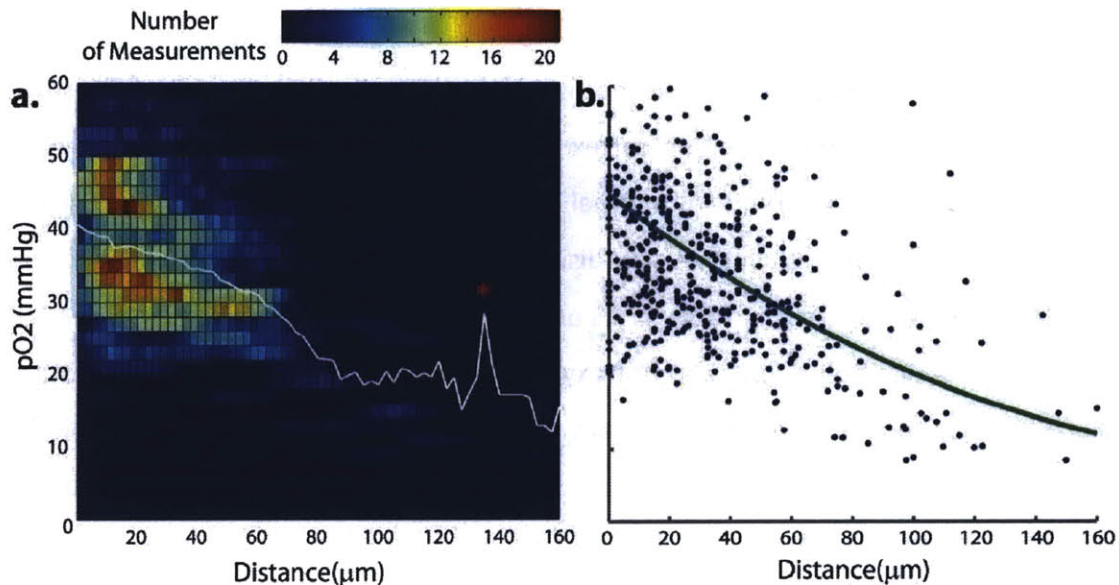


Figure IV-5 Tumor oxygen profiles and consumption. (a). Histogram of the number of measurements for a given oxygen tension at a given distance to the nearest vessel. The mean $p\text{O}_2$ profile is overlaid (white) illustrating the gradient in oxygen with distance. The effect of oxygen diffusion from vessels outside the mosaic image volume ($\sim 4 \times 4 \times 0.3\text{mm}$) is noticeable at farther distances (*). (b). Zero-order diffusion-reaction fit (green) to the $p\text{O}_2$ data in a to determine the oxygen consumption.

IV.3b TUMOR OXYGEN CONSUMPTION

The increased correlation in solid tumors between $p\text{O}_2$ and distance to nearest vessel is due both to vascular architecture and increased tissue oxygen consumption. The large avascular spaces found in most tumors coupled with the high metabolic activity of the tumors cells reduce the oxygen concentration. In reality, energy metabolism in tumors is a complex process dependent on the metabolites (oxygen and glucose) available^{48,62,63}. However, to a first approximation the decreasing level of oxygen in tumor tissue with increasing distance from the vasculature (Figure IV-5a) can be assumed to result from oxidative respiration.

Oxygen metabolism follows Michaelis-Menten kinetics in biological tissues. However, above very low oxygen concentrations, the reaction can be approximated as zero-order

kinetics⁶⁴. In this situation, the oxygen consumption was assumed to be constant at all points from the blood vessels. While the actual measurements are three-dimensional in nature, I estimated average tissue oxygen consumption for the entire tumor volume measured using a one-dimensional first-order diffusion-reaction model.

$$D_{O_2} S \frac{d^2 pO_2}{dr^2} - Q_{O_2} = 0 \quad (IV.1)$$

Here D_{O_2} is the diffusion of oxygen ($2 \times 10^{-5} \text{ cm}^2 \text{ s}^{-1}$)⁶⁵, S is the solubility of oxygen in tumor tissue ($2.05 \times 10^{-5} \text{ ml}_{O_2} \text{ cm}^{-3}$)⁶⁶, r is the three-dimensional Euclidean distance to the closest tumor vessel and Q_{O_2} is the oxygen consumption rate in $\text{ml}_{O_2} \text{ cm}^{-3} \text{ s}^{-1}$. The following boundary conditions were used to solve Equation (IV.1): pO_2 at $r = 0$ is equal to the oxygen tension within the vessel ($pO_{2_{vessel}}$) and the solution reaches a minimum ($\left. \frac{dpO_2}{dr} \right|_{r=r_{crit}} = 0$) pO_2 at some critical distance ($pO_{2_{min}}$) from the blood vessel. The solution is of the form of a second order polynomial.

$$pO_2(r) = \frac{Q_{O_2}}{2DS} r^2 - \sqrt{\frac{2Q_{O_2}(pO_{2_{vessel}} - pO_{2_{min}})}{DS}} r + pO_{2_{vessel}} \quad (IV.2)$$

The values of $pO_{2_{vessel}}$ and $pO_{2_{min}}$ were independently determined for each tumor and timepoint from the scatter plot of oxygen tension versus distance from nearest vessel (**Figure IV-5b**).

Table IV-3: Mean oxygen consumption across tumor types. Bold values indicate a significant difference from all other tumors for a given tumor at a specific timepoint.

	EO771	MDA-MB-361HK	LS174T	MCAIV-DSC	MCAIV-MFP
Day	$Q_{O_2} (\text{ml}_{O_2} \text{ cm}^{-3} \text{ s}^{-1} \times 10^{-5})$				
0	6.55±2.04	1.25±0.22	2.94±0.68	7.03±1.99	1.15±0.98
3	4.85±4.32	2.15±0.03	2.05±0.54	8.19±2.81	3.82±0.38
6	2.71±1.27	2.20±0.62	4.37±1.10	5.53±1.91	5.89±4.21
9	1.21±0.47	0.96±0.49	3.80±0.66	5.86±1.74	
ANOVA	0.251	0.44	0.049	0.526	
	<i>N</i> = 4	<i>N</i> = 8-10	<i>N</i> = 6-10	<i>N</i> = 5-6	<i>N</i> = 2

I determined the mean tumor oxygen consumption during progression across multiple tumor types and sites (Table IV-3). Previous *in vivo* measurements have all reported *local* oxygen consumption rates determined from radial vessel profiles^{24,67}. To the best of my knowledge, this is the first time that oxygen consumption has been calculated from pO_2 measurements throughout large regions of the tumor. At day 0 all tumors were approximately 4mm in diameter by enface measurement. Only the oxygen consumption of the MDA-MB-361HK tumor was significantly lower than all the other tumor types. The two murine mammary carcinomas (EO771 and MCalV) were more metabolically (aerobically) active than the other tumor types, although the difference was not significant. During tumor growth, the orthotopic EO771 murine mammary carcinoma trended toward lower oxygen consumption. The Q_{O_2} for the LS174T tumors significantly increased over time. The oxygen consumption of the other tumor types remained relatively constant during tumor progression with MCalV in the dorsal skinfold chamber demonstrating consistently higher Q_{O_2} . The range of values determined in this study were similar to those found previously for a different tumor type using profiles from single vessels²⁴.

Assessment of tumor oxygen consumption using this method is an approximation. At low, very hypoxic levels ($pO_2 < 5\text{mmHg}$), the reaction rate is first order, thus dependent on the concentration of oxygen available^{48,64}. Hypoxic regions are often found in the microenvironment of tumors including adjacent to vessels (typically with low intravascular pO_2). Additionally, the diffusion-reaction model is semi one-dimensional. Using a two-dimensional model (x and z), Dewhirst *et al* calculated oxygen consumption rates about 50% smaller than with the one-dimensional model⁶⁷. Since the radial distance from the nearest blood vessel was used in this experiment a cylindrical model could be applied^{47,68}. However, this would not be ideal in the irregular and heterogeneous vascular network found in tumors. Secondly, endothelial cells in normal vessels have been shown to consume oxygen across the vessel wall leading to sharp transverse gradients⁶⁹. Given the abnormal structure of tumor vessels on the cellular level^{70,71}, it is unclear if such gradients exist which would lead to loss of oxygen longitudinally. Finally, although MP-PQM is a three-dimensional imaging technique it is constrained by collection time from larger wide-field imaging. Further, due to signal to

noise, measurements are typically performed no deeper than 400 μ m. Therefore, vessels outside the imaging volume can contribute to the oxygen level (**Figure IV-5a**). The fitting procedure attempts to ignore these few outliers when fitting the diffusion-reaction model.

IV.4 Tumor Oxygenation during Growth and Across Models

Oxygen tension in the tumor microenvironment changes in response to numerous factors during disease progression. Typically, as tumor volume and cellular burden increase, the mean pO₂ decreases^{72,73}. In clinical patients, most tumors have large regions of hypoxic and necrotic tissue that are heterogeneously distributed⁷⁴. During tumor growth, the formation of new blood vessels, or angiogenesis, is promoted by the oxygen concentration usually through the VEGF pathway^{15,75,76}. Finally, in preclinical models, I have shown in the previous section that different tumor types display different rates of oxygen consumption. Therefore, the mean oxygen tension in the tumor microenvironment is likely different across tumor types.

Table IV-4: Comparison of mean tumor oxygenation (mmHg). Statistical comparisons across time and tumor types were determined using a single-factor ANOVA. Errors are given as standard error of the mean. Bold measurements are statistically different (P -value < 0.05) than all others on that day.

Day	EO771	MDA-MB-361HK	LS174T	MCAIV	MCAIV-MFP	ANOVA
0	32.7 \pm 4.8	23.7 \pm 1.4	30.2 \pm 2.7	33.4 \pm 2.1	41.1 \pm 2.8	4.2E-02
3	26.7 \pm 3.3	24.3 \pm 2.9	25.4 \pm 2.5	29.6 \pm 2.0	28.4 \pm 7.5	0.61
6	17.5 \pm 2.3	24.5 \pm 3.7	16.6 \pm 5.7	30.8 \pm 3.5	27.6 \pm 5.5	5.4E-02
9	13.4 \pm 3.0	18.1 \pm 3.0	32.1 \pm 4.2	21.9 \pm 3.6		1.8E-02
ANOVA	6.8E-03	0.49	0.38	7.7E-02		
	<i>N</i> = 5	<i>N</i> = 5-10	<i>N</i> = 4-10	<i>N</i> = 5-6	<i>N</i> = 2	

IV.4a TUMOR GROWTH: ANGIOGENESIS AND OXYGEN

As a solid tumor grows, it must trigger the formation of new blood vessels to support continued growth. This process, termed the angiogenic switch, occurs in most tumors after they reach a size (~400 μ m in diameter) limited by the diffusion of oxygen^{77,78}. Angiogenesis has proved a predictive indicator of disease progression and response to therapy in many tumor types⁷⁹⁻⁸¹. Further, metastatic disease and angiogenesis of the

primary tumor have been shown to be linked⁸². The level of oxygen has been shown to be an important regulator of tumor angiogenesis^{15,83}. It has even been suggested that microvessel density (MVD) and molecular markers of angiogenesis (VEGF, etc.) are measures of tumor oxygenation⁸⁴.

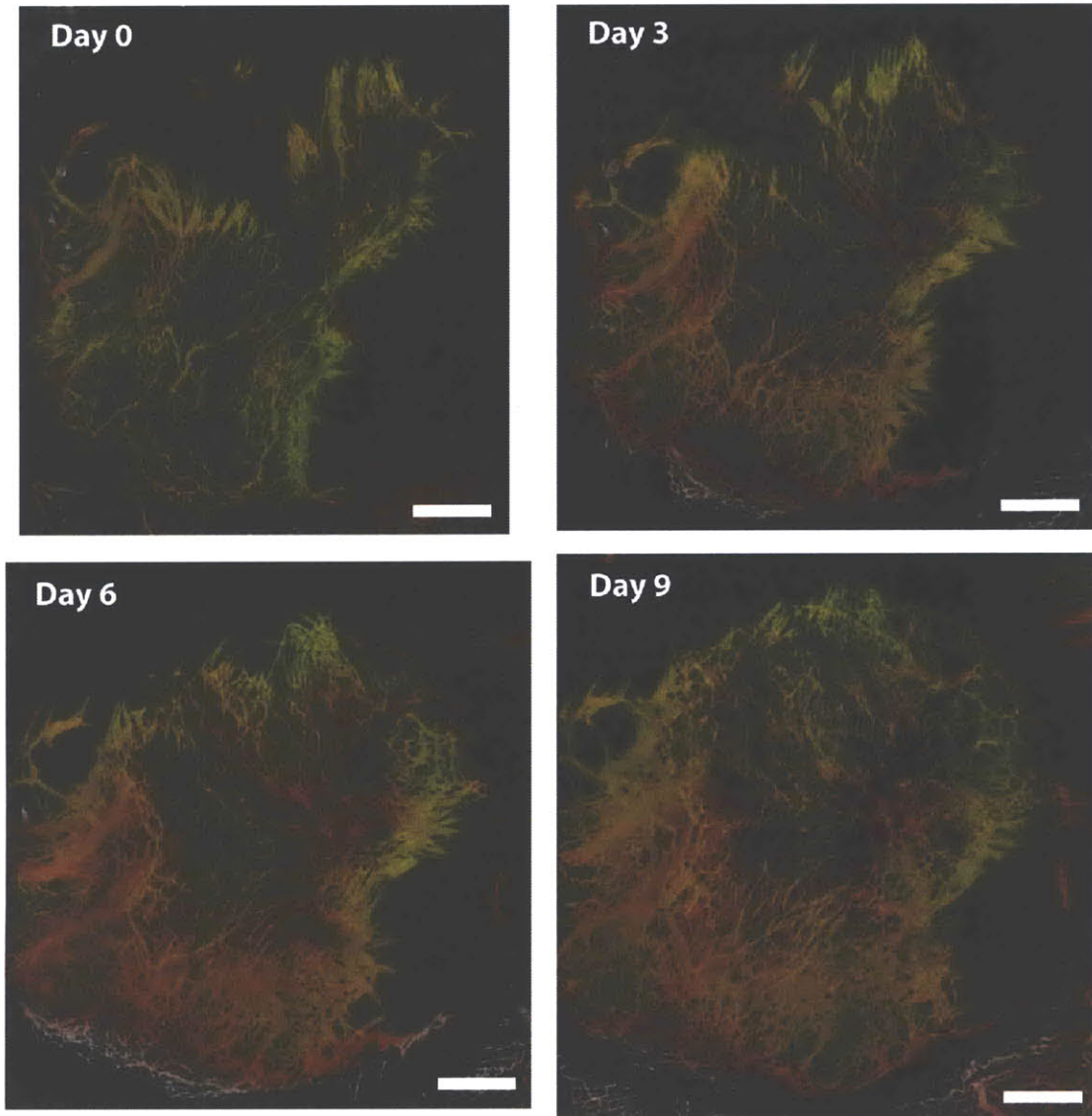


Figure IV-6 Angiogenesis during tumor growth. The vasculature of an LS174T colorectal adenocarcinoma xenograft is shown over 9 days. Increased angiogenesis is notable throughout tumor growth. Tumor vasculature is presented as a colorized depth projection (superficial to deep: green-red-white). Scale Bars - 500µm.

CHAPTER 4

Table IV-5: Comparison of mean vascular radius (μm). Statistical comparisons across tumor types were determined using a single-factor ANOVA. Errors are given as standard error of the mean. Bold measurements are statistically different (P -value < 0.05) than all other measurements on that day.

Day	EO771	MDA-MB-361HK	LS174T	MCAIV	MCAIV-MFP	ANOVA
0	11.7 \pm 0.3	12.1 \pm 0.7	13.3 \pm 0.5	18.9 \pm 1.1	18.5 \pm 2.0	1.7E-06
3	12.9 \pm 0.7	11.6 \pm 0.5	15.3 \pm 0.7	27.8 \pm 3.9	22.6 \pm 4.5	1.1E-06
6	15.5 \pm 1.4	12.9 \pm 1.0	27.5 \pm 2.2	22.7 \pm 1.8	25.9 \pm 8.4	3.1E-07
9	17.9 \pm 2.9	12.7 \pm 1.8	33.2 \pm 3.2	27.6 \pm 2.0		1.3E-04
ANOVA	4.4E-02	0.7	5.2E-04	5.2E-02		
	$N = 5$	$N = 5-10$	$N = 4-10$	$N = 5-6$	$N = 2$	

Utilizing the window chamber models in mice allows tumor vascularization to be followed over time providing critical insights into pathophysiology (Figure IV-6). Using multiphoton microscopy to perform high-resolution angiography and automated vascular tracing algorithms^{50,85}, vascular metrics such as vessel diameter and vascular volume fraction can be obtained. Correlating these morphological parameters with tumor oxygenation provided by MP-PQM provides unique access to study the tumor microenvironment during progression and across models.

Table IV-6: Comparison of vascular volume fraction. Statistical comparisons across time and tumor types were determined using a single-factor ANOVA. Errors are given as standard error of the mean. Bold measurements are statistically different (P -value < 0.05) than all other measurements on that day.

Day	EO771	MDA-MB-361HK	LS174T	MCAIV	MCAIV-MFP	ANOVA
0	5.5 \pm 0.7%	3.7 \pm 0.9%	5.1 \pm 0.4%	6.2 \pm 0.5%	9.3 \pm 1.7%	1.1E-01
3	5.6 \pm 0.8%	2.9 \pm 0.4%	6.0 \pm 0.4%	11.6 \pm 1.4%	5.6 \pm 0.6%	5.9E-08
6	5.6 \pm 0.4%	4.1 \pm 0.9%	5.9 \pm 0.7%	7.2 \pm 1.1%	3.2 \pm 0.9%	7.2E-02
9	4.1 \pm 0.5%	3.8 \pm 1.1%	9.4 \pm 2.0%	7.6 \pm 1.1%		2.2E-02
ANOVA	3.8E-01	0.76	1.2E-02	1.0E-02		
	$N = 5$	$N = 5-10$	$N = 4-10$	$N = 5-6$	$N = 2$	

I measured the mean tumor oxygenation for multiple tumor types over 9 days using MP-PQM (Table IV-4). The trend across tumors was decreasing $p\text{O}_2$ with tumor growth. However, only orthotopic EO771, a murine mammary carcinoma, displayed a significant change in mean $p\text{O}_2$ over time (P -value: 0.007). For the first week, the human and murine mammary carcinoma tumors MDA-MB-361HK and MCAIV, respectively, demonstrated little change in tumor microenvironment $p\text{O}_2$ over time. Across tumors, only at Day 0, when all tumors were $\sim 4\text{mm}$ in diameter by enface measurement, and

CHAPTER 4

Day 9 was there a statistical difference in tumor pO_2 . During the course of the experiment all tumors increased in enface diameter and potentially depth, although axial measurements are difficult in the chamber models. MDA-MB-361HK, xenotransplanted in the MFP chamber of female SCID mice, had a significantly lower pO_2 than all other tumors at Day 0. EO771, which demonstrated a significant decrease in tumor oxygenation during growth, exhibited a significantly lower mean pO_2 than all other tumors at Day 9.

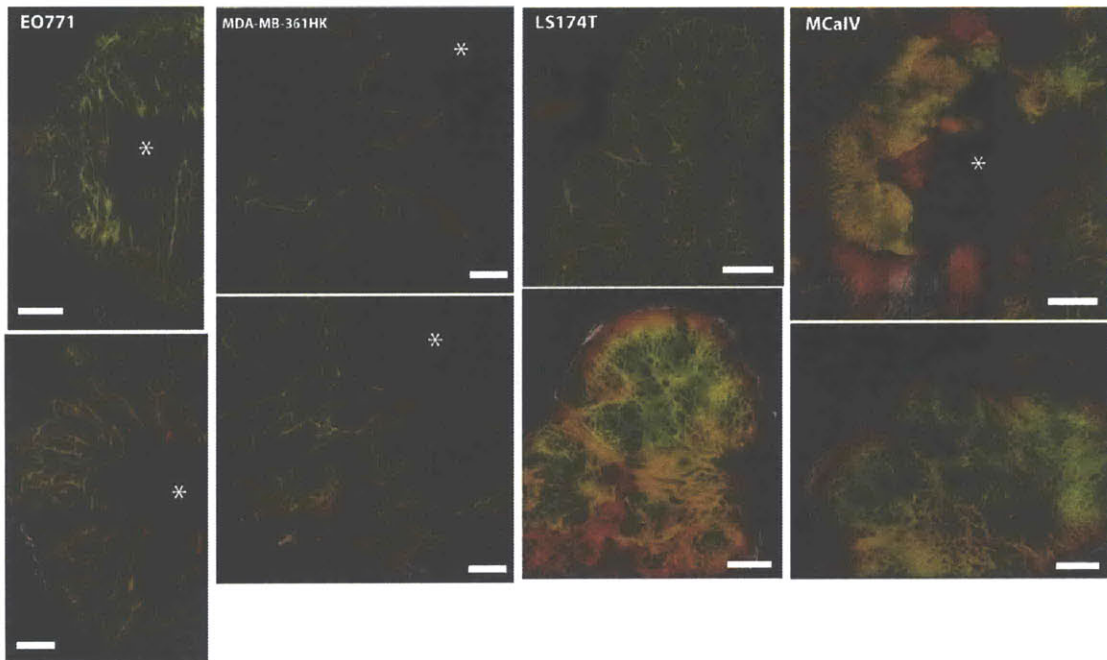


Figure IV-7 Comparison of tumor vascular networks at Day 0 (*top*) and 9 (*bottom*). The higher degree of angiogenesis is evident in LS174T and MCalV tumors. Avascular regions (*) are apparent in both EO771 and MDA-MB-361HK tumors. Images are presented as a colorized depth projections (superficial to deep: green-red-white). Scale Bars - 500 μ m.

Vascular parameters consisting of vascular radius, length and volume fraction were determined from multiphoton angiography for all tumors. For all tumor types except MDA-MB-361HK, the vascular radius significantly increased during tumor growth (**Table IV-5**). In general, the tumors grown in the dorsal skinfold chamber (LS174T and MCalV) exhibited significantly larger vascular diameters than those growing in the mammary fat pad (EO771 and MDA-MB-361HK). The trends in vascular radius nearly matched those found with vascular volume fraction (Vvf, **Table IV-6**). However, even though vascular

CHAPTER 4

radius significantly increased in EO771, the volume fraction of the vascular network did not. The human mammary adenocarcinoma, MDA-MB-361HK, also did not display any increase in VVf. This suggests that although the EO771 and MDA-MB-361HK tumors increase in size, their vascular networks maintain more avascular regions and are less angiogenic than the other tumors (Figure IV-7).

Table IV-7: Hypoxic fraction during tumor growth. Statistical comparisons across time and tumor types were determined using a single-factor ANOVA. Errors are given as standard error of the mean. Bold measurements are statistically different (P -value < 0.05) than all other measurements on that day.

Day	EO771	MDA-MB-361HK	LS174T	MCAIV	MCAIV-MFP	ANOVA
0	13.5±6.9%	18.9±4.6%	9.3±3.3%	8.7±3.7%	2.8±0.5%	0.27
3	18.5±7.1%	21.9±6.8%	16.0±6.9%	13.6±5.0%	21.3±16.9%	0.18
6	37.1±10.8%	24.2±6.1%	12.2±4.3%	13.0±5.1%	36.8±10.1%	2.7E-03
9	59.8±10.1%	31.4±11.0%	9.7±3.8%	38.3±8.7%		1.6E-04
ANOVA	1.1E-02	0.76	0.19	9.2E-03		
	<i>N</i> = 5	<i>N</i> = 5-10	<i>N</i> = 4-10	<i>N</i> = 5-6	<i>N</i> = 2	

The presence of avascular spaces in some of the tumors coupled with decrease tumor oxygenation over time could lead to regions of hypoxia. I determined the hypoxic fraction within each tumor and timepoint by calculating the number of measurements less than 10mmHg (Table IV-7). At Day 0 both EO771 and MDA-MB-361HK had higher hypoxic fractions than the tumors with higher VVf. The type of tumor does have a statistically significant impact on the level of hypoxia over time. The hypoxic fraction remained relatively high in MDA-MB-361HK tumors (~23%) and low in LS174T tumors (~12%) without significantly changing. Both murine mammary carcinomas (EO771 and MCAIV) exhibited significantly increasing hypoxic fractions over time. However, MCAIV also displayed increasing VVf, suggesting the spatial heterogeneity in relation to the vasculature of hypoxic regions may be different between tumors.

To assess spatial heterogeneity in hypoxic regions, I spatially correlated each individual MP-PQM oxygen measurement with distance to the closest vessel. The mean distance from a hypoxic measurement was then determined from the correlated oxygen and angiography measurement (Table IV-8). Overall, both MDA-MB-361HK and MCAIV tumors displayed longer distances from hypoxic regions to the nearest vessel, while

CHAPTER 4

both EO771 and LS174T had hypoxic regions closer. Only in LS174T did the distance show a significant change with tumor growth. At Day 9, the mean distance to nearest vessel was farther.

Table IV-8: Distance (μm) from hypoxic regions to closest vessel. Statistical comparisons across time and tumor types were determined using a single-factor ANOVA. Errors are given as standard error of the mean. Bold measurements are statistically different (P -value < 0.05) than all others on that day.

Day	EO771	MDA-MB-361HK	LS174T	MCAIV	MCAIV-MFP	ANOVA
0	73.1 \pm 24.7	173.5 \pm 40.1	76.6 \pm 14.3	149.9 \pm 43.3	162.1 \pm 100.1	0.27
3	53.3 \pm 14.8	175.3\pm31.8	85.3 \pm 5.6	87.9 \pm 16.6	87.9 \pm 23.1	2.8E-03
6	52.7 \pm 6.2	147.8 \pm 25.4	81.6 \pm 15.0	116.4 \pm 33.3	134.6 \pm 9.5	9.0E-02
9	94.3 \pm 25.0	90.3 \pm 26.2	117.7 \pm 6.6	77.3 \pm 7.5		0.54
ANOVA	0.83	0.41	9.6E-03	0.39		
	$N = 5$	$N = 5-10$	$N = 4-10$	$N = 5-6$	$N = 2$	

To gain a clearer understanding of the relationships between tumor angiogenesis and vasculature, I correlated the vascular metrics with oxygen throughout tumor growth (Table IV-9). Unsurprisingly, the vascular radius demonstrated no dependence on mean tumor pO_2 . This is in agreement with the results from individual tumors (Figure IV-4) and previous studies^{35,49}. However, in both MDA-MB-361HK and MCAIV, mean vascular radius was significantly correlated with the hypoxic fraction of the tumor. Specifically, over tumor progression as the mean vascular diameter increased, the hypoxic fraction also increased. Interestingly, vascular volume fraction was uncorrelated with hypoxic fraction and mean pO_2 in these tumors. Only the EO771 murine mammary carcinoma exhibited a significant correlation of VVf with both pO_2 and hypoxic fraction. In this specific tumor, these relationships indicated that increased VVf is associated with increased pO_2 and lower hypoxic fraction. For all tumors, a significant negative correlation of hypoxic fraction with mean tumor pO_2 was observed. These correlations served as a control since the hypoxic fraction was derived directly from the pO_2 measurements. Finally, most tumors demonstrated no significant correlation for the distance to nearest vessel from hypoxic regions with either the mean pO_2 or hypoxic fraction. Only LS174T exhibited a significant positive and negative correlation with pO_2 and hypoxic fraction, respectively. Therefore, in this tumor type higher tumor

oxygenation and lower hypoxic fraction is found when hypoxic regions are far away from the vessels. This makes intuitive sense when the diffusion and consumption of oxygen is taken into account.

Table IV-9: Correlation of vascular metrics with tumor oxygenation and hypoxic fraction over time. All correlation coefficients are Pearson product-moment correlations to determine if there is a linear dependence between two factors. All significant correlations (P -value < 0.05) are given in bold.

Vascular Metric	EO771		MDA-MB-361HK		LS174T		MCAIV	
	pO ₂	HypoxicF	pO ₂	HypoxicF	pO ₂	HypoxicF	pO ₂	HypoxicF
Radius	-0.416	0.388	-0.315	0.489	-0.041	0.244	-0.380	0.551
VVf	0.626	-0.682	0.050	0.055	0.207	-0.101	0.262	-0.145
HypoxicF	-0.913	1.000	-0.765	1.000	-0.845	1.000	-0.875	1.000
HypoxicD	-0.357	0.404	0.072	0.342	0.737	-0.396	-0.150	0.190

VVf – Vascular Volume Fraction; HypoxicF – Hypoxic Fraction; HypoxicD – Distance to nearest vessel from hypoxic region

Correlating measurements of tumor oxygenation and hypoxia with vascular metrics provides unique insight into the tumor microenvironment during tumor growth. It is readily apparent that different tumor types have different vascular phenotypes and even different rates of angiogenesis. Further during tumor growth, the differential between tumor oxygenation between tumor types becomes more apparent. Unsurprisingly given the differences in tumor oxygenation during growth, the hypoxic fraction also varies amongst tumor types. Hypoxia regions either remain constant over time or increase with tumor size. Additionally, the location of these hypoxic regions with respect to the vasculature is heterogeneous between tumor types. The lack of correlation over time between the vascular volume and hypoxic fractions are not unsurprising. Clinical studies using both histological and imaging modalities have shown limited correlation between such metrics and hypoxia^{84,86}. However, previous studies have demonstrated that tumor oxygenation (specifically hypoxia) can upregulate VEGF expression, a potent angiogenic molecule^{15,83,87}. It is possible that other angiogenic pathways independent of the HIF-1/VEGF axis are responsible for vascularization during tumor progression in some of the tumor lines⁸⁸.

The findings for EO771 that show a significant correlation between VVf and pO₂ or hypoxic fraction indicate that with tumor growth as hypoxic fraction increases both

tumor pO_2 and VVf decrease. A similar strong correlation using MVD as the metric of tumor vascularization has been observed for certain endocrine tumors in patients⁸⁹. With disease progression, poor prognosis was associated with hypoxic tumors with low MVD. Conversely, the human breast adenocarcinoma, MDA-MB-361HK, which over-expresses the epithelial growth factor receptor Her2/neu, demonstrates no correlation between VVf and pO_2 or hypoxic fraction. Histological studies of primary human breast tumors expressing Her2/neu in patients showed a high degree of angiogenesis and low levels of hypoxia⁹⁰. Two explanations may account for this discrepancy. First, the measures of angiogenesis and hypoxia were the histological markers of MVD and CA IX, respectively. MVD provides only a snapshot of the tumor vasculature and may in some cases serve as a poor marker of angiogenesis⁹¹. Endogenous markers of hypoxia have proved inconsistent at best and unreliable when only one molecular marker is utilized⁹². Second, the MDA-MB-361HK cell line originates from a metastatic breast tumor in the brain, so while it is implanted in the orthotopic environment of the primary tumor differences in cancer cell Pathophysiology may exist.

Finally, in most tumors, the mean distance from hypoxic regions to the nearest blood vessel was found to be uncorrelated with either pO_2 or hypoxic fraction. Across all models, the tumor vascular network is both tortuous and heterogeneous interspersed with random avascular regions (**Figure IV-7**). Non-invasive imaging studies in animal models have shown no spatial correlation between hypoxic regions and vascular labels (RGD peptides)⁹³. Further, vascular flow and delivery of oxygen is irregular and heterogeneous in tumors. *In vivo* perfused vessels have demonstrated low oxygen tensions suggesting regions of hypoxia may remain close to some detectable vessels³⁵. Hypoxic regions in most tumors are likely heterogeneously distributed with little correlation with the vasculature. This was observed with all tumors except the human colorectal adenocarcinoma xenotransplant, LS174T. For this tumor, hypoxic regions are located on average about 85 μ m from the closest vessel. On average, during tumor growth, regions of hypoxia move closer to the vessels. Instead of decreased spatial heterogeneity in hypoxic regions, this effect is possibly due to the significantly

increasing *in vivo* oxygen consumption rate demonstrated by the LS174T tumor (Table IV-3).

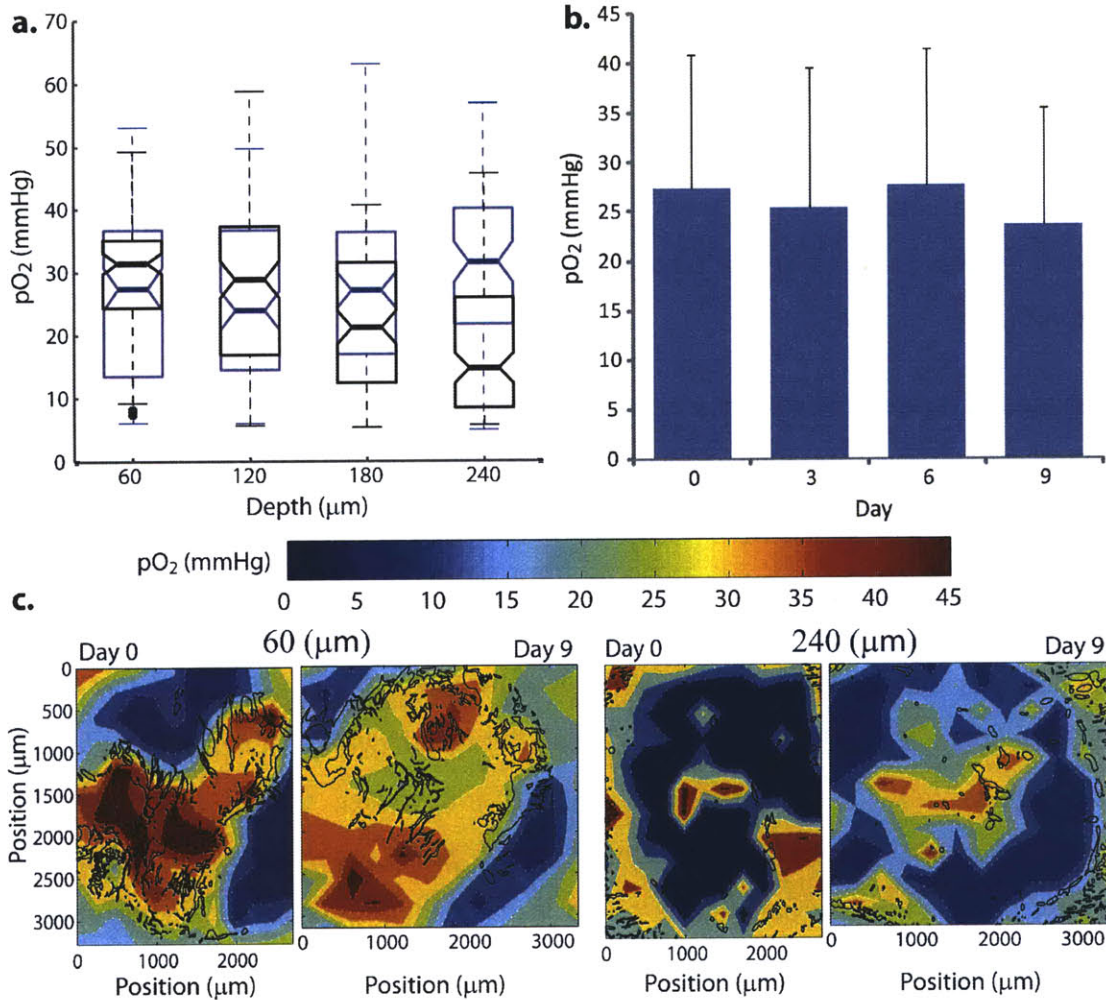


Figure IV-8 Depth gradients in pO₂ during tumor growth. (a). Median oxygen tension of an LS174T tumor in the DSC at day 0 (blue) and 9 (black) at different depths in the tumor. The edges of the boxes indicate the upper and lower quartiles with the median pO₂ value represented in the center. Whiskers extend to 1.5 times the interquartile range. Asterisks indicate outliers. (b) Mean tumor pO₂ during tumor growth remained steady. Errors are standard deviations. (c) Oxygen tension maps at 60 and 240 μm in the tumor for days 0 and 9. Vascular casts overlay the maps from the angiographic imaging. At Day 0, most deep MP-PQM measurements exhibited small signal to noise ratios and were not included (dark blue).

IV.4b TUMOR GROWTH: DEPTH GRADIENTS IN OXYGENATION

The application of MP-PQM to studying tumors allows non-invasive assessment of spatial changes in tumor oxygenation up to 400 μm deep in the tumor. Differences between the superficial and deep portions of the tumor were determined during tumor

growth. The effect of increased tumor volume and angiogenesis were observed in an LS174T tumor in the DSC (**Figure IV-8**). In earlier stages of tumor growth, the deep portions of the tumor were still supplied by oxygen diffusion from the supporting host vasculature. In this tumor model, as the tumor grew in size, the mean oxygen tension deeper in the tumor dropped (**Figure IV-8a**), while the overall average tumor pO_2 remained relatively constant (**Figure IV-8b**). In this case, the steady overall pO_2 is due to increased vascularization near the tumor surface ($\sim 60\mu\text{m}$). Further the heterogeneity in tumor oxygenation at near the tumor surface decreased, while it increased deeper (120-180 μm).

Longitudinal gradients in tumor pO_2 appear to increase from the fascial to tumor surface in this model. This contradicts with previous studies in chamber models demonstrating decreasing longitudinal gradients from the fascial to tumor surface⁹⁴⁻⁹⁶. The existence of these gradients was proposed to occur from similar gradients in other metabolites assuming that all vascular supply results from the underlying fascial vessels. In some models this may be the case, however, in my experience, as a tumor grows in the chamber models angiogenesis typically occurs across nearly the entire tumor surface by 2-3 weeks. Wide-field angiographic imaging from growing tumors in the chamber models reveals vascular branches from vessels both underneath and *around* the tumor⁶¹. For all measurements presented in this chapter, I initiated studies only on tumors with surface vascularization to eliminate any artifacts in pO_2 from transient longitudinal gradients.

IV.5 Spatial Distribution of Tumor Vascular Networks Influence Tissue Oxygenation

The combination of three-dimensional oxygen measurements with MP-PQM and high-resolution angiography by MPM present unique opportunities to study the relation of the tumor vasculature to the metabolic microenvironment. Previously in this Chapter, I determined oxygen consumption using a semi-one dimensional diffusion-reaction

equation that relied on distance to the nearest vessel. Here, I will show that the tissue volume probability distribution with respect to the vasculature qualitatively predicts the tissue oxygen profile (**Figure IV-5**) and oxygen tension probability histogram.

IV.5a CYLINDRICAL MODELS OF OXYGEN DIFFUSION IN TUMORS

Many theoretical approaches have been demonstrated for determining metabolite concentrations, particularly oxygen, outside of the vasculature in a variety of tissues. In regularly spaced capillary networks found in many normal tissues, a cylindrically symmetric model was developed by Krogh⁹⁷. Based on observations of the regular spaced packing of capillaries and muscle fibers in skeletal muscle, an analytical solution for steady state concentration was obtained. This model is now well known as the Krogh tissue cylinder model. Analytical solutions for the diffusion of oxygen in other regularly spaced planar and cylindrical geometries have been readily demonstrated⁹⁸.

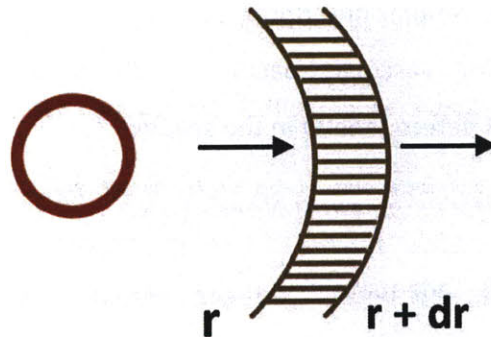


Figure IV-9 Cylindrical geometry for describing diffusive processes. Diffusion of oxygen from a vessel (red) to a cylindrical surface volume of tissue (brown) of width dr at a given radius, r .

The mass balance equation for the gradient of a diffusing species in a cylindrical coordinate system (**Figure IV-9**) across a differential element of tissue with a sink/reaction term, M_0 , is given by Eq. (IV.3).

$$-D \left. \frac{\partial C}{\partial r} \right|_r 2\pi r L + D \left. \frac{\partial C}{\partial r} \right|_{r+dr} 2\pi(r+dr)L - M_0 dV = 0 \quad (\text{IV.3})$$

Here the area and differential volume are given by $2\pi r L$ and $2\pi r L dr$, respectively. By Taylor expanding the differential change in concentration over radius [Eq. (IV.4)] and

eliminating second order terms [Eq. (IV.5)] the final cylindrical solution can be found [Eq. (IV.6)].

$$\left. \frac{\partial C}{\partial r} \right|_{r+dr} = \left. \frac{\partial C}{\partial r} \right|_r + dr \left. \frac{\partial^2 C}{\partial r^2} \right|_r + \dots \quad (\text{IV.4})$$

$$-D \left. \frac{\partial C}{\partial r} \right|_r (2\pi r L) + D \left[\left. \frac{\partial C}{\partial r} \right|_r + dr \left. \frac{\partial^2 C}{\partial r^2} \right|_r \right] (2\pi(r+dr)L) - M_0 2\pi r L dr = 0 \quad (\text{IV.5})$$

$$D \frac{\partial^2 C}{\partial r^2} + \frac{D}{r} \frac{\partial C}{\partial r} - M_0 = 0 \quad (\text{IV.6})$$

Adaptations of cylindrical geometries have been applied to theoretically model the diffusion of oxygen in tumors and prepare theoretical maps of oxygen tension^{48,65,68}. Others have utilized more complex descriptions of the tumor vasculature adapted to the cylindrical model including vascular spacing in the networks and with distance weighting⁹⁹ or an inherent heterogeneity in the spacing¹⁰⁰.

IV.5b IN VIVO OXYGEN DIFFUSION FROM NORMAL AND TUMOR VASCULAR GEOMETRIES

While cylindrical models adequately portray vascular networks with relatively homogenous descriptive parameters; they fail to account for higher-order branching hierarchies found in many tissues and the truly abnormal vascular geometries in tumors. Fractal geometries¹⁰¹ have been used to characterize vascular architecture in both normal and neoplastic tissues^{102,103}. The scale invariant behavior of fractal vascular networks can be applied to models of metabolite and drug delivery to tumors⁶⁴. However, it appears that fractal characterization may be a less than ideal choice for describing tumor vasculature given the heterogeneous networks found across tumors⁶¹. Distributions in the vascular spacing within tumors from two-dimensional histological tissue cross-sections have been used to simulate tumor oxygenation¹⁰⁴. However, this theoretical work is limited to two-dimensional geometries and is subject to the limits of

using microvessel density to describe tumor vasculature⁹¹. It has been recently demonstrated that a simple metric describing vascular network geometry in three-dimensions provides powerful insight into diffusive processes in tumors. This metric, the number of tissue voxels at a given distance from the closest vessel, $n(\delta)$, can be used to model the transport of drugs and metabolites in tissue, including tumors¹⁰⁵. In fact, theoretical simulations demonstrate that the need for scale-invariant geometry is not a constraint with $n(\delta)$ as it is with fractal descriptors.

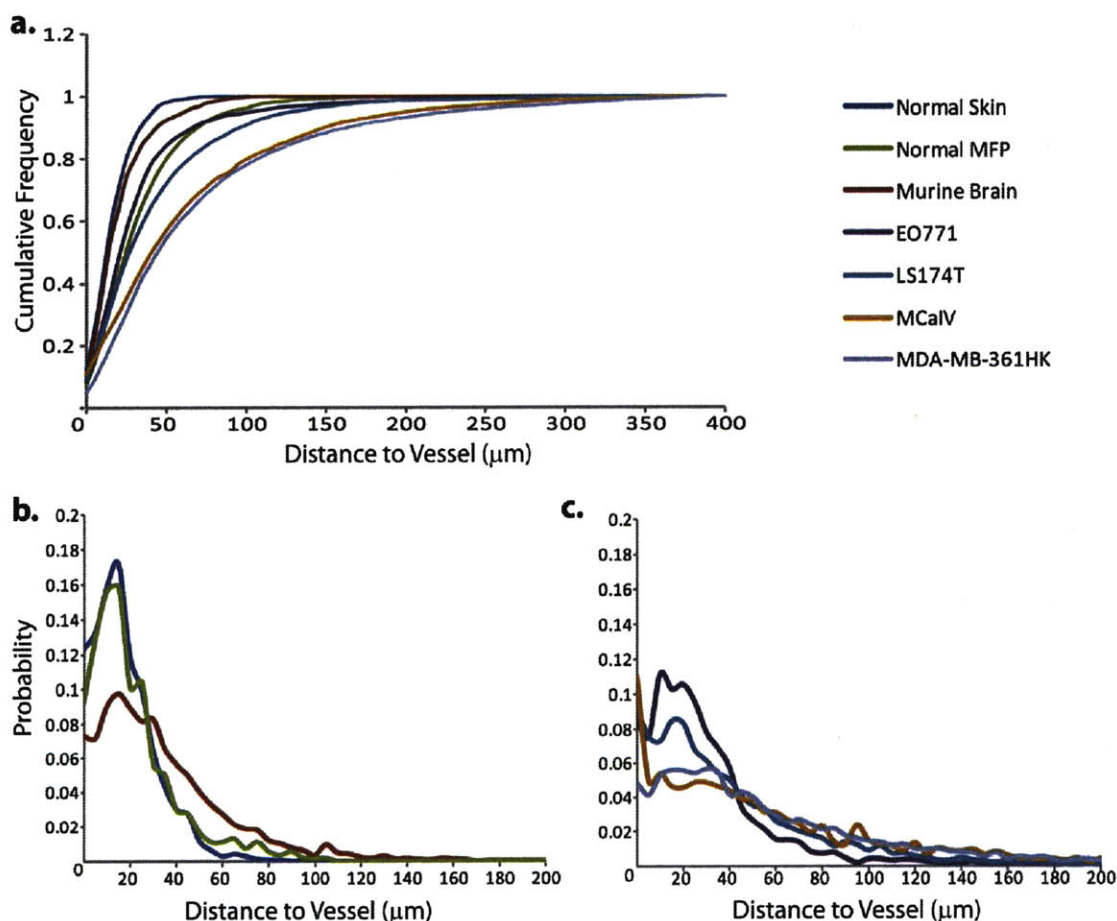


Figure IV-10 Normal and tumor tissue vascular networks described by number of tissue voxels at a given distance from a vessel. (a) Cumulative distribution frequency of tissue voxels at a given distance for each tissue type studied. **(b)** Probability distributions of $n(\delta)$ for normal tissues. **(c)** Probability distributions of $n(\delta)$ various tumors at a size of 4mm in diameter. Normal skin: $N = 4$; Normal MFP: $N = 5$; Normal Brain: $N = 3$; EO771: $N = 9$; LS174T: $N = 13$; MCalV: $N = 9$; MDA-MB-361HK: $N = 20$.

By spatially correlating the distance of each oxygen measurement to the nearest tumor vessel, I determined $n(\delta)$ across tumor types (Figure IV-10). The cumulative frequency

distributions (CFD) were determined from all tumors of a given type at the same size (4mm). A rightward shift in the CFD from normal to tumor vascular networks was readily apparent (**Figure IV-10a**). The difference between normal and tumor vascular networks was reflected in the broadening of $n(\delta)$ and decrease in a peak maximum probability distance for tumor vasculature in comparison to normal tissue (**Figure IV-10a and b**). The EO771 tumor appeared to have most similarity with the distribution found in normal MFP vasculature. An additional difference between tumors and normal tissues was found in the maximum distance (δ_{max}) of tissue volumes from vessels, which increased in tumors. Normal skin, mammary fat pad and murine cortex displayed a δ_{max} of ~ 75 , 140 and $90\mu\text{m}$, respectively. In tumors the distance was notably longer, ranging from 245 to $365\mu\text{m}$ for EO771 and MDA-MB-361HK tumors, respectively.

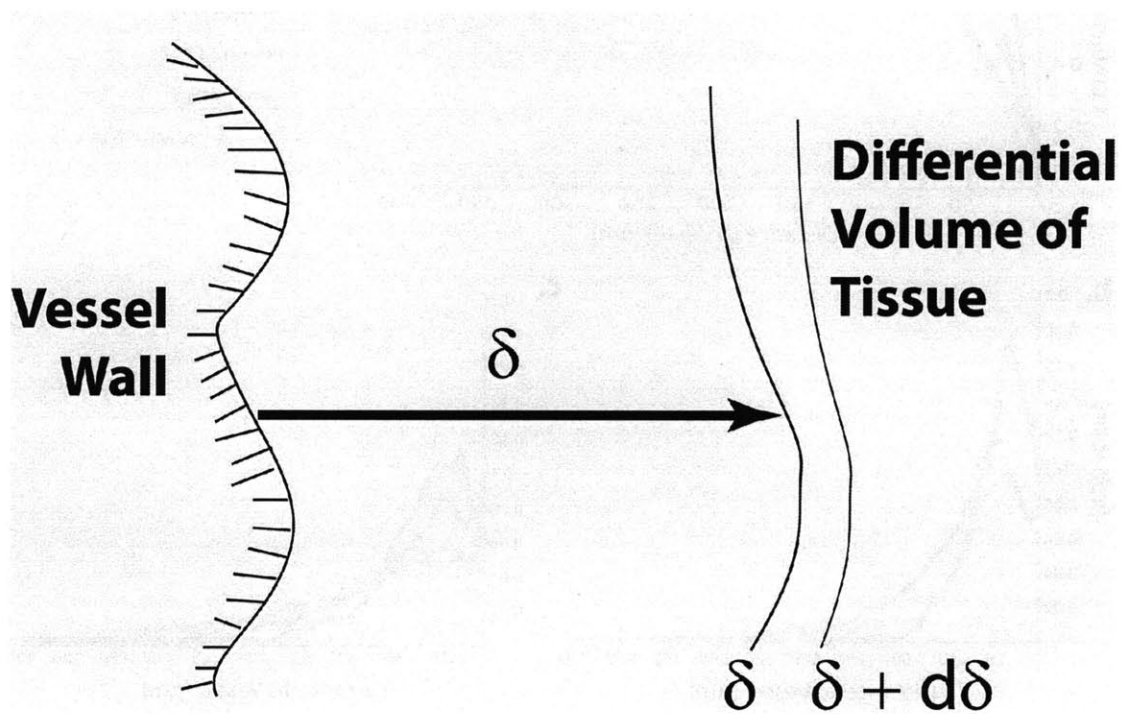


Figure IV-11 Modeling the diffusion of a small molecule in an arbitrarily defined geometry using $n(\delta)$.

Each probability distribution for the distance of tissue voxels in a vascular network reflects the tissue oxygenation or diffusion of other metabolites or drugs¹⁰⁵. If we assume that diffusion near the vessels can be approximated one-dimensionally and

scales with distance, the concentration profile of a diffusing species in an arbitrary heterogeneous vascular geometry can be determined. Given the generalized arrangement in Figure IV-11 we can describe the mass balance relationship at steady state as in Eq. (IV.7).

$$-D \left. \frac{\partial C}{\partial \delta} \right|_{\delta} n(\delta) + D \left. \frac{\partial C}{\partial \delta} \right|_{\delta+d\delta} n(\delta + d\delta) - M_0 n(\delta) d\delta = 0 \quad (\text{IV.7})$$

Similar to the derivation for the cylindrical model, we expand the loss out of the right side of the differential volume tissue element in a Taylor series.

$$\left. \frac{\partial C}{\partial \delta} \right|_{\delta+d\delta} = \left. \frac{\partial C}{\partial \delta} \right|_{\delta} + d\delta \left. \frac{\partial^2 C}{\partial \delta^2} \right|_{\delta} + \dots \quad (\text{IV.8})$$

$$n(\delta + d\delta) = n(\delta) + d\delta \left. \frac{\partial n}{\partial \delta} \right|_{\delta} + \dots \quad (\text{IV.9})$$

Substituting the second-order expansions into the mass balance relationship [Eq. (IV.7)], the final generalized form can be obtained.

$$-D \left. \frac{\partial C}{\partial \delta} \right|_{\delta} n(\delta) + D \left[\left. \frac{\partial C}{\partial \delta} \right|_{\delta} + d\delta \left. \frac{\partial^2 C}{\partial \delta^2} \right|_{\delta} \right] \left[n(\delta) + d\delta \left. \frac{\partial n}{\partial \delta} \right|_{\delta} \right] - M_0 n(\delta) d\delta = 0 \quad (\text{IV.10})$$

$$\begin{aligned} -D \left. \frac{\partial C}{\partial \delta} \right|_{\delta} n(\delta) + D \left. \frac{\partial C}{\partial \delta} \right|_{\delta} n(\delta) + D \left. \frac{\partial C}{\partial \delta} \right|_{\delta} d\delta \left. \frac{\partial n}{\partial \delta} \right|_{\delta} + D d\delta \left. \frac{\partial^2 C}{\partial \delta^2} \right|_{\delta} n(\delta) \\ + D d\delta^2 \left. \frac{\partial^2 C}{\partial \delta^2} \right|_{\delta} \left. \frac{\partial n}{\partial \delta} \right|_{\delta} - M_0 n(\delta) d\delta = 0 \end{aligned} \quad (\text{IV.11})$$

$$D \frac{\partial^2 C}{\partial \delta^2} + \frac{D}{n(\delta)} \frac{\partial n}{\partial \delta} \frac{\partial C}{\partial \delta} - M_0 = 0 \quad (\text{IV.12})$$

The generalized form demonstrates an inverse dependence on the fraction of voxels (area) at incremental distances from the vessel walls and directly proportional to the growth/change in the number of voxels.

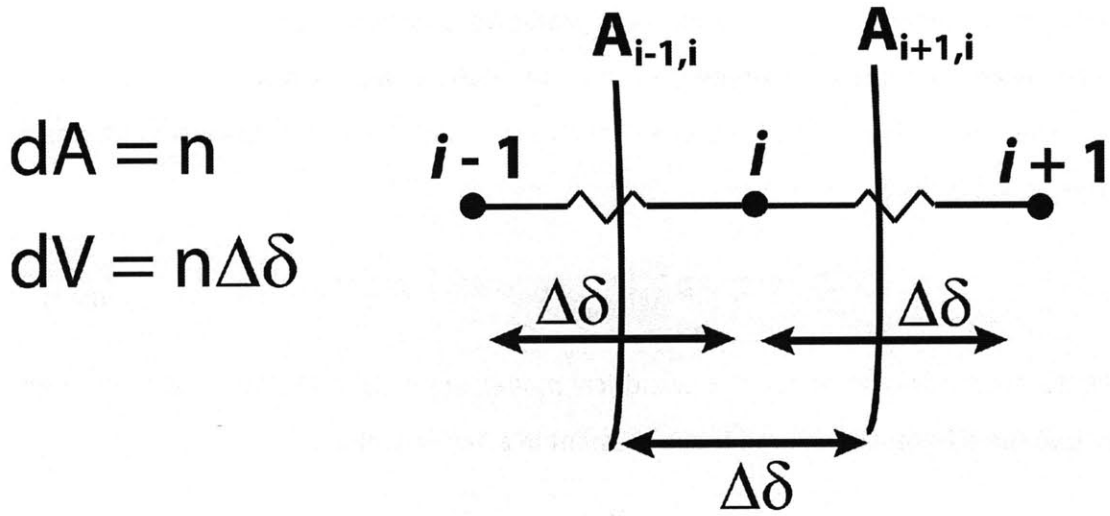


Figure IV-12 Finite volume method to numerically calculate concentration profiles for the generalized solution to the diffusion from an arbitrary vascular network. $\Delta\delta$ is the differential tissue element separating two tissue surface areas defined by n . The differential volume is the product of the two.

The finite volume method¹⁰⁶ can be used to numerically solve for the generalized diffusion equation [Eq. (IV.12)] to find the concentration at given distances from the vessel wall. Fluxes through a finite volume element are depicted in Figure IV-12, where fluxes into the volume are defined as positive.

$$\frac{DA_{i-1,i}}{\Delta\delta}(c_{i-1} - c_i) + \frac{DA_{i+1,i}}{\Delta\delta}(c_{i+1} - c_i) - M_0A_i\Delta\delta = 0 \quad (\text{IV.13})$$

The tissue surface area is directly proportional to the number of tissue voxels.

$$A_{i-1,i} = \left(\frac{n_{i-1} + n_i}{2}\right) \quad (\text{IV.14})$$

$$A_{i+1,i} = \left(\frac{n_{i+1} + n_i}{2}\right) \quad (\text{IV.15})$$

$$A_i = n_i \quad (\text{IV.16})$$

Substituting the tissue areas across which the conductance occurs into Eq. (IV.13) the final finite volume formulation can be obtained.

$$\frac{D}{\Delta\delta}\left(\frac{n_{i-1} + n_i}{2}\right)(c_{i-1} - c_i) + \frac{D}{\Delta\delta}\left(\frac{n_{i+1} + n_i}{2}\right)(c_{i+1} - c_i) - M_0n_i\Delta\delta = 0 \quad (\text{IV.17})$$

CHAPTER 4

The diffusive conductance across either side of the differential tissue volume element can now be found using the previously defined areas for the two tissue surfaces.

$$G_{i-1,i} = \frac{D}{\Delta\delta} \left(\frac{n_{i-1} + n_i}{2} \right) \quad \text{(IV.18)}$$

$$G_{i+1,i} = \frac{D}{\Delta\delta} \left(\frac{n_{i+1} + n_i}{2} \right) \quad \text{(IV.19)}$$

Using the definition of the differential tissue volume element across which consumption occurs ($V_i = n_i \Delta\delta$), the final finite volume formulation can be described.

$$G_{i-1,i}(c_{i-1} - c_i) + G_{i+1,i}(c_{i+1,i} - c_i) - M_0 V_i = 0 \quad \text{(IV.20)}$$

Using Matlab, the finite volume formula was numerically integrated over time to find a steady state solution for the concentration of oxygen in tissue given $n(\delta)$. The concentration at the vessel wall (C_0) was defined in terms of oxygen saturation (0 – 1). The diffusion coefficient of oxygen in tissue was assumed to be constant at $1.5 \times 10^{-9} \text{ m}^2/\text{s}$ ¹⁰⁷. The consumption of oxygen in tissue was assumed to follow Michaelis-Menten kinetics⁶⁸.

$$M(C_{O_2}) = M_0 \frac{C_{O_2}}{C_{O_2} + M_1} \quad \text{(IV.6)}$$

In Michaelis-Menten kinetics, the consumption of oxygen is dependent on the concentration present. Typically, oxygen consumption follows zero-order kinetics at most oxygen tensions. Only for low oxygen concentrations, defined as M_1 , does the consumption deviate from M_0 and follow first order kinetics. I assumed that in hypoxic environments, the oxygen consumption would become dependent on oxygen, so a saturation value of 0.05 was selected for M_1 .

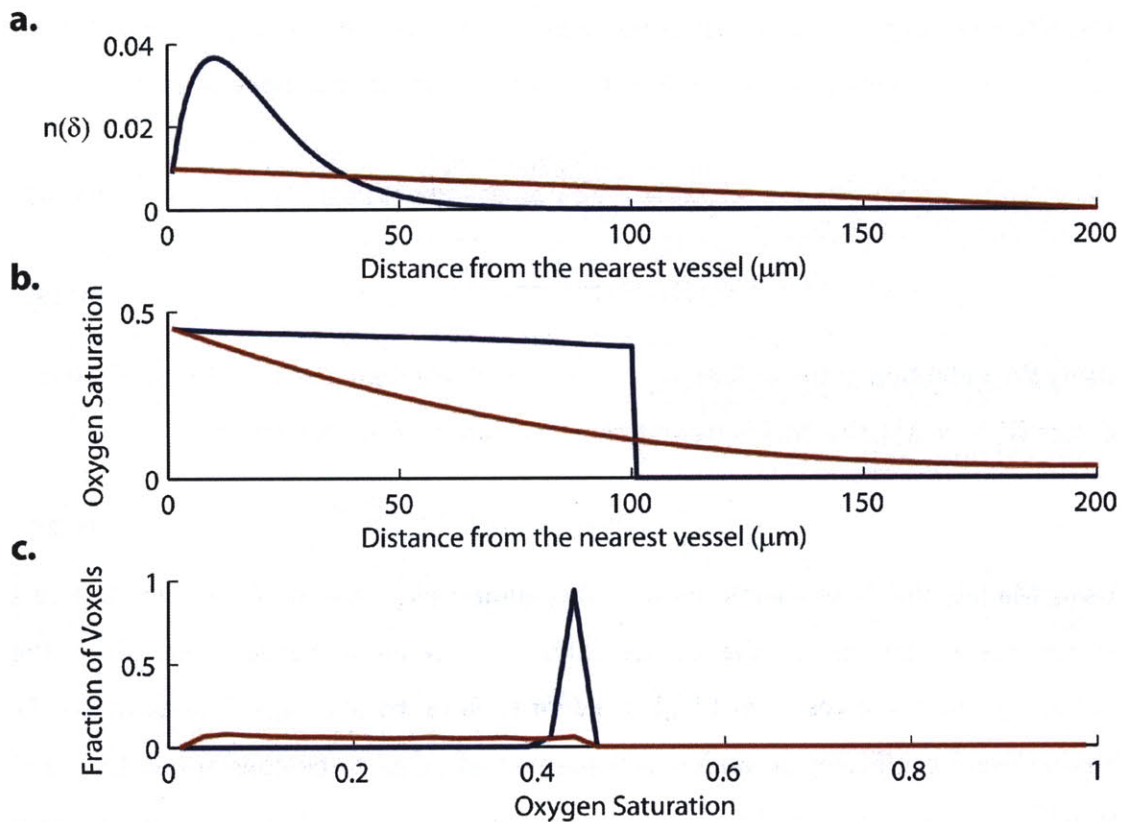


Figure IV-13 Numerical simulations using the finite volume method to determine steady state oxygen concentration profiles for generalized functions of $n(\delta)$. (a) Volume fraction probability distributions for given distances from the vasculature. (b) Oxygen concentration profiles in the tissue based on the diffusion-reaction model for arbitrary three-dimensional geometries. (c) Oxygen probability distributions determined from a and b. Normal – blue; Tumor – red.

To assess if the finite volume method was successful in determining oxygen profiles from $n(\delta)$, I tested some functions that gave representative distributions similar to those found in normal and tumor tissue. The functions $f(x) = xe^x$ and $f(x) = -mx + C$ adequately describe $n(\delta)$ for normal and tumor tissue (**Figure IV-10**), respectively. The steady-state oxygen concentration profiles were found for each of these functions (**Figure IV-13**). The zero-order oxygen consumption (M_0) was assumed to be twice as high in tumors as normal tissue (0.1 versus 0.05). Given that many tumors exhibited average tissue oxygenation values that were close to that of normal tissue ($\sim 30\text{mmHg}$), I applied the same source term ($C_0 = 0.45$) to both representative $n(\delta)$ functions. In the true tissue metabolic micronenvironment there would be a distribution of source concentrations supplying the tissue.

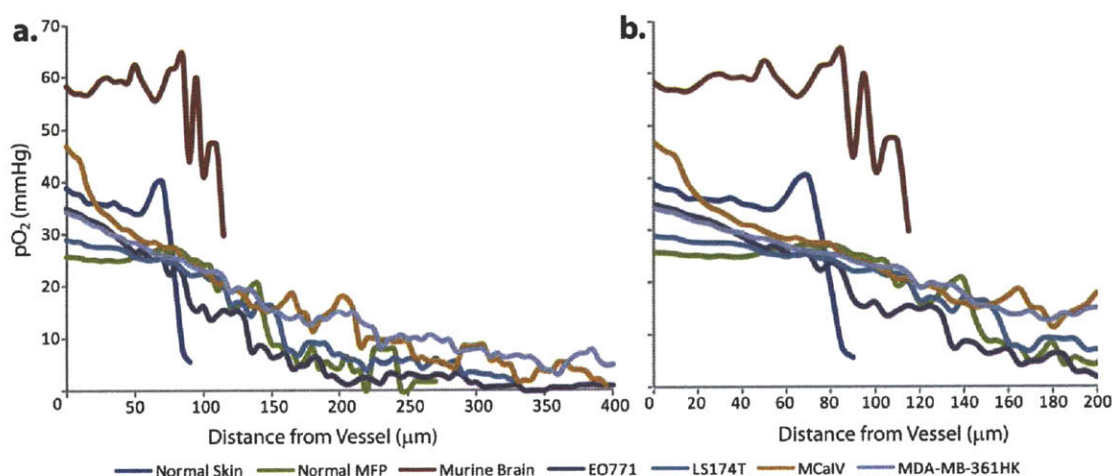


Figure IV-14 *In vivo* pO_2 profiles for normal and neoplastic tissue determined from MP-PQM measurements. (a) The normal tissues remain relatively flat up to δ_{max} . Everything after this point is artifact due to single measurement points potentially outside of the tissue. The tumors uniformly display decreasing pO_2 profiles out to significant distances. Due to a limited number of points, this region is noisier. (b) A truncated view of a.

The qualitative oxygen profiles and probability distributions shown in Figure IV-13 demonstrate many of the distinguishing features of those found in normal and neoplastic tissue. The test function for normal tissue matches remarkably well to that found in normal skin (Figure IV-10b). Similarly, the general linear function for the tumor matches quite well to that found in MCAIV and MDA-MB-361HK (Figure IV-10c). It also exhibits similar parabolically decreasing pO_2 profiles to those found *in vivo* (Figure IV-14). Given greater probability of tissue voxels closer to the vessels in normal tissue, the pO_2 profile is fairly flat as the tissue is well oxygenated matching the *in vivo* results.

For the simulation, oxygen probability distributions were determined from the functions for $n(\delta)$ and the pO_2 profile (Figure IV-13c). The oxygen probability distribution found for normal tissue is too narrow in comparison to *in vivo* measurements (Figure IV-15b). This is due to the fact that intravascular longitudinal pO_2 gradients are found in the normal tissue vascular networks broadening the oxygen distribution³⁸. For the representative tumor, the oxygen probability distributions reveal a similar broadness, but lack the normoxic and hypoxic peaks found with *in vivo* measurements (Figure IV-15c). This is reflective of the fact that a distribution, possibly heterogeneous, of source terms due to convective dispersion was not taken into account¹⁰⁵.

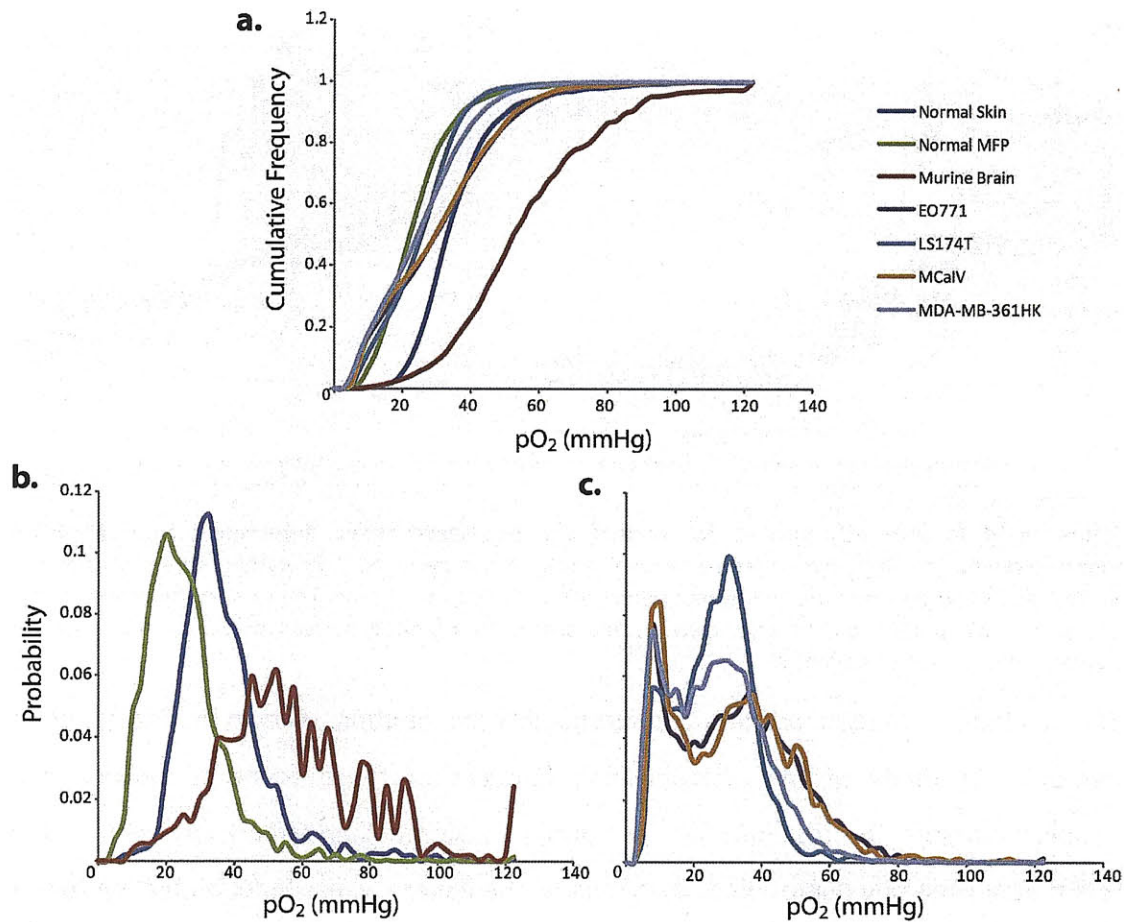


Figure IV-15 In vivo oxygen tension probability distributions. (a) Cumulative frequency distributions demonstrate a rightward shift to higher pO₂ in normal tissues. Multiple inflection points (normoxic and hypoxic regions) in the tumor distributions are observable. (b) pO₂ probability distributions in normal tissues. (c) pO₂ probability distributions in tumors reveal a bimodal nature.

I applied the numerical method to find steady-state oxygen profiles for the tissue volume fraction spatial distributions determined from *in vivo* MP-PQM. The zero-order oxygen consumption (M_0) for the tumors was assumed to be twice that of murine skin. Given the measurements of oxygen consumption (Table IV-3) and gradients in the single vessel profiles (Figure IV-1), this appears to be a good approximation. The source oxygen saturation value was selected for each tissue type from the peak of the oxygen probability distributions measured by MP-PQM. Given the *in vivo* $n(\delta)$, the simulated spatial oxygen profiles and probability distributions for LS174T, MCalV and skin demonstrate striking similarities with the measured profiles and distributions (Figure III-16). The results using LS174T illustrate a transition between normal vascular

networks and the grossly abnormal vasculature found in MCalV. This is reflected also in the shape of $n(\delta)$, which has features found in the distributions for both normal and MCalV vascular networks. Since a distribution of source terms was not applied to the numerical procedure, the oxygen distributions lack the broadness found in the MP-PQM measurements. This is particularly the case for the normal tissue, which is nearly a Dirac delta function.

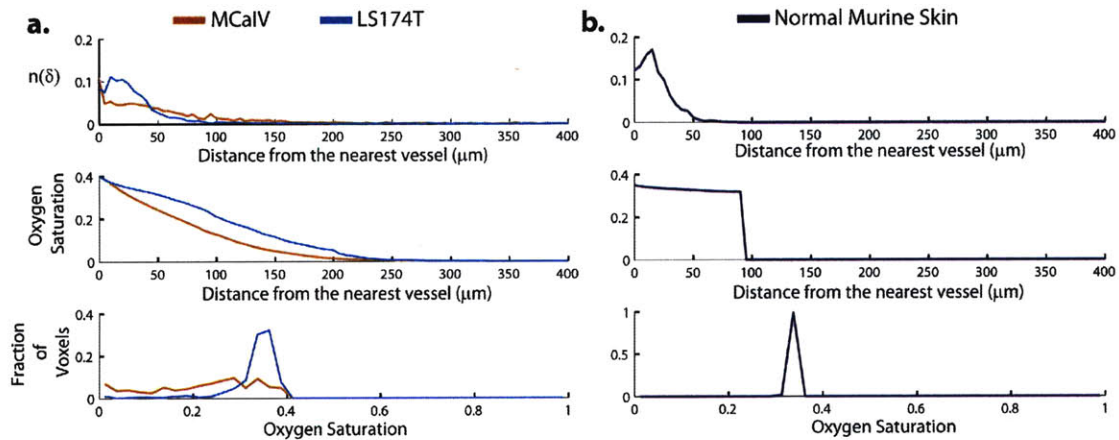


Figure IV-16 Numerical calculation of oxygen profiles and associated oxygen probability distributions from *in vivo* measurements of $n(\delta)$. (a) MCalV and LS174T tumor tissue voxel distribution predict decreasing $p\text{O}_2$ profiles and broadened oxygen distributions. (b) Conversely, tissue voxel distributions for normal murine skin predict a very flat truncated oxygen profile and narrow oxygen distribution.

The oxygen probability distributions for the tumors obtained from the steady-state solutions found using Eq. (IV.20) lack the bimodal distributions observed *in vivo* (Figure IV-15). The limitations due to not accounting for a distribution in oxygen concentrations from the vessels are likely not the only factors affecting these bimodal features. Large heterogeneously distributed hypoxic regions have been demonstrated in tumors by both imaging and histological methods^{84,108-111}. Additionally, the vascular architecture of many of the tumors studied in this chapter display random avascular regions that are hypoxic as measured by MP-PQM (Figure IV-7). This coupled with the findings by myself and others that highly-vascularized regions of the tumor microenvironment are well oxygenated suggests two tissue populations exist⁴⁹.

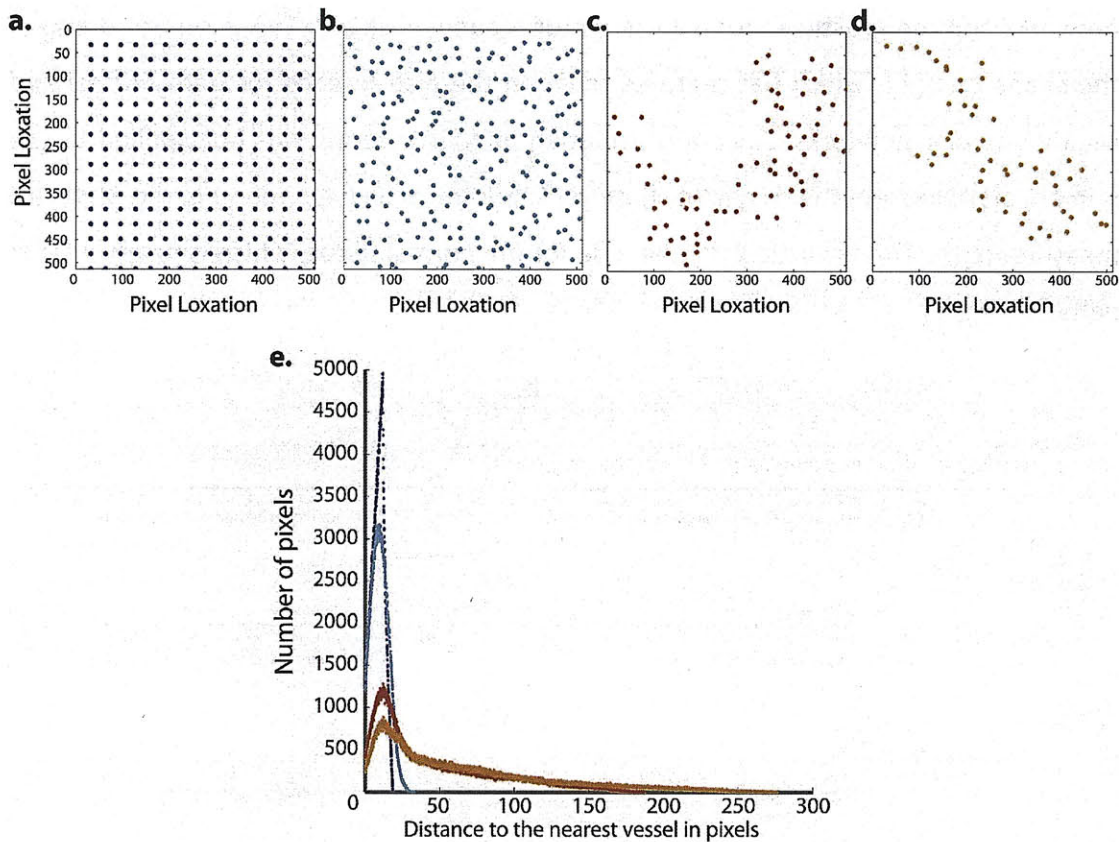


Figure IV-17 Invasion percolation networks reveal large avascular regions and define $n(\delta)$. (a) Regularly spaced capillary network. (b) Normal tissue vascular network with some heterogeneity due to the hierarchical vascular structure. (c) Representative tumor vascular network at the percolation threshold. Large avascular regions outside the diffusion range of oxygen exist. (d) 2D vascular network below the percolation threshold. e. Distance to nearest vessel histograms for $a - d$.

As mentioned, fractal analysis has been used to describe tumor vasculature. However, large avascular regions found in tumors promote deviation of the vascular network from the self-similarity required of fractal analysis. This has been well described using invasion percolation networks to model the growth and transport of vascular networks⁶⁴. This previous study also modeled the transport and diffusion of oxygen in two-dimensions from these networks revealing the presence of significant hypoxic regions. With the invasion percolation model, the introduction of large avascular regions amongst highly vascularized regions is observed as the occupancy of the network is reduced (**Figure IV-17a-d**). These large avascular regions are chronically hypoxic and diffusion of oxygen into them does not occur. However, the highly vascularized regions are likely well oxygenated as observed *in vivo*. This model helps explain the existence of the

bimodal peaks in the oxygen distributions. In fact, even in two-dimensions, defining the structure of the vascular network at various occupancies using invasion percolation demonstrates tissue volume fraction probability distributions, $n(\delta)$, with similar features to those found *in vivo* (Figure IV-17e).

IV.6 Tumor Oxygenation during Targeted Therapy

As previously discussed, fluctuations in the tumor metabolic microenvironment during therapy can have profound implications for optimizing combined treatment regimens. In particular, the application of agents that either directly or indirectly target the tumor vasculature can alter tumor oxygenation. Antiangiogenic therapy, which directly affects endothelial cells, has been shown to promote morphological, architectural, cellular and functional changes in the tumor vasculature^{27,28,33}. In 2001, my thesis advisor, Dr. Jain proposed that judicious application of antiangiogenic therapy can improve vascular function and thereby drug delivery by “normalizing” the vasculature of the tumor^{31,32,34,112}. What remains unanswered is how these changes affect the metabolic microenvironment of the tumor, i.e. does the metabolic microenvironment undergo “normalization”. The application of MP-PQM to multiple tumor models to assess response to targeted therapy reveals insight into alterations in the tumor microenvironment and the potential impact on combined therapies.

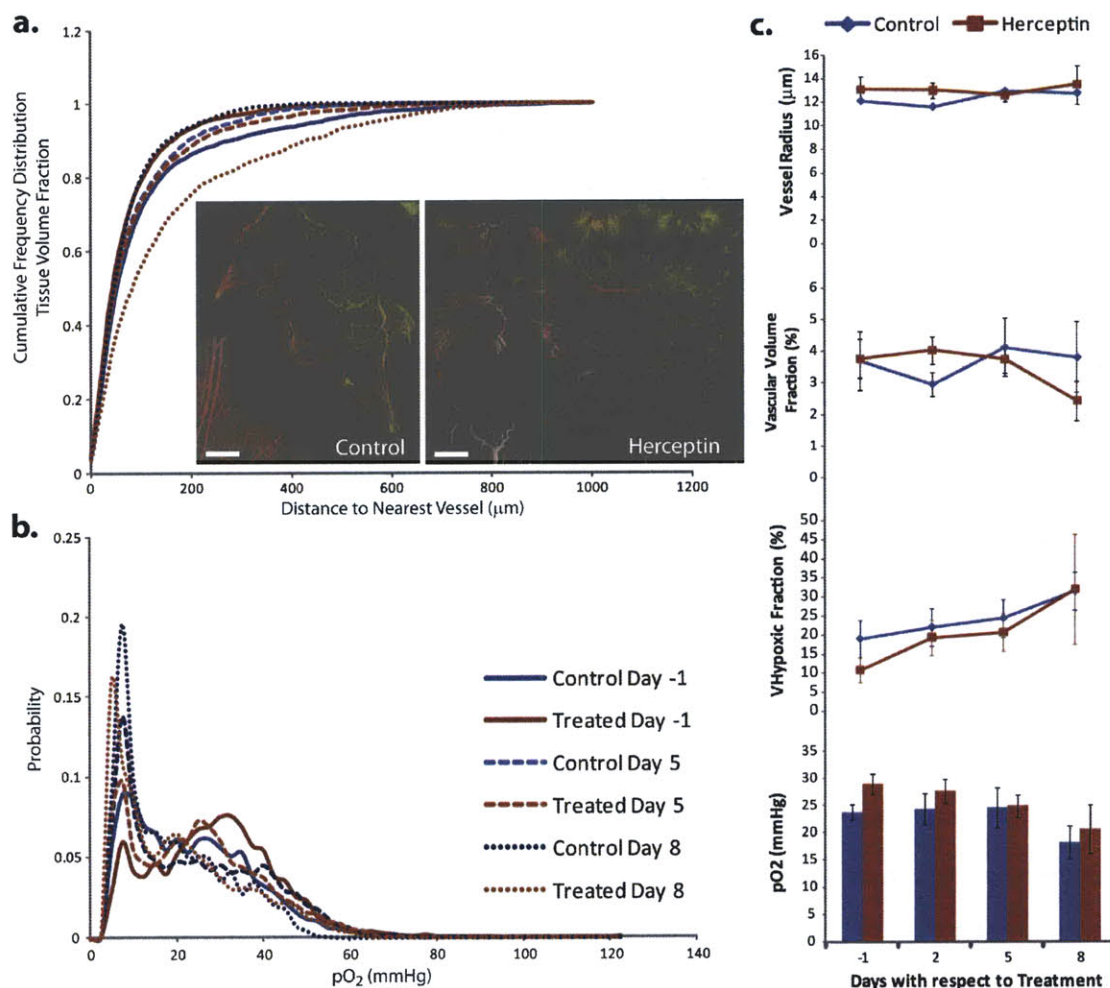


Figure IV-18 Breast tumor response to Herceptin. (a) The CFD of the tissue voxel fraction within a given distance from the nearest vessel during treatment with either trastuzumab or rat IgG. *Inset* – Colorized depth projection of the tumor vasculature in control and treated MDA-MB-361HK tumors. (b) Probability histograms of $p\text{O}_2$ for day -1, 5 and 8 with respect to treatment initiation. (c) Changes in metrics of both the tumor vasculature and oxygenation during treatment. $N = 6-10$, both groups. Scale Bars – $500\mu\text{m}$. Errors are standard error.

IV.6a MEASUREMENT OF $p\text{O}_2$ IN A BREAST TUMOR MODEL DURING THERAPY WITH TRASTUZUMAB

Trastuzumab (Herceptin) inhibits the HER2/neu cell surface receptor, which is over-expressed in a particularly aggressive form of breast cancer¹¹³. Recently, trastuzumab was shown to down-regulate a spectrum of vascular growth factors and in a xenograft metastatic breast cancer model modify the tumor vasculature in a manner analogous to many vascular targeted antiangiogenic agents¹¹⁴. Similar to other single-agent cancer

therapies with antiangiogenic or cytotoxic agents, trastuzumab is likely to modify the tumor metabolic microenvironment.

Using MP-PQM, I monitored the tumor vasculature and pO_2 in mice bearing mammary fat pad window chambers implanted with MDA-MB-361HK treated with either trastuzumab or non-specific rat-IgG. Mice were treated every third day for 3 treatments with MP-PQM occurring a day prior to each treatment timepoint. The overall response to therapy by either angiographic or oxygen measurements was inconclusive (**Figure IV-18**). The vascular structure appeared to exhibit increased avascular regions at the conclusion of the treatment as indicated by the rightward shift in the CFD of the tissue volume fraction at a given distance from the vessels (**Figure IV-18a**). Review of MP angiography revealed no distinct vascular anatomical features between the two treatment groups (**Figure IV-18c**). No statistical difference in mean tumor oxygenation, hypoxic fraction or pO_2 probability distributions was found with therapy (**Figure IV-18b** and **c**). In both groups, the hypoxic fraction increased over time as exemplified in the redistribution of oxygenation to lower values. No trend over time was found to be significant within or between groups.

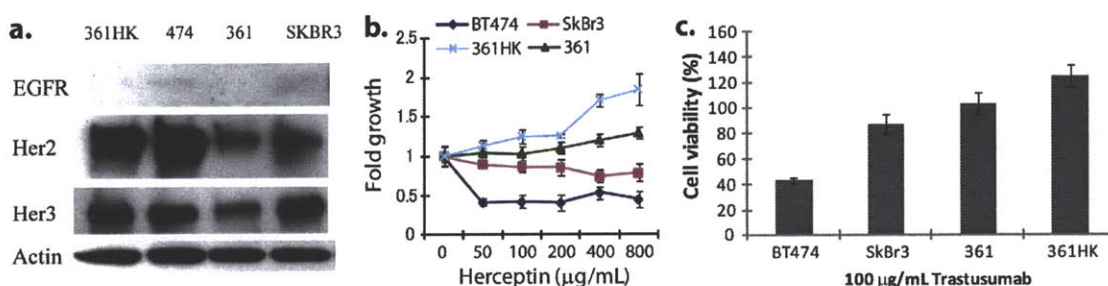


Figure IV-19 In vitro Her2 assay of MDA-MB-361HK in comparison to other cell lines. (a) Western blot of Her2 expression. (b) WST-1 assay of cell proliferation at different media concentrations of trastuzumab. Fold growth is with respect to the cells growing in the absence of antibody. (c) Cell viability of the 100µg dosage from b. 361HK: MDA-MB-361HK; 474: BT474; 361: MDA-MB-361.

The lack of response to trastuzumab was surprising given the same cell line was used by Izumi and co-workers¹¹⁴. Further, another group has recently demonstrated transient increases in pO_2 with trastuzumab treatment in a human cancer cell line induced to over-express HER2/neu¹¹⁵. Either the antibody used was defective and not delivered to

the tumor cells, or the cells are no longer responsive. To differentiate between the two possibilities, MDA-MB-361HK cells were subjected to *in vitro* growth assays in the presence or absence of trastuzumab. The results of these experiments indicate that the growth of the cell line, which still maintains very high levels of HER2 expression, is uncoupled from the HER2 pathway (Figure IV-19). Others have shown *in vitro* inhibition of the MDA-MB-361HK cell line with trastuzumab at doses as low as 100µg/ml¹¹⁶, suggesting that the current cell line must have been altered during passaging.

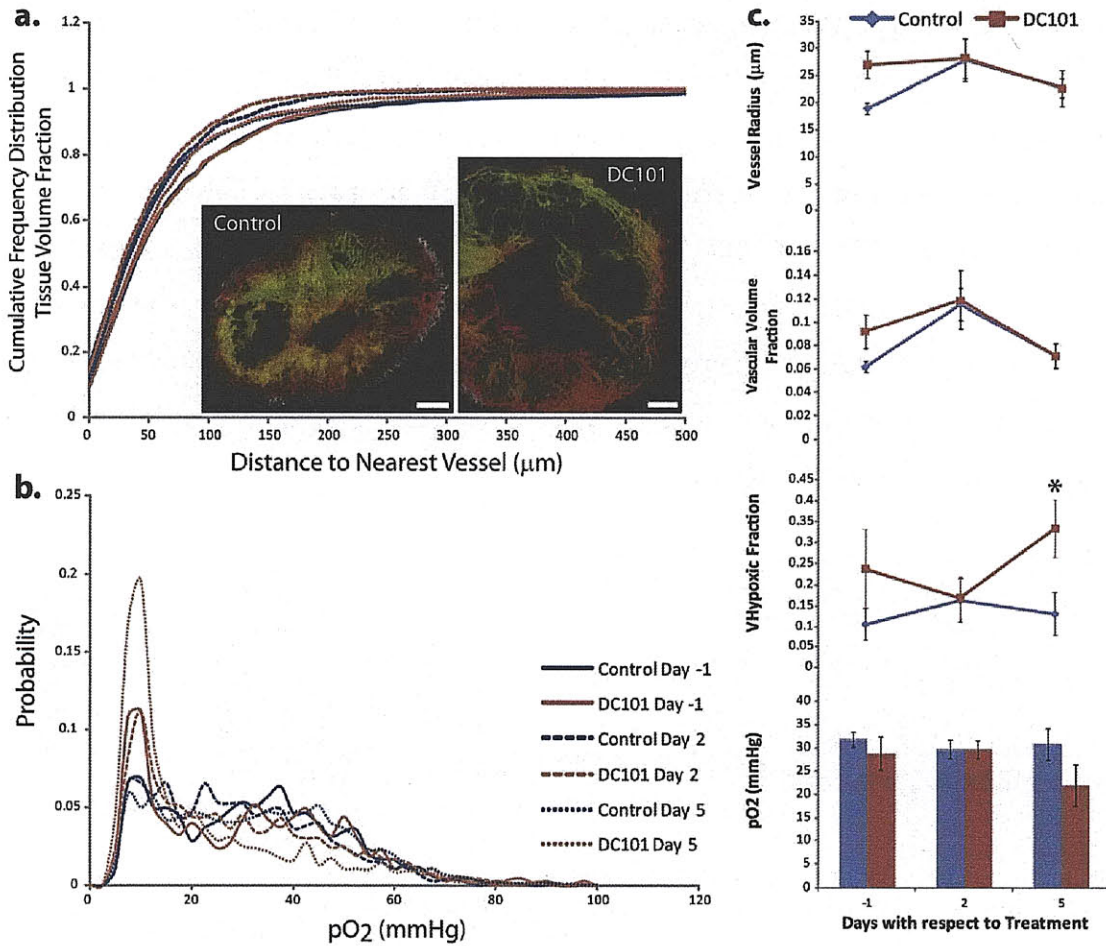


Figure IV-20 Murine mammary carcinoma (MCAIV) response to VEGF-R2 blockade. (a). The CFD of the tissue voxel fraction within a given distance from the nearest vessel during treatment with either DC101 or rat IgG. Inset – Colorized depth projection of the tumor vasculature in control and treated tumors at Day 5. (b). Probability histograms of pO₂ for day -1, 2 and 5 with respect to treatment initiation. (c) Changes in metrics of both the tumor vasculature and oxygenation during treatment. N = 6 Control N = 4 treated. Scale Bars – 500µm. * - P-value < 0.05. Errors are standard error.

IV.6b MEASUREMENT OF PO₂ DURING VEGF-R2 BLOCKADE

Angiogenesis is a fundamental process in the progression of solid tumors. A central regulatory pathway in the process of angiogenesis is that of the vascular endothelial growth factors (VEGF)^{117,118}. Many antiangiogenic therapies have been designed to target either the soluble ligands (bevacizumab)¹¹⁹ or receptors in the VEGF pathway. Blockade of this pathway in animal models has demonstrated decreases in angiogenesis and tumor growth¹²⁰⁻¹²². In preclinical tumor models, an antibody against VEGF-Receptor 2 (VEGF-R2) known as DC101¹²³ has proved successful in combination therapies^{25,26,28,124} and potentially “normalizing” the tumor vasculature²⁷. However, little is known about the spatio-temporal effects of VEGF-R2 blockade on the metabolic microenvironment.

The study of Tong *et al* demonstrated vascular “normalization” in both MCalV and LS174T tumors in SCID mice. “Normalization” in this case was defined by a reduction in vascular diameter, vessel length density, permeability and interstitial fluid pressure, all of which are typically increased in tumors. I performed survey studies on the effect of treatment by DC101 in these two tumor types. In a treatment schedule analogous to the trastuzumab study, I administered DC101 every three days for 3 timepoints. Similarly, imaging with MP-PQM was performed a day prior to each treatment.

In the case of the murine mammary carcinoma (MCalV) implanted in the DSC, the vascular architecture appeared to change by visual inspection for most tumors. However this was not reflected in the quantitative parameters (**Figure IV-20a and b**). By Day 5, the mean tumor oxygenation decreased in the treated tumors. A shift to lower pO₂ is reflected in the redistribution of the oxygen probabilities to more hypoxic values (**Figure IV-20b**). Further, a statistical difference is observed in hypoxic fraction between the two groups.

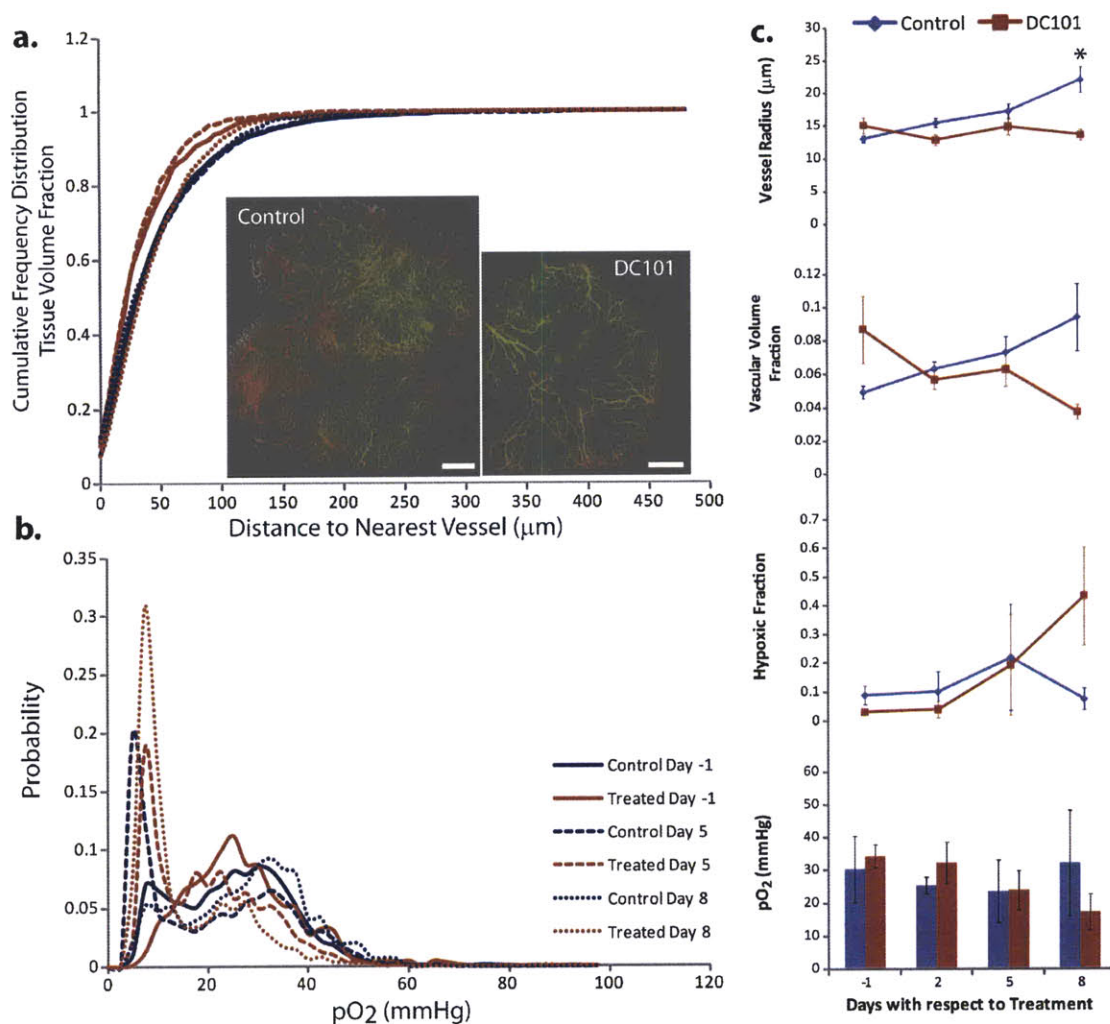


Figure IV-21 Human colorectal adenocarcinoma xenograft (LS174T) response to VEGF-R2 blockade. (a) The CFD of the tissue voxel fraction within a given distance from the nearest vessel during treatment with either DC101 or rat IgG. *Inset* – Colorized depth projection of the tumor vasculature in control and treated tumors at Day 8. (b) Probability histograms of pO_2 for day -1, 5 and 8 with respect to treatment initiation. (c) Changes in metrics of both the tumor vasculature and oxygenation during treatment. $N = 4-10$ Control $N = 3$ treated. Scale Bars – 500 μm . * - P -value < 0.05. Errors are standard error.

The response of the human colorectal adenocarcinoma xenograft, LS174T, followed the same trends as MCalV with decreasing oxygenation and increasing hypoxic fraction (Figure IV-21). Visually, the vasculature was strikingly different at day 8 between the DC101 treated and control tumors. This was reflected in analysis of the vascular morphology which revealed a significant difference in diameter by Day 8 and a trend toward separation in the vascular volume fractions (Figure IV-21c). In the control group, the growth in both vascular diameter and volume fraction were significant over time (P -

value < 0.05). Again MP-PQM revealed an increasing hypoxic fraction and redistribution of the overall tumor oxygenation to lower values in the DC101 treated group. However, these trends were not significant over the course of the experiment.

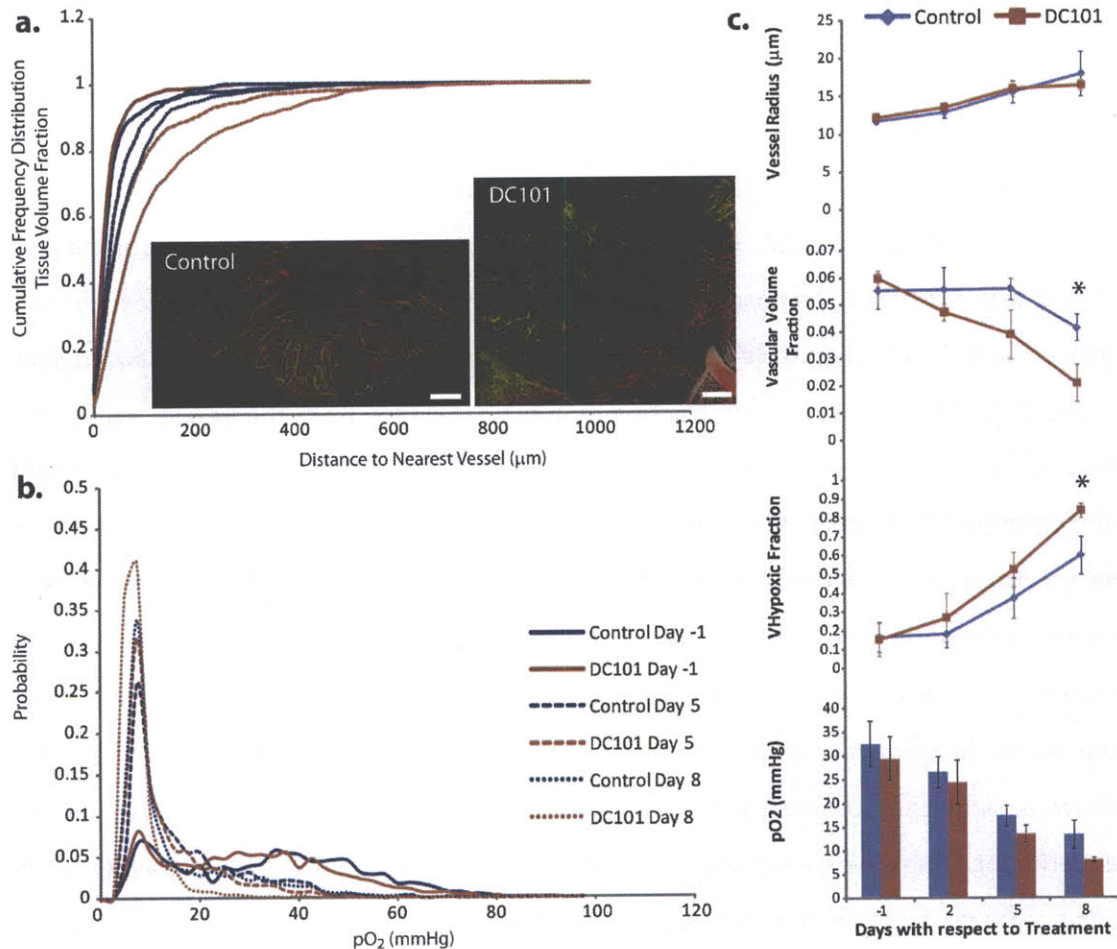


Figure IV-22 Orthotopic murine mammary adenocarcinoma (EO771) response to VEGF-R2 blockade. (a) The CFD of the tissue voxel fraction within a given distance from the nearest vessel during treatment with either DC101 or rat IgG. *Inset* – Colorized depth projection of the tumor vasculature in control and treated tumors at Day 8. (b) Probability histograms of pO₂ for day -1, 5 and 8 with respect to treatment initiation. (c) Changes in metrics of both the tumor vasculature and oxygenation during treatment. *N* = 4-5 Control *N* = 4-5 treated. Scale Bars – 500μm. * - *P*-value < 0.05. Errors are standard error.

The previous tumor models treated with DC101 were implanted in an ectopic location (skin) and in the case of LS174T a human tumor xenograft. The effect of the host tissue microenvironment has been shown to play a role in angiogenesis and the progression of disease for many tumor types, including breast cancer^{1,125,126}. The metabolic

microenvironment is different depending upon the surrounding stromal cells and tissue structure. Therefore, the response to therapy likely depends upon the tissue in which the tumor is growing.

To eliminate the issues associated with the potential effects of the host tissue microenvironment, I repeated the DC101 experiment with a syngeneic murine mammary adenocarcinoma (EO771) implanted in the mammary fat pad of female SCID mice. The experimental course was identical to that previously applied to the other tumors treated with DC101. In this tumor model, the response of the vasculature to DC101 was dramatic. The vascular network was almost entirely pruned in most tumors treated with DC101 (**Figure IV-22a**). This effect is readily apparent in the rightward shift in the CFD of the tissue volume fraction at a given distance from the vessels across the treatment duration. This indicates increasing avascular regions as seen in MPM angiography. While vascular volume fraction is significantly different by Day 8, the mean vessel diameters between groups did not change (**Figure IV-22c**). In fact the average vessel diameter in EO771 tumors was only slightly larger than those found in the normal mammary fat pad ($\sim 10\mu\text{m}$). Because a significant portion of vessels are pruned away, the tumor oxygenation drops over time. However, the two treatment groups did not show a significant difference at any time point or over the entire course of the experiment. There was a significant difference in the hypoxic fraction at Day 8, which again can be seen in a redistribution of the pO_2 to lower levels (**Figure IV-22b**). Interestingly the tumors continued to grow in the DC101 treated group although at a slower rate than the controls based on observations of the enface tumor diameter.

Overall, the administration of DC101 to each tumor type at the dose used in previous studies decreased tumor oxygenation. However, it is apparent, particularly in the EO771 experiment, that DC101 significantly inhibited angiogenesis and promoted regression of the vascular network (**Figure IV-23**). This effect is not observed in human patients treated with antiangiogenic agents like bevacizumab (Avastin) due to toxicity levels at the doses required^{29,30,127}. These results suggest that for “normalization” of the tumor

microenvironment to occur, the antiangiogenic agent needs to be titrated to prevent complete abolition of the tumor vasculature. At lower doses it is possible that the tumor oxygenation may increase if the vascular supply is made more efficient.

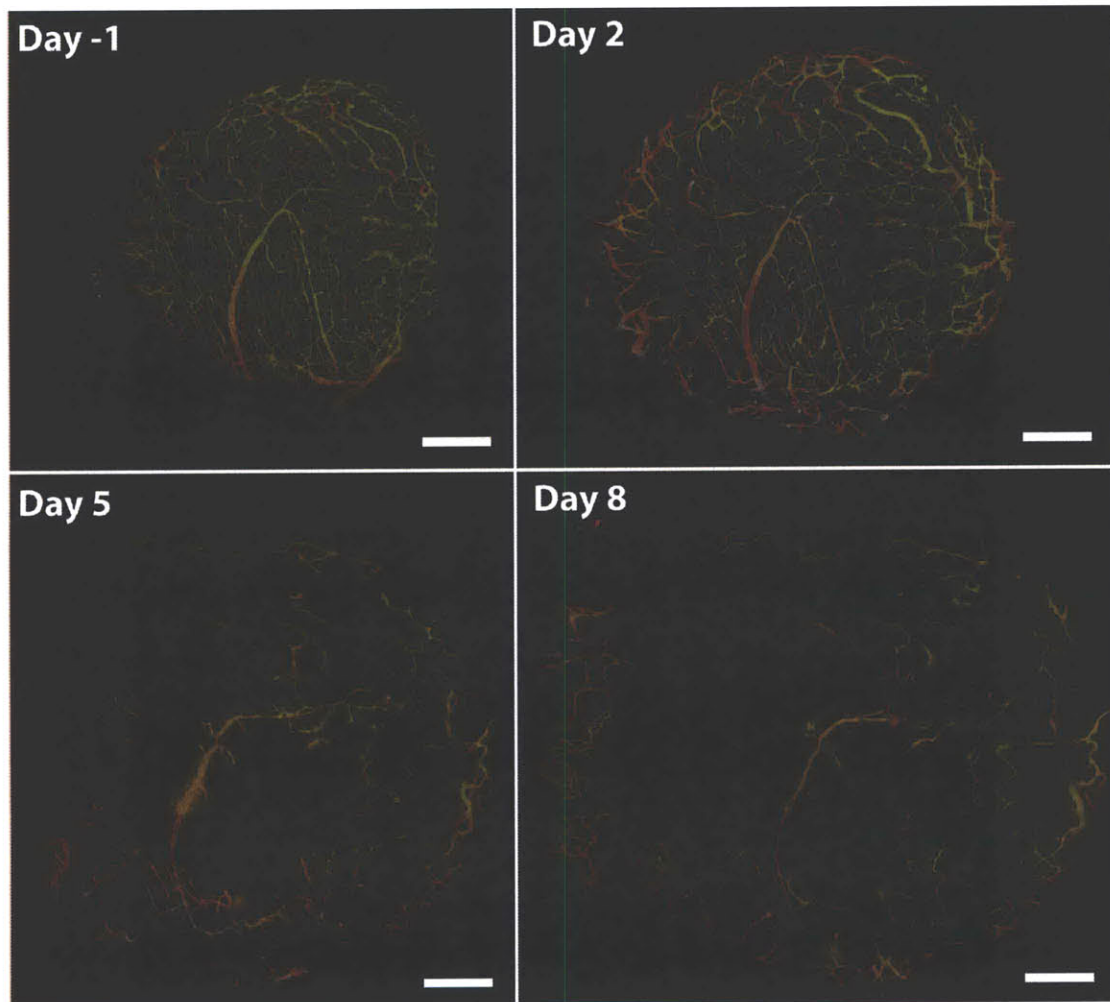


Figure IV-23 Pruning of the vascular network in an EO771 tumor by VEGF-R2 blockade with DC101. Multiphoton angiography images are presented as colorized depth projections (green-red-white). Scale Bars - 500 μ m.

IV.7 Summary

In this Chapter, I have applied the technique of multiphoton phosphorescence quenching microscopy developed in Chapter III to study the metabolic microenvironment during tumor progression and response to targeted therapy. Oxygen tension profiles from single vessels in normal and neoplastic tissue were acquired. The

profiles in a melanoma tumor uniformly demonstrated lower pO_2 values from the vessel wall into the interstitial space than those found in normal tissue. In fact, pO_2 gradients in normal tissue were difficult to obtain unless adjacent vessels were occluded using nanovascular surgery techniques with the multiphoton microscope.

Because tumors display spatially heterogeneous fluctuations in blood flow over relatively short time periods, relying on a limited number of pO_2 gradients from single vessels reveals only a small part of the tumor metabolic microenvironment. The high three-dimensional resolution and deep penetration ($\sim 400\mu\text{m}$) of MP-PQM permitted oxygen tension mapping in three-dimensional space over large regions ($4 \times 4\text{mm}$) of the tumor. Coupling the pO_2 maps with angiography performed by MPM allowed correlation of the pO_2 measurements with morphometric analysis of the tumor vasculature. Correlation of pO_2 with vascular metrics demonstrated a lack of correlation with vascular diameter and a strong negative correlation with distance from the blood vessel. Fitting a one-dimensional diffusion-reaction model for oxygen to the spatial distribution of pO_2 from the blood vessels allowed quantification of average tumor oxygen consumption. A range of oxygen consumption rates was observed for different tumor types that in many cases increased with tumor progression.

The vascular networks and oxygen tension mapping was compared across tumors. In almost all cases, angiogenesis occurred as defined by an increase in both vascular diameter and volume fraction during tumor growth. However, different tumor types displayed various degrees of correlation with the tumor vasculature during the process of angiogenesis. In some tumors, the vascular diameter correlated significantly with hypoxic fraction, while in others the VVf displayed a negative correlation. Interestingly, the human colorectal adenocarcinoma displayed a significant correlation of pO_2 with the mean distance from hypoxic regions to the nearest vessel. Applying the depth sectioning ability of MPM to the oxygen measurements allowed changes in mean pO_2 at given depths in the tumor to be observed during growth. This revealed that often the tumor surface remained well-oxygenated, while the deep core decreased in oxygen content.

Quantitative assessment of the vascular architecture through the use of a simple metric describing the tissue volume fraction at a given distance from the closest blood vessel was shown to predict the tumor oxygenation measured by MP-PQM. Using a generalized formula for oxygen diffusion based on the spatial probability distribution of tissue volume with respect to the vessels simulations of both the tumor oxygen gradient and probability distribution were performed. The results exhibited good agreement with *in vivo* measurements in most cases except for an increasing redistribution to hypoxic oxygenation in the tumor oxygen probability distributions. The bimodal nature of these oxygen distributions is most probably due to the existence of two tissue populations (normoxic and hypoxic) in the tumor microenvironment. Describing tumor vascular networks using an invasion percolation model reveals large avascular regions exist in tumors that have spatial probability distributions of tissue volume with features identical to those found in living tumors.

Finally, the metabolic microenvironment was probed with MP-PQM during targeted therapy. Treating a human breast cancer xenograft model with trastuzumab revealed minimal changes in both vascular metrics and tumor oxygenation. Further experiments demonstrated that the cell line previously used in other studies no longer responded to trastuzumab even though the drug target (HER2) was still over-expressed. Antiangiogenic therapy in the form of VEGF-R2 blockade (DC101) was then administered to 3 other tumor models including an orthotopic murine mammary adenocarcinoma. The results of these studies demonstrated that antiangiogenic therapy with DC101 reduced both vascular volume fraction and tumor oxygenation. These outcomes suggest that antiangiogenic therapies should be titrated for a limited dose response for potential “normalization” of the tumor metabolic microenvironment.

IV.8 Materials and Methods

IV.8a ANIMAL MODELS

Dorsal skinfold chambers (DSC) were prepared on male SCID mice using previously described methods¹²⁸. Mammary fat pad windows were prepared in SCID mice as previously described¹²⁹. Briefly, prior to chamber implantation, the entire lateral flank of the animal is shaved and depilated and the third nipple from the top is identified. A fold is formed which contains the skin and nipple, mammary gland, adipose tissue and cutaneous muscle layers on one side and the dorsal skin, adipose tissue and cutaneous muscle layers on the other side. Two symmetrical titanium frames (weight 2.5 g; Workshop, Department of Radiation Oncology, MGH), which are mirror images of each other, are implanted centered over the third nipple so as to sandwich the extended double layer of skin. A layer of skin on the dorsal surface is dissected in a circular area approximately 15 mm in diameter to reveal the fascial plane of the internal mammary vein. The remaining layer of tissue, consisting of epidermis with nipple, subcutaneous tissue, and mammary fat pad is covered with a glass coverslip incorporated into one of the frames. Following implantation of the transparent access chamber, animals are allowed to recover from microsurgery and anesthesia for 48 hours before tumor implantation or intravital microscopy.

For both models, the appropriate tumor type was then implanted in the center of the chamber 2-3 days after the initial surgery. The murine mammary adenocarcinomas (MCAIV and EO771), and human colorectal adenocarcinoma (LS174T) were transplanted from subcutaneous tumors grown in isogenic mice. The human mammary adenocarcinoma (MDA-MB-361HK) was implanted as a single cell suspension of $\sim 3 \times 10^6$ cells in 30 μ l of Hank's Buffered Salt Solution (HBSS).

Cranial windows were prepared in nude mice as previously described¹³⁰. In SCID mice, the surface of the skin atop the skull is depilated and sanitized with antimicrobial solution. After stereotaxically fixing the mouse skull, a longitudinal incision of the skin is

made between the occiput and forehead. Then the skin is cut in a circular manner on top of the skull, and the periosteum underneath is scraped off to the temporal crests. A 6-mm circle of the skull over the frontal and parietal lobes is removed using a high speed air-turbine drill (CH4201S; Champion Dental Products, Placentia, CA) with a burr-tip 0.5 mm in diameter. After careful removal of the bone flap from the dura mater, the dura and arachnoid membranes are cut completely from the surface of both hemispheres, avoiding any damage to the sagittal sinus. The window is sealed with a 6-mm cover glass which is glued to the bone with histocompatible cyanoacrylate glue.

Animals were anesthetized with Ketamine/Xylene(10/1 mg/ml) for surgeries and Isoflurane (1% in medical grade air) for all experiments. All animal work was approved by the MGH institutional review board on animal care.

IV.8b MP-PQM

The principles and application of multiphoton phosphorescence quenching microscopy was described in detail in the previous Chapter. MP-PQM was performed with a custom-modified confocal laser scanning microscope (Olympus 300; Optical Analysis Corp., Center Valley, PA) using a broadband femtosecond source (High Performance MaiTai, SpectraPhysics, Mountain View, CA) using a 25 \times , 0.95 NA water emersion lens (Olympus XLUMPlanFI, Optical Analysis, Center Valley, PA) for imaging. Excitation pulses for time-domain measurement of phosphorescence lifetime were selected using a Pockel's Cell (ConOptics, Model: 350-50; Conoptics, Inc., Danbury, CT) driven by custom electronics and a digital pulse delay generator (DG535, SRS, Sunnyvale, CA). Phosphorescence emission was detected through a 690/90 emission filter (690/90M, Chroma Technology Corp., Rockingham, VT) using a GaAs photon counting PMT (H7421P-50, Hamamatsu, Inc., Bridgewater, NJ). Counts were binned and accumulated for 2500 repetitions using a multichannel scaler (SR430, SRS, Sunnyvale, CA). All experimental protocols were automated using custom instrumentation control created in LabView (National Instruments, Austin, TX). Lifetimes were fit in real-time using built-in MatLab (MathWorks, Natick, MA) code in order to display the tissue oxygenation.

To prepare animals for MP-PQM measurements, a mixture (200 μ l) of 10mg/ml Oxyphor R2 (Oxygen Enterprises Ltd, Philadelphia, PA) was injected retro-orbitally using a 28.5G needle. This allows the sensor to diffuse into the tumor, where it binds to proteins in the interstitium. Fifteen minutes prior to MP-PQM measurements, the animal was anesthetized by Isoflurane (3% for 4 minutes) administered as an inhalant, Immediately following a mixture (200 μ l) of 10mg/ml Oxyphor R2 with 8mg/ml 2M MW FITC-dextran was injected retro-orbitally. This allows both highlighting the vasculature and real-time measurements of pO₂.

For oxygen profiles from single vessels, the laser beam was parked at given distances (5-10 μ m steps) from the vascular wall. Five to ten repeated measurements were then collected at each point. For oxygen tension maps, a rectangular region of interest was manually selected using a motorized stage and input into the control software. An automated series of mosaic multiphoton microscopy images was then collected covering the ROI. Each image contained an axial series up to 400 μ m deep in the tissue at a 5 μ m step size. Following collection of the angiography, phosphorescence lifetime measurements were performed in a series of 144 points based on a 12 \times 12 covering the ROI at four equally spaced depth planes. Total data collection time ranged from two to three hours depending upon the size of the ROI.

IV.8c OXYGEN TENSION MAPPING DATA ANALYSIS

Prior to processing the oxygen measurements, the angiography images were prepared and analyzed. A depth projection was created of each individual mosaic MPM image and semi-manually assembled in ImageJ (NIH, Bethesda, MD) using the MosaicJ plugin. Custom code written in Matlab employs the log file from the MosaicJ output to assemble the entire three-dimensional mosaic image stack. Overlap between adjacent images was blended using an intensity weighting procedure based from the center of the panel outward. Often times, angiographic contrast agent extravasates from the permeable tumor vessels obscuring vessels below. To eliminate this artifact in preparation of vascular tracing, a binary mask of the mosaic image was semi-manually

created in ImageJ. A final mosaic image was created from the original MPM image mosaic stack and the binary mask. Colorized depth projections were created from this processed image using custom code in Matlab. Each depth layer was assigned to a colormap level, opacity factor (for superficial depths) and corrected for optical scattering loss by an exponential factor. Semi-automated vascular tracing was performed on the mosaic image stack using an algorithm that models vascular segments as superellipsoids to obtain three-dimensional trajectories and morphology^{50,85}.

The output of the tracing algorithm was then correlated with each individual oxygen measurement to quantify distance to nearest vessel and diameter of that vessel. Phosphorescence lifetimes were determined by fitting to a two-component exponential decay model to find the fraction of free and bound Oxyphor R2. Oxygen tension values were then calculated using the Stern-Volmer relationship and the quenching constant and anoxic lifetime determined from *in vitro* calibrations (Chapter III). Oxygen tension maps were then created in Matlab using custom code to overlay the mesh grid of pO₂ values with the outlines of the vascular tracing. Mean oxygen tension was determined over all the measurements and at each depth plane at which they were acquired. Oxygen consumption was calculated by fitting the one-dimensional diffusion-reaction equation [Eq. (IV.2)] to the scatter plot of all pO₂ measurements versus distance to closest vessel. A nonlinear Levenburg-Marquardt algorithm was employed in Matlab to determine Q_{O₂}. The probability distribution of the number of tissue voxels at a given distance from the closest vessel was calculated from distance maps obtained from the traced vasculature. The tumor oxygen profile was determined using a sliding averaging procedure with a 10mmHg window and 2.5mmHg stepsize in Matlab. For each tumor type, the distributions are a collection of all tumors imaged at that time-point or within a specific treatment group.

IV.8d NUMERICAL SIMULATIONS OF OXYGEN PROFILES AND DISTRIBUTIONS FROM IN VIVO MEASUREMENTS

Using Matlab, the finite volume method was employed to numerically solve for the generalized oxygen diffusion equation based on the tissue volume fraction spatial distribution. The derivations of the appropriate formulas were described in detail in Section IV.5b. For test functions, the integration time step could be selected at fairly long times. The time-integration procedure was allowed to iterate until steady state was reached. This was defined as no change in the oxygen concentration profile if the maximum integration time was increased. For *in vivo* data, the time-step needed to be reduced due to irregular features requiring more precise integration steps. The minimum time-step was determined by comparing steady-state results at the same time for multiple time steps. Once the steady-state oxygen concentration profile was reached with no change between time steps, the minimum step was selected. Oxygen probability distributions were determined using the numerically determined oxygen gradient and the spatial probability distribution of tissue volume.

IV.8e INVASION PERCOLATION MODEL

The invasion percolation model accounts for the connectivity of a vascular network according to occupied points on a two- or three-dimensional lattice⁶⁴. Essentially, the invasion percolation network grows along paths of least resistance according to randomly assigned “strength” values to each lattice point. The process is repeated until a given fraction of lattice points are occupied. A vascular network is then described by connecting each adjacent lattice point by a vessel segment. Flow through the network is then simulated through one arbitrarily designated point on the lattice and segments with zero flow are pruned. All simulations were performed using MatLab.

IV.8f TARGETED THERAPIES

Trastuzumab (Herceptin) was obtained by patient donations through the MGH oncology pharmacy. Female SCID mice bearing MFP chambers implanted with MDA-MB-361HK

CHAPTER 4

tumors were treated with trastuzumab or nonspecific rat IgG administered intraperitoneally at 30mg/kg as previously prescribed in this tumor type¹¹⁴. In the other tumor models, antiangiogenic VEGF-R2 blockade treatments with DC101 (ImClone Systems Inc., New York, NY) or nonspecific rat IgG were administered intraperitoneally at 40mg/kg as prescribed in previous studies²⁷. Mice were imaged the day immediately prior to each treatment. Therapeutic initiation was determined through monitoring of tumor growth by visual inspection of the enface tumor diameter and angiogenesis of the tumor. Animals were selected based on the criteria that 1) the tumor diameter was approximately 4mm in diameter 2) the entire core of the tumor was functionally vascularized and 3) the animal was in good health. Three treatments at three-day intervals were given (defined as day 0, 3, 6), and imaging was performed through day 8.

IV.8g IN VITRO TRASTUZUMAB INHIBITION ASSAY

MDA-MB-361HK cells were seeded in a 96-well plate (10,000 cells/well) in 10% Dulbecco's modified eagle medium (DMEM). The following day, the cells were treated with trastuzumab (0-800 μ g/ml) in 5% DMEM. After six days, the number of viable cells was determined by a WST-1 proliferation assay (Cat. No 11 644 807 001), Roche Diagnostics Corp., Indianapolis, IN). The concentration of the free formazan dye cleaved by viable cells from WST-1 was quantified at 480/600nm in a (Benchmark plus, Bio-Rad Life Science Research, Hercules, CA) plate reader.

IV.8h STATISTICAL ANALYSIS

Data are presented as mean \pm standard error of the mean (SEM). Significant differences between groups were assessed by a multivariate repeated measures ANOVA accounting for response to treatment over time (Systat, Systat Software, Inc., Chicago, IL). Individual timepoints were compared using a two sample Student's t-Test. $P < 0.05$ was considered statistically significant for all comparisons. All correlations were determined using the Pearson product-moment correlation.

IV.9 References

1. Kallinowski, F., *et al.* Blood flow, metabolism, cellular microenvironment, and growth rate of human tumor xenografts. *Cancer Res* **49**, 3759-3764 (1989).
2. Vaupel, P., Kallinowski, F. & Okunieff, P. Blood flow, oxygen and nutrient supply, and metabolic microenvironment of human tumors: a review. *Cancer Res* **49**, 6449-6465 (1989).
3. Brizel, D.M., Sibley, G.S., Prosnitz, L.R., Scher, R.L. & Dewhirst, M.W. Tumor hypoxia adversely affects the prognosis of carcinoma of the head and neck. *Int J Radiat Oncol Biol Phys* **38**, 285-289 (1997).
4. Loncaster, J.A., *et al.* Carbonic anhydrase (CA IX) expression, a potential new intrinsic marker of hypoxia: correlations with tumor oxygen measurements and prognosis in locally advanced carcinoma of the cervix. *Cancer Res* **61**, 6394-6399 (2001).
5. Swinson, D.E., *et al.* Carbonic anhydrase IX expression, a novel surrogate marker of tumor hypoxia, is associated with a poor prognosis in non-small-cell lung cancer. *J Clin Oncol* **21**, 473-482 (2003).
6. Vaupel, P. Hypoxia and aggressive tumor phenotype: implications for therapy and prognosis. *Oncologist* **13 Suppl 3**, 21-26 (2008).
7. Chan, D.A. & Giaccia, A.J. Hypoxia, gene expression, and metastasis. *Cancer Metastasis Rev* **26**, 333-339 (2007).
8. Dachs, G.U. & Tozer, G.M. Hypoxia modulated gene expression: angiogenesis, metastasis and therapeutic exploitation. *Eur J Cancer* **36**, 1649-1660 (2000).
9. Rofstad, E.K., Galappathi, K., Mathiesen, B. & Ruud, E.B. Fluctuating and diffusion-limited hypoxia in hypoxia-induced metastasis. *Clin Cancer Res* **13**, 1971-1978 (2007).
10. Sullivan, R. & Graham, C.H. Hypoxia-driven selection of the metastatic phenotype. *Cancer Metastasis Rev* **26**, 319-331 (2007).
11. Graeber, T.G., *et al.* Hypoxia-mediated selection of cells with diminished apoptotic potential in solid tumours. *Nature* **379**, 88-91 (1996).
12. Harris, A.L. Hypoxia--a key regulatory factor in tumour growth. *Nat Rev Cancer* **2**, 38-47 (2002).
13. Marx, J. Cell biology. How cells endure low oxygen. *Science* **303**, 1454-1456 (2004).
14. Pouyssegur, J., Dayan, F. & Mazure, N.M. Hypoxia signalling in cancer and approaches to enforce tumour regression. *Nature* **441**, 437-443 (2006).
15. Fukumura, D., *et al.* Hypoxia and acidosis independently up-regulate vascular endothelial growth factor transcription in brain tumors in vivo. *Cancer Res* **61**, 6020-6024 (2001).
16. Tsuzuki, Y., *et al.* Vascular endothelial growth factor (VEGF) modulation by targeting hypoxia-inducible factor-1alpha--> hypoxia response element--> VEGF cascade differentially regulates vascular response and growth rate in tumors. *Cancer Res* **60**, 6248-6252 (2000).
17. Li, X.F., *et al.* Visualization of hypoxia in microscopic tumors by immunofluorescent microscopy. *Cancer Res* **67**, 7646-7653 (2007).
18. Li, X.F. & O'Donoghue, J.A. Hypoxia in microscopic tumors. *Cancer Lett* **264**, 172-180 (2008).
19. Weinberg, R.A. *The biology of cancer*, (Garland Science, New York, 2007).
20. Barnhart, B.C. & Simon, M.C. Metastasis and stem cell pathways. *Cancer Metastasis Rev* **26**, 261-271 (2007).

CHAPTER 4

21. Gray, L.H., Conger, A.D., Ebert, M., Hornsey, S. & Scott, O.C. The concentration of oxygen dissolved in tissues at the time of irradiation as a factor in radiotherapy. *Br J Radiol* **26**, 638-648 (1953).
22. Teicher, B.A., Lazo, J.S. & Sartorelli, A.C. Classification of antineoplastic agents by their selective toxicities toward oxygenated and hypoxic tumor cells. *Cancer Res* **41**, 73-81 (1981).
23. Carmeliet, P. & Jain, R.K. Angiogenesis in cancer and other diseases. *Nature* **407**, 249-257 (2000).
24. Hansen-Algenstaedt, N., et al. Tumor oxygenation in hormone-dependent tumors during vascular endothelial growth factor receptor-2 blockade, hormone ablation, and chemotherapy. *Cancer Res* **60**, 4556-4560 (2000).
25. Kozin, S.V., et al. Vascular endothelial growth factor receptor-2-blocking antibody potentiates radiation-induced long-term control of human tumor xenografts. *Cancer Res* **61**, 39-44 (2001).
26. Lee, C.G., et al. Anti-Vascular endothelial growth factor treatment augments tumor radiation response under normoxic or hypoxic conditions. *Cancer Res* **60**, 5565-5570 (2000).
27. Tong, R.T., et al. Vascular normalization by vascular endothelial growth factor receptor 2 blockade induces a pressure gradient across the vasculature and improves drug penetration in tumors. *Cancer Res* **64**, 3731-3736 (2004).
28. Winkler, F., et al. Kinetics of vascular normalization by VEGFR2 blockade governs brain tumor response to radiation: role of oxygenation, angiopoietin-1, and matrix metalloproteinases. *Cancer Cell* **6**, 553-563 (2004).
29. Jain, R.K., Duda, D.G., Clark, J.W. & Loeffler, J.S. Lessons from phase III clinical trials on anti-VEGF therapy for cancer. *Nat Clin Pract Oncol* **3**, 24-40 (2006).
30. Willett, C.G., et al. Complete pathological response to bevacizumab and chemoradiation in advanced rectal cancer. *Nat Clin Pract Oncol* **4**, 316-321 (2007).
31. Jain, R.K. Normalizing tumor vasculature with anti-angiogenic therapy: a new paradigm for combination therapy. *Nat Med* **7**, 987-989 (2001).
32. Jain, R.K. Normalization of tumor vasculature: an emerging concept in antiangiogenic therapy. *Science* **307**, 58-62 (2005).
33. Jain, R.K. Antiangiogenic therapy for cancer: current and emerging concepts. *Oncology (Williston Park)* **19**, 7-16 (2005).
34. Jain, R.K. Taming Vessels to Treat Cancer. *Scientific American* **298**, 56-63 (2008).
35. Helmlinger, G., Yuan, F., Dellian, M. & Jain, R.K. Interstitial pH and pO₂ gradients in solid tumors in vivo: high-resolution measurements reveal a lack of correlation. *Nat Med* **3**, 177-182 (1997).
36. Ziemer, L.S., Lee, W.M., Vinogradov, S.A., Sehgal, C. & Wilson, D.F. Oxygen distribution in murine tumors: characterization using oxygen-dependent quenching of phosphorescence. *J Appl Physiol* **98**, 1503-1510 (2005).
37. Tsai, A.G., Cabrales, P., Winslow, R.M. & Intaglietta, M. Microvascular oxygen distribution in awake hamster window chamber model during hyperoxia. *Am J Physiol Heart Circ Physiol* **285**, H1537-1545 (2003).
38. Tsai, A.G., Johnson, P.C. & Intaglietta, M. Oxygen gradients in the microcirculation. *Physiol Rev* **83**, 933-963 (2003).
39. Vinogradov, S.A.F.-S., M.A.; Dugan, B.W.; Wilson, D.F. Frequency domain instrument for measuring phosphorescence lifetime distributions in heterogeneous samples. *Review of Scientific Instruments* **72**, 3396-3406 (2001).

40. Koch, C.J. Measurement of absolute oxygen levels in cells and tissues using oxygen sensors and 2-nitroimidazole EF5. *Methods Enzymol* **352**, 3-31 (2002).
41. Sacconi, L., *et al.* In vivo multiphoton nanosurgery on cortical neurons. *J Biomed Opt* **12**, 050502 (2007).
42. Wang, B.G. & Halbhuber, K.J. Corneal multiphoton microscopy and intratissue optical nanosurgery by nanojoule femtosecond near-infrared pulsed lasers. *Ann Anat* **188**, 395-409 (2006).
43. Galbraith, J.A. & Terasaki, M. Controlled damage in thick specimens by multiphoton excitation. *Mol Biol Cell* **14**, 1808-1817 (2003).
44. Cardenas-Navia, L.I., *et al.* The pervasive presence of fluctuating oxygenation in tumors. *Cancer Res* **68**, 5812-5819 (2008).
45. Intaglietta, M., Myers, R.R., Gross, J.F. & Reinhold, H.S. Dynamics of microvascular flow in implanted mouse mammary tumours. *Bibl Anat*, 273-276 (1977).
46. Lanzen, J., *et al.* Direct demonstration of instabilities in oxygen concentrations within the extravascular compartment of an experimental tumor. *Cancer Res* **66**, 2219-2223 (2006).
47. Pogue, B.W., Paulsen, K.D., O'Hara, J.A., Wilmot, C.M. & Swartz, H.M. Estimation of oxygen distribution in RIF-1 tumors by diffusion model-based interpretation of pimonidazole hypoxia and eppendorf measurements. *Radiat Res* **155**, 15-25 (2001).
48. Kirkpatrick, J.P., Brizel, D.M. & Dewhirst, M.W. A mathematical model of tumor oxygen and glucose mass transport and metabolism with complex reaction kinetics. *Radiat Res* **159**, 336-344 (2003).
49. Torres Filho, I.P., Leunig, M., Yuan, F., Intaglietta, M. & Jain, R.K. Noninvasive measurement of microvascular and interstitial oxygen profiles in a human tumor in SCID mice. *Proc Natl Acad Sci U S A* **91**, 2081-2085 (1994).
50. Tyrrell, J.A., *et al.* Robust 3-D modeling of vasculature imagery using superellipsoids. *IEEE Trans Med Imaging* **26**, 223-237 (2007).
51. Yaegashi, K., Itoh, T., Kosaka, T., Fukushima, H. & Morimoto, T. Diffusivity of oxygen in microvascular beds as determined from PO₂ distribution maps. *Am J Physiol* **270**, H1390-1397 (1996).
52. Tsai, A.G., *et al.* Microvascular and tissue oxygen gradients in the rat mesentery. *Proc Natl Acad Sci U S A* **95**, 6590-6595 (1998).
53. Shibata, M., Ichioka, S., Ando, J. & Kamiya, A. Microvascular and interstitial PO₂ measurements in rat skeletal muscle by phosphorescence quenching. *J Appl Physiol* **91**, 321-327 (2001).
54. Vovenko, E. Distribution of oxygen tension on the surface of arterioles, capillaries and venules of brain cortex and in tissue in normoxia: an experimental study on rats. *Pflugers Arch* **437**, 617-623 (1999).
55. Kindig, C.A., Howlett, R.A. & Hogan, M.C. Effect of extracellular PO₂ on the fall in intracellular PO₂ in contracting single myocytes. *J Appl Physiol* **94**, 1964-1970 (2003).
56. Intaglietta, M., Johnson, P.C. & Winslow, R.M. Microvascular and tissue oxygen distribution. *Cardiovasc Res* **32**, 632-643 (1996).
57. Torres Filho, I.P., Kerger, H. & Intaglietta, M. pO₂ measurements in arteriolar networks. *Microvasc Res* **51**, 202-212 (1996).
58. Baish, J.W. & Jain, R.K. Cancer, angiogenesis and fractals. *Nat Med* **4**, 984 (1998).
59. Baish, J.W. & Jain, R.K. Fractals and cancer. *Cancer Res* **60**, 3683-3688 (2000).
60. Baish, J.W., Netti, P.A. & Jain, R.K. Transmural coupling of fluid flow in microcirculatory network and interstitium in tumors. *Microvasc Res* **53**, 128-141 (1997).

61. Vakoc, B.J., *et al.* Three-dimensional microscopy of the tumor microenvironment in vivo using optical frequency domain imaging. *Nature Medicine Accepted*(2009).
62. Cochran, D.M., Fukumura, D., Ancukiewicz, M., Carmeliet, P. & Jain, R.K. Evolution of oxygen and glucose concentration profiles in a tissue-mimetic culture system of embryonic stem cells. *Ann Biomed Eng* **34**, 1247-1258 (2006).
63. Helmlinger, G., Sckell, A., Dellian, M., Forbes, N.S. & Jain, R.K. Acid production in glycolysis-impaired tumors provides new insights into tumor metabolism. *Clin Cancer Res* **8**, 1284-1291 (2002).
64. Baish, J.W., *et al.* Role of tumor vascular architecture in nutrient and drug delivery: an invasion percolation-based network model. *Microvasc Res* **51**, 327-346 (1996).
65. Tannock, I.F. Oxygen diffusion and the distribution of cellular radiosensitivity in tumours. *Br J Radiol* **45**, 515-524 (1972).
66. Mueller-Klieser, W. Method for the determination of oxygen consumption rates and diffusion coefficients in multicellular spheroids. *Biophys J* **46**, 343-348 (1984).
67. Dewhirst, M.W., Secomb, T.W., Ong, E.T., Hsu, R. & Gross, J.F. Determination of local oxygen consumption rates in tumors. *Cancer Res* **54**, 3333-3336 (1994).
68. Secomb, T.W., Hsu, R., Dewhirst, M.W., Klitzman, B. & Gross, J.F. Analysis of oxygen transport to tumor tissue by microvascular networks. *Int J Radiat Oncol Biol Phys* **25**, 481-489 (1993).
69. Tsai, A.G., Friesenecker, B., Cabrales, P., Hangai-Hoger, N. & Intaglietta, M. The vascular wall as a regulator of tissue oxygenation. *Curr Opin Nephrol Hypertens* **15**, 67-71 (2006).
70. Hagendoorn, J., *et al.* Onset of abnormal blood and lymphatic vessel function and interstitial hypertension in early stages of carcinogenesis. *Cancer Res* **66**, 3360-3364 (2006).
71. Morikawa, S., *et al.* Abnormalities in pericytes on blood vessels and endothelial sprouts in tumors. *Am J Pathol* **160**, 985-1000 (2002).
72. De Jaeger, K., *et al.* Heterogeneity of tumor oxygenation: relationship to tumor necrosis, tumor size, and metastasis. *Int J Radiat Oncol Biol Phys* **42**, 717-721 (1998).
73. Freyer, J.P. & Sutherland, R.M. Regulation of growth saturation and development of necrosis in EMT6/Ro multicellular spheroids by the glucose and oxygen supply. *Cancer Res* **46**, 3504-3512 (1986).
74. Vaupel, P. Tumor microenvironmental physiology and its implications for radiation oncology. *Semin Radiat Oncol* **14**, 198-206 (2004).
75. Fukumura, D. & Jain, R.K. Tumor microenvironment abnormalities: causes, consequences, and strategies to normalize. *J Cell Biochem* **101**, 937-949 (2007).
76. Cvetkovic, D., *et al.* Increased hypoxia correlates with increased expression of the angiogenesis marker vascular endothelial growth factor in human prostate cancer. *Urology* **57**, 821-825 (2001).
77. Gimbrone, M.A., Jr., Leapman, S.B., Cotran, R.S. & Folkman, J. Tumor dormancy in vivo by prevention of neovascularization. *J Exp Med* **136**, 261-276 (1972).
78. Hanahan, D. & Folkman, J. Patterns and emerging mechanisms of the angiogenic switch during tumorigenesis. *Cell* **86**, 353-364 (1996).
79. Folkman, J. Role of angiogenesis in tumor growth and metastasis. *Semin Oncol* **29**, 15-18 (2002).
80. Fox, S.B., Gasparini, G. & Harris, A.L. Angiogenesis: pathological, prognostic, and growth-factor pathways and their link to trial design and anticancer drugs. *Lancet Oncol* **2**, 278-289 (2001).

81. Toi, M., Bando, H. & Kuroi, K. The predictive value of angiogenesis for adjuvant therapy in breast cancer. *Breast Cancer* **7**, 311-314 (2000).
82. Kirsch, M., Schackert, G. & Black, P.M. Metastasis and angiogenesis. *Cancer Treat Res* **117**, 285-304 (2004).
83. Liao, D. & Johnson, R.S. Hypoxia: a key regulator of angiogenesis in cancer. *Cancer Metastasis Rev* **26**, 281-290 (2007).
84. West, C.M., Cooper, R.A., Loncaster, J.A., Wilks, D.P. & Bromley, M. Tumor vascularity: a histological measure of angiogenesis and hypoxia. *Cancer Res* **61**, 2907-2910 (2001).
85. Tyrrell, J.A., et al. A 2-D/3-D model-based method to quantify the complexity of microvasculature imaged by in vivo multiphoton microscopy. *Microvasc Res* **70**, 165-178 (2005).
86. Cherk, M.H., et al. Lack of correlation of hypoxic cell fraction and angiogenesis with glucose metabolic rate in non-small cell lung cancer assessed by 18F-Fluoromisonidazole and 18F-FDG PET. *J Nucl Med* **47**, 1921-1926 (2006).
87. Heinzman, J.M., Brower, S.L. & Bush, J.E. Comparison of angiogenesis-related factor expression in primary tumor cultures under normal and hypoxic growth conditions. *Cancer Cell Int* **8**, 11 (2008).
88. Mizukami, Y., Kohgo, Y. & Chung, D.C. Hypoxia inducible factor-1 independent pathways in tumor angiogenesis. *Clin Cancer Res* **13**, 5670-5674 (2007).
89. Couvelard, A., et al. Microvascular density and hypoxia-inducible factor pathway in pancreatic endocrine tumours: negative correlation of microvascular density and VEGF expression with tumour progression. *Br J Cancer* **92**, 94-101 (2005).
90. Blackwell, K.L., et al. HER-2 gene amplification correlates with higher levels of angiogenesis and lower levels of hypoxia in primary breast tumors. *Clin Cancer Res* **10**, 4083-4088 (2004).
91. Hlatky, L., Hahnfeldt, P. & Folkman, J. Clinical application of antiangiogenic therapy: microvessel density, what it does and doesn't tell us. *J Natl Cancer Inst* **94**, 883-893 (2002).
92. Mayer, A., Hockel, M. & Vaupel, P. Endogenous hypoxia markers: case not proven! *Adv Exp Med Biol* **614**, 127-136 (2008).
93. Picchio, M., et al. Intratumoral spatial distribution of hypoxia and angiogenesis assessed by 18F-FAZA and 125I-Gluco-RGD autoradiography. *J Nucl Med* **49**, 597-605 (2008).
94. Wilson, D.F., et al. Oxygen distributions within R3230Ac tumors growing in dorsal flap window chambers in rats. *Adv Exp Med Biol* **454**, 603-609 (1998).
95. Dewhirst, M.W., et al. Quantification of longitudinal tissue pO₂ gradients in window chamber tumours: impact on tumour hypoxia. *Br J Cancer* **79**, 1717-1722 (1999).
96. Walenta, S., et al. Tissue gradients of energy metabolites mirror oxygen tension gradients in a rat mammary carcinoma model. *Int J Radiat Oncol Biol Phys* **51**, 840-848 (2001).
97. Krogh, A. The number and distribution of capillaries in muscles with calculations of the oxygen pressure head necessary for supplying the tissue. *J Physiol* **52**, 409-415 (1919).
98. Hill, A.V. The Diffusion of Oxygen and Lactic Acid through Tissues. *Proc. R. Soc. Lond. B* **104**, 39-96 (1928).
99. Toma-Dasu, I., Dasu, A., Waites, A., Denekamp, J. & Fowler, J.F. Theoretical simulation of oxygen tension measurement in the tissue using a microelectrode: II. Simulated measurements in tissues. *Radiother Oncol* **64**, 109-118 (2002).
100. Nilsson, J., Lind, B.K. & Brahme, A. Radiation response of hypoxic and generally heterogeneous tissues. *Int J Radiat Biol* **78**, 389-405 (2002).

CHAPTER 4

101. West, G.B., Brown, J.H. & Enquist, B.J. The fourth dimension of life: fractal geometry and allometric scaling of organisms. *Science* **284**, 1677-1679 (1999).
102. Gazit, Y., *et al.* Fractal characteristics of tumor vascular architecture during tumor growth and regression. *Microcirculation* **4**, 395-402 (1997).
103. Gazit, Y., Berk, D.A., Leunig, M., Baxter, L.T. & Jain, R.K. Scale-invariant behavior and vascular network formation in normal and tumor tissue. *Phys Rev Lett* **75**, 2428-2431 (1995).
104. Dasu, A., Toma-Dasu, I. & Karlsson, M. Theoretical simulation of tumour oxygenation and results from acute and chronic hypoxia. *Phys Med Biol* **48**, 2829-2842 (2003).
105. Baish, J.W., Stylianopoulos, T. & Jain, R.K. Scaling behavior of drug delivery in tumors: Implications for antiangiogenic therapy. *In Preparation* (2009).
106. Tannehill, J.C., Anderson, D.A. & Pletcher, R.H. *Computational fluid mechanics and heat transfer*, (Taylor & Francis, Washington, DC, 1997).
107. Swabb, E.A., Wei, J. & Gullino, P.M. Diffusion and convection in normal and neoplastic tissues. *Cancer Res* **34**, 2814-2822 (1974).
108. Bruehlmeier, M., Roelcke, U., Schubiger, P.A. & Ametamey, S.M. Assessment of hypoxia and perfusion in human brain tumors using PET with 18F-fluoromisonidazole and 15O-H₂O. *J Nucl Med* **45**, 1851-1859 (2004).
109. Evans, S.M., *et al.* Imaging and analytical methods as applied to the evaluation of vasculature and hypoxia in human brain tumors. *Radiat Res* **170**, 677-690 (2008).
110. He, F., *et al.* Noninvasive molecular imaging of hypoxia in human xenografts: comparing hypoxia-induced gene expression with endogenous and exogenous hypoxia markers. *Cancer Res* **68**, 8597-8606 (2008).
111. Nordsmark, M., *et al.* Measurements of hypoxia using pimonidazole and polarographic oxygen-sensitive electrodes in human cervix carcinomas. *Radiother Oncol* **67**, 35-44 (2003).
112. Kerbel, R. & Folkman, J. Clinical translation of angiogenesis inhibitors. *Nat Rev Cancer* **2**, 727-739 (2002).
113. Slamon, D.J., *et al.* Studies of the HER-2/neu proto-oncogene in human breast and ovarian cancer. *Science* **244**, 707-712 (1989).
114. Izumi, Y., Xu, L., di Tomaso, E., Fukumura, D. & Jain, R.K. Tumour biology: herceptin acts as an anti-angiogenic cocktail. *Nature* **416**, 279-280 (2002).
115. Hardee, M.E., *et al.* Her2/neu signaling blockade improves tumor oxygenation in a multifactorial fashion in Her2/neu+ tumors. *Cancer Chemother Pharmacol* **63**, 219-228 (2009).
116. Konecny, G.E., *et al.* Activity of lapatinib a novel HER2 and EGFR dual kinase inhibitor in human endometrial cancer cells. *Br J Cancer* **98**, 1076-1084 (2008).
117. Ferrara, N. Vascular endothelial growth factor: molecular and biological aspects. *Curr Top Microbiol Immunol* **237**, 1-30 (1999).
118. Hicklin, D.J. & Ellis, L.M. Role of the vascular endothelial growth factor pathway in tumor growth and angiogenesis. *J Clin Oncol* **23**, 1011-1027 (2005).
119. Ferrara, N., Hillan, K.J., Gerber, H.P. & Novotny, W. Discovery and development of bevacizumab, an anti-VEGF antibody for treating cancer. *Nat Rev Drug Discov* **3**, 391-400 (2004).
120. Jain, R.K. Tumor angiogenesis and accessibility: role of vascular endothelial growth factor. *Semin Oncol* **29**, 3-9 (2002).

CHAPTER 4

121. Jain, R.K., *et al.* Endothelial cell death, angiogenesis, and microvascular function after castration in an androgen-dependent tumor: role of vascular endothelial growth factor. *Proc Natl Acad Sci U S A* **95**, 10820-10825 (1998).
122. Yuan, F., *et al.* Time-dependent vascular regression and permeability changes in established human tumor xenografts induced by an anti-vascular endothelial growth factor/vascular permeability factor antibody. *Proc Natl Acad Sci U S A* **93**, 14765-14770 (1996).
123. Prewett, M., *et al.* Antivascular endothelial growth factor receptor (fetal liver kinase 1) monoclonal antibody inhibits tumor angiogenesis and growth of several mouse and human tumors. *Cancer Res* **59**, 5209-5218 (1999).
124. Klement, G., *et al.* Continuous low-dose therapy with vinblastine and VEGF receptor-2 antibody induces sustained tumor regression without overt toxicity. *J Clin Invest* **105**, R15-24 (2000).
125. Boudreau, N. & Myers, C. Breast cancer-induced angiogenesis: multiple mechanisms and the role of the microenvironment. *Breast Cancer Res* **5**, 140-146 (2003).
126. Monsky, W.L., *et al.* Role of host microenvironment in angiogenesis and microvascular functions in human breast cancer xenografts: mammary fat pad versus cranial tumors. *Clin Cancer Res* **8**, 1008-1013 (2002).
127. Duda, D.G., Batchelor, T.T., Willett, C.G. & Jain, R.K. VEGF-targeted cancer therapy strategies: current progress, hurdles and future prospects. *Trends Mol Med* **13**, 223-230 (2007).
128. Leunig, M., *et al.* Angiogenesis, microvascular architecture, microhemodynamics, and interstitial fluid pressure during early growth of human adenocarcinoma LS174T in SCID mice. *Cancer Res* **52**, 6553-6560 (1992).
129. Goldman, R.D. & Spector, D.L. *Live cell imaging : a laboratory manual*, (Cold Spring Harbor Laboratory Press, Cold Spring Harbor, N.Y., 2005).
130. Yuan, F., *et al.* Vascular permeability and microcirculation of gliomas and mammary carcinomas transplanted in rat and mouse cranial windows. *Cancer Res* **54**, 4564-4568 (1994).

V. Nanocrystal construct FRET-based pH sensing in solid tumors

Parts of this chapter will be published:

Somers, R, Lanning RM, Greytak AB, McLaurin EJ, Fukumura D, Jain RK, Bawendi MG,
and Nocera D

Manuscript in Preparation

V.1 Introduction and Motivation:

This Chapter describes the development and application of an *in vivo* pH biosensor based on resonance energy transfer between a fluorescent semiconductor nanocrystal (NC)^{1,2} and pH sensitive dye. The work shown here is the result of an active collaboration between the Bawendi and Nocera labs at MIT and the Steele Lab for Tumor Biology at MGH. The motivation for this work was the development of a reversible internally ratiometric pH sensor capable for use with multiphoton microscopy to quantify pH in the tumor microenvironment. The ideal pH sensor design for this application should be characterized by the following parameters:

1. Physiologically relevant pKa (~7.0-7.4)
2. Biocompatibility (minimal charge and size)
3. Biostability and Photostability (robust construct and no photobleaching)
4. Appreciable two-photon excitation ($\sigma_{2,NC} \gg \sigma_{2,dye}$)
5. Broad two-photon excitation cross-section

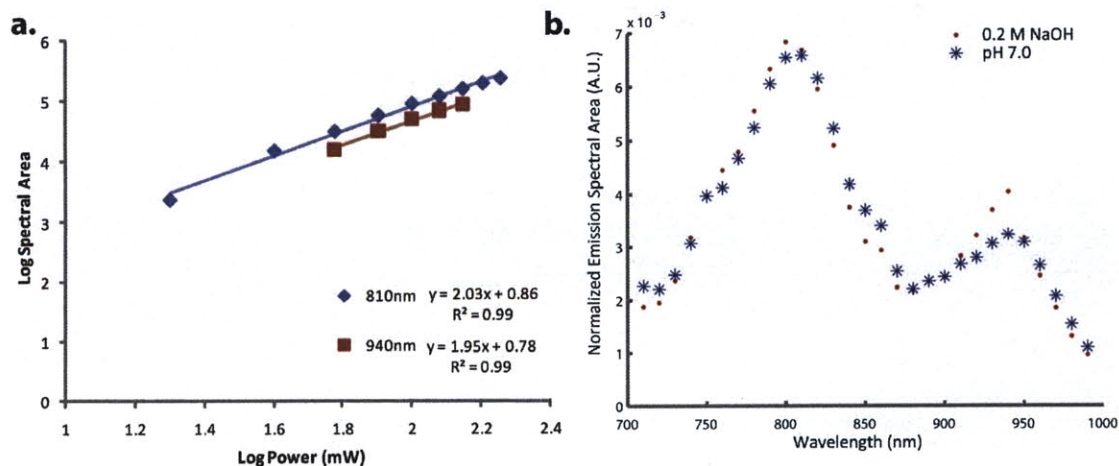


Figure V-1 Two-photon excitation of BCECF. (a). The fluorescent emission of BCECF at pH 7.0 obeys quadratic dependence on the excitation power for both 810 and 940nm incident laser wavelength. (b). The two different acid and base forms of BCECF are visible in both a solution of 0.2M NaOH and PBS at pH 7 in the normalized action cross-section. It is readily apparent that the two species have different two-photon absorption cross-sections.

While methods for measuring *in vivo* pH exist, none is characterized by both high three-dimensional spatial resolution and significant depth penetration in tissue (**Chapter II**). Further, most are unable to probe the tumor metabolic microenvironment in the context of the vascular network. Multiphoton microscopy permits simultaneous fluorescence ratiometric imaging and non-invasive angiography. The common pH sensitive dyes cannot be applied individually to FRIM in the two-photon regime due to different two-photon cross-sections of the acid and base forms³ (**Figure V-1**). The pH-sensitive lifetime of BCECF has been used to quantify pH in murine skin using MPM, but depth penetration in two-photon fluorescence lifetime imaging was limited to only 20 μm ⁴. Another study has demonstrated *in vitro* an emission ratiometric pH-sensitive fluorescent dye (dicyanohydroquinone) that is not subject to differences in two-photon absorption of the acid and base forms⁵. However, the dye is potentially toxic *in vivo* as a byproduct is hydrogen cyanide. Therefore, the need for an *in vivo* pH sensor compatible with multiphoton microscopy still exists.

Numerous obstacles needed to be surmounted for the development of a ratiometric pH-sensitive NC-construct. Foremost among these were biocompatibility, stability and *in vivo* delivery of the construct. The steps from the synthetic chemistry of these constructs to application in living tumors was constantly evolving to design and implement the ideal *in vivo* pH probe. This Chapter will focus on the development and application components of the design. Synthetic methods of all constructs discussed in this chapter are described in detail elsewhere⁶⁻⁸.

V.2 Multiphoton Multispectral and FRIM System

To study the NC pH biosensors under multiphoton excitation, a system that combined both ratiometric imaging and multispectral fluorescence emission detection were required (**Figure V-2**). Ratiometric imaging with multiphoton microscopy requires only the selection of appropriate dichroic and bandpass filters to split and select the emission signals of interest. Two-photon ratiometric imaging has been used to successfully detect both zinc⁹ and calcium¹⁰ levels in cells using fluorescent emission ratiometric constructs.

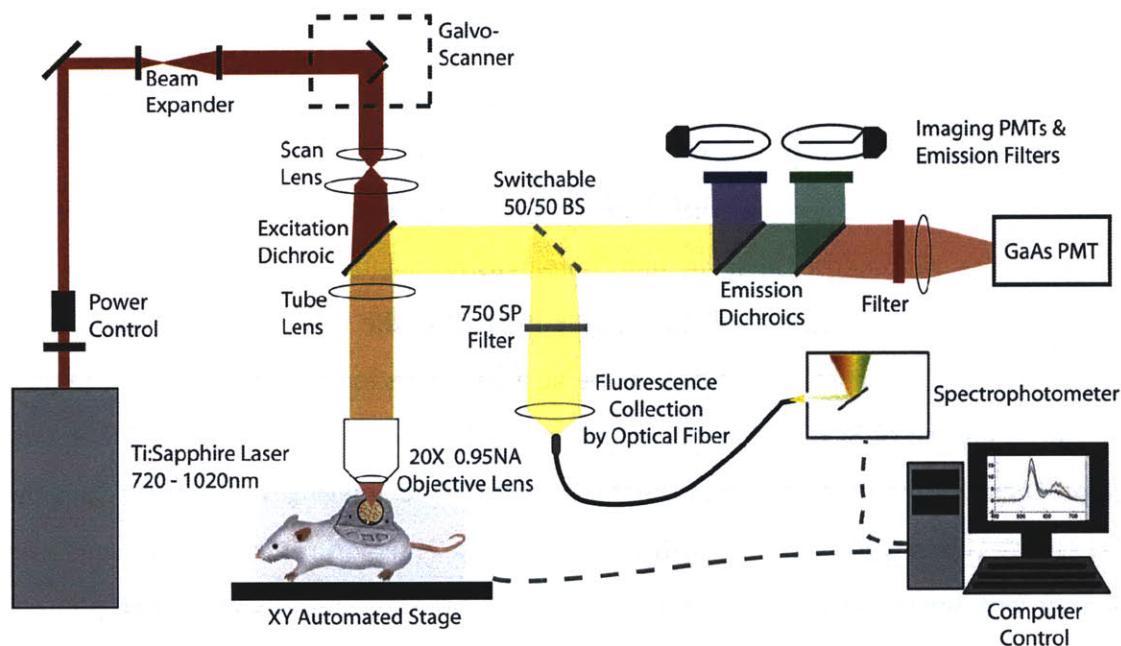


Figure V-2 Setup for ratiometric pH measurements using multiphoton microscopy. The addition of a fiber coupled spectrometer to the emission path of the system permits spectral characterization of the two-photon excited emission.

Multiphoton spectroscopy requires modification to the emission path of a typical MPM for multispectral detection. Multicolor multiphoton imaging has been performed using an optical grating and multichannel PMT with good signal to noise¹¹. However, with typically only 16 channels, the spectral resolution is lower than needed for photophysical studies. To achieve a high degree of spectral analysis, emission light from multiphoton excitation can be coupled into a spectrophotometer¹²⁻¹⁴. In proper configurations both high-resolution spectral analysis and ratiometric imaging can be performed nearly simultaneously. An additional design employs the use of a liquid crystal tunable filter (LCTF) to reject all light outside a narrow bandwidth (~20-30nm) with sequential imaging to obtain a multispectral imaging¹⁵. Preliminary work with a LCTF in the setting of *in vivo* multiphoton microscopy demonstrated very low collection efficiency. It should be noted that anytime fluorescence emission is split, the signal intensity incident upon each detector decreases requiring increased integration time.

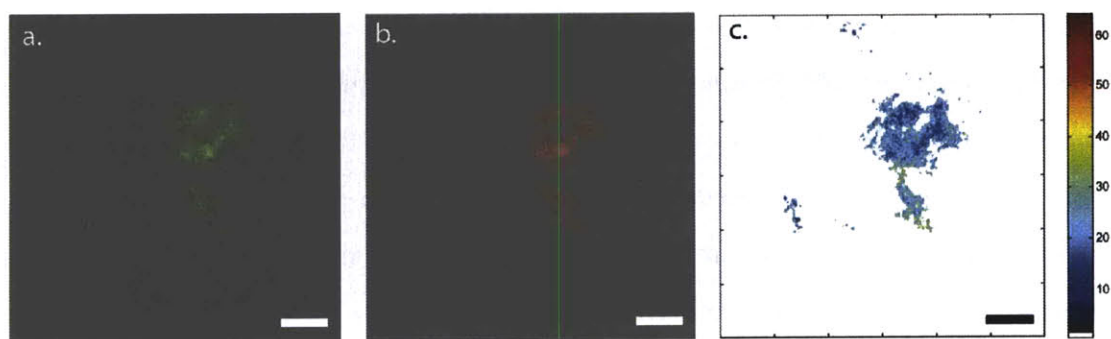


Figure V-3 Ratiometric imaging of NC-biosensor constructs with multiphoton microscopy. (a). Nanocrystal channel (540/40 filter). (b) Coupled dye channel (635/40 filter). (c) Image ratio map obtained from dividing b by a . A colormap indicates the ratio values obtained from the 12-bit images (0-4095). Scale bars - 100 μ m.

All ratiometric imaging and spectral measurements in this Thesis were taken on custom-built multiphoton laser scanning microscopes with selection of an emission output fiber-coupled to a spectrometer. Multiphoton excitation was performed by a diode pumped Ti:Sapphire laser (MaiTai; Spectra-Physics, Mountain View, California) using 800 - 1020 nm light at sample powers ranging from 10-60mW. The output of the laser was adjusted using a zero-order half-wave plate (10RP52-2, Newport Corp., Irvine, CA) and Glan-Laser polarizer (10GL08AR.16, Newport Corp., Irvine, CA). The multiphoton microscope system contained a scan-head (MRC600, Bio-Rad, Hemel Hempstead, England or Fluoview 300, Olympus America Inc., Center Valley, PA) coupled to an upright microscope (Axioskop20, Zeiss, Jena, Germany or BX50W, Olympus America Inc., Center Valley, PA). All measurements were collect using either a 20 \times /0.5NA (Zeiss Achroplan, Jena, Germany) or 20 \times /0.95 (Olympus XLUMPlanFL, Olympus America Inc., Center Valley, PA) water immersion objective. Fluorescence emission was split by a 50/50 beamsplitter (HQSP720M Chroma Technology, Rockingham, Vermont) directed to both an imaging and spectral analysis path.

For ratiometric imaging, non-descanned fluorescence emission was detected by different photomultiplier tubes depending if the emission was less than 620nm (HC125-02, Hamamatsu Photonics, Bridgewater, New Jersey) or longer, requiring a GaAs PMT (H7421-50, Hamamatsu, Inc., Bridgewater, NJ). Nanocrystal and dye fluorescence was

directed to separate PMTs using either a 565nm or 585nm shortpass dichroic (564DCXPR or 585DCXPR Chroma Technology Corp., Rockingham, VT) depending on the construct design. The nanocrystal and dye channels were further selected according to appropriate antireflective-coated broadband emission filters (Chroma Technology Corp., Rockingham, VT). For three-dimensional ratiometric imaging, image stacks (512×512 pixels and 5-micron z-step) were collected simultaneously for both the NC and dye channels. The two detection channels (nanocrystal and dye) were corrected for non-uniform illumination and ratiometric images (**Figure V-3**) were created using Matlab (Mathworks, Natick, MA). To assess for any potential artifacts due to the detectors, the ratiometric response of the PMTs was determined. The fluorescence emission of a sample of free NCs was split using a 50/50 beamsplitter (21000, Chroma Technology Corp., Rockingham, VT) and directed at both detectors used for all experiments. Image stacks were collected with the MPM every 5min for 90 total minutes. The average ratio was calculated for each image stack and timepoint. No drift was observed in the response of either PMT (**Figure V-4**).

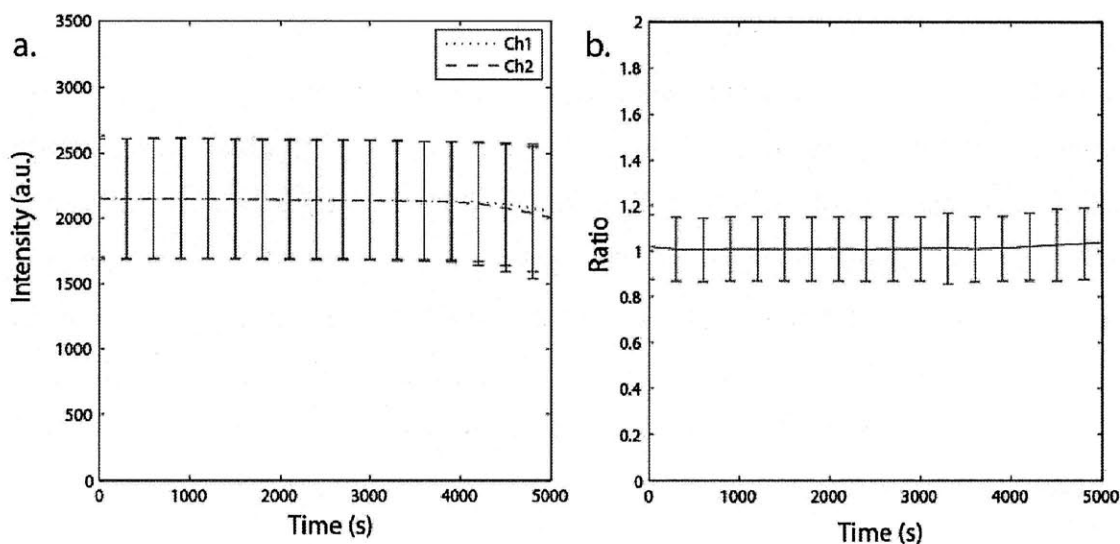


Figure V-4 PMT response over time for ratiometric imaging with NCs. (a). The mean channel intensities over time for both PMTs. (b) The mean ratio of the two channels over time. Errors are given as standard deviations of all image pixels (512×512×100).

For spectral analysis, the excitation laser was parked in the field of view and emission light was coupled into a 100 μm core fiber bundle after passing through a 720 nm short-pass filter (HQSP720m Chroma Technology, Rockingham, Vermont). Spectra of the fiber-coupled emission were collected on a spectrograph (Shamrock 303, Andor Technology, Belfast, Northern Ireland) with CCD detector system (Newton DU-420, Andor Technology, Belfast, Northern Ireland) using a 100 μm slit opening and 20ms to 1s detector integration depending on the signal. All post-processing of the spectra was performed using custom code in the Matlab programming environment.

V.3 Multiphoton excitation of NC-constructs

Fluorescent semiconductor nanocrystals possess broad two-photon excitation spectra (700-1000nm) and significant cross-sections up to nearly 50k GM^{16,17}. They have been successfully applied to MPM in both cellular and *in vivo* environments¹⁸⁻²¹. Initial design considerations in the development of a NC-biosensor for use with MPM are the photophysical properties of FRET-based NC constructs under two-photon excitation. Recently, much emphasis has focused on the application of semiconductor nanocrystals as two-photon antennas for other fluorescent dyes with minimal nonlinear excitation cross-sections²².

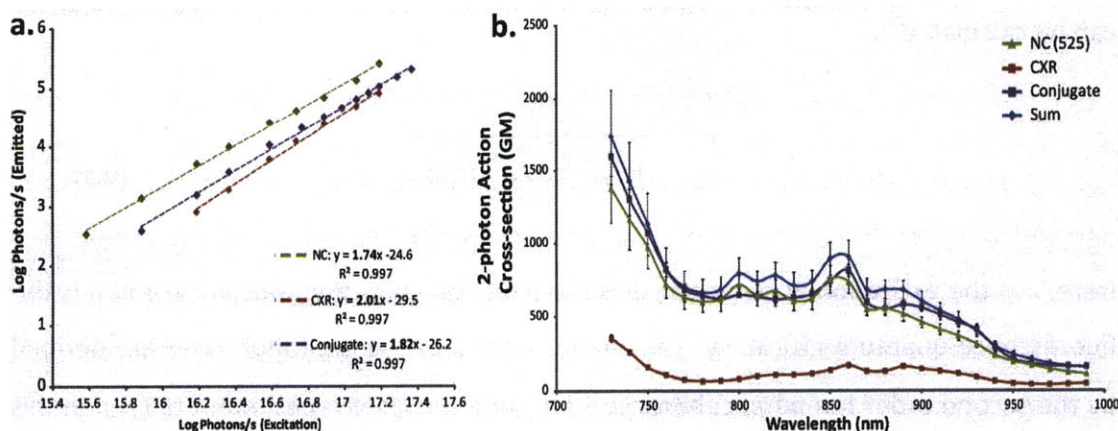


Figure V-5 Two photon excitation of NC-CXR construct: demonstration of a two-photon antenna. (a). Nonlinear excitation of each component (NC and CXR dye) and the construct at 800nm. **(b)** Two-photon action cross-sections for each component and the construct.

V.3a SEMICONDUCTOR NANOCRYSTALS AS TWO-PHOTON ANTENNAS

We chose to perform such an experiment with a dye molecule (carboxy-X-rhodamine, CXR) that exhibits a significant two-photon absorption cross-section in its own right. We hypothesized that the larger two-photon absorption cross-section of the NC would determine the photophysical characteristics of a bound construct incorporating CXR. Both components and the construct demonstrated nonlinear responses to excitation by the femtosecond laser source (**Figure V-5a**). The nanocrystal exhibited near quadratic dependence on the excitation power (1.74), which has been observed by others¹⁶. NCs can easily reach excitation saturation under normal two-photon protocols, which decreases the quadratic dependence and increases the focal volume. The rhodamine dye, CXR, demonstrated no excitation saturation and excellent quadratic dependence of fluorescence (2.01) at the same powers as the NC. The NC-CXR construct displayed the same near quadratic dependence as the free NC (1.82).

Two-photon absorption cross-sections (σ_2) were determined at wavelengths ranging from 730-990nm for the NC, CXR and construct (**Figure V-5b**). The absorption cross-section was calculated from the fluorescence emission spectra of each molecule during two-photon excitation using the fiber-coupled spectrometer. If both the time averaged fluorescence $\langle F(t) \rangle$ and incident laser power $\langle P(t) \rangle$ on the sample are known, then σ_2 can be calculated²³.

$$\sigma_2 = \frac{\pi\lambda\langle F(t) \rangle}{4\phi\eta C g^{(2)} / f_\tau \langle P(t) \rangle^2} \quad (\text{V.1})$$

Here, λ is the excitation wavelength, ϕ is the emission collection efficiency, and η is the fluorescence quantum efficiency. The characteristics of the excitation laser are defined by the second order temporal coherence ($g^{(2)}$) and the laser repetition rate (f_τ). In this study the laser source was 80MHz and assumed to consist of Gaussian shaped pulses giving a value of 73500 for $\frac{g^{(2)}}{f_\tau}$. Free acid fluorescein was used as a reference sample to determine the collection efficiency of the multiphoton microscope detection path. The

collection efficiency was found to be $0.40 \pm 0.04\%$ based on measured values of the two-photon action cross-section at multiple wavelengths and those reported in the literature²⁴. Excitation power was measured directly at the focal point of the objective for each wavelength.

The two-photon absorption cross-section (σ_2) for the NC was found to be much higher (1400-100GM) than that of CXR (350-50GM) at all wavelengths from 730 – 990nm. The NC-CXR construct exhibited similar values (1600-160GM) across its excitation spectrum to that of the free NC. By comparison, the sum of the two-photon absorption cross-sections for the two independent species is slightly higher than the free NC or construct at most wavelengths (1700-150). Only at longer excitation wavelengths (>950nm) does the construct excitation spectrum begin to mirror the sum of the two components. It is likely that at longer wavelengths, when σ_2 for the NC nears a minimum, there is direct excitation of CXR. It is also possible that there is an exchange between the construct and solution whereby CXR is separating from the construct at a given rate. In this case, low concentrations of free CXR could be interfering with the measurement.

V.3b MULTIPHOTON EXCITATION OF NC pH BIOSENSOR

Initial construct designs for a pH biosensor were based on coupling a squaraine dye²⁵ with the NC. The squaraine dye itself does undergo significant two-photon excitation²⁶, but as shown above the NC antenna defines the photophysics at most excitation wavelengths. The problem with this construct was a basic pKa, which precluded its use in biological environments. Instead a new construct was designed incorporating the red-shifted pH-sensitive dye, SNARF-5F²⁷. The pKa of this dye is around 7.2 making it ideal for *in vivo* applications²⁷. The other common pH dye, BCECF²⁸, could not be used because the absorption was too high in energy for efficient resonance energy transfer from a luminescent NC. We determined the normalized two-photon excitation cross-sections for free SNARF, free NC and the NC-SNARF construct at a pH of 7.0 (Figure V-6). The concentrations of the unbound species were equal to those in the construct from the total emission spectra. The NC-SNARF construct exhibits similar features to that of

the free NC from 760-990nm. In particular, the construct does not demonstrate the significant SNARF action cross-section maximum at 860nm. Therefore at wavelengths 900nm and below, two-photon excitation the NC-SNARF construct should occur through the NC and all fluorescence from the bound SNARF dye should result from resonance energy transfer processes.

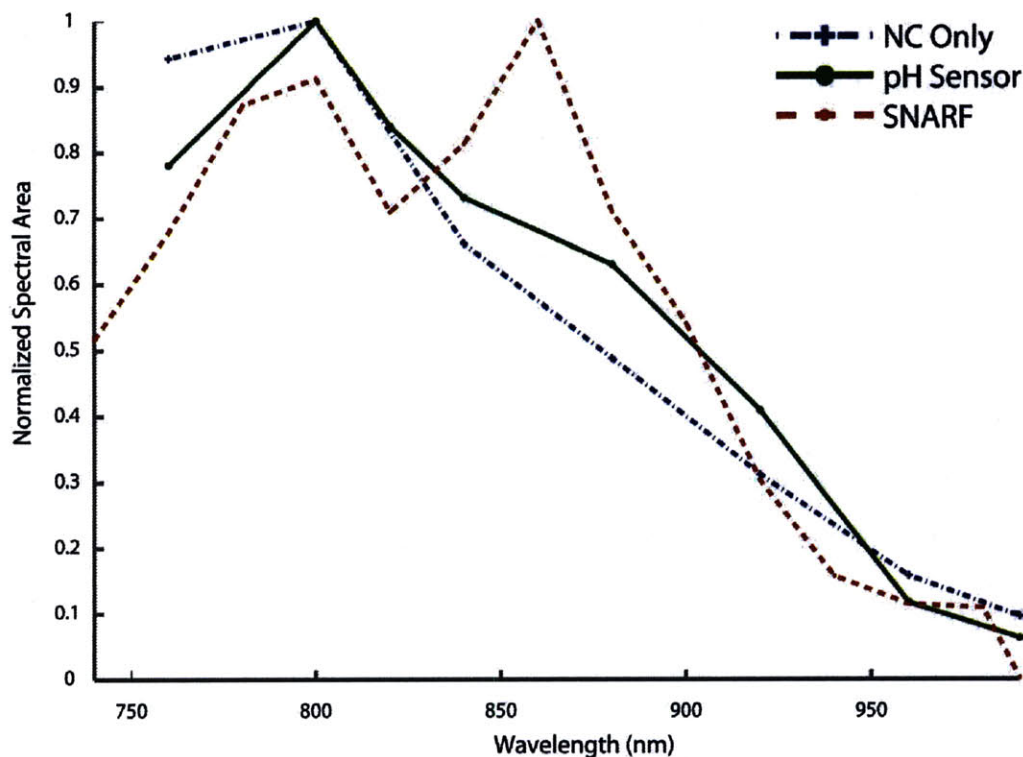


Figure V-6 Normalized two-photon action cross-sections for an NC-SNARF pH biosensor compared to its free components. NC – nanocrystal.

V.4 Biocompatibility of NC-Biosensors

The greatest challenge in developing the NC-biosensor for pH is creating a stable construct that does not interact with *in vivo* biomolecules. In their native state, fluorescent nanocrystals are hydrophobic inorganic compounds². The surface of the nanocrystal must be passivated to be made soluble in an aqueous environment. Typically NCs are capped with thiols through disulfide linkages onto the inorganic surface of the NC. These thiols are typically attached to polymers with hydrophilic

endgroups, such as carboxyl (-COOH) or hydroxyl (-OH) groups, or polyethylene glycol (PEG)^{29,30}.

Complicating the design of an NC-biosensor is coupling the analyte sensitive dye to the nanocrystal coating. Initial designs consisted of ester linkages⁶, due to the ease of coupling the dye molecules onto a carboxylated PEG backbone³¹. However, such coupling would be susceptible to esterases in the *in vivo* environment, particularly if the construct was delivered intravenously. Amide linkages provide robust stability to enzymatic degradation in biological tissues and were selected for second generation NC-biosensor designs. Using amine surface functionalized nanocrystals allowed amide bond formation between dyes modified with N-hydroxysulfosuccinimide (NHS)⁷.

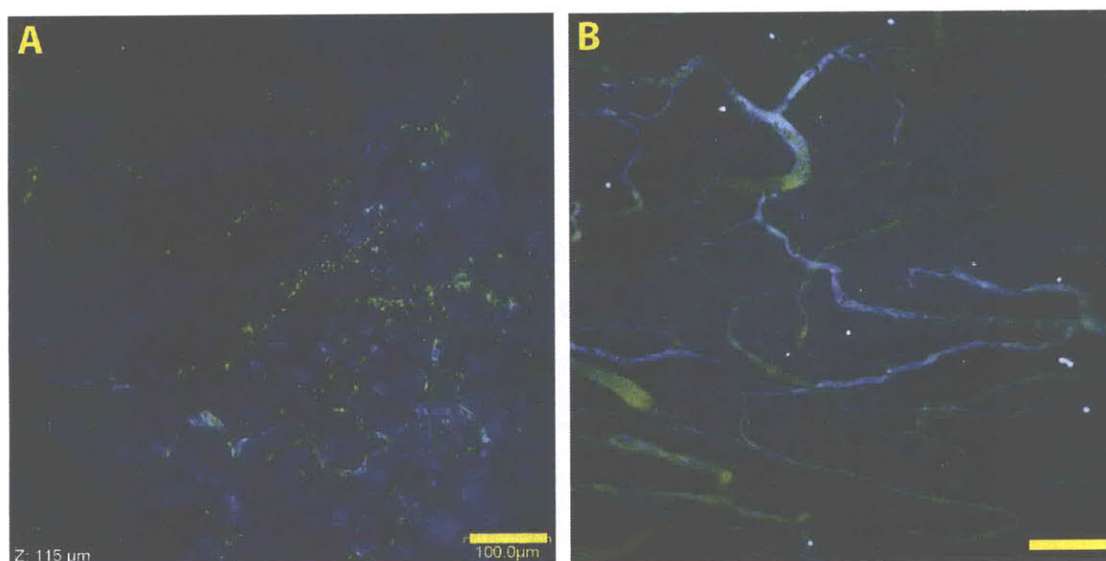


Figure V-7 NC-construct *in vivo* biocompatibility after intravenous injection. (a) The construct based on a dendrimer coating around the nanocrystal exhibited significant non-specific binding and aggregation within normal vasculature upon imaging by MPLSM. Second harmonic generation from adipocytes is notable around the vasculature. (b) Amine (NH₂) - capped DHLA-PEG constructs demonstrated good distribution within tumor vasculature. Here cascade-blue dextran-500k was also injected intravenously as a vascular tracer. Scale bars - 100 μ m.

Once the stable linker was determined different surface capping strategies were explored for their *in vivo* biocompatibility. Dendrimer-capped NCs using poly(amido amine) dendrimer ligands provided ample amines for conjugation with the dye molecules³². The dendrimer ligands were able to couple numerous dyes to a single NC,

thereby increasing the FRET efficiency. However, upon intravenous introduction into a mouse bearing a dorsal skinfold chamber (DSC) without a tumor, non-specific binding was observed intravascularly for dendrimer constructs (**Figure V-7a**). The dendrimer ligands possess a high positive charge, while both albumin³³ and the angiogenic vasculature in tumors and sites of inflammation possess significant anionic charges³⁴. Therefore, non-specific aggregation and binding with dendrimer-NCs preclude their use as sensing moieties in the tumor microenvironment. Similar aggregation results were also found with quantomer (octylamine-modified poly(acrylic acid)) functionalized NCs. Using cysteine as a zwitterionic organic coating for NC construct enables small hydrodynamic diameters (~5.5nm) and renal clearance upon intravenous injection³⁵. However, the stability of dye conjugates to the cysteine moieties was found to be questionable.

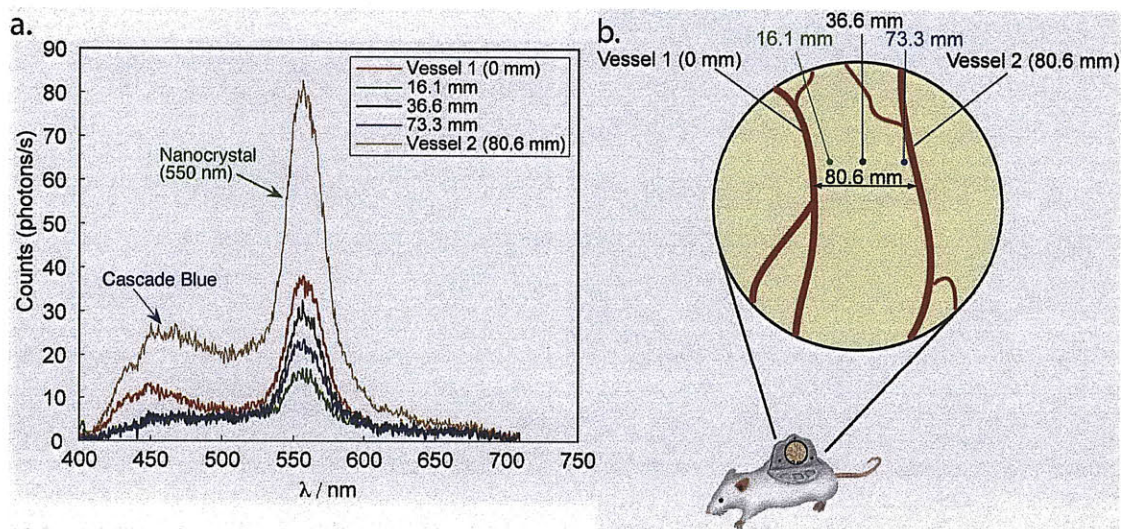


Figure V-8 *In vivo* extravasation of DHLA-PEG nanocrystal constructs from the tumor vasculature. (a) Multiphoton spectral emission measurements were collected on and between two tumor vessels in a DSC. (b) Emission spectra collected at the different points shown in a. When a tumor vessel is imaged, emission spectra show both cascade blue - 500k MW dextran (~450nm) and NCs (~555nm). Only the NC emission is present in the interstitial space of the tumor (black, blue and green). Measurements were collected 150 μ m below the tumor surface.

Recently, nanocrystals solubilized with dihydrolipoic acid conjugated to PEG (DHLA-PEG) were shown to extravasate from blood vessels in an inflammatory model³⁶. Utilizing this design, our collaborators in the Bawendi and Nocera groups developed new biosensor

constructs employing DHLA-PEG functionalized with amine groups for coupling. Intravenous injection of this construct exhibited no aggregation or binding intravascularly within the tumor microvasculature of a mouse model (Figure V-7b). Further investigation demonstrated that intravenously injected amino-DHLA-PEG NC-constructs extravasate from the tumor vasculature less than 30 minutes post-injection. When a tumor vessel is imaged, emission spectra showed both the fluorescence of the vascular tracer (cascade blue - 500k MW dextran) and NCs. However, within the interstitium, only the NC emission is detectable while the larger cascade blue molecule remains in the vascular space (Figure V-8).

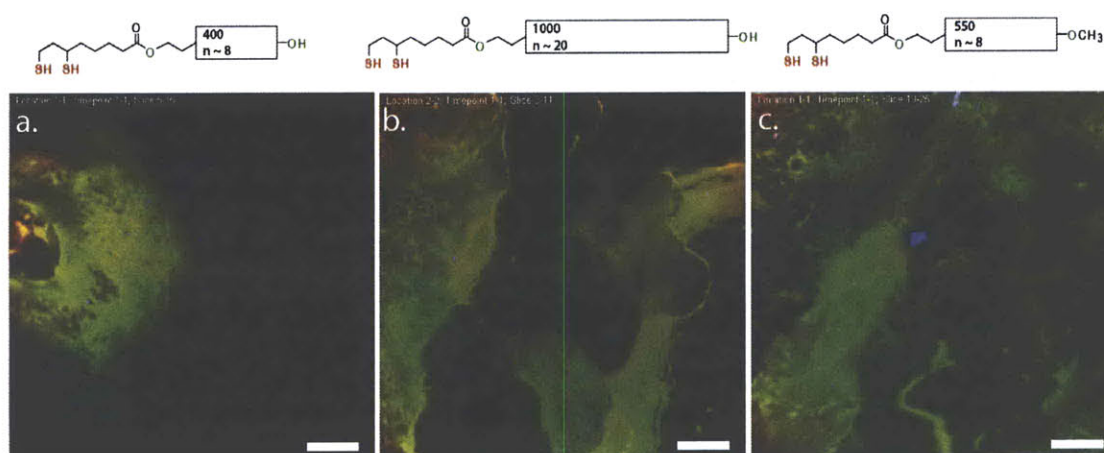


Figure V-9 *In vivo* distribution of NC-CXR constructs functionalized with various biocompatible ligands. (a) DHLA-PEG400-OH (b) DHLA-PEG1000-OH (c) DHLA-PEG550-OCH₃. The ligand structure is given for each construct above the representative *in vivo* image. All constructs were microinjected into the same tumor type. The green color is the colocalization of both the NC and CXR emissions. Scale bars - 100 μ m.

Once the amino-DHLA-PEG nanocrystal construct was settled upon, the charge and size needed to be adjusted for *in vivo* application. It is well known that size and charge play a significant role in the delivery and transport of nanoparticles to and through the tumor microenvironment³⁷. While maintaining a concentration of 20% amino-DHLA-PEGs on the NC surface for coupling to NHS prepared dye molecules, the remaining DHLA-PEGs were adjusted for size and charge by modifying the PEG length and terminal functionality. Three characteristic DHLA-PEG scaffolds (Figure V-9) were prepared and incorporated into NC-constructs utilizing a dye molecule (CXR) insensitive to the *in vivo* microenvironment. This construct design (a two-photon antenna) underwent FRET as

shown in Section V.3. Therefore, the ratio of this dye should be equivalent at all locations when imaged by multiphoton microscopy. The different NC-CXR constructs were directly microinjected into a colorectal adenocarcinoma xenograft (LS174T) implanted in the DSC of male SCID mice. Over a period of 90 minutes, the injection site and nearby interstitium were monitored with MPM at 800nm. Each construct displayed different interactions with the tumor microenvironment characterized by the diffusion distance from the injection site (**Figure V-9**). The methoxy-terminated DHLA-PEG ligand was found to distribute to the greatest extent in the tumor interstitial space (**Figure V-9c**). The shorter hydroxy-terminated DHLA-PEG exhibited the greatest non-specific binding, barely diffusing from the injection site (**Figure V-9a**).

Table V-1: Summary of NC construct results *in vitro* and *in vivo*. Constructs are identified by the type of nanocrystal biocompatible coating utilized. DHLA - dihydrolipoic acid. PEG - polyethelyne glycol (chain length). NH₂ - amine caps on PEGs (cationic with degree depending on %). OH - hydroxyl caps on pegs (neutral charge). OCH₃ - methoxy caps on PEGs (neutral).

Nanocrystal Construct	<i>In vitro</i> and <i>in vivo</i> results
Dendrimer	Sticks to endothelial, stromal cells and tumor cells. Self-aggregation and quenching.
Cysteine	Permeable to tumor vessels, but questionable stability
Quantomer	Non-specific binding and reduced FRET efficiency. Larger size. Good intravascular stability.
DHLA-PEG, 0% NH ₂	Non-specific binding. Poor tissue penetration. Significantly reduced FRET efficiency. Good intravascular stability.
DHLA-PEG, 10% NH ₂	Non-specific binding. Poor tissue penetration. Significantly reduced FRET efficiency. Good intravascular stability.
DHLA-PEG, 20% NH ₂	Non-specific binding. Poor tissue penetration. pH biosensor ratio similar to tumor slurry calibration, but significantly different from PBS calibration. Good intravascular stability.
DHLA-PEG, 25% NH ₂	Non-specific binding. Poor tissue penetration. Good intravascular stability.
DHLA-PEG(400)-OH + DHLA-PEG, 20% NH ₂	Non-specific binding. Poor tissue penetration. pH biosensor ratio different from PBS calibration. Good intravascular stability.
DHLA-PEG(1000)-OH + DHLA-PEG, 20% NH ₂	Non-specific binding significant. Sensor ratio different from PBS calibration. Good intravascular stability.
DHLA-PEG(550)-OCH ₃ + DHLA-PEG, 20% NH ₂	Improved tissue penetration. Reduced non-specific interaction. pH biosensor ratio different from PBS calibration. Good intravascular stability.

The modulation of functionalized ligands on the NC-biosensor constructs does not alter the ratiometric behavior in aqueous buffers containing no biomolecules. However, it

does affect the ratio in *ex vivo* calibrations as the next section will demonstrate. All *in vitro* and *in vivo* biocompatibility results with different NC-constructs are summarized in Table V-1.

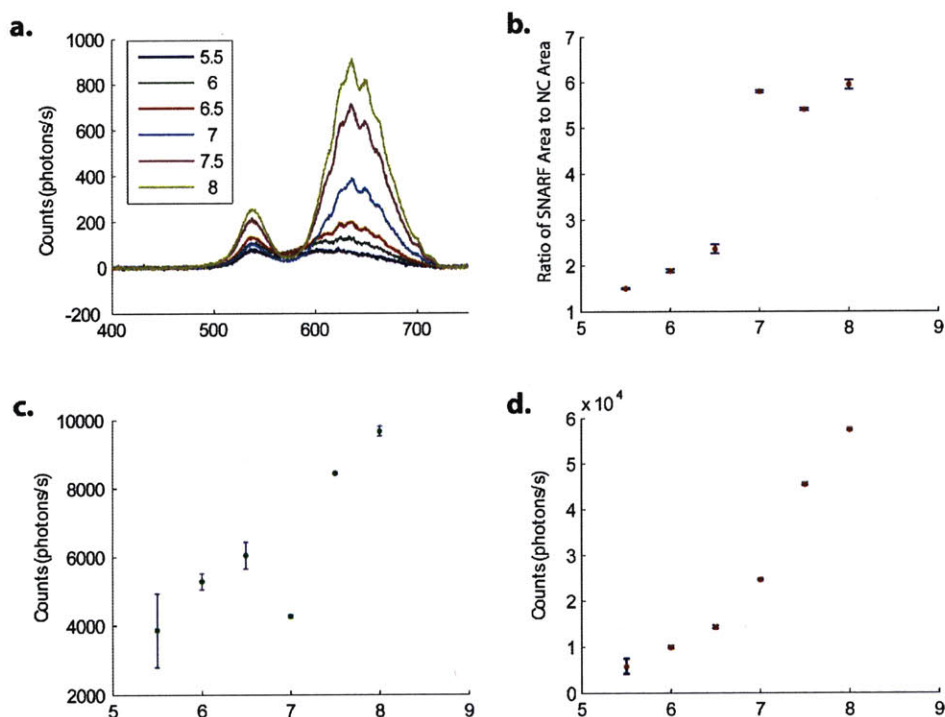


Figure V-10 Multiphoton ratiometric spectral calibration of an NC-SNARF pH biosensor in PBS. (a) Emission spectra at different pH buffers. (b) Calibration ratio of integrated emission areas for SNARF to NC. (c) NC emission area at different pH. (d) SNARF emission area at different pH.

V.5 pH Calibration

Each new NC pH biosensor must be calibrated for response to solutions of known pH. During synthesis of the NC-biosensor a variable number of SNARF molecules are conjugated to the construct (typically between 1 and 6). This alters the FRET efficiency and therefore the ratio. Additionally, the measured ratio values will depend on the quantum efficiencies of the detectors and optical filters employed in the emission path. Therefore, an appropriate calibration has to be performed with the same instrument on which *in vivo* measurements are collected. We performed different calibration protocols on each NC pH biosensor to determine any potential effects on the calibration ratio.

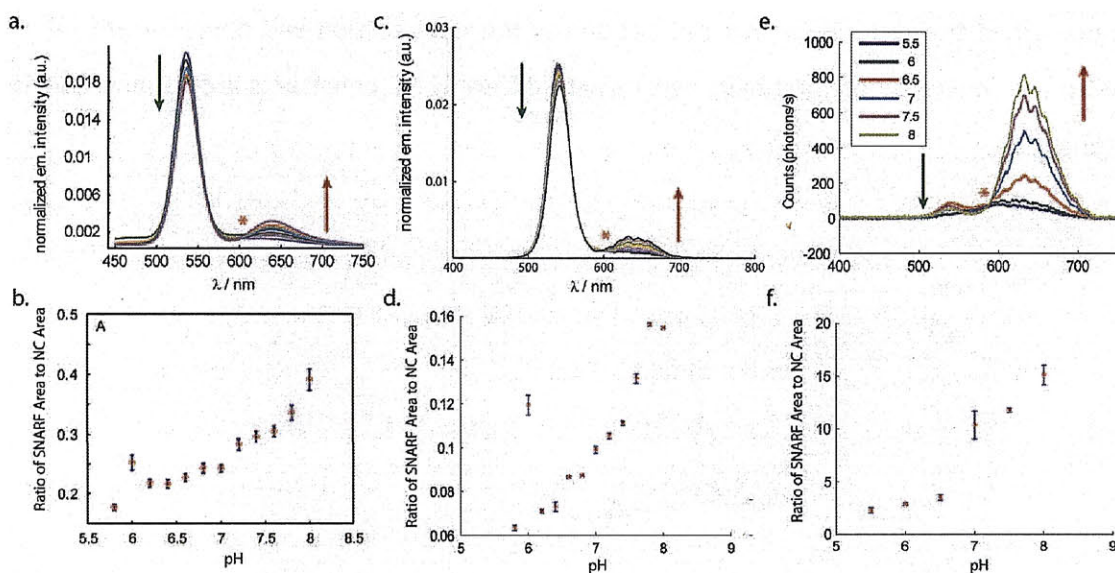


Figure V-11 Calibration of NC-SNARF pH biosensor in phosphate buffered saline with 4% bovine serum albumin. (a) and (b) Single photon excitation – normalized emission spectra and ratio of emission areas at given pH. (c) and (d) Two photon excitation – normalized emission spectra and ratio of emission areas at given pH. (e) and (f) Calibration example of a probe with bound SNARF:NC ratio ~6-7. Arrows indicate shift in peak height with increasing pH (NC – green; SNARF – red). * - isosbestic point.

The simplest calibration we performed involved determining the spectral ratios for the SNARF to NC emissions in solutions of different pH phosphate buffered saline. The emission areas for both components are easily obtained from the collected emission spectra under two-photon excitation allowing calculation of a calibration curve (**Figure V-10**). A slightly modified calibration of the NC pH biosensor was also performed in phosphate buffers containing 4% bovine serum albumin (BSA) from pH 6 to 8 at 37°C (**Figure V-11**). The introduction of BSA explores the effect of scattering media and potential binding on the ratiometric emission of the pH biosensor. Data collected by a spectrometer revealed both emission peaks of the NC and SNARF. Additionally, the isosbestic point exhibited by SNARF was still observable in the NC-biosensor (**Figure V-11a, c, e**). The calibration ratios were defined by the ratio of the spectral areas of SNARF to the NC. Excitation either by single or two-photon processes exhibit different ratio values. However, this is due to completely different detection schemes and not different photophysical processes. Energy transfer processes and fluorescent emission are independent of the excitation for one- and two-photon processes^{38,39}. Constructs

with different molecular ratios of dye to dot exhibit different FRET efficiencies; highlighting the requirement of calibrating each new NC-biosensor (Figure V-11Error! Reference source not found.e and f).

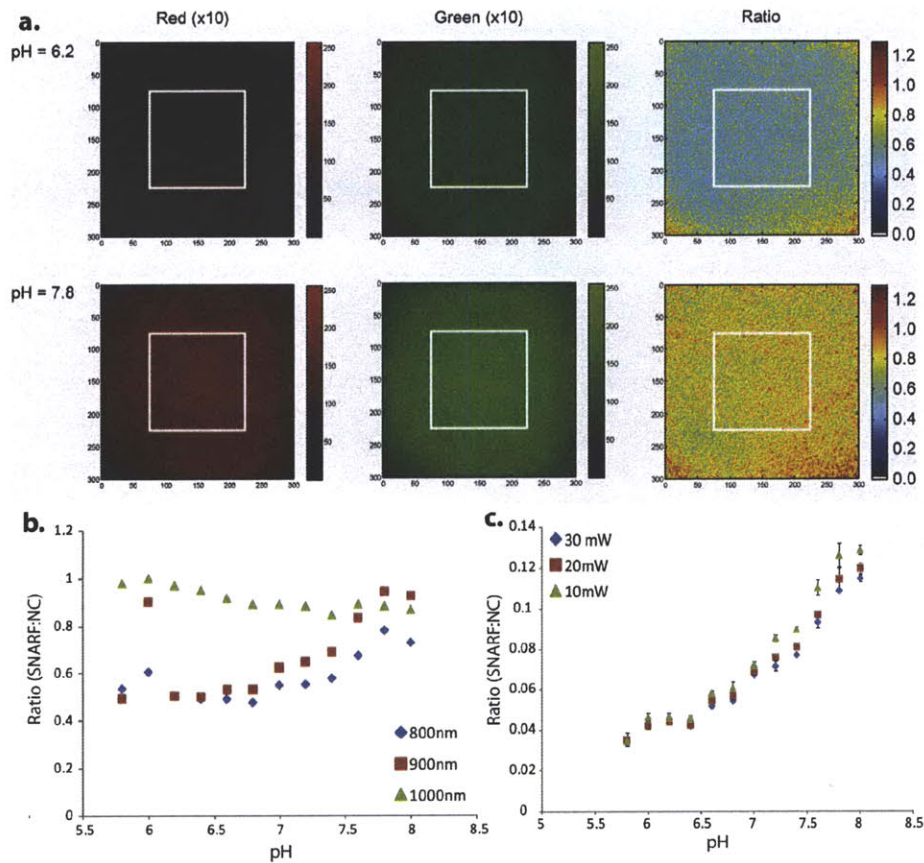


Figure V-12 Calibration using multiphoton FRIM. (a) Examples of emission channels for both SNARF (red) and NC (green) at different pH in PBS. Colormaps on the ratiometric images reveal the different ratios for each environmental pH. **(b)** Effect of multiphoton excitation wavelength on calibration for the samples in a. **(c)** Effect of multiphoton excitation power on calibration.

Calibration for MP-FRIM was obtained using a dichroic filter at the isosbestic point (~585 - 600nm) of the NC-biosensor and imaging with two PMTs employing appropriate bandpass filters to separately integrate the emission from the NC and dye molecules. Mean depth projections for each emission channel obtained from axial image stacks with the MPM were divided to determine the average ratio at each pH (Figure V-12). The calibration values for PBS solutions are different using this method from those

obtained by the spectrometer due to the altered detection mechanism and emission path. We also investigated the effect of both two-photon excitation wavelength and

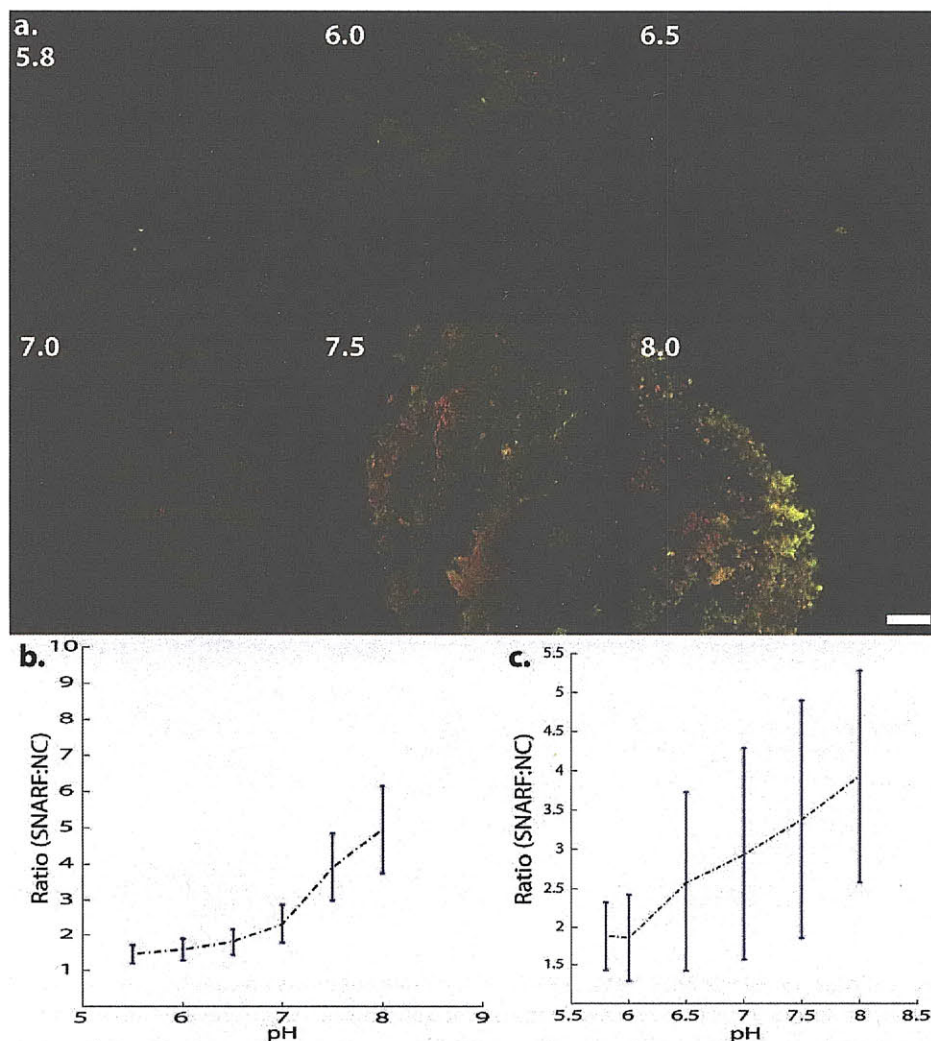


Figure V-13 *Ex vivo* MP-FRIM calibration of NC-biosensor. (a) LS174T tumor slices in different PBS pH buffers. Each image is a maximum intensity projection of 400 μ m of tissue. The emission color changes (green to red) as pH increases. Binding and resonance energy stabilization of the NCs are notable on the damaged (due to removal of tumor) edge of the tumor slices by the increased green fluorescence. These areas were ignored for calibration. (b) The ratiometric image calibrations for all image slices in *a*. Calculated ratio values are the mean of 512 \times 512 \times 41 pixels. The standard deviations are large due to the heterogeneous nature of the tumor tissue. (c) MP-FRIM calibration in PBS. Scale bar - 100 μ m.

power on the calibration using MP-FRIM. Excitation between 800 and 900nm demonstrated no significant difference in calibration values (Figure V-12b). However, the signal to noise ratio was too low at 1000nm excitation to accurately calibrate the

NC-biosensor. Further, as was demonstrated in Section V.3, at longer excitation wavelengths, the SNARF dye may undergo direct excitation rather than resonance energy transfer. Altering the excitation power had no effect on the calibration at 800nm (**Figure V-12c**). This is expected as the NC-biosensor is internally referenced and should not exhibit a change in either emission peak due to different excitation powers since only the NC is excited in principle.

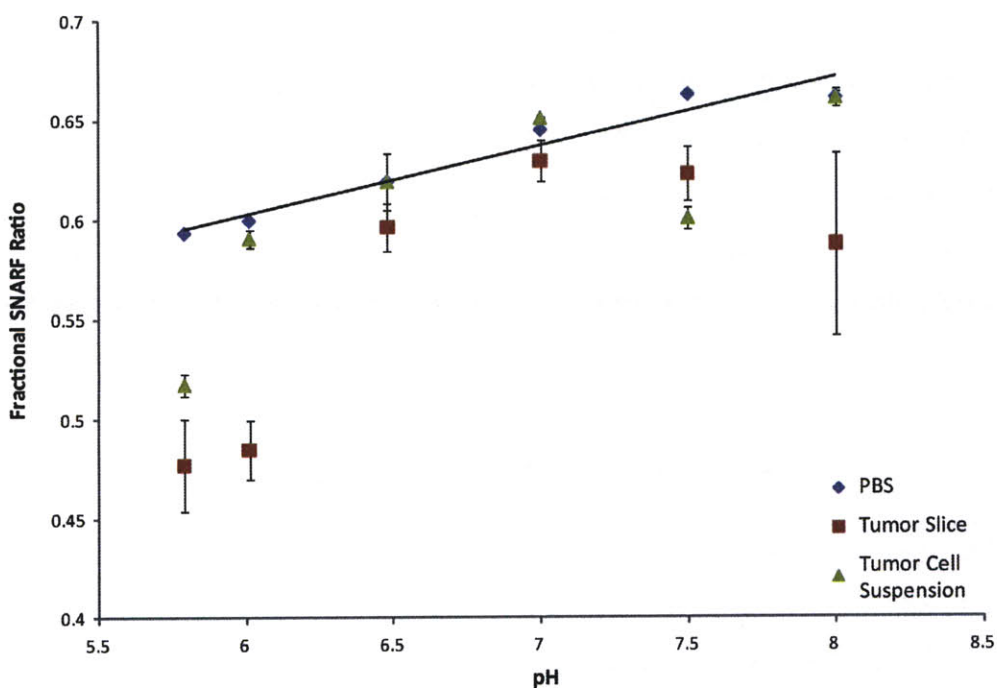


Figure V-14 Comparison of pH calibrations with the NC pH biosensor using MP-FRIM in both solution and *ex vivo* tumor tissue. Black line indicates a linear fit to the PBS calibration data.

With many of our early constructs, we found that the solution calibrations did not reliably match the *in vivo* ratiometric values measured in tumor models. Previous work has suggested that calibration of fluorescent pH sensors like BCECF is best served in an environment that mimics that encountered *in vivo*⁴⁰. Interactions with biological molecules in the local tissue environment may alter the FRET efficiency of the NC-biosensor. To examine the effects of tumor tissue on pH calibrations with the NC-biosensor, I developed two *ex vivo* systems. The first method involved performing calibrations in *ex vivo* tumor slices obtained from subcutaneously grown tumors (**Figure**

V-13). Preferably, the tumor type should be identical to those planned for *in vivo* measurements to account for differences in interstitial components and cell types. MP-FRIM of NC pH biosensors allowed to passively diffuse into tumor slices equilibrated in phosphate buffers of known pH demonstrated a distinct change in fluorescent emission (**Figure V-13a**). The pH calibrations from *ex vivo* tumor slices were slightly different from those obtained in phosphate buffers (**Figure V-13b and c**).

An alternate method for calibrating the NC-biosensor employed single cell suspensions obtained from the tumor type to be investigated. Similar to the *ex vivo* tumor slice methods, the cell suspension, which contains both cancer and stromal cells, were equilibrated in phosphate buffers prior to addition of the NC-biosensor. To compare between calibration methods, the fractional SNARF emission ratio was used. The fractional ratio was calculated from the individual PMT intensity ratios measured by MP-FRIM:

$$\text{Fractional Ratio} = \frac{I_{SNARF}}{I_{SNARF} + I_{NC}} \quad (\text{V.2})$$

The fractional ratio constrains the values to between 0 and 1 making comparisons between calibrations and with *in vivo* data easier. Calibrating an NC pH biosensor with both *ex vivo* methods and phosphate buffer solutions showed that the tumor tissue may have a buffering capacity at low and high pH (**Figure V-14**). It appears that the *ex vivo* tissue samples do not fully equilibrate with the phosphate buffers, thereby altering the expected pH. From these results, it seems that solution calibrations with the NC-biosensor may be all that is required for *in vivo* measurements.

V.6 In Vivo Demonstration of NC-Biosensor

The ultimate goal in the development of ratiometric NC-biosensors for MP-FRIM is studying the tumor metabolic microenvironment during progression and response to therapy. However, prior to characterizing pH changes with targeted cancer therapies such as antiangiogenic agents, we chose to confirm the ability of the NC pH biosensor to

monitor experimentally imposed dynamic changes of *in vivo* pH in the tumor microenvironment. An ideal agent to perturb the tumor acidity is the introduction of intravenous or intraperitoneal glucose. Investigators have shown that the administration of glucose leads to transient acidosis in the tumor microenvironment^{40,41}. The decreased pH from hyperglycemia is due to a number of mechanisms including increased blood viscosity in the tortuous tumor vasculature^{42,43} and acidic byproducts of glycolysis due to increased metabolic supply⁴⁴.

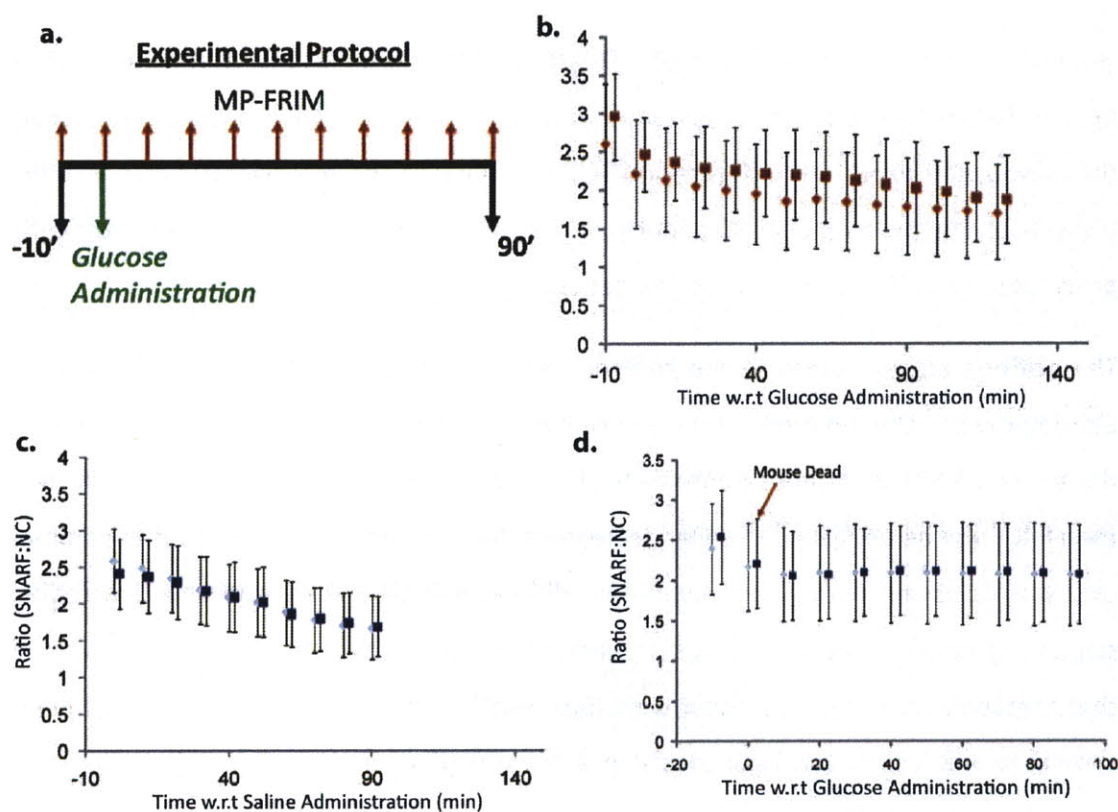


Figure V-15 Metabolic acidosis due to intramuscular anesthetics. (a) Experimental protocol for hyperglycemia experiments with MP-FRIM. (b) Administering glucose intravenously appeared to lower the pH in the tumor. However, (c) control animals injected with saline exhibited similar dynamics over the measurement period. (d) In a mouse that expired 20 minutes into the experiment, no change in pH was observed.

V.6a NC pH BIOSENSORS MEASURE QUALITATIVE CHANGES IN pH DUE TO GLUCOSE ADMINISTRATION.

We performed hyperglycemia experiments using the NC pH biosensor and MP-FRIM in xenograft colorectal adenocarcinoma tumors (LS174T). In the first study, SCID mice bearing DSC with implanted LS174T were anesthetized with ketamine/xylazine (10:1) and glucose or saline was administered intravenously. Prior to initiating the study, NC-biosensor was superfused onto the tumor surface and allowed to diffuse into the tissue. Multiple locations were imaged every 10 minutes for 90 to 120 minutes (**Figure V-15a**). The glucose treated tumors exhibited decreasing pH as indicated by a reduction in the NC-biosensor emission ratio (**Figure V-15b**). However, the saline treated tumors also showed a similar trend to lower pH (**Figure V-15c**). These results contrasted with a mouse that expired after introduction of glucose. In this case, the ratio did not change throughout the experiment (**Figure V-15d**). According to the pH calibrations in PBS for this sensor, the pH drop over 90 minutes in treated tumors was 0.2units, consistent with previous studies in the same tumor model using FRIM with BCECF⁴⁰.

The acidosis also occurred in the control animals suggesting other mechanisms were altering the pH. One possibility is *in vivo* stability of the NC-SNARF construct over time. If the bound SNARF undergoes photobleaching or the linking PEGs dissociate from the NC, then FRET will be abolished thereby decreasing the apparent ratio. However, the animal that was deceased during the experiment did not exhibit a change in emission ratios, suggesting neither mechanism was at work. Literature on various anesthetics revealed that metabolic acidosis may occur with their use⁴⁵⁻⁴⁷. In particular, ketamine has been shown to induce metabolic acidosis in a variety of animal models^{48,49}. Conversely, inhaled anesthetics like isoflurane have not demonstrated metabolic acidosis^{50,51}. From this experiment, it was apparent that the NC-biosensor could measure changes in pH, but also that all such studies should be carried out with inhaled anesthetics to reduce other potential sources of acidosis.

We repeated the previous hyperglycemia study using the same animal models, but with anesthesia induced by inhaled isoflurane. In addition, we monitored trends in pH modulation due to intraperitoneal glucose administration. Both intravenous and

intraperitoneal routes of glucose administration have demonstrated acidosis in the tumor microenvironment⁵². In this case, the NC pH biosensor was coated with DHLA-PEG, 25% -NH₂/75% -OH exhibiting an average hydrodynamic radius of 7-8nm. Our results, show a statistically significant decrease in pH (lower ratio) over time (P -value: 0.002) after glucose administration in comparison to mice injected with PBS (**Figure V-16**). Furthermore, the rate of change in pH is significantly different between both groups (P -value: 0.016). Differences in starting ratios between the two groups are likely due to the heterogeneity in pH found in the tumor microenvironment⁵³. Quantitative assessment was not possible because the ratios measured *in vivo* differing from those in a PBS calibration.

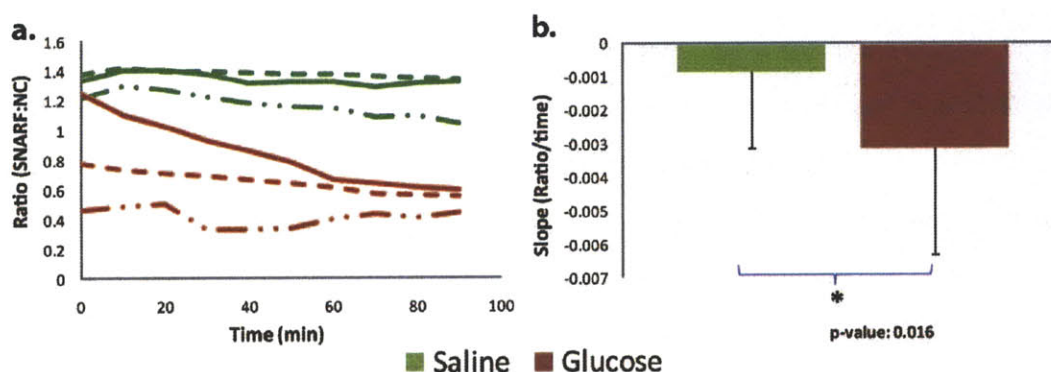


Figure V-16 Acidosis of the tumor microenvironment due to hyperglycemia. (a) In tumors treated with glucose administered intraperitoneally, the pH was qualitatively reduced in comparison to control animals treated with saline. Each line represents the mean of 5-6 different tumor regions in one animal. (b). The change over time of the NC-biosensor (slope) was significant between the two groups (P -value: 0.016. $N = 3$ for both groups).

The same experiment was repeated a second time with NC-biosensors that could be directly microinjected into the tumor interstitium. Nanocrystals passivated with 20% amino-PEG/80% methoxy-PEG were utilized in the synthesis of a new NC-SNARF construct. As shown in Section V.4, the methoxy-PEGylated NCs demonstrated excellent *in vivo* tissue penetration. When injected directly into tumors, these NC-biosensors distributed throughout the tumor tissue within 15 minutes (**Figure V-17a**). Again treated tumors exhibited acidosis in the microenvironment as demonstrated by a decreasing NC-biosensor emission ratio (**Figure V-17b**). By correcting the emission from different

depths for scattering using an exponential factor, the average ratio was shown not to change with depth in the tumor. The glucose and saline treated groups were found to be statistically different over the course of the experiment (P – value: 0.001). The *in vivo* ratio values were found to be lower than those determined by a PBS calibration (Figure V-14). However, if only the change in ratio is taken into account, a linear fit to the calibration data can be used to qualitatively estimate the pH drop. For the ~ 0.02 drop in SNARF emission fractional ratio for this study, a pH drop of ~ 0.6 units is estimated. This is within the range found in previous studies^{40,42,43,54}.

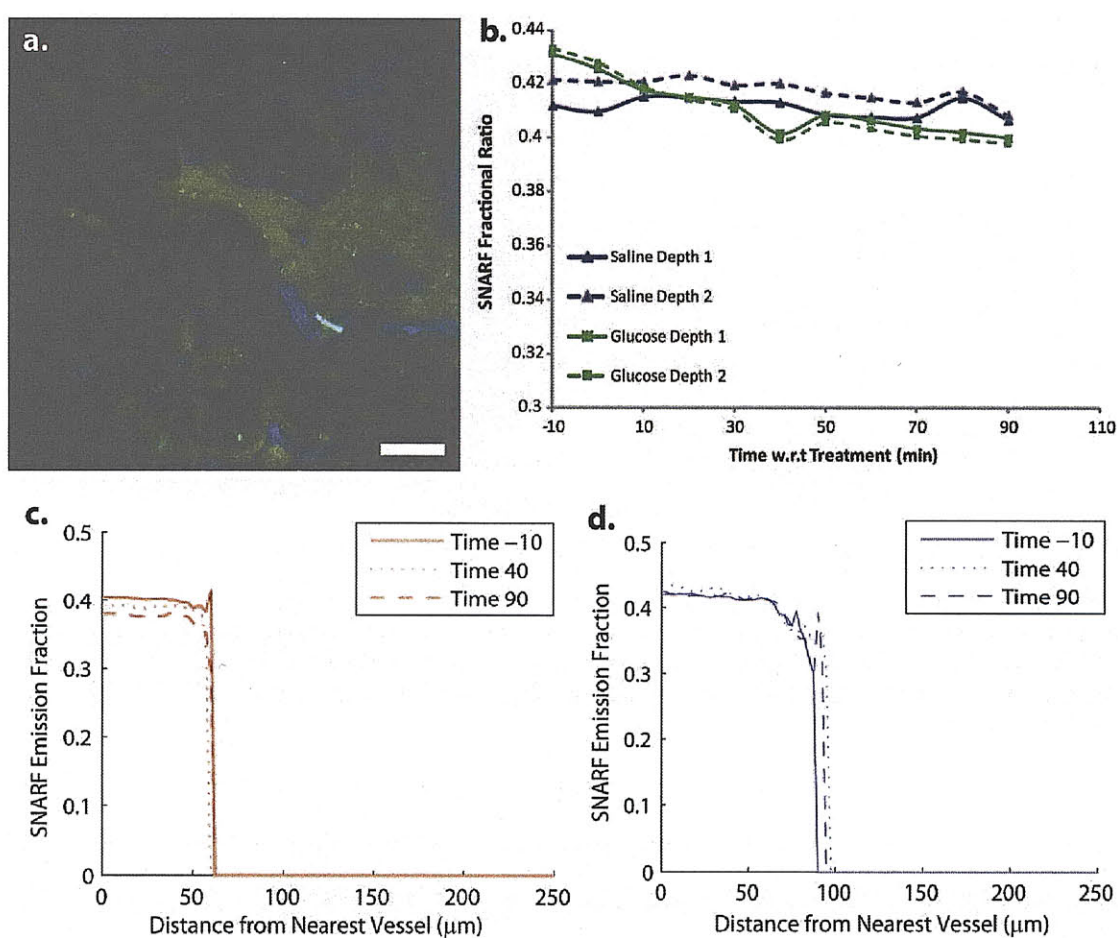


Figure V-17 In vivo pH sensing during hyperglycemia using methoxy-PEG NC-biosensors. (a) Maximum intensity projection of tumor vessels (blue) highlighted by Cascade blue 500K dextran and NC-biosensor (green/red). (b) Acidosis in tumors treated by glucose (green) versus those injected with PBS (blue). SNARF fraction ratio means at two different depth regions (50-100 and 100-150 μm) are shown to nearly overlap during the course of the experiment. $N = 4$ for each group. (c) and (d) Spatial correlation of the

CHAPTER 5

NC-biosensor ratios with the nearest tumor vessel. Glucose treated animals (red) exhibit a drop in pH of the distance, while those treated with saline (blue) do not. Scale bar - 100 μ m.

MP-FRIM coupled with angiography permitted spatial correlation of the measured ratio with distance from the nearest tumor vessel (**Figure V-17c and d**). In both groups, a substantial pH gradient from the vessel wall was not found. This contrasts with previous studies which demonstrated pH drops up to 0.4 units away from the vessel wall⁵³. However, in those experiments profiles were collected from only single vessels and the method did not allow true three-dimensional measurements unlike MP-FRIM. Interestingly, the glucose treated animals did show a drop in pH at every distance from the vessel wall over the course of the study, although a gradient was never observed. Using the combination of MPM angiography and MP-FRIM with the NC-biosensor, these changes in ratio over time can be observed in the context of the vasculature in three dimensions (**Error! Reference source not found.**). Using colormaps to represent the ratio, the heterogeneous response over time of a glucose treated tumor is observable even in a single slice from the three-dimensional image stack. Generally, the control animals maintained similar ratio distributions throughout the experiment as expected from the stable mean ratio values.

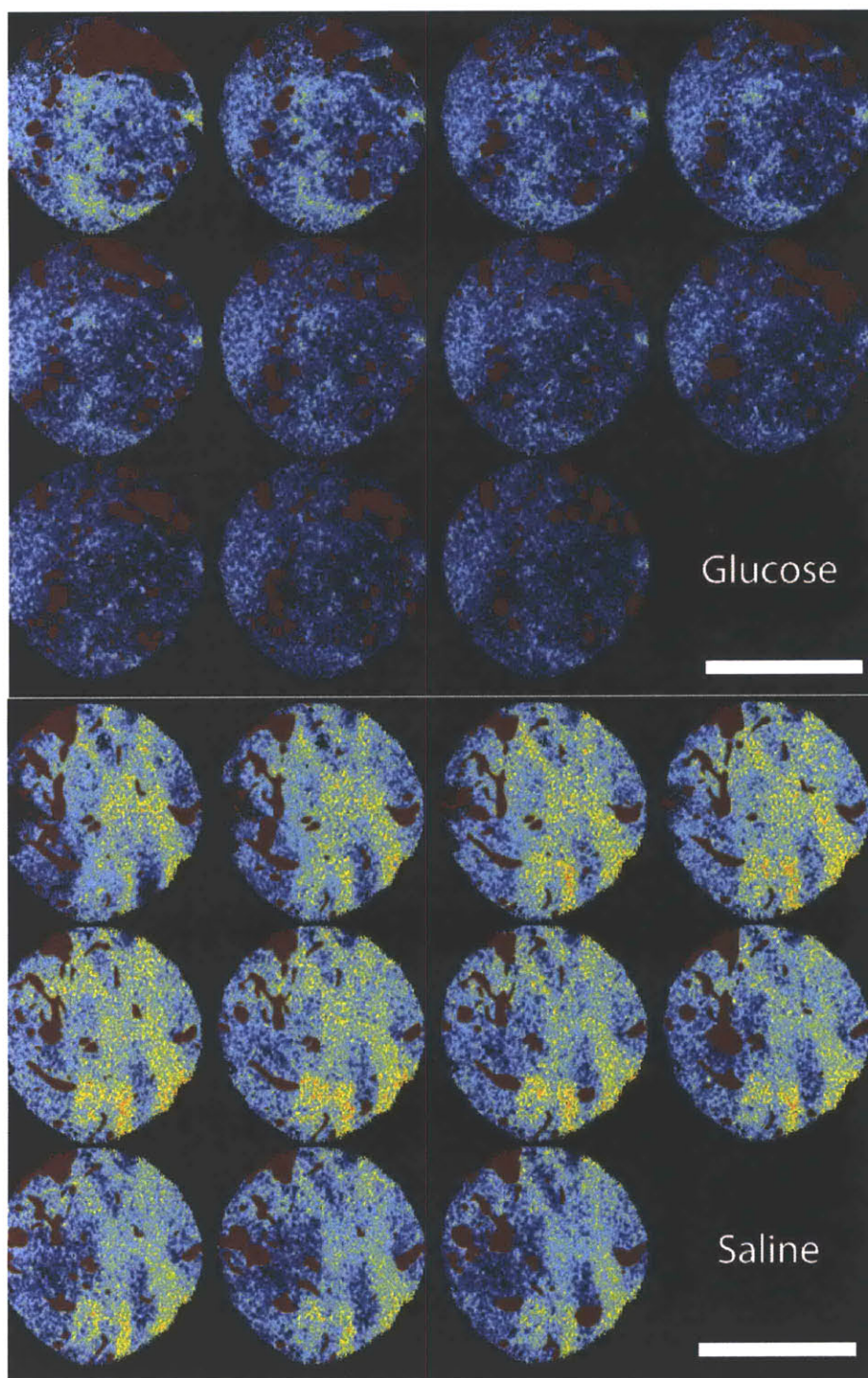


Figure V-18 MP-FRIM ratiometric images with the tumor vasculature imaged by MPM. The vasculature (red) was semi-automatically traced in three-dimensions and the resulting cast was overlaid with the ratiometric images. Here a representative slice from a single region of a glucose and saline treated tumor are shown over the course of the study. Higher ratios are represented by warmer colors. Scale bar - 500 μ m.

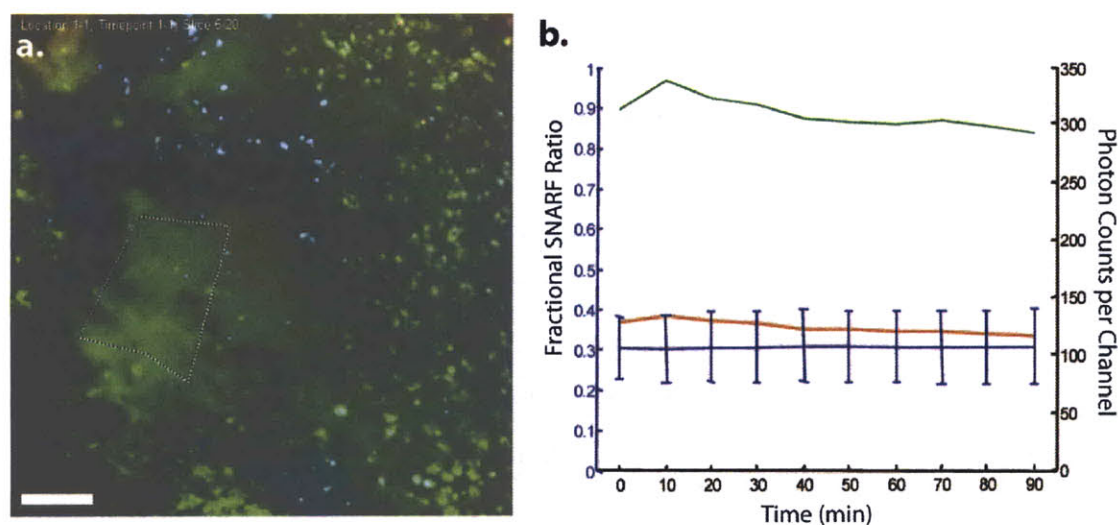


Figure V-19 NC-CXR control construct demonstrates no ratiometric change with pH alteration by glucose administration. (a) Representative example of an LS174T tumor containing diffused NC-Rhodamine construct imaged by multiphoton microscopy. The tumor blood vessels are highlighted by cascade-blue dextran-500k, while the NC construct is green. Scale Bar - 100 μm . (b) The photon counts in both the red (CXR) and green (NC) channels are shown for the image in a. The normalized ratio (red:red+green channels) is also shown on the right-hand axis. No change in ratio is observed after glucose is administered at time 0.

V.6b NC-BIOSENSORS ARE UNAFFECTED *IN VIVO* BY TISSUE OPTICAL PROPERTIES

To address the effects of *in vivo* tissue optical properties on our ratiometric sensing measurements, we synthesized control NC-constructs that were insensitive to pH and repeated the glucose modulation experiment. The control NC-biosensors consisted of a pH-insensitive carboxy-rhodamine dye attached to the nanocrystal. This is a similar construct to that used to demonstrate the two-photon antenna (**Figure V-5**). We applied the constructs *in vivo* to both LS174T and murine mammary carcinoma (MCalV) tumors during hyperglycemia. In all of our animals, we found little deviation in control construct ratio over the 90 minutes (Fig. 5). These important studies illustrate the robustness of the NC-biosensor construct within the *in vivo* tumor microenvironment. Further, the constant ratio observed indicates that the measured ratio is not affected by differential scattering or absorption of the two fluorescent components. The emission spectra of the NC-CXR control construct are very similar in wavelength to that of the NC-SNARF pH biosensor. Therefore, ratios determined from the NC pH sensor should also be just as robust as the control construct.

V.7 Summary

In this Chapter, I have presented the results of a collaborative effort to develop a FRET-based semiconductor nanocrystal biosensor for *in vivo* measurements of pH in tumors. The particular focus has been on implementing these novel NC-biosensors under two-photon excitation with multiphoton fluorescence ratiometric imaging. This technique allows for three-dimensional imaging up to depths of 400-500 μ m in murine tumor models. The application of FRET with NCs under two-photon excitation was confirmed for both pH sensitive and control constructs. The ability to employ a NC as a two-photon antenna was demonstrated; confirming that excitation in the nonlinear regime occurs through the NC due to its large two-photon absorption cross-section. Through a collaborative process, the design of the NC constructs evolved to materials with improved *in vivo* biocompatibility and negligible non-specific binding. Multiple protocols for calibrating a NC-SNARF pH biosensor were presented and compared. Later generations of the NC-SNARF construct design limited interactions with the local environment reducing differences between the *in vitro* and *ex vivo* calibrations. Application of the NC-SNARF pH biosensor to the tumor microenvironment demonstrated qualitative measurement of acidosis due to hyperglycemia in a number of experiments. The ability of MP-FRIM coupled with the NC-biosensor was shown to permit correlation of the ratiometric pH measurements with the local tumor vasculature. The basic design of the latest generation NC-biosensor was demonstrated to be robust *in vivo* and ratiometric measurements were shown to be independent of tissue optical properties. Future work will focus on vascular delivery of the NC-biosensor and more stable calibrations.

V.8 Additional Materials and Methods

V.8a ANIMAL MODELS

Dorsal skinfold chambers (DSC) were prepared on 8-10 week old male SCID mice using previously described methods⁵⁵. After recovery, a small piece of tumor (~1 mm

diameter) either from a human colorectal adenocarcinoma tumor (LS174T) or murine mammary adenocarcinoma (MCalV) obtained from a serially passaged subcutaneous *in vivo* source from the same murine background was implanted in the center of the chamber. At 1 - 2 weeks time the tumor in the chamber is of appropriate size for experiments (~ 4 mm diameter). Animals were anesthetized with either Ketamine/Xylene(10/1 mg/ml) or Isoflurane (1% in medical grade air) for all experiments. All animal work was approved by the MGH institutional review board on animal care.

V.8b IN VIVO BIOCOMPATIBILITY STUDIES

For NC construct extravasation studies with PEGylated nanocrystals, cascade blue ~500 kDa dextran (10 mg/mL) was tail-vein injected. After 20 minutes, 0.2 mL of 10% aminoPEG/90% hydroxyPEG 555 nm emitting NCs were intravenously administered. Five data points in the tumor were taken starting 30 minutes post-injection of the NCs. Emission spectra were integrated for 2.5 seconds on the multispectral MPM (**Error! Reference source not found.**).

The intravascular biocompatibility experiments with dendrimer and PEGylated NC constructs were performed in male SCID mice bearing DSC implanted with an HT1080 human fibrosarcoma tumor. Studies were initiated on tumors at least 4mm in diameter by enface measurement. NC constructs were co-injected into the tail-vein with cascade blue 500kDa dextran (10mg/ml). Randomly selected regions of the tumor and normal tissue were imaged using multiphoton microscopy. Nanocrystal construct emission ranged from 530-580nm, so a 540/100 bandpass emission filter was used for fluorescence collection.

Comparison of NC constructs with different terminated PEGs was performed in SCID mice bearing DSC implanted with either LS174T or MCalV tumors. Experiments were initiated after the tumors reached ~4mm in diameter by enface measurement. NC constructs were delivered to the tumor through either superfusion onto the tumor

surface or direct microinjection into the tumor at depths of 200 μ m. Randomly selected regions of the tumor were imaged using multiphoton microscopy.

For all samples administered to *in vivo* tumors, solutions of NC constructs were diluted to at least 2×10^6 M in PBS and filtered with a 0.2 μ m syringe filter (Acrodisc 13mm 0.2 μ m HT Tuffryn Membrane, Pall Corp., East Hills, NY).

V.8c IN VITRO CALIBRATION MEASUREMENTS

NC-biosensors were diluted in appropriate standard pH phosphate buffers for pH 5.8-8. Potassium phosphate buffered solutions with 4% by weight BSA were prepared with continued adjustments in pH due to the buffering capacity of the albumin. pH was confirmed using an electrode pH meter (Acumet AB15, Fisher Scientific, Pittsburgh, PA). Single photon steady-state fluorescence measurements were obtained in a 1 cm pathlength cuvette from a custom-built fluorometer (Photon Technology Instruments, Inc. West Suffix, UK) installed with a photomultiplier tube (Hamamatsu R928) and a 150 W Xe excitation lamp. Size measurements were obtained using a dynamic light scatterer (DynaPro Titan, ProteinSolutions). Samples were filtered through a 0.2 μ m syringe filter and microcentrifuged to remove large particulates before measurements were taken at 25 °C. For multispectral MPM and MP-FRIM calibrations, aqueous samples were diluted to at least 0.5×10^6 M in PBS and placed in deep well microscope slides (1527-006, VWR International, LLC, West Chester, PA). All calibration measurements were performed at 37 °C. Spectral analysis and image processing were performed with custom-code prepared in Matlab (Mathworks, Inc., Natick, MA).

V.8d EX VIVO TUMOR TISSUE CALIBRATION

A subcutaneously grown LS174T tumor from a single SCID mouse is removed and thin slices (~1mm) are obtained from it using surgical blades. These slices are equilibrated for 1 hour in PBS buffers across the physiologic range (pH 5.8 to 8.0). After equilibration, the NC-biosensor is added to the slices at a concentration of 50-100 μ M. Following the addition of NC-biosensor, the slices are placed in individual deep well microscope slides

for each pH calibration point. The samples are set aside for 15 minutes at 25-37 °C to permit diffusion into the tumor slices. To obtain a calibration curve, four random fields of view are taken in each tumor slice at depths from 0 to 400 μm with 5 μm steps using MP-FRIM. Fluorescent emission from the NC and dye are collected by employing a 585nm longpass dichroic filter to split the signal into two PMTs with a 535/40nm and 635/40nm broadband filter, respectively. A ratiometric signal for each pH was obtained by post-process filtering of the images with a 3X3 pixel Gaussian filter and taking the ratio of the dye channel (635/40) to the NC channel (535/40) at each depth.

V.8e EX VIVO CALIBRATION IN TUMOR CELL SLURRY

Subcutaneously grown LS174T tumors in SCID mice are removed at a size of 5-6mm in diameter and homogenized. 1% trypsin is added to the homogenate in Hanks' balanced salt solution (HBSS) and mixed for 5 minutes. Then the mixture is centrifuged at 1200 rpm for 5 minutes. After removal of the supernatant, the pellet is resuspended in HBSS. For pH calibration, the cell free suspension is centrifuged again followed by removal of the HBSS and addition of PBS buffers (pH 5.6 - 8.0) containing the NC-biosensor. The mixture is then added to separate deep well microscope slides and MP-FRIM performed as described above.

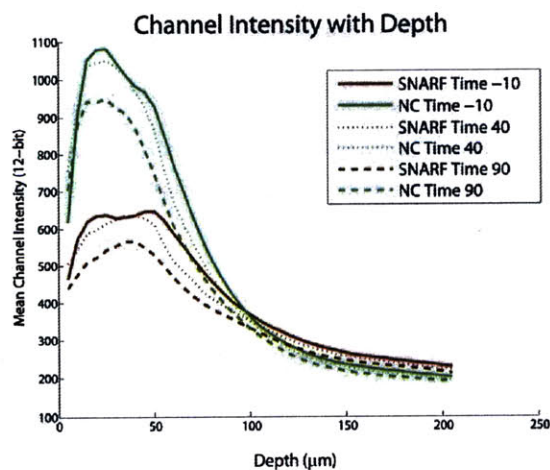


Figure V-20 Differences in tissue scattering with depth for the NC and SNARF emission channels over the course of a hyperglycemia experiment.

V.8f IN VIVO HYPERGLYCEMIA EXPERIMENTS

The NC-biosensor was applied either by superfusion onto the tumor or direct intratumoral injection at 200 μm depths. To highlight the tumor vasculature, cascade-blue dextran-500k was intravenously injected into each animal. For each tumor, 5-6 locations were randomly selected and imaged by MP-FRIM immediately prior to intraperitoneal or intravenous injection of a 300 μl bolus of 6mg/kg glucose in PBS. Over 90 minutes, each location was imaged every ten minutes. Ratios of the pH-sensitive dye (SNARF) emission (red channel) to the 540nm emission of the nanocrystal (green channel) were determined for each location using custom algorithms prepared in Matlab (Mathworks, Natick, MA). Briefly, the field of view was normalized for uneven excitation using standardized solutions. Secondly, the difference in tissue scattering (**Figure V-20**) for the red and green fluorescent emissions was corrected by fitting to a single exponential function. A threshold was then applied to each 12-bit image to remove low (<200) and high (4095) values that could be artifacts or were too low in signal to noise ratio. A semi-automated vascular tracing algorithm^{56,57} was then applied to create a three-dimensional mask of the tumor vasculature. These areas and also regions of extravasated angiographic contrast were then masked out of the images. Finally, the ratio of the dye to NC channel was taken to create the final ratiometric images. Correlation with the tumor vasculature was performed by created distance maps with respect to the traced vasculature. Using the distance map, each pixel from the ratiometric image within an averaging window (10 μm) centered at a given distance was determined to obtain the distance profile.

V.8g STATISTICAL ANALYSIS

Data are presented as mean \pm standard error of the mean (SEM). Significant differences between groups were assessed by a multivariate repeated measures ANOVA accounting for response to treatment over time (Systat, Systat Software, Inc., Chicago, IL). Individual timepoints were compared using a two sample Student's t-Test. $P < 0.05$ was considered statistically significant for all comparisons.

V.9 References

1. Dabbousi, B.O., *et al.* (CdSe)ZnS Core - Shell quantum dots: Synthesis and Characterization of a size series of highly luminescent nanocrystallites. *J phys Chem B* **101**, 9463-9475 (1997).
2. Murray, C.B., Norris, D.J. & Bawendi, M.G. Synthesis and Characterization of nearly monodisperse CdE (E=S, Se, Te) semiconductor nanocrystallites. *J Am Chem Soc* **115**, 8706-8715 (1993).
3. Baker, G.A.M., C.A.; Bukowski, E.J.; Baker, S.N; Bright, F.V. Assessment of One- and Two-Photon Excited Luminescence for Directly Measuring O₂, pH, Na⁺, Mg²⁺, or Ca²⁺ in Optically Dense and Biologically Relevant Samples. *Appl Spec* **56**, 455-463 (2002).
4. Hanson, K.M., *et al.* Two-photon fluorescence lifetime imaging of the skin stratum corneum pH gradient. *Biophys J* **83**, 1682-1690 (2002).
5. Jobsis, P.D., Combs, C.A. & Balaban, R.S. Two-photon excitation fluorescence pH detection using 2,3-dicyanohydroquinone: a spectral ratiometric approach. *J Microsc* **217**, 260-264 (2005).
6. Snee, P.T., *et al.* A ratiometric CdSe/ZnS nanocrystal pH sensor. *J Am Chem Soc* **128**, 13320-13321 (2006).
7. Somers, R.C. Doctoral, MIT (2008).
8. Somers, R.C., Bawendi, M.G. & Nocera, D.G. CdSe nanocrystal based chem-/bio- sensors. *Chem Soc Rev* **36**, 579-591 (2007).
9. Taki, M., Wolford, J.L. & O'Halloran, T.V. Emission ratiometric imaging of intracellular zinc: design of a benzoxazole fluorescent sensor and its application in two-photon microscopy. *J Am Chem Soc* **126**, 712-713 (2004).
10. Mank, M., *et al.* A genetically encoded calcium indicator for chronic in vivo two-photon imaging. *Nat Methods* **5**, 805-811 (2008).
11. Buehler, C., Kim, K.H., Greuter, U., Schlumpf, N. & So, P.T. Single-photon counting multicolor multiphoton fluorescence microscope. *J Fluoresc* **15**, 41-51 (2005).
12. Bergey, E.J.W., X.P.; Krebs, L.J.; Pudavar, H.E.; Kapoor, R.; Friend, C; Liebow, C.; Prasad, P.N. Multicolored two-photon fluorescent microscopy and localized two-photon fluorescent spectroscopy in living cells. *Proc SPIE* **4264**, 82-88 (2001).
13. Lansford, R., Bearman, G. & Fraser, S.E. Resolution of multiple green fluorescent protein color variants and dyes using two-photon microscopy and imaging spectroscopy. *J Biomed Opt* **6**, 311-318 (2001).
14. Wang, X., *et al.* Studies on the mechanism of action of a targeted chemotherapeutic drug in living cancer cells by two photon laser scanning microspectrofluorometry. *J Biomed Opt* **6**, 319-325 (2001).
15. Haraguchi, T., Shimi, T., Koujin, T., Hashiguchi, N. & Hiraoka, Y. Spectral imaging fluorescence microscopy. *Genes Cells* **7**, 881-887 (2002).
16. Larson, D.R., *et al.* Water-soluble quantum dots for multiphoton fluorescence imaging in vivo. *Science* **300**, 1434-1436 (2003).
17. Banfi, G.P., Degiorgio, V.V., Ghigliazza, M., Tan, H.M. & Tomaselli, A. Two-photon absorption in semiconductor nanocrystals. *Phys Rev B Condens Matter* **50**, 5699-5702 (1994).
18. Grecco, H.E., *et al.* Ensemble and single particle photophysical properties (two-photon excitation, anisotropy, FRET, lifetime, spectral conversion) of commercial quantum dots in solution and in live cells. *Microsc Res Tech* **65**, 169-179 (2004).

19. Jain, R.K. & Stroh, M. Zooming in and out with quantum dots. *Nat Biotechnol* **22**, 959-960 (2004).
20. Stroh, M., *et al.* Quantum dots spectrally distinguish multiple species within the tumor milieu in vivo. *Nat Med* **11**, 678-682 (2005).
21. Wang, T., *et al.* Thiol-Capped CdTe Quantum Dots with Two-Photon Excitation for Imaging High Autofluorescence Background Living Cells. *J Fluoresc* (2008).
22. Dayal, S. & Burda, C. Semiconductor quantum dots as two-photon sensitizers. *J Am Chem Soc* **130**, 2890-2891 (2008).
23. Lakowicz, J.R. *Topics in fluorescence spectroscopy: Nonlinear and two-photon induced fluorescence.*, (Plenum Press, New York, 1997).
24. Albota, M.A., Xu, C. & Webb, W.W. Two-Photon Fluorescence Excitation Cross Sections of Biomolecular Probes from 690 to 960 nm. *Appl Opt* **37**, 7352-7356 (1998).
25. Ajayaghosh, A. Chemistry of squaraine-derived materials: near-IR dyes, low band gap systems, and cation sensors. *Acc Chem Res* **38**, 449-459 (2005).
26. Chung, S.J., *et al.* Extended squaraine dyes with large two-photon absorption cross-sections. *J Am Chem Soc* **128**, 14444-14445 (2006).
27. Liu, J., Diwu, Z. & Leung, W.Y. Synthesis and photophysical properties of new fluorinated benzo[c]xanthene dyes as intracellular pH indicators. *Bioorg Med Chem Lett* **11**, 2903-2905 (2001).
28. Rink, T.J., Tsien, R.Y. & Pozzan, T. Cytoplasmic pH and free Mg²⁺ in lymphocytes. *J Cell Biol* **95**, 189-196 (1982).
29. Riegler, J. & Nann, T. Application of luminescent nanocrystals as labels for biological molecules. *Anal Bioanal Chem* **379**, 913-919 (2004).
30. Medintz, I.L., Uyeda, H.T., Goldman, E.R. & Mattoussi, H. Quantum dot bioconjugates for imaging, labelling and sensing. *Nat Mater* **4**, 435-446 (2005).
31. Uyeda, H.T., Medintz, I.L., Jaiswal, J.K., Simon, S.M. & Mattoussi, H. Synthesis of compact multidentate ligands to prepare stable hydrophilic quantum dot fluorophores. *J Am Chem Soc* **127**, 3870-3878 (2005).
32. Wisher, A.C., Bronstein, I. & Chechik, V. Thiolated PAMAM dendrimer-coated CdSe/ZnSe nanoparticles as protein transfection agents. *Chem Commun (Camb)*, 1637-1639 (2006).
33. Quinlan, G.J., Martin, G.S. & Evans, T.W. Albumin: biochemical properties and therapeutic potential. *Hepatology* **41**, 1211-1219 (2005).
34. Thurston, G., *et al.* Cationic liposomes target angiogenic endothelial cells in tumors and chronic inflammation in mice. *J Clin Invest* **101**, 1401-1413 (1998).
35. Choi, H.S., *et al.* Renal clearance of quantum dots. *Nat Biotechnol* **25**, 1165-1170 (2007).
36. Zimmer, J.P., *et al.* Size series of small indium arsenide-zinc selenide core-shell nanocrystals and their application to in vivo imaging. *J Am Chem Soc* **128**, 2526-2527 (2006).
37. Jain, R.K. Delivery of molecular medicine to solid tumors. *Science* **271**, 1079-1080 (1996).
38. Chen, Y. & Periasamy, A. Characterization of two-photon excitation fluorescence lifetime imaging microscopy for protein localization. *Microsc Res Tech* **63**, 72-80 (2004).
39. Elangovan, M., *et al.* Characterization of one- and two-photon excitation fluorescence resonance energy transfer microscopy. *Methods* **29**, 58-73 (2003).
40. Dellian, M., Helmlinger, G., Yuan, F. & Jain, R.K. Fluorescence ratio imaging of interstitial pH in solid tumours: effect of glucose on spatial and temporal gradients. *Br J Cancer* **74**, 1206-1215 (1996).

CHAPTER 5

41. Evelhoch, J.L., Sapareto, S.A., Jick, D.E. & Ackerman, J.J. In vivo metabolic effects of hyperglycemia in murine radiation-induced fibrosarcoma: a ³¹P NMR investigation. *Proc Natl Acad Sci U S A* **81**, 6496-6500 (1984).
42. Jain, R.K., Shah, S.A. & Finney, P.L. Continuous noninvasive monitoring of pH and temperature in rat Walker 256 carcinoma during normoglycemia and hyperglycemia. *J Natl Cancer Inst* **73**, 429-436 (1984).
43. Sevick, E.M. & Jain, R.K. Blood flow and venous pH of tissue-isolated Walker 256 carcinoma during hyperglycemia. *Cancer Res* **48**, 1201-1207 (1988).
44. Jahde, E. & Rajewsky, M.F. Tumor-selective modification of cellular microenvironment in vivo: effect of glucose infusion on the pH in normal and malignant rat tissues. *Cancer Res* **42**, 1505-1512 (1982).
45. Cullen, G.E., Austin, J.H., Kornblum, K. & Robinson, H.W. The initial acidosis in anesthesia. *The Journal of Biological Chemistry*, 625-659 (1923).
46. Cullen, G.E., Austin, J.H., Kornblum, K. & Robinson, H.W. ANÆSTHESIA AND BLOOD REACTION. *British Journal Anaesthesia* **2**, 56-75 (1924).
47. Stehle, R.L. & Bourne, W. Concerning the mechanism of acidosis in anethesia. *The Journal of Biological Chemistry* **60**, 17-29 (1924).
48. Alva, N., Palomeque, J. & Carbonell, T. Nitric oxide induced by ketamine/xylazine anesthesia maintains hepatic blood flow during hypothermia. *Nitric Oxide* **15**, 64-69 (2006).
49. Bonath, K., Hirche, H. & Lange, S. [Effect of ketamine hydrochloride-halothane-oxygen anesthesia on respiration, blood gases and acid-base status of the rabbit]. *Berl Munch Tierarztl Wochenschr* **93**, 462-468 (1980).
50. Matsuda, Y., *et al.* Comparison of newly developed inhalation anesthesia system and intraperitoneal anesthesia on the hemodynamic state in mice. *Biol Pharm Bull* **30**, 1716-1720 (2007).
51. Wen, B., Urano, M., O'Donoghue, J.A. & Ling, C.C. Measurements of partial oxygen pressure pO₂ using the OxyLite system in R3327-AT tumors under isoflurane anesthesia. *Radiat Res* **166**, 512-518 (2006).
52. Ward, K.A., DiPette, D.J., Held, T.N. & Jain, R.K. Effect of intravenous versus intraperitoneal glucose injection on systemic hemodynamics and blood flow rate in normal and tumor tissues in rats. *Cancer Res* **51**, 3612-3616 (1991).
53. Helmlinger, G., Yuan, F., Dellian, M. & Jain, R.K. Interstitial pH and pO₂ gradients in solid tumors in vivo: high-resolution measurements reveal a lack of correlation. *Nat Med* **3**, 177-182 (1997).
54. DiPette, D.J., Ward-Hartley, K.A. & Jain, R.K. Effect of glucose on systemic hemodynamics and blood flow rate in normal and tumor tissues in rats. *Cancer Res* **46**, 6299-6304 (1986).
55. Leunig, M., *et al.* Angiogenesis, microvascular architecture, microhemodynamics, and interstitial fluid pressure during early growth of human adenocarcinoma LS174T in SCID mice. *Cancer Res* **52**, 6553-6560 (1992).
56. Tyrrell, J.A., *et al.* Robust 3-D modeling of vasculature imagery using superellipsoids. *IEEE Trans Med Imaging* **26**, 223-237 (2007).
57. Tyrrell, J.A., *et al.* A 2-D/3-D model-based method to quantify the complexity of microvasculature imaged by in vivo multiphoton microscopy. *Microvasc Res* **70**, 165-178 (2005).

VI. Three-dimensional microscopy of vascular networks, lymphatics, cell viability and tissue microenvironment *in vivo* using optical frequency domain imaging

Parts of this Chapter have been published:

Vakoc, BJ*, Lanning, RM*, Tyrrell, JA, Padera, TP, Bartlett, L, Stylianopoulos, T, Munn, LL, Tearney, GJ, Fukumura, D, Jain, RK, and Bouma, BE. *Nat. Med.* (2009) *In Press*.

VI.1 Introduction and Motivation:

This Chapter introduces novel techniques using optical frequency domain imaging (OFDI), a coherent microscopy, to non-invasively probe the tumor microenvironment. The work presented here is the result of collaboration between Professors Ben Vakoc and Brett Bouma of the Wellman Laboratories for Photomedicine and the Steele Lab for Tumor Biology. The instrumentation and data collection algorithms were pioneered by the Wellman labs, while the animal models and biological questions were developed and proposed by the Steele Lab. Integrating the two biomedical areas of expertise fostered the joint development and implementation of unique methods using intravital OFDI to image both microanatomy and function in solid tumors.

The application of multiphoton microscopy^{1,2} (MPM) to the study of solid tumor biology *in vivo* has elucidated pathways and mechanisms of cancer progression and has led to new therapeutic strategies³. Current high-resolution intravital imaging techniques, however, can be used to visualize tumor microstructure and vascular morphology only superficially (300-400 μm depth) and only over volumetric regions that are a fraction of the total tumor volume in small animal models. Additionally, longitudinal imaging is often limited in frequency due to the accumulation of exogenous contrast agents. Consequently, nearly a decade after the introduction of MPM to tumor biology, significant gaps remain in our understanding of critical aspects of tumor biology including the vascularization of tumors, the multifaceted interactions between tissues and vessels within the heterogeneous tumor mass, and the response of blood vessels, lymphatic vessels and cancer cells to therapy. Filling these gaps will require complementing existing MPM techniques with new methods for probing the microenvironment over wider-fields and broader timescales.

Through the adoption of time-of-flight techniques to perform depth sectioning, optical coherence tomography⁴ (OCT) alleviates the requirement for high numerical aperture optics, thereby simplifying wide-field imaging. Through the integration of Doppler detection principles, OCT can also circumvent the need for exogenous labels to identify

vasculature. However, attempts to apply OCT to high-resolution three-dimensional vascular imaging have been hampered by poor sensitivity in the Doppler-based approaches techniques employed to achieve vascular contrast⁵⁻⁹. Additionally, methods for characterizing biological parameters of tumor microenvironment and structure have not been developed for OCT and existing angiographic OCT systems have not achieved both high sensitivity and the rapid imaging speeds required for large-volume vascular morphometry.

Here, we overcome these limitations through the development of new methods and instrumentation building on a second generation OCT technology termed optical frequency domain imaging¹⁰. We apply these newly advanced techniques to a range of tumor models *in vivo* and demonstrate the ability of OFDI to perform 1) high-resolution, wide-field, and deep imaging of tumor vasculature, 2) morphological and fractal characterization of vascular networks, 3) frequent and prolonged monitoring of vascular network dynamics, 4) contrast-free functional lymphangiography, and 5) characterization of tissue viability. Further, we demonstrate the application of these capabilities to reveal the responses of murine tumor models *in vivo* to vascular-targeted and cellular-targeted therapies.

VI.2 Novel OFDI Instrumentation and Methods

We used a newly developed OFDI instrument to characterize the tumor microenvironment across multiple tumor models and at multiple sites in mice. The OFDI instrument scanned a focused laser beam onto the sample to acquire the reflected light signal as a function of wavelength and time at each transverse location. From this recorded signal, the static and dynamic scattering properties of the tissue in three-dimensions were derived (**Figure VI-1**). Imaging was performed over fields ranging from 20-100 mm², and to a depth of approximately 1.5 mm for vascular signals and up to 2.5 mm for structural signals. The optical signals reflected from the sample were recorded and processed offline to extract images and quantitative data describing several biological parameters (see Methods and Materials).

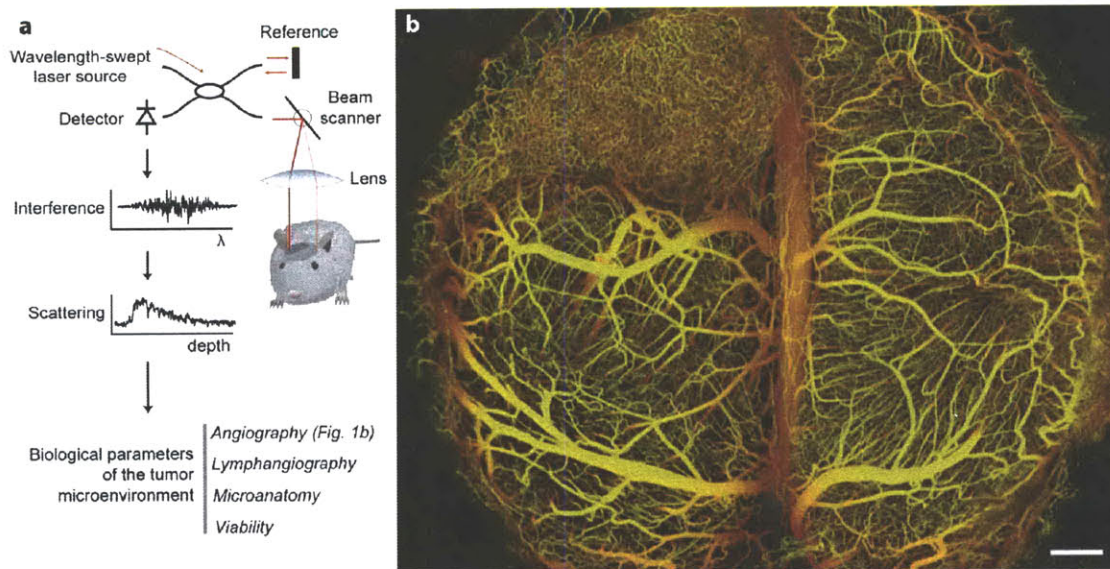


Figure VI-1 Principles of *in vivo* multiparametric imaging with optical frequency domain imaging (OFDI). (a) An optical beam is focused into the tissue. The light reflected across all depths is interfered with a reference beam and that interference signal is recorded as a function of light wavelength from 1,220 nm to 1,360 nm. The amplitude and phase of the reflected light as a function of wavelength is used to localize the reflected signal as a function of depth. At a given depth, the amplitude and phase of the reflected signal as a function of time is used to derive the optical scattering properties and thereby the tissue structure and function. (b) The depth-projected vasculature within the first 2 mm of mouse brain bearing a xenotransplanted U87 human glioblastoma multiforme tumor imaged with OFDI. Depth is denoted by color: yellow (superficial) to red (deep). Scale bar - 500 μm .

VI.3 Wide-field three-dimensional angiography

The microvasculature of solid tumors plays a critical role in both progression and response to therapy¹¹. Multiphoton microscopy is currently the preferred method for obtaining three-dimensional vascular data *in vivo*¹. With MPM, however, it is nearly impossible to study central regions of relatively large tumor volumes, and impractical to image across wide fields in multiple animals and at multiple time points. To detect vessels in OCT, contrast is derived from the Doppler shift¹²⁻¹⁷ induced by the circulating red blood cells. Using novel implementations of Doppler principles and OFDI¹⁸, we enabled wide-field angiography with sufficient sensitivity to map smaller vessels, specificity to discriminate vascular motion from physiological motion, and speed to perform imaging over wide-fields. Three-dimensional angiographic datasets were

derived from the acquired OFDI signals, and were reduced to en face vascular projections using color to encode depth (**Figure VI-1b**).

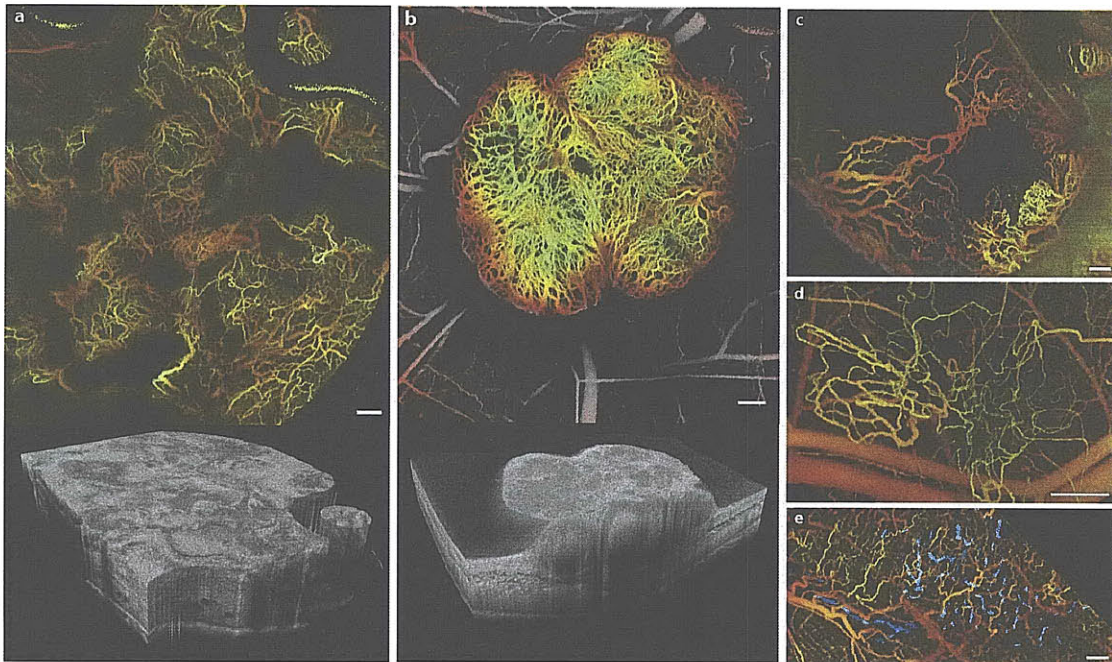


Figure VI-2 OFDI angiography across tumor types and sites. (a) A human breast cancer cell line (MDA-MB-361HK) growing in the mammary fat pad window chamber model of a female SCID mouse. Large avascular regions are notable in the vascular image (top) and reflected in the topographically diffuse tumor microstructure (bottom). (b) Tumor vasculature of a human colorectal adenocarcinoma (LS174T) implanted in the dorsal skinfold chamber of a SCID mouse (top). Non-viable tissue is evident within the tumor nodules on cross-section (lighter regions) in the tissue scattering intensity image (bottom). (c) Angiography of a subcutaneous orthotopic human breast tumor xenograft (MDA-MD-231BR) imaged by the skin flap preparation. (d) Limited vasculature of the human soft-tissue sarcoma (HSTS-26T) growing orthotopically in the dorsal skinfold chamber. (e) Simultaneous vascular and lymphatic imaging of a tumor and nearby normal tissue in the ear of a nude mouse, a commonly utilized model in the study of tumor-associated lymphatics. Scale bars - 500 μm .

VI.3a NEOPLASTIC AND NORMAL MICROVASCULATURE ACROSS TYPES AND SITES

Vascular projections were obtained across multiple tumor types at various sites. Different tumor types display strikingly different vascular network architecture and vessel densities. The utility of the OFDI technique allowed imaging in a variety of tumor models including window chambers (**Figure VI-2a,b,d**) and subcutaneous tumors (**Figure VI-2c and e**). Penetration through the higher scattering skin around the subcutaneous tumors required a lower numerical aperture lens to improve depth penetration, but also

reduced radial resolution. Light scattering intensity from the tumor tissue also provided the ability to perceive the tumor vasculature in context of the microanatomy. Additionally, *in vivo* vascular networks in normal tissues including the mammary fat pad and marrow space within the calvarium were imaged with OFDI. The capillary networks in normal murine skin are readily identifiable (**Figure VI-3a**). In the murine mammary fat pad, the significant vascular supply to the areolar region is observable penetrating from the subcutaneous tissue (**Figure VI-3b**). OFDI is capable of penetrating through bone, which minimally scatters incident photons. This permitted the vasculature within the bone marrow space between the skull surface and meninges to be imaged without the use of contrast or a window chamber model (**Figure VI-3c**).

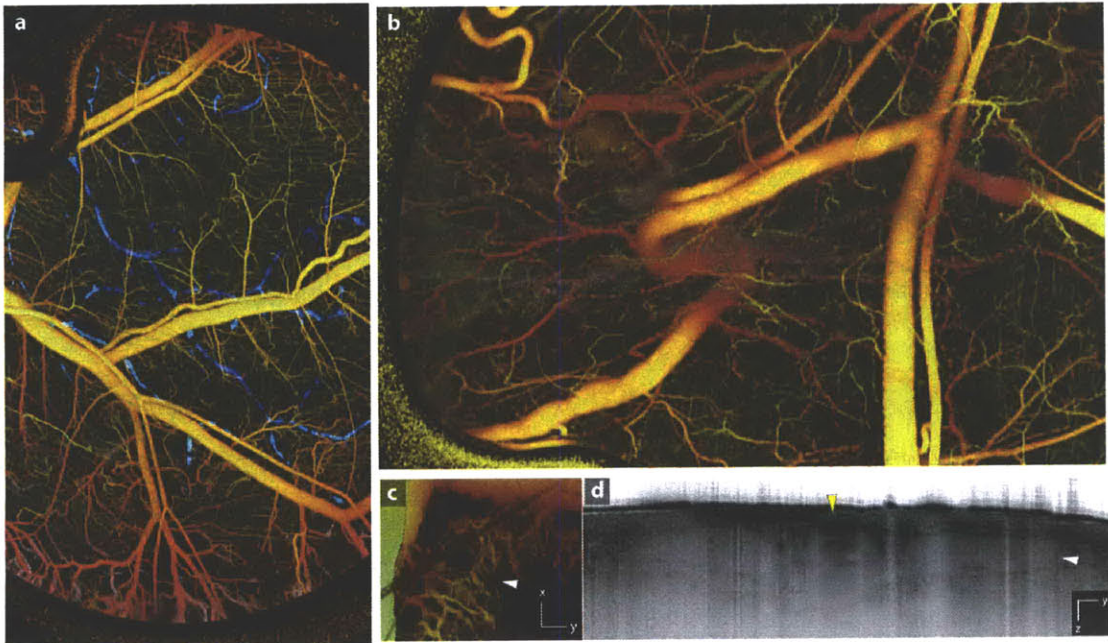


Figure VI-3 OFDI angiography of normal tissues. (a) Vascular and lymphatic networks in normal skin within the dorsal skinfold chamber window model implanted on a SCID mouse. (b) Normal vasculature of the mammary fat pad window model implanted around the third mammary gland. The collection of large vessels near the center of the field are supplying the areola on the underside of the chamber. (c) and (d) OFDI microscopy of marrow within the murine calvarium revealing vasculature within the marrow space (c) and corresponding microanatomy depicted in the cross-sectional structural image (d) showing marrow regions (\blacktriangleright) and the central sinus (\blacktriangleright).

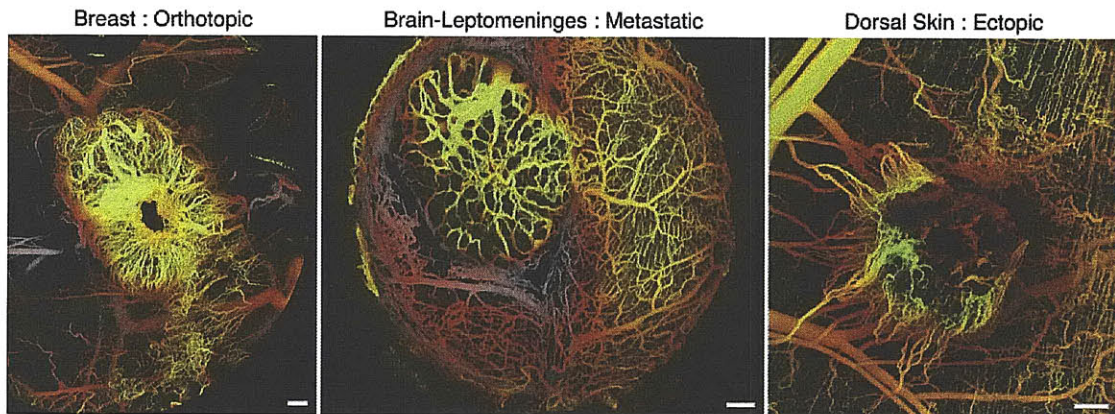


Figure VI-4 Imaging across tissue microenvironments reveals strikingly different vascular networks. The murine mammary carcinoma is shown in three different anatomical locations representative of both primary and metastatic disease. Scale bars - 500 μm .

It has been proposed that the tumor vasculature forms during angiogenesis in response to both the microstructure and growth factor gradients found in the tumor microenvironment¹⁹⁻²¹. We used OFDI to image a murine mammary carcinoma (MCAIV) implanted in orthotopic (mammary fat pad), metastatic (brain), and ectopic (skin) sites. The tumor exhibits visually different vascular architecture depending on the host tissue microenvironment (**Figure VI-4**). The degree of vascularization is strikingly different between tumors of approximately the same size ($\sim 4\text{mm}$). Interestingly, in this tumor type, the morphometry of the individual vessels as typified by vascular diameter was found to be similar. It has been demonstrated that the level of angiogenesis in a variety of breast cancer models depends on the tumor location in the host²². These differences are possibly due to varying concentrations of vascular growth factors, which have been shown to modulate the extent of angiogenesis during tumor growth²³.

VI.3b MONITORING ANGIOGENESIS

The ability to non-invasively image tumor vasculature over wide-fields at significant depths using OFDI allowed monitoring of angiogenesis over the course of tumor growth (**Figure VI-5**). Initially, the tumor implant induces dilation of the capillary network below followed by sprouting of vascular branches from these dilated vessels upwards into the tumor mass. This is followed by sprouting from the lateral arteries and arterioles at a

farther distance from the tumor mass. The differential response of the regions surrounding the tumor mass over time is due to diffusion gradients of angiogenic factors produced by both cancer and stromal cells. Seminal studies by Ausprunk *et al* demonstrated that the tumor vasculature is entirely reliant on the surrounding host vasculature and gradients of vascular growth factors²⁴. Further, cancer cells have been shown to induce the stromal cells within the tumor microenvironment to produce VEGF and other vascular growth factors²⁵⁻³⁰. As the tumor continues to grow, the interior vessel within the tumor mass appear to either spread apart or are compressed due to cancer cell proliferation³¹ maintaining a relatively small diameter to those at the margins. The laterally induced vessels cover the margins of the tumor and remain large and dilated during tumor progression in this model.

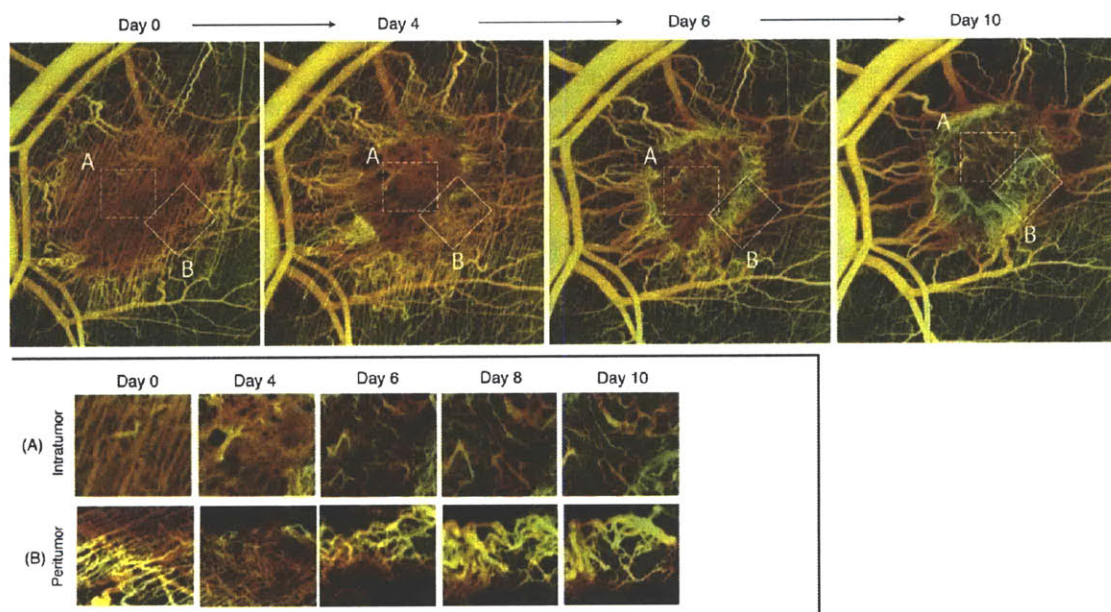


Figure VI-5 Angiogenesis in a murine mammary carcinoma model. The incorporation of the capillary bed and larger arterioles into the tumor vascular network is observable during tumor growth. *Inset:* Differences in the morphologies of the vessels in the center of the tumor versus the margins.

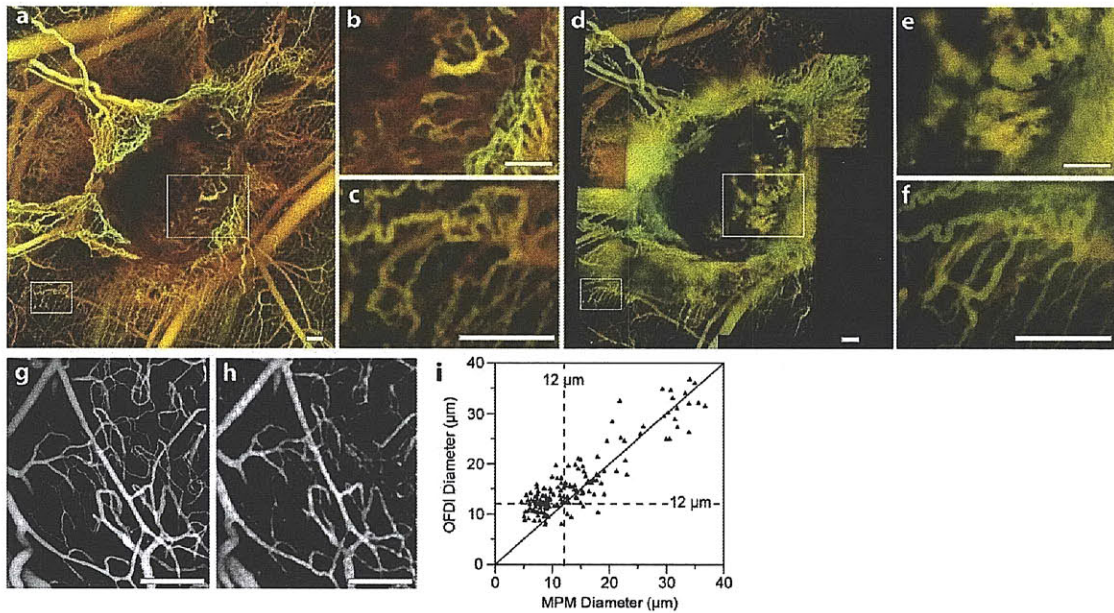


Figure VI-6 Comparison of multiphoton and OFDI angiography. (a) and (d) Wide-field tumor imaging using MPM required 2 hours (d), while imaging using OFDI required only 10 minutes (a) for an MCalV tumor implanted in the dorsal skinfold chamber. (b) and (e), Highlighted regions in a and d demonstrate the enhanced ability of OFDI to visualize deeper vessels and distinguish morphology in regions of vascular leakage. (c) and (f), Differences in resolution of the techniques showing the greater detail of finer vascular structures obtainable by MPM. (g-h), The application of automated vascular tracing to registered datasets of normal brain vasculature acquired with MPM (g) and OFDI (h) allows quantification of the resolution of OFDI angiography and validation of the morphological measurements obtained from OFDI (i). Scale Bars - 250 μm

VI.3c OFDI COMPLEMENTS MPM IN IMAGING TUMOR VASCULATURE

To compare Doppler OFDI and MPM angiography, tumors were imaged sequentially with each modality. MPM required the acquisition and subsequent alignment of 30-40 separate three-dimensional image stacks to sample a field of view equivalent to that of the OFDI instrument. Imaging durations ranged from 2-4 hours for MPM, and 10-20 minutes for Doppler OFDI, depending upon the imaged field. To provide the greatest depth of penetration for MPM, we utilized a high numerical aperture (20X, 0.95 NA) objective lens. Faster imaging times could be obtained using lower magnification lenses at the expense of penetration depth and resolution. Vascular projections derived from each modality were compared to provide gross perspective of the relative merits and complementary nature of the two methods (Figure VI-6a,d). Whereas MPM excelled at visualizing the smallest superficial capillaries (Figure VI-6c,f), OFDI was superior in

discerning vessels deeper within the central regions of the tumor and in regions where fluorescent tracers extravasated (**Figure VI-6b,e**). Vessels beyond 1.0 mm in depth were routinely observed with OFDI while with MPM the maximum penetration depth in the surveyed tumor models ranged from 250-400 μm . The difference in depth of penetration for the two methods was most dramatic in regions where superficial diffuse contrast agent masked underlying vessels in MPM, or where highly scattering necrotic regions differentially attenuated the shorter wavelength (800 nm) multiphoton excitation light relative to the longer wavelength (1300 nm) OFDI light. The unique Doppler acquisition techniques incorporated into the OFDI instrument allowed rapid visualization of the tumor vasculature inclusive of its connectivity with host vessels, complementing the higher resolution but relatively superficial MPM angiography.

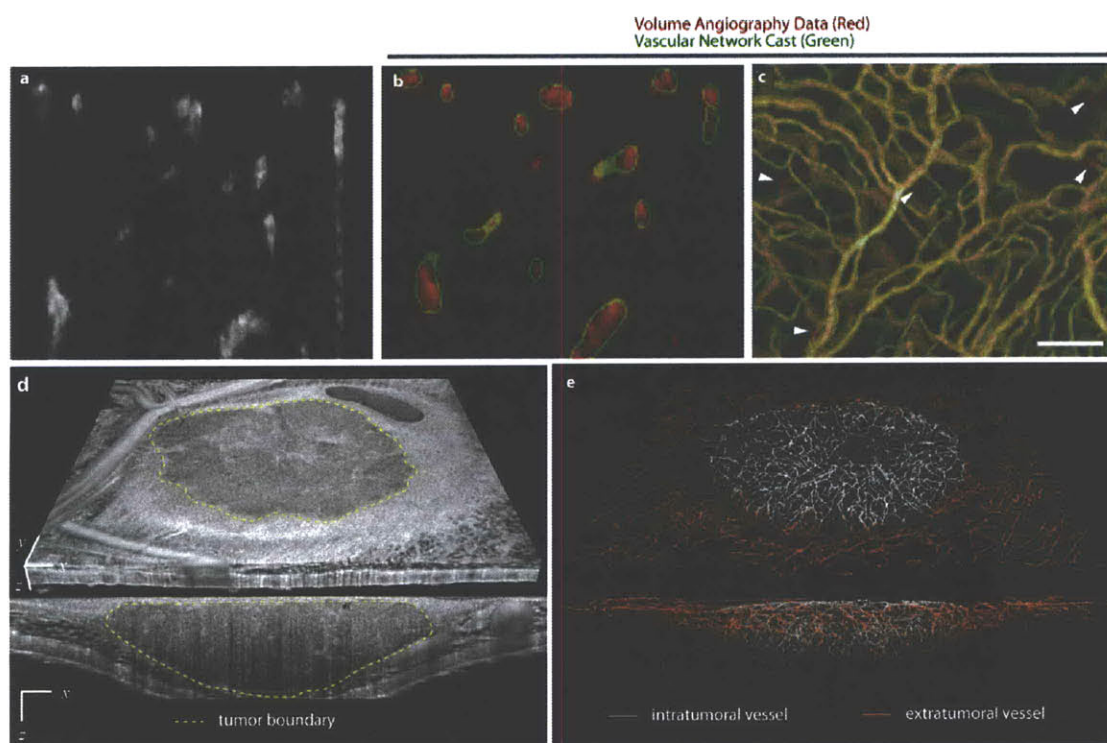


Figure VI-7 Vascular tracing and structural correlation. (a) Cross-sectional OFDI angiographic data showing vessels and shadow artifacts extending below the vessels. (b) Dataset showing bitmap data (red) after shadow removal and vascular tracing contours (green). (c) Merged enface image of the vascular dataset (red) and a cast of the traced vessels (green) illustrating the inclusion of all but a few vessels () within the cast. Scale Bar: 250 μm . (d) Microanatomical display showing tumor boundary definition in a three-dimensional tissue volume. (e) Skeletonized traced vessels differentiated between intratumoral and extratumoral for the tumor depicted in d. Transverse extent in d,e: 5 mm (x), 4.4 mm (y).

VI.4 Morphological and Fractal Characterization of Vascular Networks

Morphological characterization of blood vessels in tumors provides insight into resistance to transport, angiogenic mechanisms, and response to therapy^{32,33}. Previous characterization methods, based on intravital microscopy and MPM angiography, however, have been limited to small fields-of-view and superficial depths. To extract quantitative vascular measurements from the OFDI angiograms, we developed a fully automated three-dimensional vascular tracing and analysis algorithm, optimized specifically to operate on the OFDI datasets.

VI.4a VASCULAR MORPHOLOGY FROM OFDI ANGIOGRAMS

Briefly, the vascular networks were then manually masked to remove Doppler artifacts due to Brownian motion in extracellular fluid or noise from airspaces between the tumor surface and initial image plane. Then the three-dimensional OFDI angiograms were processed to reduce the effects of shadowing³⁴ due to high backscatter from large vessels. The shadowing effect can be enhanced in tumors due to increased vascular hematocrit³⁵. This can prevent access to deeper vessels, but is mitigated to some extent through image processing using an exponential filter referenced to the higher signal vessels (**Figure VI-7a** and **b**). Finally, a semi-automated vascular tracing algorithm reduced three-dimensional OFDI angiograms to networks of interconnected vessel segments modeled as superellipsoids^{36,37} (**Figure VI-7c**). From the centerlines and shape parameters of these superellipsoids, the trajectories and morphology of vessel segments were extracted.

To spatially correlate the vascular parameters with the tumor boundaries, the three-dimensional tumor volume was determined from the OFDI scattering amplitude. The tumor cells are higher scattering than the surrounding tissue due to the increased nuclear to cytoplasm ratio³⁸⁻⁴¹. Briefly, the approximate en face center of the tumor was determined and axial sections across the tumor at regular intervals of 22.5° were

created (**Figure VI-8**). The tumor boundary on each section was then manually drawn. These boundaries were then used by automated algorithms to interpolate a three-dimensional tumor volume. The vascular casts output from the semi-automated vascular tracing were then correlated with distance from the tumor boundary. Using these methods, the intratumoral vasculature could be separately characterized for morphological parameters (**Figure VI-7d** and **e**).

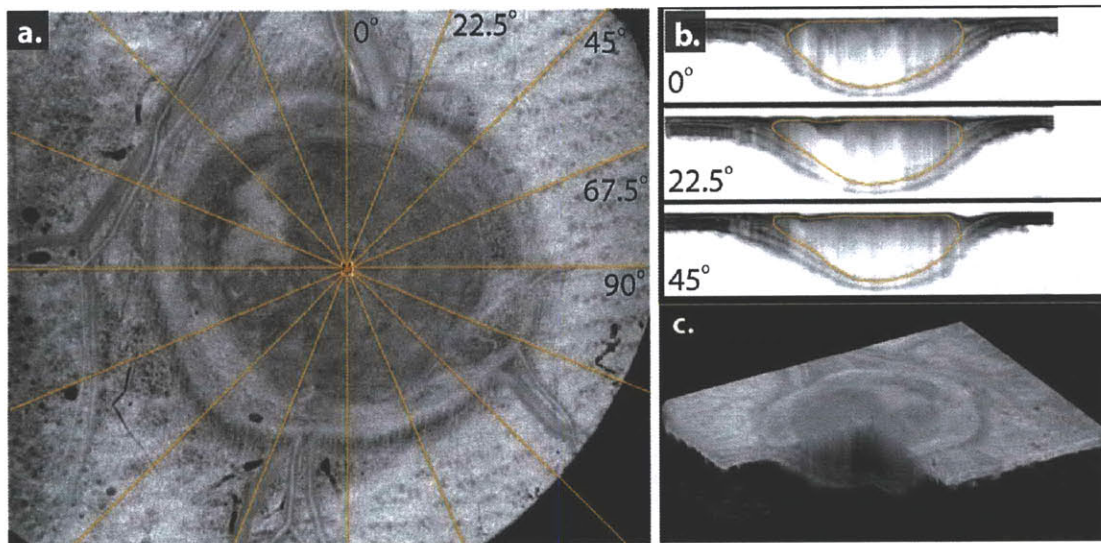


Figure VI-8 Determination of tumor boundaries and volume in three-dimensional space. (a) Semi-automated algorithms enabled definition of the tumor boundaries from the differences in scattering amplitude between the tumor and host tissue. (b) Manual tracing of the tumor boundary on axial slices. (c) Three-dimensional volume illustrating the differences in tumor scattering.

To evaluate OFDI morphometry, we obtained MPM (**Figure VI-6g**) and OFDI (**Figure VI-6h**) angiograms of the same region of a normal mouse brain in vivo. Previously established tracing and morphometry techniques³⁶ were applied to the MPM data. We compared vessel diameter measurements of 402 precisely co-registered segments (each approximately 100 μm in length) and found a high correlation ($r = 0.87$) for vessels larger than 12 μm in diameter (**Figure VI-6i**). OFDI methods often located and traced smaller vessels but overestimated the diameter of these capillaries and thus the correlation of diameter measurements for vessels with diameters under 12 μm as measured by MPM was low ($r = 0.36$).

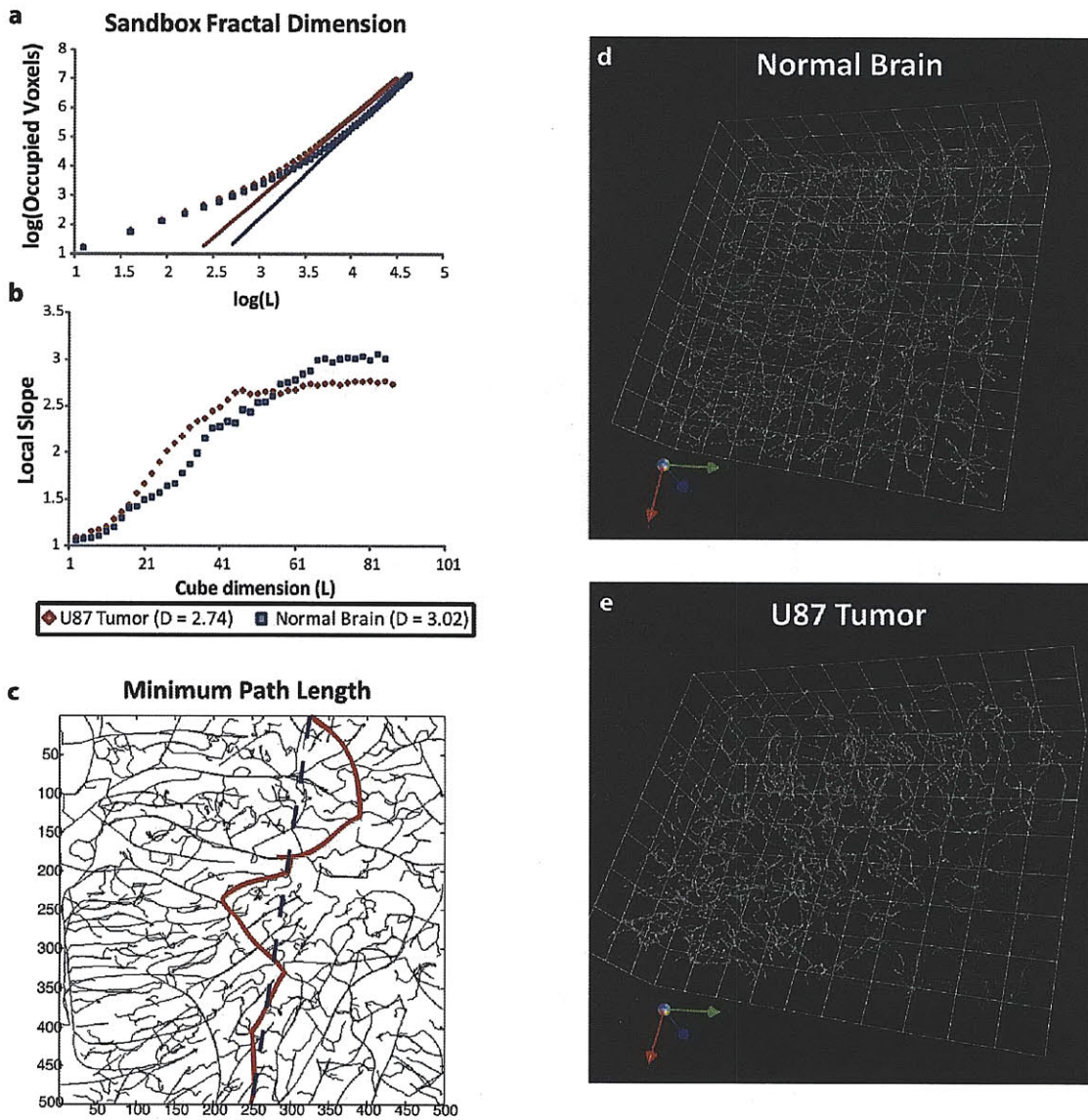


Figure VI-9 Fractal characterization of tumor vascular networks imaged by OFDI angiography. (a) Representative example of the sandbox method for determining the fractal dimension of the vasculature of both normal murine cortex and a human tumor glioblastoma multiforme (U87) tumor implanted in the murine brain. A natural log of the mean number of occupied voxels within cubes of dimension (L) covering the three-dimensional network is plotted versus the natural log of the cube dimension. The slope of the linear portion of the plot determines the fractal dimension. (b) The local slope of the curves in a for each cube dimension. The fractal dimension is observed from the plateau regions corresponding to the linear portions in a (2.74 for the U87 tumor and 3.02 for normal brain). (c) Depiction of the minimum path length for a given three-dimensional vascular network. Here, each path traversed from one face to the other is projected through the axial dimension with the minimum path length highlighted in red. The projection of the Pythagorean distance is shown as a dashed blue line. Tortuosity is determined from the ratio of these two distances. (d) and (e) The three-dimensional skeletonized vascular networks geometrically characterized in a and b. Each gridline is 250 μm .

VI.4b THREE-DIMENSIONAL FRACTAL ANALYSIS OF TUMOR VASCULATURE

The ability of OFDI to extract vascular parameters over larger volumes presents new opportunities for fractal analysis of the network. Fractal analysis has been invoked to quantify the ability of a vascular network to provide an efficient transport of blood-borne nutrients, oxygen, or drugs within the tumor³². The fractal dimension is a statistical measure of a network indicating how completely that network fills space. In three-dimensional geometries, an optimal space-filling network has a fractal dimension of 3; lower fractal dimensions indicate a lesser degree of space filling. A complementary metric is the tortuosity defined by the ratio of the minimum vascular path between two points and the geometric distance between those points. As the tortuosity parameter increases from its minimum value of 1.0, the transport efficiency of the vascular network decreases.

Using the topology and branching patterns derived from the OFDI datasets, we have analyzed, for the first time, the three-dimensional fractal dimension of tumor vasculature *in vivo*. The fractal dimension was calculated from skeletonized vascular networks (obtained by the vascular tracing algorithm) using the sandbox method⁴² (**Figure VI-9a and b**). Tortuosity was determined from the ratio of the minimum path length across the vascular network to the Pythagorean distance measured between the first and last point of the path (**Figure VI-9c**). An analysis of the vascular network depicted in Figure VI-1b yielded a fractal dimension of 2.74 in the tumor region in agreement with results expected from prior 2D analyses, and 3.02 in a normal region of the right hemisphere consistent with a fully developed capillary network filling three-dimensional space^{42,43} (**Figure VI-9d and e**).

VI.5 Imaging Vascular Dynamics during Tumor Growth and Treatment

Vascular responses to anti-angiogenic and anti-vascular therapies occur continuously over time-scales of hours to days⁴⁴. With MPM, however, it is impractical to measure

the dynamic changes over broad fields due to contrast agent accumulation and the time required for imaging. Using OFDI, we imaged murine mammary carcinoma tumors (MCalV) implanted in the dorsal skinfold chamber every 4 hours for 48 hours. We administered either an anti-angiogenic agent (DC101, a blocking monoclonal anti-vascular endothelial growth factor receptor (VEGFR)-2 antibody) or non-specific rat-IgG immediately after the initial imaging session. Promptly following administration of DC101, the mean vessel diameter began to decrease while the tumor volume continued to expand. These trends continued throughout the 48-hour time course of the study (**Figure VI-10**). Timelapse images of vascular responses acquired every 2 hours for 48 hours highlight the unprecedented ability of OFDI angiography to monitor vascular dynamics over wide fields.

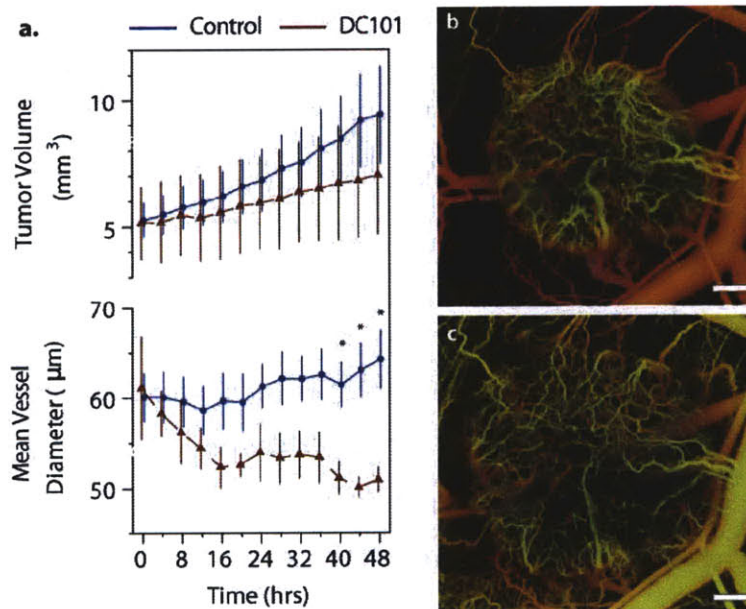


Figure VI-10 Vascular dynamics of fields and time intervals not accessible with traditional approaches. (a) Angiography at a 4 hour interval over 48 hours reveals the rapid response in vascular parameters to VEGFR-2 blockade. Vascular tracing registered to 3D tumor boundaries allows quantification of the vascular changes within the tumor mass, showing nearly immediate changes to vascular diameter (*bottom*). The tumor growth rate of the treated group trends slower than control tumors, but is not significant over 48 hours. (*top*). Control: n=4, DC101 n=3. (b) and (c) Vascular network of a treated tumor at 0 and 48 hours with respect to DC101 administration.

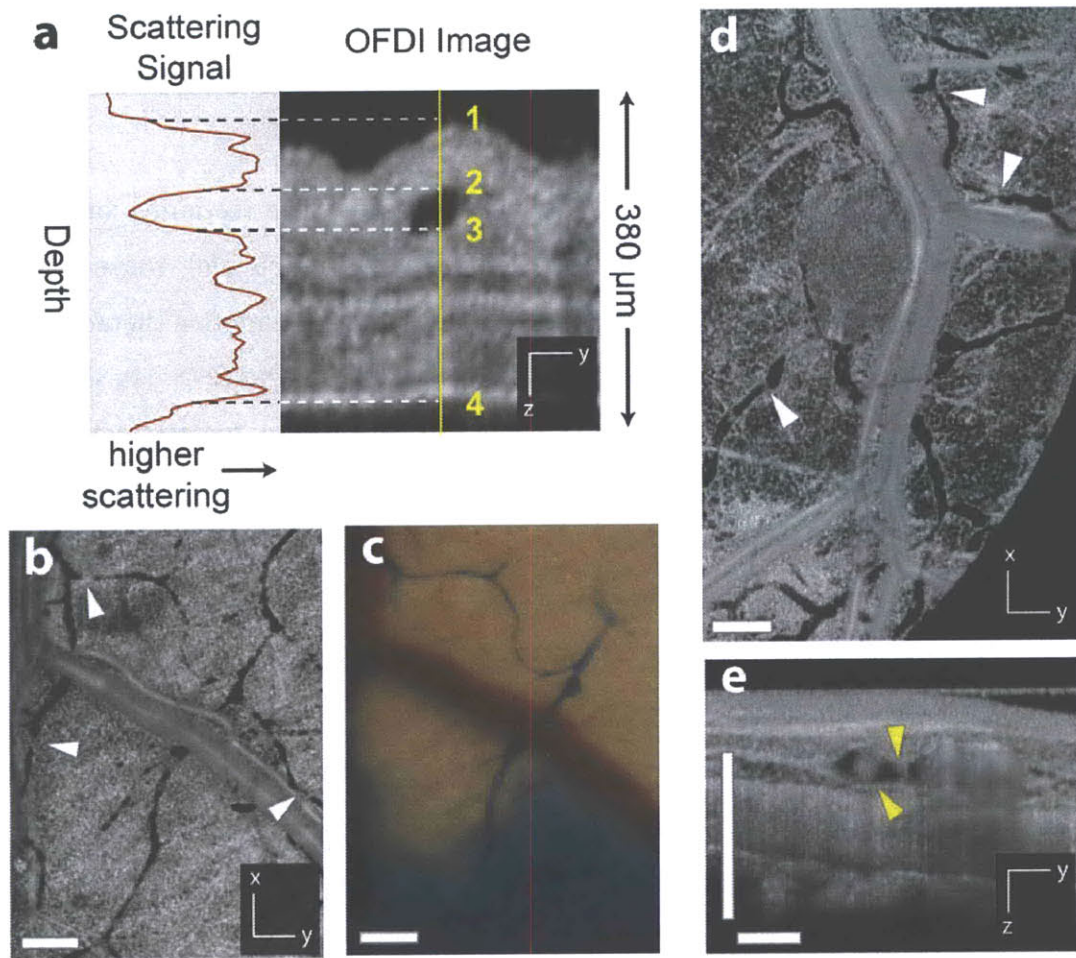


Figure VI-11 Contrast-free lymphangiography using OFDI. (a) The scattering signal along a single depth scan within an OFDI image of a murine ear shows the reduced scattering between the upper (2) and lower (3) boundaries of a patent lymphatic vessel. Scattering within the vessel is similar to background levels above the upper surface of the ear (1) or below the lower surface (4). (b) and (c), In addition to lymphatic vessels revealed by traditional cutaneous injection of Evan's blue dye (c), OFDI is able to detect numerous additional vessels in the normal dorsal skin (b) and resolve the lymphatic valves found between individual lymphangions (\triangleright). (d) HSTS26T tumor-associated lymphatics are found to be dilated in comparison to those in normal tissue. (e), Cross-sectional presentations of a lymphatic vessel showing cellular masses (\blacktriangleright) located near the tumor in d. Scale bars - 500 μm .

VI.6 Contrast-Free Lymphangiography

Lymphatic vessels and their associated lymph nodes have been imaged to reveal their importance in fluid balance (edema), as avenues for cancer cell dissemination and as prognostic indicators of disease progression^{45,46}. Lymphangiography is typically performed by directly injecting a visible or fluorescent dye into the tissue, which

obscures structures near the site of injection and highlights only those lymphatic vessels draining the region of the injection. Further, the accumulation of dye is a severe constraint for longitudinal studies.

Lymphatic networks *in vivo* appear as structures with negligible scattering intensity in OFDI. The reduced scattering of the lymph relative to surrounding tissue is likely associated with its hypocellularity (**Figure VI-11a**). Using these scattering characteristics, lymphatic vessels were identified, mapped, and segmented in the OFDI datasets. OFDI images of lymphatic networks in normal mouse skin showed functional lymphatic vessels highlighted with conventional Evan's blue lymphangiography, as well as additional functional lymphatic vessels draining other regions of the skin where Evan's blue injections were not made (**Figure VI-11b,c**). Lymphatics surrounding tumors were observed for murine breast cancer (MCalV) and human sarcoma (HSTS) models (**Figure VI-11d**) growing in the dorsal skinfold of mice. OFDI cross-sectional images were helpful in identifying cellular masses within the lymphatics (**Figure VI-11e**). Quantitative measurements of lymphatic vessel diameters with OFDI showed peritumor lymphatic vessel hyperplasia consistent with previous measurements using fluorescence microscopy^{45,47}. For the tumor in **Figure VI-11c**, a significant difference (P -value < 0.05) was found between the mean diameters of lymphatic vessels in the normal tissue ($40 \pm 3 \mu\text{m}$; >2mm from tumor) and those in the peritumoral region ($81 \pm 4 \mu\text{m}$; <2mm from tumor). By eliminating the need for exogenous contrast agents, OFDI allowed the monitoring of functional lymphatic vessels throughout tumor progression (**Figure VI-12**). Importantly, OFDI lymphangiography can be performed simultaneously with OFDI angiography; the two techniques differ only in the methods for post-processing of the OFDI data. This is demonstrated in a subcutaneous model in the murine ear⁴⁸ used to study lymphatic metastasis (**Figure VI-2e**)

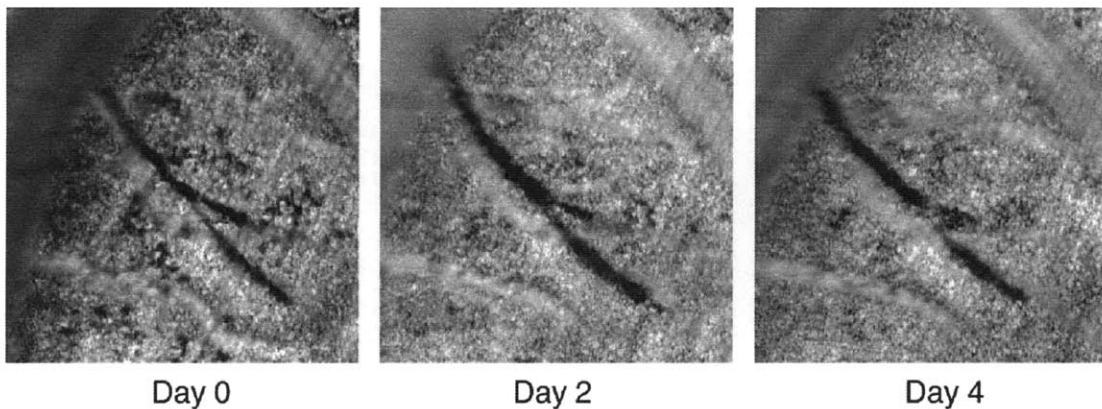


Figure VI-12 Longitudinal tracking of lymphatics using OFDI. Changes in lymphatic vessel diameters are evident over 4 days during tumor (MCalV) progression.

VI.7 Imaging Tissue Viability

Currently available intravital microscopy techniques do not allow measurements of tissue viability in tumors. As a result, cell-targeted therapies are traditionally studied through assessment of tumor growth delay and histological examinations. These techniques, however, have their inherent limitations. Through the dependence of tissue scattering on cellular structures⁴⁹, it is possible to differentiate necrotic/apoptotic regions within a tumor from viable regions in three-dimensions using OFDI. Higher scattering regions within tumors correlate with necrotic/apoptotic regions defined by corresponding hematoxylin and eosin staining (**Figure VI-13a**). Longitudinal imaging of tumor progression in MCalV tumors revealed the growth of necrotic/apoptotic regions (**Figure VI-13b**). During tumor progression, viable areas were limited to $\sim 65 \mu\text{m}$ from the vessel wall. The fraction of necrotic/apoptotic tissue increased (from $\sim 24\%$ to $\sim 46\%$) while the vascular volume fraction remained relatively constant (**Figure VI-13c**). The unique capability of OFDI to longitudinally image tissue viability and to spatially co-register this information with tumor vasculature opens new possibilities for the evaluation of existing therapeutic approaches and the rational design of therapeutic regimens.

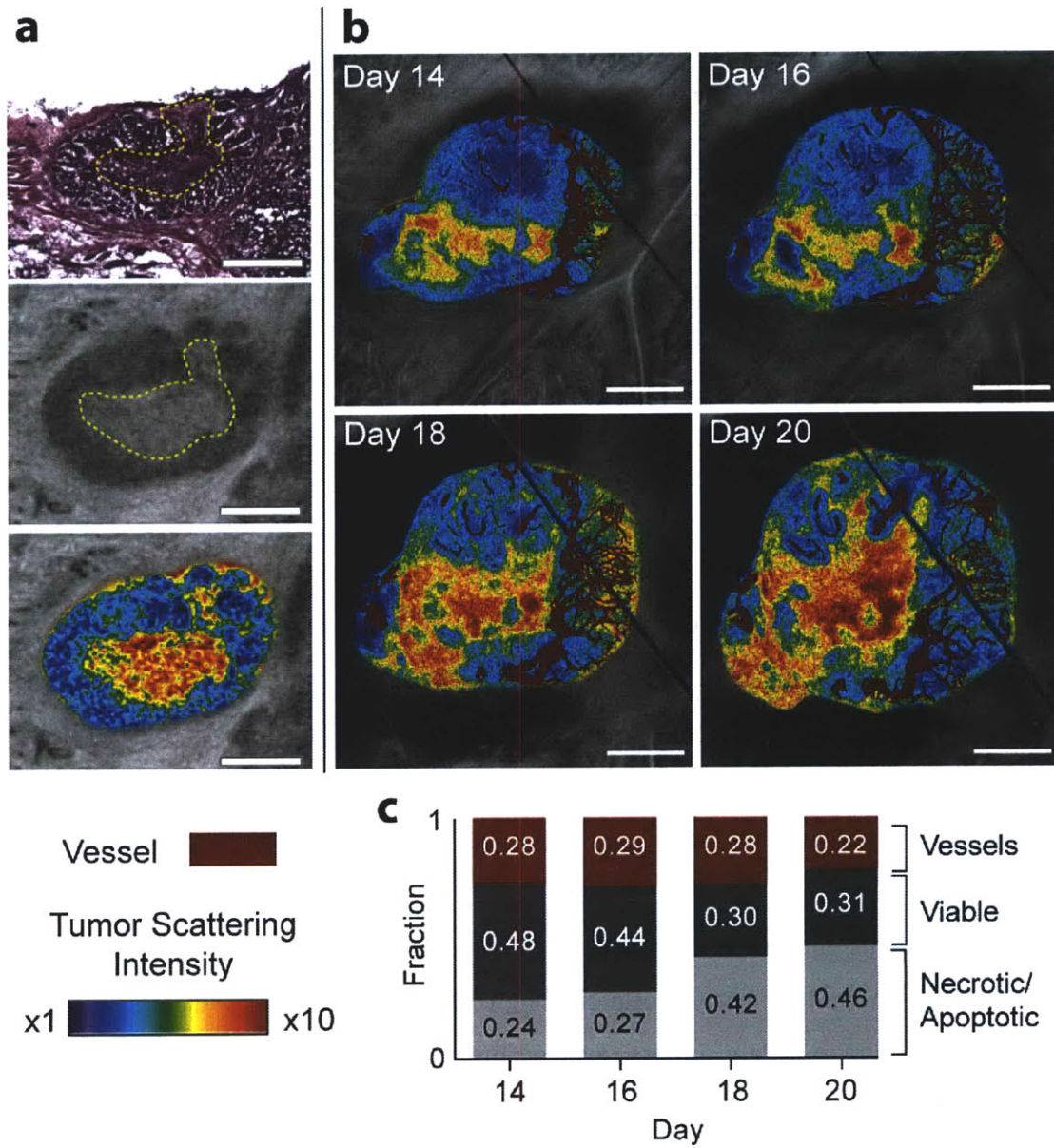


Figure VI-13 Imaging tissue viability. (a) Comparison of standard hematoxylin and eosin staining (*top*) with OFDI (*middle*) reveals association of tissue necrosis with highly scattering regions. Viable and necrotic regions within the same tumor highlighted by color gradients indicating scattering intensity (*lower*). (b) Scattering properties correlated with the microvasculature during tumor progression illustrate increasing regions of unviable tissue with viable areas constrained to regions within $\sim 65 \mu\text{m}$ of the vessels. (c) Quantitative analysis of tissue viability and vascular regions *in vivo* revealed an increasing fraction of necrotic/apoptotic tissue. Scale bars *a*: $500 \mu\text{m}$; *b*: 1.0 mm .

VI.8 Multiparametric Monitoring of Therapeutic Response

To demonstrate the application of OFDI to the study of tumor response to therapy, we monitored changes induced by vascular or cellular targeted therapy. OFDI allows multiple parameters in the tumor microenvironment to be probed simultaneously during treatment. Assessment of changes in the microenvironment with OFDI may provide a means to screen for new anti-cancer agents or design more efficacious therapeutic regimens for translation to the clinic.

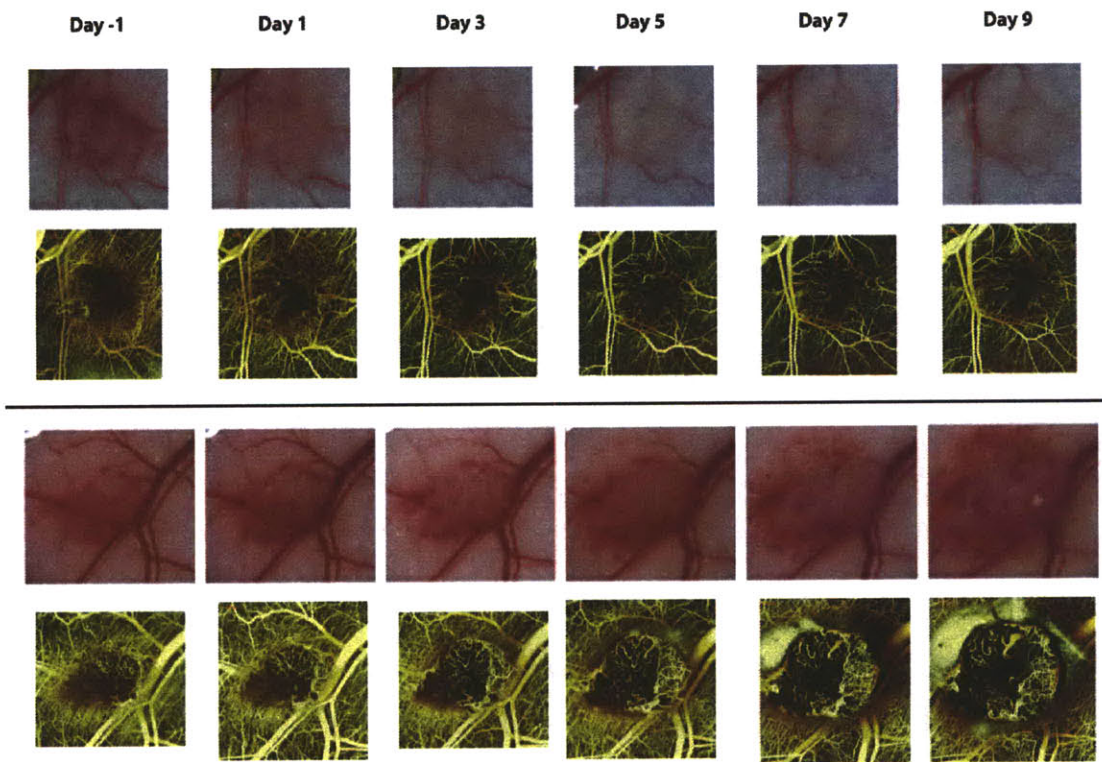


Figure VI-14 Antiangiogenic response to VEGF-R2 blockade imaged by OFDI. Both digital camera images and OFDI angiograms are shown for a DC101 treated and control animal bearing MCalV tumors. The top panel is a representative example of the treated group. Loss of dilated vasculature in the host tissue bed is notable at Day 1 after treatment. By Day 9 there is very limited intratumoral vasculature and what exists is small in diameter and density. This is apparent even in the digital camera images by lack of redness due to lower blood volume. The lower panel is an example of the control group treated with Rat IgG. In this untreated tumor, the host vascular bed remains dilated and large tortuous blood vessels form within the tumor mass. The increased blood volume is apparent in the digital camera images. Each image is approximately 3 X 3 mm. The Doppler OFDI images are maximum intensity projections over a depth of $\sim 500 \mu\text{m}$.

VI.8a ANTIANGIOGENIC THERAPY: VEGF-R2 BLOCKADE

In the first set of experiments, mice with murine mammary carcinoma tumors were imaged every other day up to 9 days during treatment with VEGFR-2 blocking monoclonal antibody DC101. Control animals had the same tumor preparation but received non-specific rat IgG. Our preliminary imaging studies using OFDI with this model found high inter-animal variability in the tumor angiogenesis following implantation and prior to therapy. We therefore used OFDI to normalize the starting point of longitudinal studies for each mouse; we imaged every two days post-implantation and defined starting points for each animal based on the status of the vascular network and the tumor volume (**Figure VI-14**). OFDI measurements of pre-treatment and control mean vessel diameters in 11 total tumors were consistent with previously published results using MPM⁴⁴ ($55.8 \pm 3.4 \mu\text{m}$ versus $49.8 \pm 5.1 \mu\text{m}$ respectively). OFDI angiograms, acquired at day 5, consistently demonstrated a more dense and chaotic vascular network in the control group relative to the treated group (**Figure VI-15a**). We found a reduction in both mean intratumor vessel length (P -value: 0.001) and diameter (P -value: 0.029) with DC101 treatment, which is consistent with those obtained in the previous study⁴⁴ (**Figure VI-15b**). To assess intratumoral spatial differences in response to anti-angiogenic therapy, we correlated morphological parameters of all traced vessel segments with distance from the tumor boundary. The mean vascular volume in the control group within 200 μm of the boundary was found to dramatically increase with tumor growth, while DC101 treatment restrained vascular volume in this region (**Figure VI-16**). At day 7, the mean tumor volume within the treated group was 25% of that of the control group (**Figure VI-15b**). The VEGFR-2 blockade induced a less defined response on fractal parameters compared with morphological parameters of the vasculature over this timecourse (**Figure VI-15b**). The fractal dimensions of both treatment and control groups reached plateaus (2.54 ± 0.04 and 2.60 ± 0.01 , respectively) at day 3, and the mean tortuosity in the treated group was slightly lower than that of the control group at the end of the study.

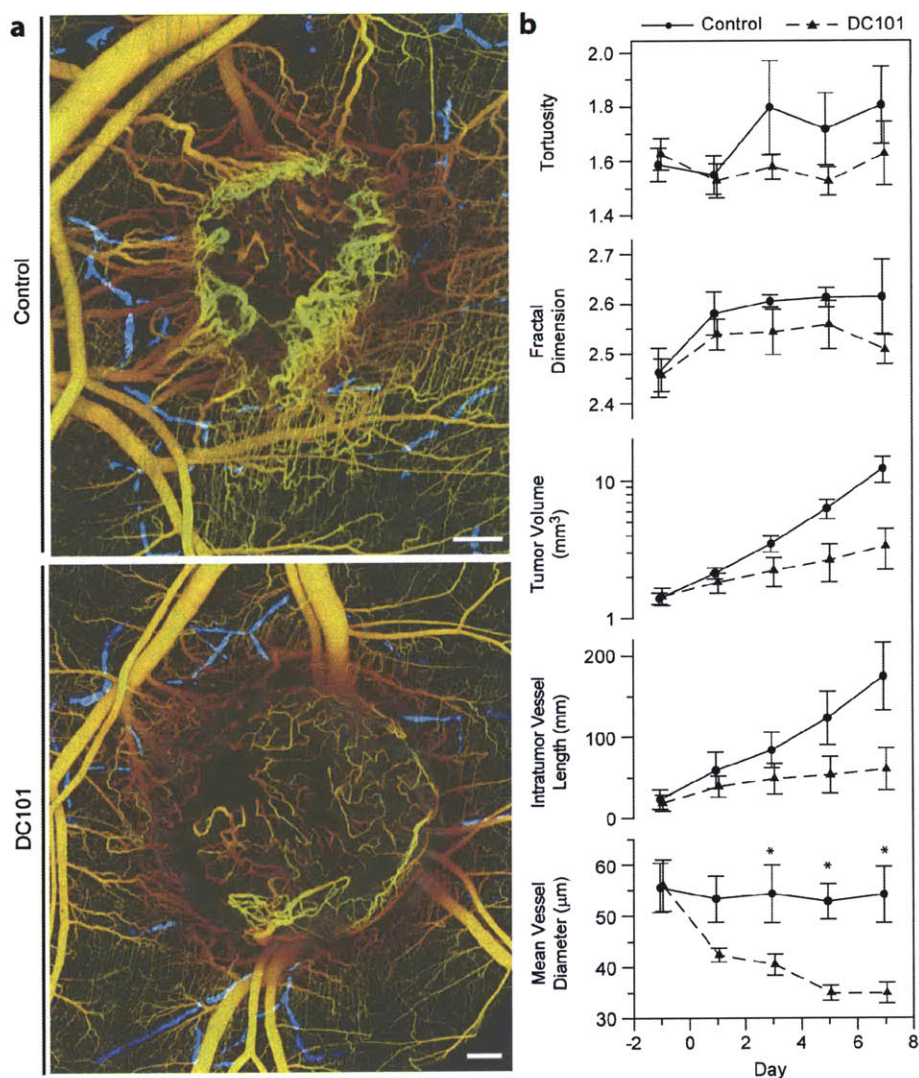


Figure VI-15 Therapeutic response to VEGFR-2 blockade characterized by OFDI. (a) Representative control and treated tumors 5 days after initiation of therapy showing strikingly different vascular morphologies. The lymphatic vascular networks are also identifiable (blue) for both tumors. (b) Quantification of tumor volume and vascular geometry and morphology in response to treatment. DC101 treated tumors exhibited a growth delay over the course of this study (P -value: 0.060). Both total vascular length (P -value: 0.001) and mean intratumoral vessel diameter (P -value: 0.029) significantly decreased over time for treated tumors. Geometrical properties of the tumor vasculature, i.e., the fractal dimension and tortuosity, showed a less distinct response between groups. Control $N=5$, Treated $N=6$. Scale bars 500 μm . Statistically significant differences (P -value < 0.05) at given time points are denoted by asterisks.

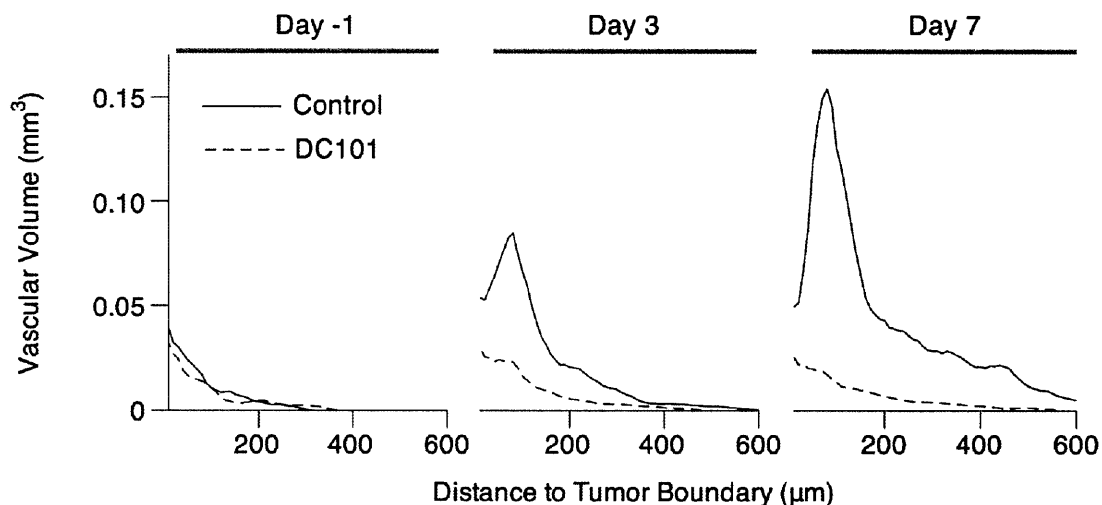


Figure VI-16 DC101 treatment restrains intratumoral vascular growth near tumor margin. The mean vascular volume spatially correlated with the tumor boundaries across all animals reveals a region of specific increase within 200 μm of the tumor margin in control animals that is restricted in animals treated by anti-angiogenic therapy. (Control $N=5$, Treated $N=6$).

VI.8b CYTOTOXIC THERAPY: DIPHTHERIA TOXIN

In the second set of experiments, we applied OFDI to investigate direct targeting of tumor cells. Diphtheria toxin accumulates in human cells, halting protein synthesis and eventually inducing apoptosis, but does not affect murine cells^{31,50}. Therefore, in mouse xenograft models, diphtheria toxin can be used to model a cytotoxic treatment that is not confounded by direct damage to vascular endothelial cells that can result from chemo- and radiotherapy. When we administered diphtheria toxin into mice bearing a human colorectal adenocarcinoma xenograft (LS174T) grown in the dorsal skin chamber, apoptosis was evident within two days through associated changes in tumor scattering properties (**Figure VI-17a**). During the first 24 hours, the tumor volume remained approximately constant (**Figure VI-17b**). After 24 hours, widespread necrotic/apoptotic regions within the volume of the treated tumors were observed and the mean tumor volume began to decrease rapidly in response. After 48 hours, the intratumor vessel length rapidly decreased, presumably due to the down-regulation or depletion of tumor cell-derived angiogenic growth factors (**Figure VI-17b**).

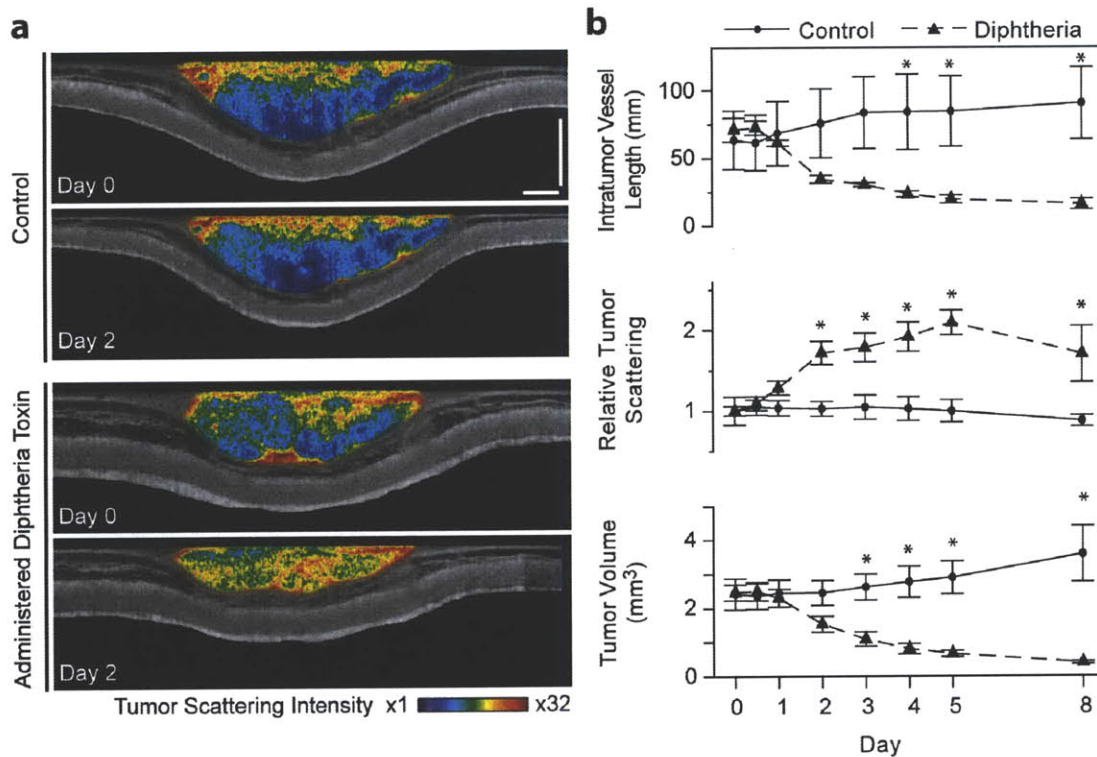


Figure VI-17 Directed cytotoxic therapy and multiparametric analysis by OFDI. (a) Images of tissue scattering immediately prior to and two days following administration of diphtheria toxin or saline to mice bearing human tumor xenografts (LS174T) in dorsal skinfold chambers. Apoptosis induced by diphtheria toxin is manifest as increased tissue scattering relative to control animals. (b) Quantification of the response to diphtheria toxin administration. *Top:* A reduction in tumor volume was apparent 48 hours after administration, reaching 10% of the original volume after 8 days. *Middle:* The tissue scattering within the tumor relative to day 0 showed a statistically significant increase in treated animals 48 hours after administration and a maximum after 5 days. *Bottom:* The vascular length within the treated tumors dropped continuously after administration of the toxin likely due to down regulation of tumor-cell derived growth and survival factors. Scale bars 500 μm . Statistically significant differences (P -value < 0.05) at given time points are denoted by asterisks.

In a separate experiment with only a single tumor, the administration of diphtheria toxin was followed by tumor regrowth after an initial response (**Figure VI-18**). During the first 24 hours, the tumor volume remained constant while the tumor vascular volume fraction (VVF) decreased, presumably due to the down-regulation or depletion of tumor cell-derived growth factors. After 24 hours, necrotic/apoptotic regions within the volume of the tumor were observed and the tumor volume began to decrease. In the same time period, the VVF reversed its previous trend and rapidly increased. Previous studies have suggested that the increasing VVF following targeted tumor cell killing by diphtheria toxin in xenograft tumors is due to a reduction of solid stress caused

by cellular compression³¹. At +120 hours, the tumor volume and VVF reached measured extremes and necrotic/apoptotic regions were observed nearly throughout the tumor with only small regions possessing viable tumor cells (**Figure VI-18c,d**). After the VVF peak, the tumor mass began to recover. Due to physicochemical barriers to macromolecular diffusion in the tumor microenvironment⁵¹, the toxin was likely unable to reach a subsection of the tumor leaving viable tumor cells that, coupled with the improved perfusion, led to relapse.

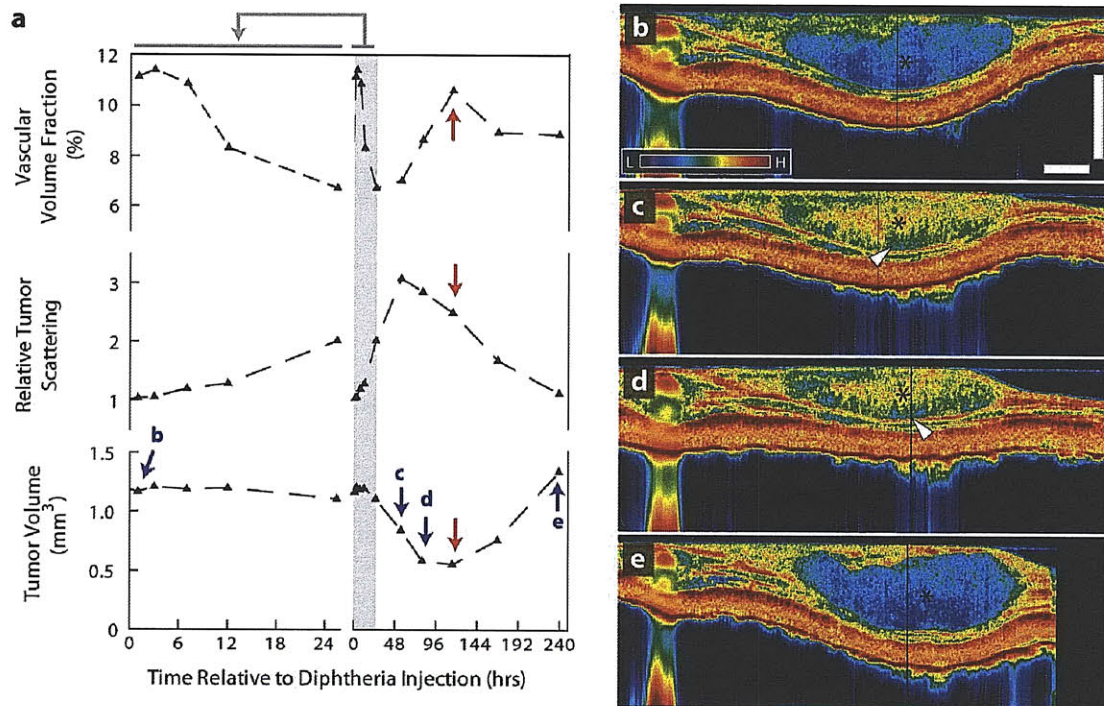


Figure VI-18 Quantification of the response of an LS174T tumor implanted in the dorsal skinfold chamber to a single diphtheria toxin administration. (a). The initial 24-hours (left) show a marked decrease in vascular volume fraction (VVF) and increase in tumor tissue scattering due to cellular apoptosis, while tumor volume remains constant. The following 72 hours find these trends reversing as tumor volume decreases, while VVF and tissue scattering reach maximal values. At the lowest tumor volume, compression of the vasculature by tumor cells is at a minimum allowing maximal VVF (→). It is after this time that increasing viable tissue is observed through decreasing tissue scattering leading to regrowth of the tumor mass. (b-e) Images of tissue scattering at timepoints given in a (→). Color gradients illustrate the tissue viability ranging from blue (viable, low scattering) to yellow/red (unviable/apoptotic, high scattering). White arrows indicate regions of potentially viable cells located at the tumor base. Scale bars 500 μm .

VI.9 Discussion

The application of automated vessel tracing algorithms to OFDI angiography permitted *in vivo* quantitative morphological and geometrical characterization of three-dimensional vascular networks over relatively large volumes, and, in some models, over entire tumors. Although the spatial resolution of OFDI is inferior to that of MPM, our results indicate that OFDI can provide accurate quantitative data for vessels as small as 12 μm in diameter. OFDI bridges a gap between subcellular resolution optical microscopies such as MPM and techniques such as Doppler ultrasonography, magnetic resonance imaging, and micro-computed tomography (CT), which can penetrate deeper into tissue but are limited to resolutions above $\sim 50 \mu\text{m}$. Further, our results illustrate the utility of the technique for studying anti-angiogenic agents by demonstrating that VEGFR-2 blockade decreased intratumoral diameter and vascular length, consistent with previous studies⁴⁴. Through fractal analysis, the effect of anti-angiogenic therapy on vascular density and transport efficiency, which have profound implications in the design of therapeutic regimens, can be studied. We note that since OFDI angiography requires flow for contrast, it can only detect perfused vessels.

Repeated angiographic imaging over brief intervals is limited with current technologies by both the need to administer intravenous contrast and interference of contrast leakage by permeable blood vessels. Many important vascular dynamics ranging from alterations in cerebral blood flow in cognition, to sprouting or intussusception during angiogenesis, to the effects of vascular disruptive agents or anti-angiogenic agents occur on time scales of short duration^{11,52}. Our results show frequent angiographic imaging over extended periods in the context of therapeutic intervention is possible using OFDI. This method may therefore have utility in the screening of vascular-targeted agents in the development of cancer therapies.

The ability to perform tracer-free lymphangiography of functional lymphatic networks with OFDI is a critical advance in the field. In addition to quantitatively measuring functional peritumoral lymphatics, the ability of OFDI to image lymphatic networks may

have clinical application, e.g., in monitoring the functionality of lymphatic networks in lymphedema, particularly in breast cancer patients after axillary dissection and radiation. In such applications, the development of methods to quantify lymph flow with this technology would further its diagnostic capability.

Combining the vascular and structural signatures of OFDI, we performed multiparametric imaging during cytotoxic treatment of a solid tumor. OFDI revealed both the direct and indirect effects of tumor cell death through the assessment of viability and tumor vasculature, respectively. The higher optical scattering of non-viable tissue is presumably due to an increased number of scatterers from dispersed cellular components. Because both apoptosis and necrosis increase cellular particles in the interstitial space, OFDI is unable to differentiate the two mechanisms of cell death. The structural OFDI signal also allowed delineation of the tumor boundaries providing a means to non-invasively measure tumor growth delay during treatment and spatially correlate the vasculature into intratumoral and peritumoral regions.

The deep penetration and wide-field, high-resolution imaging of three-dimensional tissue volumes enabled by OFDI presents a powerful new tool for the study of solid tumors and other diseases that complements MPM and is likely to become as widely used.

VI.10 Summary

Through the development of novel techniques, instrumentation and algorithms, we have demonstrated the unique capabilities of OFDI to image *in vivo* the microenvironment of model tumors rapidly and persistently over time without requiring exogenous contrast agents. These capabilities provide a new tool to probe the dynamics of tumor growth and response to therapy. The wide field of view, deep imaging penetration, and high speed of OFDI relative to MPM provide experimental advantages as well as a biologically important capability to probe substantially more of the tumor volume.

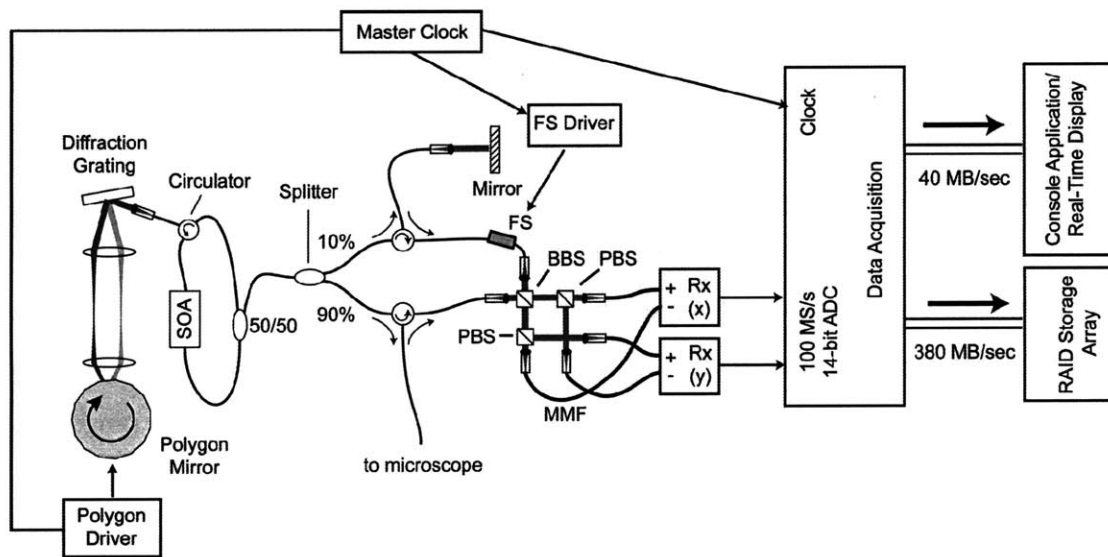


Figure VI-19 OFDI instrumentation. The optical frequency domain imaging system uses a swept-wavelength laser source comprising a semiconductor optical amplifier (SOA) as the gain element inside a fiber ring cavity. The swept filter is based on a polygon mirror (Lincoln Laser). The laser output is split by a 10%/90% coupler to the reference arm/sample arm. The sample arm light is directed to the microscope with an optical circulator (), while the reference arm light is directed to a fixed reflector. An acousto-optic frequency shifter (FS) at 25 MHz offsets to coherence range from DC. A free-space polarization-diverse and balanced optical demodulation circuit comprising broadband beam splitters (BBS) and polarization beam splitters (PBS) generates four optical signals coupled to multimode fiber (MMF). These fibers relay the optical signals to two balanced receivers (Rx, New Focus), outputting two electrical signals. A two-channel 100 MS/s digitizer (Signatec) is used to acquire these signals and transfers this data directly to a RAID storage array. Approximately 10% of this data is processed in real-time on the CPU to provide image feedback. A single master clock is used to lock the polygon driver, frequency shifter, and data acquisition board to achieve high phase sensitivity.

VI.11 Materials and Methods

VI.11a OFDI SYSTEM

OFDI provides high resolution imaging of the elastic light scattering properties of a sample in three dimensions¹. Beam focusing provides transverse (x,y) discrimination of signals. Interferometric measurements of optical delay gate signals across the axial (z) dimension. The measurements first sample in parallel the interference signal between light scattered at all detectable depths and an external reference beam as a function of wavelength. Subsequent Fourier analysis of this interference signal across wavelength separates the combined signals across all depths into a depth-resolved scattering

profile. To measure interference signals across wavelength, a wavelength-swept laser source with an instantaneous narrow linewidth (<0.17 nm) is used (**Figure VI-19**). This laser source used a semiconductor optical amplifier (Covega Corp., Jessup, MD) as a broadband gain medium in combination with a polygon scanner as a scanned wavelength filter (Lincoln Laser Corp., Phoenix, AZ). Wavelengths sampled continuously a 140 nm window centered at 1300 nm, resulting in a depth resolution of 6 mm in tissue. Depth scans (A-lines) were acquired at a rate of 50 kHz. Through inclusion of an acousto-optic frequency shifter (Brimrose Corp., Sparks, MD), a 5.8 mm scan range was achieved². A polarization diverse optical demodulator generated an optical interference signal for each of two orthogonal polarization states, preventing artifacts due to polarization signal fading. The interference signals were digitized using a two-channel 100 MHz acquisition board (Signatec, Inc., Newport Beach, CA), and were continuously archived to a high-speed hard-drive storage array. Real-time display of structural and vascular images at approximately 10% of the acquisition rate allowed monitoring of the imaging sessions and interactive definition of the imaging field. Transverse sampling patterns were developed to achieve rapid scanning across large volumes while simultaneously matching the Doppler detection range to the empirically determined optimal motion sensitivity. Data was acquired along the x-dimension at either a 5.0 μm pitch across a transverse field of 5.0 mm or a 7.62 μm pitch across a 7.8 mm transverse field, both at 16.3 frames per second. Each frame comprised 3072 A-lines that were combined in post-processing to provide 1024 structural and Doppler image lines. Data was collected in the y-dimension at a 0.56 μm pitch naively, and integrated in post-processing to yield a reduced dataset with isotropic sampling in the x-y dimensions of 5.0 μm /7.62 μm . Scanning along the y-dimension utilized physical translation of the animal at 9 $\mu\text{m}/\text{sec}$. The scanned field along this dimension was limited only by the chamber window aperture. Data along the depth dimension was acquired natively at a 4.1 μm pitch (in tissue) and signal was acquired over the first 1.5 mm to 2.5 mm in tissue, depending on scattering levels.

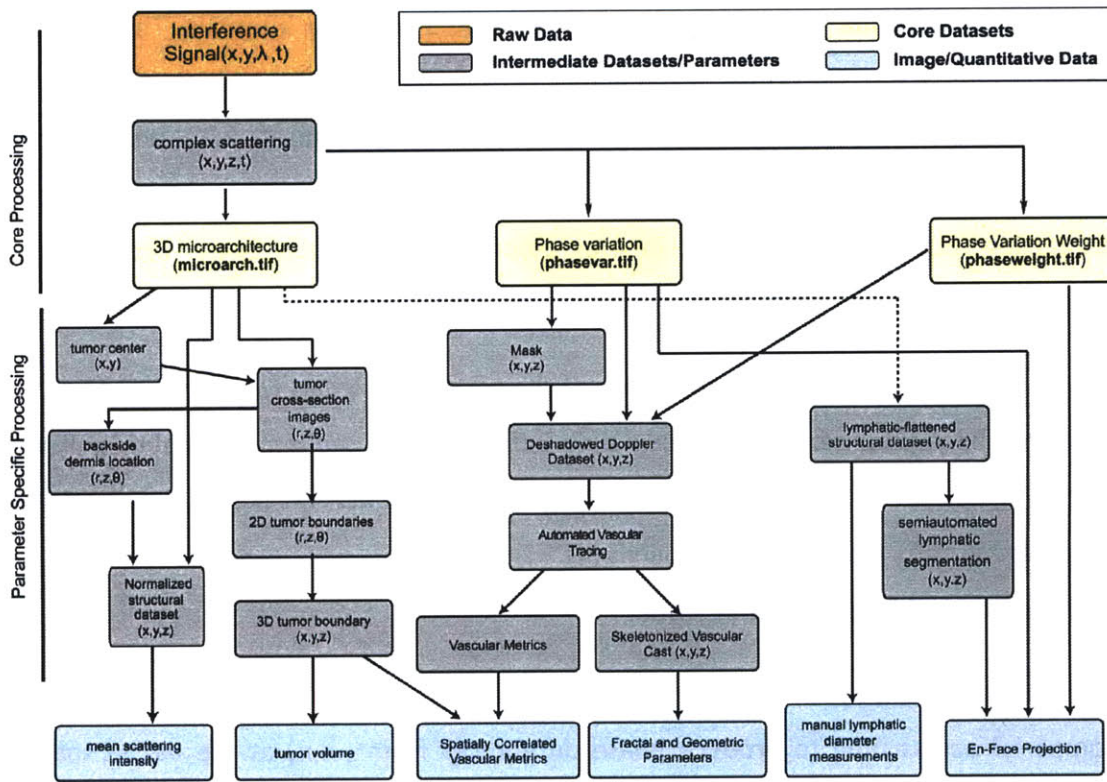


Figure VI-20 Signal processing algorithms and quantitative analysis. Using the raw spatiotemporal reflectance data from OFDI, all of the angiographic, lymphangiographic and microanatomical images, as well as the biological metrics, are obtained through a series of processes represented here.

VI.11b OFDI SIGNAL AND IMAGE PROCESSING AND QUANTIFICATION.

Processed images and quantitative data describing microanatomy, blood and lymphatic vascular networks, and tissue viability in tumors were derived from a single raw data format using a series of core processing routines followed by parameter specific algorithms. These methods and algorithms are described here and summarized in a flowchart format (**Figure VI-20**).

Core Processing Routines. The OFDI system recorded the interference signal across wavelength (λ) between a reference beam and an optical probe beam directed at a particular transverse locations of the sample (x,y) and at a particular timepoints (t). From this raw data, the optical scattering (complex parameter including amplitude and phase) as a function of (x,y,z,t) was generated as described above. This data was spaced at either a $5 \mu\text{m}$ or $7.62 \mu\text{m}$ pitch in the x dimension and at a $0.56 \mu\text{m}$ pitch in the y

dimension. The same locations were resampled at 9 ms time intervals. This dataset described the scattering properties of a specific spatial location at multiple timepoints. From the complex scattering dataset, a set of three further datasets were derived that highlight specific properties of the scattering signal and formed the basis for subsequent processing (custom code written in programming language C). These datasets are described as follows:

(i) Microarchitecture: The magnitude of the scattering signals were averaged across time and the y-dimension to produce a time-independent three-dimensional magnitude scattering dataset with isotropic pitch in the (x,y) dimensions. This dataset was saved in log-scale to an 8-bit file (microarch.tif). This dataset was used to reveal the microanatomical features of the tissue.

(ii) Phase Variation: The scattering signals at the sample transverse locations were compared across time to produce phase differences from $(-\pi, \pi)$ at the native spatial pitch (5.0/7.62 μm x 0.56 μm x 4.1 μm). Each phase difference was weighted by the magnitude of the average signal from that point. The circular variances (from 0 to 1) of these amplitude-weighted phase-difference datasets over 50 μm depth windows were calculated at each point in three-dimensional space. A three-dimensional angiographic dataset was then obtained by combining (median) appropriate sample counts in the y-dimension to yield isotropic pitch in the transverse dimensions. The data was saved to an 8-bit dataset (phasevar.tif). The use of the amplitude-weighted circular variance over this limited depth window both minimized phase decorrelation and optical noise artifacts by amplitude weighting the phase-differences and reduced artifacts due to background motion resulting from respiration, muscular contractions, and environmental instabilities. This dataset was used to reveal the vascular regions in the tissue.

(iii) Phase Variation Weight: The magnitude of the scattered signals that were used to derive the phase variation signal was calculated at the native spatial pitch, and then combined in the y-dimension (mean) to yield isotropic pitch in the transverse

dimensions. The data was saved to an 8-bit dataset (phaseweight.tif). This dataset was used to weight the phase variation signal and discriminate between vascular regions and low-signal regions.

These datasets formed the basis for further analysis yielding images and quantitative data for specific biological parameters as is described in the following sections. Unless otherwise noted, the parameter specific processing was performed in Matlab (The Mathworks, Natick, MA).

VI.11c THREE-DIMENSIONAL TUMOR VOLUME AND BOUNDARY CALCULATION.

For tumor volume calculations, an en face projected image was calculated by averaging the signals from 160 μm to 240 μm in depth from the microarchitectural dataset (microarch.tif). The location of the tumor center in (x,y) was recorded manually from this image. Using this location and the microarchitectural dataset (microarch.tif), a series of 8 cross-sectional images was generated through the tumor center at equally spaced angular increments, i.e., along the meridian planes through the tumor center defined by 0/180°, 22.5/202.5°, 45/225°, 67.5/247°, 90/270°, 112.5/292.5°, 135/315°, and 157.5/337.5°. To improve contrast in these images, the scattering signal was integrated over 80 μm in the transverse dimension perpendicular to the plane of each cross-sectional image. The tumor boundaries were manually segmented in these images using ImageJ (ImageJ 1.39, open source NIH software, <http://rsb.info.nih.gov/ij/index.html>). From the tumor boundaries in the 8 meridian planes, the tumor boundaries in three-dimensional Cartesian space were calculated by interpolation yielding a tumor mask defining the intratumoral volume and extratumoral volume within the three datasets (microarch.tif, phasevar.tif, phaseweight.tif). The tumor volume was calculated from this mask and the known pitch of these datasets.

VI.11d NORMALIZED SCATTERING/VIABILITY.

The mean scattering intensity within tumors grown in window models was derived from the set of 8 cross-sectional images after normalizing for scattering intensity across

depth. In these eight cross-sectional images, the location of the backside Dermis was identified using ImageJ. The scattering signal intensity of this layer was used to derive the average scattering attenuation with depth for every depth scan within each cross-sectional image. Normalized cross-sectional images were generated by applying a uniform signal gain across depth that compensated the derived attenuation. From these normalized cross-sectional images and the tumor mask, the average scattering within the tumor volume was calculated.

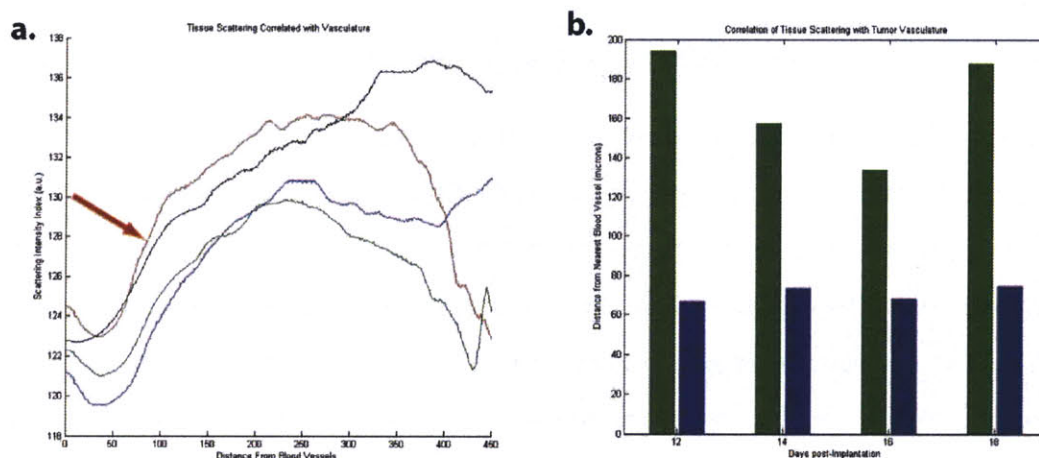


Figure VI-21 Method for determining viable/necrotic fractions with OFDI. (a) The mean scattering amplitude is determined for each distance from the nearest vessel wall for each timepoint. A threshold value is selected from the inflection point (red arrow) on each curve to determine tissue fractions. (b). The cutoff scattering amplitude is also used to determine the mean distance from the vessels for both necrotic (green) and viable (blue) tissue.

VI.11e QUANTIFICATION OF VIABLE FRACTION.

To assess the viable fraction, depth-matched 20-40 μm en face projections of both the phase variation (phasevar.tif) and microarchitectural (microarch.tif) datasets were manually selected. The tumor margins were manually identified from the scattering differences in the microarchitectural dataset and a mask was created to restrict further analysis to the tumor region. Using the phase variation dataset, the vascular signal was identified by thresholding the image to create a binary mask highlighting the vascular network (Figure VI-21). A vascular distance map (distance of each pixel in the intravascular space to the nearest vessel) was then determined using a 2-dimensional

Euclidean distance transform in Matlab. The mean scattering index for distances from 0-1000 μm were determined using the distance map and the pixel values in the microarchitectural datasets. Plots of mean scattering index versus distance from nearest vessel revealed sigmoid shaped curves. For each timepoint, the scattering index at the inflection point was selected as the threshold value to differentiate viable from non-viable tissue in the microarchitectural dataset and determine the area in pixels of each region in the intravascular space. For each timepoint, the tissue fractions of vascular, viable, and necrotic/apoptotic regions were then determined from the area in pixels of each over the total pixel area of the tumor. Additionally, the mean distance of each pixel region (viable or necrotic/apoptotic) to the nearest vessel was determined using the distance map and thresholded pixels from the microarchitectural dataset. To visually illustrate the different regions of viable tissue in the tumor, a colormap was selected and adjusted so that the threshold scattering index for each timepoint was indexed to the green region of the colormap (blue/light blue indicating viable and yellow/red indicating non-viable).

VI.11f ANIMAL MODELS.

Dorsal skinfold chambers and mammary fat pad windows were prepared in SCID mice as previously described⁵³⁻⁵⁵. The appropriate tumor type was then implanted in the center of the chamber 2-3 days after the initial surgery. The murine mammary adenocarcinoma (MCAIV), human colorectal adenocarcinoma (LS174T), and human soft tissue sarcoma (HSTS26T) were transplanted from subcutaneous tumors grown in isogenic mice. The human mammary adenocarcinoma (MDA-MB-361HK) was implanted as a single cell suspension of $\sim 3 \times 10^6$ cells in 30 μl of Hank's Buffered Salt Solution (HBSS). Cranial windows were prepared in nude mice as previously described⁵⁵ and either human glioblastoma multiforme (U87) tumor tissue was implanted 400 μm deep in the posterior cortex or MCAIV tissue was implanted in the leptomeninges of the left hemisphere. Tumors were generally allowed to grow for 2 weeks to a size of 4 mm in diameter by en face measurement depending on experimental protocol. Animals were

anesthetized using either Ketamine/Xylene(10/1 mg/ml) or Isoflurane (1% in 100% oxygen), as indicated for each specific experiment. All animal work was approved by the by the MGH Institutional Animal Care and Use Committee.

VI.11g ANTI-ANGIOGENIC THERAPY: VEGF-R2 BLOCKADE.

DC101 (ImClone Systems Inc., New York, NY) or nonspecific rat IgG were administered intraperitoneally at 40mg/kg as prescribed in previous studies⁴⁴. Mice were imaged every 2 days beginning 5 or 6 days after tumor implantation. Therapeutic initiation was determined through monitoring of tumor growth by both visual inspection and OFDI angiography. Animals were selected for the study based on the criteria that 1) the tumor diameter was approximately 4 mm in diameter by en face measurement 2) the entire margin of the tumor was functionally vascularized and 3) the animal was in good health. Treatment group assignment was made randomly and masked during the duration of therapy to remove bias. Three treatments at three-day intervals were given (defined as day 0, 3, 6), and imaging was performed through day 9. Tumor growth delay was calculated from measurements of tumor volume by OFDI microanatomy measurements.

VI.11h CYTOTOXIC THERAPY.

Diphtheria toxin (Sigma-Aldrich Co., St. Louis, MO) was administered intraperitoneally at 30 µg/kg as previously described³¹. For control animals, a similar volume of saline was injected intraperitoneally. Male SCID mice bearing human colorectal adenocarcinoma tumors in the DSC were treated once and monitored over 10 days. During the initial 24 hours, OFDI multiparametric measurements were made every 12 hours followed by measurements every other day as described in the Supplementary Methods.

VI.11i PROLONGED TIME-LAPSE IMAGING.

Imaging was performed under gas anesthesia (1% Isoflurane in oxygen) every 4 hours for 48 total hours in mice bearing MCalV murine mammary carcinoma tumors in the DSC. Each imaging session was 5-10 minutes in duration, between which the

experimental animal was returned to its cage. DC101 or non-specific Rat IgG (40 mg/kg i.p.) was administered once after the first imaging session. To generate the shorter interval time-lapse video, a separate SCID mouse bearing M_{Ca}V in the DSC was imaged every 2 hours for 48 total hours. DC101 was administered (40 mg/kg i.p.) once 8 hours after the first imaging session. The resulting angiographic images for each timepoint were manually cropped and aligned using Adobe Photoshop (Adobe Systems Inc., San Jose, CA) and ImageJ to generate the time-lapse video.

VI.11j QUANTITATIVE ANGIOGRAPHY.

Vascular quantification was performed through automated vessel tracing. To condition the vascular dataset for tracing, the following steps were performed:

- (i) If necessary, a mask file was generated manually (ImageJ) that delineates the vascular signatures in the phase variation dataset (phasevar.tif) from artifacts associated with low-signal intensities in the air or Brownian motion in the fluid above the non-planar tissue surface.
- (ii) Doppler techniques suffer from artifacts due to forward scattering of red blood cells that result in signal shadows extending below the deepest extent of a vessel. For large vessels with high local hematocrit, shadowing can extend to nearly all of the lower depths. These artifacts frustrate the automated three-dimensional analysis of vascular networks. To reduce this shadowing, we further processed the angiographic datasets by applying a step down exponential filter. Working from the surface of the tissue downward, the magnitudes of the vascular signal (phasevar.tif) of all points below the current point were attenuated according to the magnitude of the current point. A deshadowed dataset (phasevar_noshadow.tif) was generated as the output. A result of this technique is that small vessels underneath very large vessels were obscured and not traced.

After shadow removal, an automated three-dimensional vessel tracing algorithm was applied to the deshadowed datasets (phasevar_noshadow.tif) (**Figure VI-7**). The tracing

algorithm was developed and adapted for the OFDI images from a model previously applied to angiographic images from multiphoton microscopy^{36,37}. Briefly, the model traverses the vascular network with cylindroidal superellipsoids fit to the vessel boundaries by minimizing region-based statistics using a likelihood ratio test to differentiate between noise and other artifacts. In addition to providing the three-dimensional geometry of vessels segmented by the superellipsoids, the model defines vessel centerlines, intersections, and branches. Novel seeding algorithms were developed for the OFDI datasets to provide robust initial guesses for vascular regions without the requirement of segmentation procedures.

Prior to commencement of the vascular tracing algorithm, homomorphic filtering was applied to each deshadowed phase variation dataset. Homomorphic filtering consisted of first convolving a low-pass Gaussian filter across each transverse (XY) slice of the deshadowed datasets to lower the background signal. The intensity in the resultant image was then homogenized at both the low and high ends of the intensity spectrum to increase contrast. To remove any remaining specular noise resulting from the filtering process, a median filter was applied to each transverse slice of the three-dimensional OFDI dataset.

For each superellipsoid describing a "vascular segment", the parameters output from the tracing algorithm provided a centroid, major, minor and longitudinal axes and quaternary rotation parameters defining the rotation of the axes from image space to fitting space. Vessels were defined by the fitting algorithm as a series of vascular segments between intersections, branching points or dead ends. The model fit to each vascular segment was performed in unitary space rotated from the actual image space so that all superellipsoid axes rested on the axes defining Cartesian coordinates of this space. To obtain quantitative measures in image space, the superellipsoid axes were rotated back into image space and the magnitudes in microns of each axis were determined by the pixel dimensions in three-dimensional space.

Due to the shadow removal processing, vessel morphology in the xz or yz planes were altered in some cases. Therefore, morphological measurements were always made as projections onto the xy plane. The two shortest superellipsoid axes were used for the projection onto the xy plane. To determine the length of each vascular segment, the distances between adjacent centroids (as defined by the tracing algorithm) were determined. Vascular diameter for a given set of segments (i.e. intratumoral) was determined by weighting the xy-projected diameter for each segment by its length. Vascular length of a given volume of tissue was simply the sum of the length of all vascular segments in that region. Vascular volume was determined by calculating the area containing the segment centroid and then multiplying by the segment length and summing over all segments of interest.

Three-dimensional image casts or skeletons of the vascular networks were obtained from the parameters output by the vascular tracing algorithm using Matlab. Visualization was obtained using either Volocity (Improvision, Inc, Waltham, MA) or OsiriX (The OsiriX Foundation, Open-Source Software).

VI.11k FRACTAL ANALYSIS

The fractal dimension was calculated using the sandbox method⁴² adjusted for the voxel size anisotropy in three-dimensions. Skeletonized vascular networks were obtained using the vessel parameters defined by the vascular tracing algorithm. A three-dimensional rectangular region of the image volume was selected for geometrical analysis. For analysis of tumor vascular networks, the rectangular region of largest size was selected that was within the tumor boundary. A point near the center of the structure was randomly selected and surrounded by cubes of increasing dimension through multiple iterations. The mean number of occupied voxels within each cube of a particular length scale was determined by averaging over all selected voxels. The linear slope of the log-log plot of mean occupied voxels versus cube dimension defined the fractal dimension (**Figure VI-9**). The minimum path length was found by determining the minimum length between occupied voxels on each pair of opposite faces in the

skeletonized vascular network defined above. Tortuosity was calculated by taking the ratio of the minimum path length to the Pythagorean distance measured between the first and last point of the path.

VI.111 VISUALIZATION.

The generation of combined blood and lymphatic vascular projections required segmentation of the lymphatic networks from the surrounding tissue. The lymphatic networks were semi-automatically segmented by the manual selection of points within lymphangions followed by the expansion of these points using a three-dimensional region growing algorithm. The resulting segmented lymphatic network described the interluminal volume of the identified lymphatic vessels in three-dimensional space registered to the vascular dataset (phasevar.tif).

Reduction of the three-dimensional vascular (blood and/or lymph) datasets to a single en face image utilized a customized volume up rendering technique. The vascular dataset (phasevar.tif) was three-dimensional median filtered with a kernel size of (3×3×3). The blood vessel signals in this filtered dataset were then colorized according to their depth. Within the segmented lymphatic network image, lymph vessels were colored blue. These datasets were then merged if rendering both blood and lymph vessels. Finally, the vascular (blood) or merged (blood and lymph) dataset were reduced to an en face presentation using volume up rendering techniques⁵⁶ wherein each pixel is assigned an opacity and more superficial features are layered over deeper structures. The opacity of each pixel was calculated as a product of the vascular signal magnitude (phasevar.tif) and the signal weight of that vascular signal (phasevarweight.tif).

VI.11m QUANTITATIVE LYMPHANGIOGRAPHY.

Lymphatic vessels are identified through the diminished scattering signal within the microarchitectural dataset (microarch.tif) from the intraluminal lymph, likely attributed to hypocellularity and lower protein concentration. The distinct network topology and vessel characteristics coupled with the correspondence of these scattering structures

with Evan's blue lymphangiography (**Figure VI-11**) confirm their identification as lymphatic vessels. Presentations of the lymphatic networks were generated by manual selection of the lymphatic bed depth within the microarchitectural dataset (microarch.tif) at a series of transverse locations. A curved but continuous depth plane through the lymphatic bed was defined by first interpolating the location of the lymphatic bed across all transverse points using three-dimensional cubic interpolation through Delaunay triangulation, and then smoothing this curve through application of a two-dimensional Gaussian filter of kernel size of 250 μm . Minimum intensity projections across depth over regions within $\pm 50 \mu\text{m}$ of the lymphatic bed were then generated to reveal the network in a two-dimensional image (**Figure VI-11**). The maximum diameter of lymphangions (lymphatic vessel segments) were measured in the XY plane with ImageJ software.

Evan's Blue lymphangiography was performed by injecting 10 μl of 4% Evan's Blue into the tissue and observing nearby lymphatic vessels with a dissecting scope.

VI.11n MULTIPHOTON MICROSCOPY AND REGISTRATION.

Multiphoton imaging was performed with a custom-modified confocal laser scanning microscope (Olympus 300; Optical Analysis Corp., Center Valley, PA) using a broadband femtosecond source (High Performance MaiTai, SpectraPhysics, Mountain View, CA). Angiographic contrast was achieved through intravenous administration of 200 μl of 8 mg/ml fluorescein isothiocyanate dextran 2M molecular weight (FITC-Dex 2M, Sigma-Aldrich, St. Louis, MO) in phosphate buffered saline. Image stacks were taken at 800nm excitation ($\sim 60 \text{ mW}$ at sample surface) with depths ranging to 500 μm depending on animal model and tumor type. To image tumors or organs (brain) over wide-fields, collections of mosaic images were taken in raster pattern using a motorized stage (H101, Prior Scientific, Inc., Rockland, MA) and customized automation software (LabView, National Instruments, Austin, TX). Mosaic stacks were assembled using ImageJ (NIH, Bethesda, MD) and Matlab (MathWorks, Natick, MA). Registration between MPM and OFDI of the same sample was conducted by denoting imaging

regions on the window coverglass by histological markers and manually comparing the locations of large vessels. All multiphoton imaging studies were performed with a 20X magnification, 0.95NA water immersion objective (Olympus XLUMPlanFI, 1-UB965, Optical Analysis, Center Valley, PA) with estimated $1/e^2$ radii of 0.27 μ m radially and 1.14 μ m axially.

VI.11o STATISTICAL ANALYSIS.

Data are presented as mean \pm standard error of the mean (SEM). Significant differences between groups were determined by a multivariate repeated measures ANOVA accounting for response to treatment over time (Systat, Systat Software, Inc., Chicago, IL). For quantitative metrics calculated by the vascular tracing algorithm, such as vascular diameters, significant differences at each time-point were determined by a two-sample Student's t-test. For tumor growth, statistical differences at each time-point were determined by the non-parametric Mann-Whitney test. Statistical differences at given time-points are denoted on the plots by asterisks. p-value \leq 0.05 was considered statistically significant for all comparisons. The multiphoton and OFDI measurements of vessel diameters (**Figure VI-6i**) were compared using the Pearson product-moment correlation.

VI.12 References

1. Brown, E.B., *et al.* In vivo measurement of gene expression, angiogenesis and physiological function in tumors using multiphoton laser scanning microscopy. *Nat Med* **7**, 864-868 (2001).
2. Masters, B.R. & So, P.T. *Handbook of Biomedical Nonlinear Optical Microscopy*, (Oxford University Press, New York, 2008).
3. Jain, R.K. Normalization of tumor vasculature: an emerging concept in antiangiogenic therapy. *Science* **307**, 58-62 (2005).
4. Huang, D., *et al.* Optical coherence tomography. *Science* **254**, 1178 (1991).
5. Mason, C., Markusen, J.F., Town, M.A., Dunnill, P. & Wang, R.K. Doppler optical coherence tomography for measuring flow in engineered tissue. *Biosens Bioelectron* **20**, 414-423 (2004).

6. Aalders, M.C., *et al.* Doppler optical coherence tomography to monitor the effect of photodynamic therapy on tissue morphology and perfusion. *J Biomed Opt* **11**, 044011 (2006).
7. Skliarenko, J.V., *et al.* Effects of the vascular disrupting agent ZD6126 on interstitial fluid pressure and cell survival in tumors. *Cancer Res* **66**, 2074-2080 (2006).
8. Yang, V.X., *et al.* Endoscopic Doppler optical coherence tomography in the human GI tract: initial experience. *Gastrointest Endosc* **61**, 879-890 (2005).
9. Li, H., *et al.* Feasibility of interstitial Doppler optical coherence tomography for in vivo detection of microvascular changes during photodynamic therapy. *Lasers Surg Med* **38**, 754-761 (2006).
10. Yun, S.H., Tearney, G.J., de Boer, J.F., Iftimia, N. & Bouma, B.E. High-speed optical frequency-domain imaging. *Optics Express* **11**, 2953-2963 (2003).
11. Carmeliet, P. Angiogenesis in life, disease and medicine. *Nature* **438**, 932-936 (2005).
12. Chen, Z.P., Milner, T.E., Dave, D. & Nelson, J.S. Optical Doppler tomographic imaging of fluid flow velocity in highly scattering media. *Optics Letters* **22**, 64-66 (1997).
13. Collins, H.A., *et al.* Blood-vessel closure using photosensitizers engineered for two-photon excitation. *Nature Photonics* **2**, 420-424 (2008).
14. Izatt, J.A., Kulkarni, M.D., Yazdanfar, S., Barton, J.K. & Welch, A.J. In vivo bidirectional color Doppler flow imaging of picoliter blood volumes using optical coherence tomography. *Optics Letters* **22**, 1439-1441 (1997).
15. Vakoc, B.J., Yun, S.H., de Boer, J.F., Tearney, G.J. & Bouma, B.E. Phase-resolved optical frequency domain imaging. *Optics Express* **13**, 5483-5493 (2005).
16. Wang, R.K.K. & Hurst, S. Mapping of cerebro-vascular blood perfusion in mice with skin and skull intact by optical micro-angiography at 1.3 μm wavelength. *Optics Express* **15**, 11402-11412 (2007).
17. Zhao, Y., *et al.* Phase-resolved optical coherence tomography and optical Doppler tomography for imaging blood flow in human skin with fast scanning speed and high velocity sensitivity. *Optics Letters* **25**, 114-116 (2000).
18. Yun, S.H., *et al.* Comprehensive volumetric optical microscopy in vivo. *Nature Medicine* **12**, 1429-1433 (2006).
19. Baish, J.W., *et al.* Role of tumor vascular architecture in nutrient and drug delivery: an invasion percolation-based network model. *Microvasc Res* **51**, 327-346 (1996).
20. Fukumura, D., Yuan, F., Monsky, W.L., Chen, Y. & Jain, R.K. Effect of host microenvironment on the microcirculation of human colon adenocarcinoma. *Am J Pathol* **151**, 679-688 (1997).
21. Monsky, W.L., *et al.* Role of host microenvironment in angiogenesis and microvascular functions in human breast cancer xenografts: mammary fat pad versus cranial tumors. *Clin Cancer Res* **8**, 1008-1013 (2002).
22. Boudreau, N. & Myers, C. Breast cancer-induced angiogenesis: multiple mechanisms and the role of the microenvironment. *Breast Cancer Res* **5**, 140-146 (2003).
23. Dellian, M., Witwer, B.P., Salehi, H.A., Yuan, F. & Jain, R.K. Quantitation and physiological characterization of angiogenic vessels in mice: effect of basic fibroblast growth factor, vascular endothelial growth factor/vascular permeability factor, and host microenvironment. *Am J Pathol* **149**, 59-71 (1996).
24. Ausprunk, D.H., Knighton, D.R. & Folkman, J. Vascularization of normal and neoplastic tissues grafted to the chick chorioallantois. Role of host and preexisting graft blood vessels. *Am J Pathol* **79**, 597-618 (1975).

25. Elenbaas, B. & Weinberg, R.A. Heterotypic signaling between epithelial tumor cells and fibroblasts in carcinoma formation. *Exp Cell Res* **264**, 169-184 (2001).
26. Fukumura, D. & Jain, R.K. Tumor microvasculature and microenvironment: targets for anti-angiogenesis and normalization. *Microvasc Res* **74**, 72-84 (2007).
27. Fukumura, D., *et al.* Tumor induction of VEGF promoter activity in stromal cells. *Cell* **94**, 715-725 (1998).
28. Jain, R.K. & Xu, L. alphaPIGF: a new kid on the antiangiogenesis block. *Cell* **131**, 443-445 (2007).
29. Liotta, L.A. & Kohn, E.C. The microenvironment of the tumour-host interface. *Nature* **411**, 375-379 (2001).
30. Weinberg, R.A. *The biology of cancer*, (Garland Science, New York, 2007).
31. Padera, T.P., *et al.* Cancer cells compress intratumour vessels. *Nature* **427**, 695 (2004).
32. Baish, J.W. & Jain, R.K. Fractals and cancer. *Cancer Res* **60**, 3683-3688 (2000).
33. Jain, R.K. Molecular regulation of vessel maturation. *Nature Medicine* **9**, 685-693 (2003).
34. Zhao, Y., *et al.* Three-dimensional reconstruction of in vivo blood vessels in human skin using phase-resolved optical Doppler tomography. *IEEE Journal of Selected Topics in Quantum Electronics* **7**, 931-935 (2001).
35. Sun, C., Jain, R.K. & Munn, L.L. Non-uniform plasma leakage affects local hematocrit and blood flow: implications for inflammation and tumor perfusion. *Ann Biomed Eng* **35**, 2121-2129 (2007).
36. Tyrrell, J.A., *et al.* Robust 3-D modeling of vasculature imagery using superellipsoids. *IEEE Transactions on Medical Imaging* **26**, 223-237 (2007).
37. Tyrrell, J.A., *et al.* A 2-D/3-D model-based method to quantify the complexity of microvasculature imaged by in vivo multiphoton microscopy. *Microvasc Res* **70**, 165-178 (2005).
38. Zysk, A.M. & Boppart, S.A. Computational methods for analysis of human breast tumor tissue in optical coherence tomography images. *J Biomed Opt* **11**, 054015 (2006).
39. Pan, Y., *et al.* Detection of tumorigenesis in rat bladders with optical coherence tomography. *Med Phys* **28**, 2432-2440 (2001).
40. Boppart, S.A., Luo, W., Marks, D.L. & Singletary, K.W. Optical coherence tomography: feasibility for basic research and image-guided surgery of breast cancer. *Breast Cancer Res Treat* **84**, 85-97 (2004).
41. Bohringer, H.J., *et al.* Time-domain and spectral-domain optical coherence tomography in the analysis of brain tumor tissue. *Lasers Surg Med* **38**, 588-597 (2006).
42. Gazit, Y., *et al.* Fractal characteristics of tumor vascular architecture during tumor growth and regression. *Microcirculation* **4**, 395-402 (1997).
43. Gazit, Y., Berk, D.A., Leunig, M., Baxter, L.T. & Jain, R.K. Scale-invariant behavior and vascular network formation in normal and tumor tissue. *Phys Rev Lett* **75**, 2428-2431 (1995).
44. Tong, R.T., *et al.* Vascular normalization by vascular endothelial growth factor receptor 2 blockade induces a pressure gradient across the vasculature and improves drug penetration in tumors. *Cancer Res* **64**, 3731-3736 (2004).
45. Padera, T.P., *et al.* Lymphatic metastasis in the absence of functional intratumor lymphatics. *Science* **296**, 1883-1886 (2002).
46. Swartz, M.A., *et al.* Mechanics of interstitial-lymphatic fluid transport: theoretical foundation and experimental validation. *Journal of Biomechanics* **32**, 1297-1307 (1999).

CHAPTER 6

47. Isaka, N., Padera, T.P., Hagendoorn, J., Fukumura, D. & Jain, R.K. Peritumor lymphatics induced by vascular endothelial growth factor-C exhibit abnormal function. *Cancer Research* **64**, 4400-4404 (2004).
48. Hoshida, T., *et al.* Imaging Steps of Lymphatic Metastasis Reveals That Vascular Endothelial Growth Factor-C Increases Metastasis by Increasing Delivery of Cancer Cells to Lymph Nodes: Therapeutic Implications. *Cancer Res* **66**, 8065-8075 (2006).
49. Sharma, M., Verma, Y., Rao, K.D., Nair, R. & Gupta, P.K. Imaging growth dynamics of tumour spheroids using optical coherence tomography. *Biotechnology Letters* **29**, 273-278 (2007).
50. Arbiser, J.L., *et al.* Isolation of mouse stromal cells associated with a human tumor using differential diphtheria toxin sensitivity. *American Journal of Pathology* **155**, 723-729 (1999).
51. Jain, R.K. The next frontier of molecular medicine: delivery of therapeutics. *Nat Med* **4**, 655-657 (1998).
52. Carmeliet, P. & Jain, R.K. Angiogenesis in cancer and other diseases. *Nature* **407**, 249-257 (2000).
53. Jain, R.K., Brown, E.B., Munn, L.L. & Fukumura, D. Intravital microscopy of normal and diseased tissues in the mouse. in *Live cell imaging : a laboratory manual* (eds. Goldman, R.D. & Spector, D.L.) pp 435-466 (Cold Spring Harbor Laboratory Press, Cold Spring Harbor, N.Y., 2005).
54. Leunig, M., *et al.* Angiogenesis, microvascular architecture, microhemodynamics, and interstitial fluid pressure during early growth of human adenocarcinoma LS174T in SCID mice. *Cancer Res* **52**, 6553-6560 (1992).
55. Yuan, F., *et al.* Vascular permeability and microcirculation of gliomas and mammary carcinomas transplanted in rat and mouse cranial windows. *Cancer Res* **54**, 4564-4568 (1994).
56. Levoy, M. Display of surfaces from volume data. *Computer Graphics and Applications, IEEE* **8**, 29-37 (1988).

VII. Concluding Statements and Future Directions

VII.1 Introduction:

Understanding the effects of disease progression and therapy on the tumor microenvironment is critical for elucidating the pathophysiologic mechanisms that underlie clinical prognosis and designing more efficacious combinatorial therapeutic regimens. While clinical imaging modalities and mechanical sensors exist to probe the anatomical, functional and metabolic aspects of the tumor microenvironment, they all lack high-resolution capabilities ($< 50\mu\text{m}$) and many are indirect measures of these parameters. The focus of this thesis has been to develop and apply new minimally invasive microscopic tools to study the tumor microenvironment in preclinical tumor models.

Principle characteristics of the tumor microenvironment are the metabolic parameters of oxygen tension ($p\text{O}_2$) and pH. Solid tumors are often found to be hypoxic and acidic; both determinants of metastatic progression, clinical prognosis, gene expression, angiogenesis, and therapeutic response. In Chapters 3 and 4, I developed and applied a new microscopic method for quantifying $p\text{O}_2$ by combining the techniques of phosphorescence quenching and multiphoton microscopy. This method, multiphoton phosphorescence quenching microscopy (MP-PQM), was fully characterized (Chapter 3) and used to successfully study $p\text{O}_2$ during tumor progression and in response to targeted therapy with either antiangiogenic agents or trastuzumab (Chapter 4). The significant outcomes from these experiments were 1) characterizing preclinical tumor models with respect to progression, 2) methods for correlating tumor microvascular parameters with oxygenation including metabolic consumption, 3) a new model for tissue oxygenation based on a simple parameter describing vascular structure and 4) an understanding that antiangiogenic therapy should be titrated to potentially “normalize” the metabolic microenvironment for improved therapeutic response.

In collaboration with investigators in the MIT Chemistry department, a novel biosensor for pH was developed and implemented under multiphoton excitation to perform high-resolution mapping of pH (Chapter 5). This sensor combined the attractive

photophysical and stability properties of luminescent semiconductor nanocrystals (NCs, quantum dots) with fluorescent dye molecules sensitive to pH. Using the principles of Förster resonance energy transfer (FRET), this construct enabled reversible internally referenced ratiometric measurements of pH using multiphoton multispectral and fluorescence ratiometric imaging (MP-FRIM). Critical advancements presented in this work were 1) the application of nanocrystals as two-photon antennas even for dyes with substantial two-photon action cross-sections, 2) biocompatible coatings for nanoscale materials that exhibit minimal physical interactions with the tissue (and tumor) microenvironment components, 3) techniques for calibrating pH sensors in environments mimicking the tumor microenvironment and 4) methodology for qualitatively measuring pH changes in the tumor microenvironment and correlating with the vasculature using MP-FRIM and NC biosensors for pH.

In addition to the metabolic parameters defining the tumor microenvironment, the structural and cellular components including the tumor vasculature, peritumoral lymphatics, and microanatomic features all influence tumor progression and response to therapy. Furthermore, the ability to probe these aspects dynamically and over wide fields on short (minutes) and long (days-weeks) timescales with microscopic resolution has profound implications in the study of tumor biology and drug development. The coherent microscopy optical frequency domain imaging (OFDI) enabled the simultaneous investigation of the tumor microenvironment with these characteristics (Chapter 6). Through a collaboration with scientists in the Wellman Laboratories for Photomedicine, we developed and implemented new techniques and methods for OFDI to non-invasively probe the tumor vasculature, lymphatics and cellular microenvironment. Importantly, we demonstrated 1) the capability to perform non-invasive three-dimensional imaging and morphometric and geometric characterization of tumor microvasculature without the need for angiographic contrast agents, 2) identification of tumor-associated lymphatics based entirely on their optical scattering signal, 3) *in vivo* histological assessment of tumor necrosis and apoptosis and 4)

multiparametric monitoring of vascular and cellular targeted therapies in preclinical tumor models.

VII.2 Optimizing and Advancing MP-PQM

While the technique of MP-PQM was proven successful (Chapter 3) and effective in quantifying *in vivo* pO₂ in the tumor microenvironment, many aspects could be improved to increase signal to noise and therefore measurement time. The methods proposed in this Thesis employ time-domain lifetime measurements using an electro-optic modulator (EOM) for impulse selection. The use of any optics in the path of a pulsed mode-locked laser induces group delay dispersion which increases the temporal duration of the pulse¹. In the case of EOMs or especially acousto-optic modulators, the laser pulse duration is increased due to significant group delay dispersion. In multiphoton excitation, the fluorescent emission is inversely proportional to the laser pulse duration². Longer pulses decrease the peak power in the focal volume reducing the excitation rate of MPM. Through a process termed “pulse shaping”, the excitation laser pulse can be pre-chirped to counteract the effects of optics in the laser path³. Numerous methods exist to perform pulse compression in this fashion including prism pairs⁴, diffraction grating pairs⁵, and adaptive optics⁶.

Secondary to pulse shaping is the repetition rate of the pulse laser. Typically 80MHz Ti:Sapphire lasers are used in MPM because the temporal separation between pulses is longer than the luminescent lifetime of most fluorophores. However, luminophores with longer lifetimes may be more efficient at lower repetition rates. In fact, many studies using phosphorescence with nonlinear excitation employed lasers in the kilohertz range^{7,8}. However, these lasers typically also have longer (nanosecond versus femtosecond) pulse durations. Therefore, little or no improvement may be observed with this pulsed laser source given very similar duty cycles (pulse duration × repetition rate).

The original concept behind the development of MP-PQM was its adaptability to existing MPM setups. However, pulse shaping may dramatically increase phosphorescence of the pO₂ sensor, a phosphorescent porphyrin, which has a reduced two-photon action cross-section compared to commonly used fluorophores. Another possibility, which will be explored in the next section, is the development of oxygen sensors with improved two-photon action cross-section. Other investigators have developed phosphorescent porphyrins with two-photon antennas for improved quantum yield under two-photon excitation^{7,9}. However, these probes have not been fully characterized for *in vivo* application. If adaptations to MP-PQM or improved two-photon oxygen sensors are developed, the measurement time may be significantly reduced. MP-PQM may therefore someday be applied in a beam scanning fashion analogous to normal MPM function instead of stationary beam photon counting. This would permit imaging of pO₂ over wider fields and increased sampling rate.

VII.3 New NC-Biosensor Constructs and Designs

The novel nanocrystal biosensor design introduced in Chapter 5 is adaptable to other sensing strategies. Two additional sensing schemes not introduced in Chapter 5 are 1) protease sensing through cleavage of a peptide linking abrogating FRET 2) binding of an analyte altered the Förster distance (R_0) and therefore the FRET efficiency. The designs reported in Chapter 5 can also be applied to a number of analytes dependent only on the dye selected. Fluorescent dyes exist that are sensitive to biologically important ions including calcium, magnesium, and sodium¹⁰. These chemosensors change their fluorescence emission intensity dependent on the concentration of a specific ion in solution. As there is no change in absorption spectrum, the nanocrystal emission acts as a two-photon antenna and internal reference as demonstrated in Chapter 5. As such, the photophysical properties of the construct are determined entirely by the nanocrystal abrogating any differences observed between single or two-photon direct excitation of the dye molecule.

The NC biosensor construct employed in the fashion of a two-photon antenna would also improve the excitation rate of the oxygen sensors utilized in Chapters 3 and 4. In collaboration with the Bawendi and Nocera groups at MIT, initial experiments have been performed providing evidence to support this hypothesis. A Pd-porphyrin (Pd-meso-tetra(4-carboxyphenyl) porphyrin; Oxyphor R0, Oxygen Enterprises, Ltd., Philadelphia, PA) coupled to a nanocrystal emitting at an absorption maxima for the porphyrin does demonstrate response to oxygen (**Figure VII-1**). Similar to pH, the NC emission is again unresponsive to the local environment, particularly oxygen, regardless of the solvent used. This probe could be applied in a ratiometric fashion or lifetime measurements could be performed to quantify oxygen. In fact, given the broad excitation spectrum of the NC and high quantum yield, a sensor designed with maximum FRET efficiency could be employed for frequency domain lifetime measurements. Here, the duty cycle of the experiment would be vastly improved compared to the time-domain, speeding up the *in vivo* measurement time. However, as seen in Chapter 5, again the issue is delivering the probes to the tumor microenvironment.

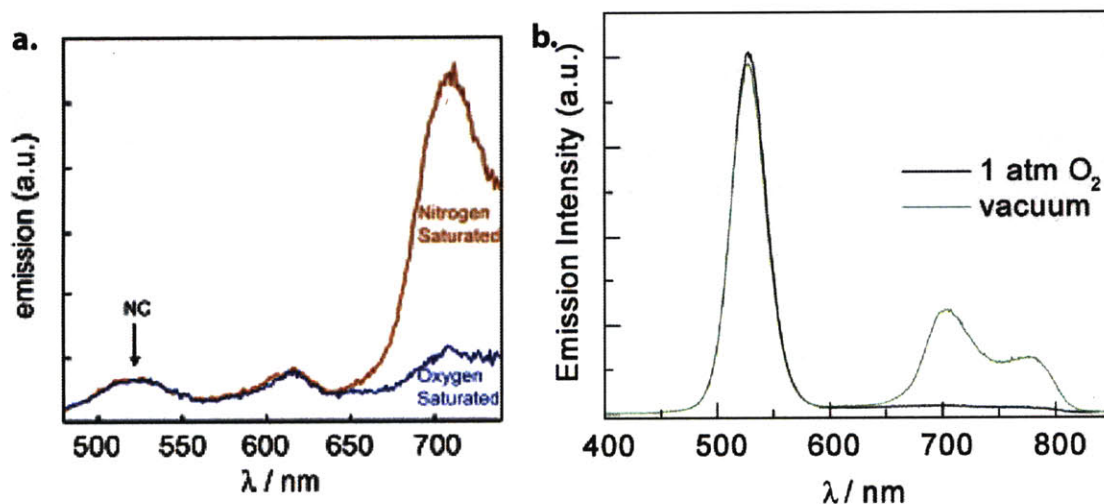


Figure VII-1 Nanocrystal biosensor for oxygen. A NC construct containing a bound Pd-porphyrin demonstrated response to changes in oxygen in both dimethylformamide (a) and aqueous solution (b). The NC emission was unaffected by pO_2 in either situation.

The issue of transporting NC biosensors directly to the tumor microenvironment may be resolved by direct targeting. Coupling NCs to antibodies or peptides against molecular markers found in the tumor microenvironment may improve both delivery and retention for long-term studies. It has been demonstrated that conjugation of antibodies or peptides to fluorescent nanocrystals is possible for immunohistochemistry¹¹, cellular labeling¹²⁻¹⁴ and *in vivo* cancer cell¹⁵ and vascular targeting¹⁶. The majority of these studies have been performed *ex vivo* or the *in vivo* results were not microscopic (whole-body imaging) or hindered by aggregation in the vasculature. Our collaborators have recently demonstrated targeted NC constructs with limited non-specific binding to cells¹⁷. These constructs had an attached dye molecule (CXR) and still exhibited FRET during cell labeling.

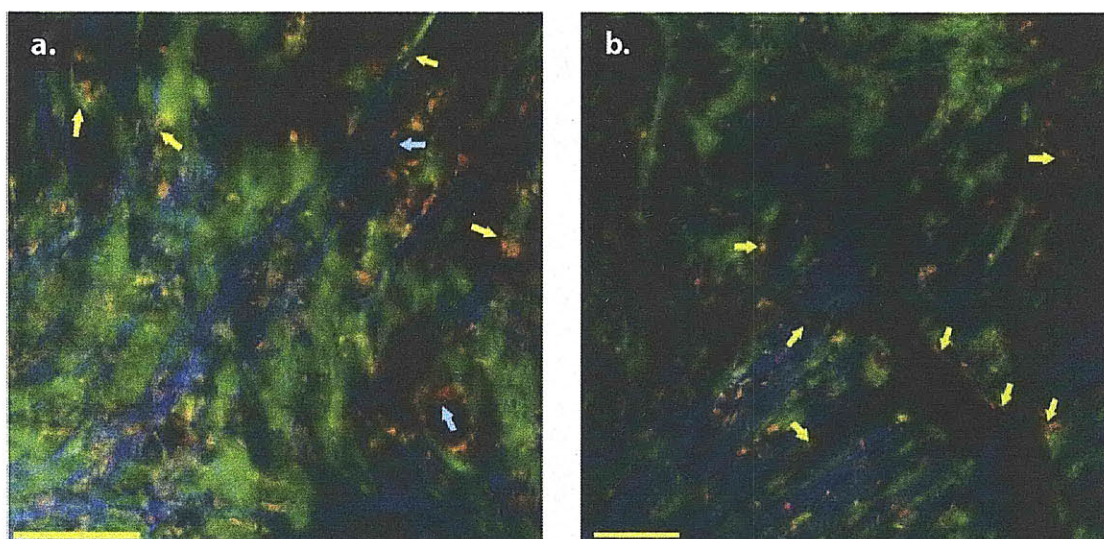


Figure VII-2 *In vivo* imaging of NC-immunoconstructs, fibroblast-like stromal cells, and collagen matrix in a sarcoma tumor model. (a) GFP-positive stromal cells interacting with the collagen matrix in integrin $\beta 1$ labeled areas (yellow arrows). GFP negative cells positive for $\beta 1$ interacting with the collagen matrix (light blue arrows). (b) Integrin $\beta 1$ is also expressed near the tumor vasculature; (yellow arrows) – colocalization of integrin $\beta 1$ immunostaining and GFP-negative endothelial cells. Red – NC-immunoconstructs; Green – VEGF-GFP host cells. Blue – signal from Collagen I. Scale Bars - 50 μ m.

I have investigated *in vivo* targeting in the murine tumor models using NCs bound to antibodies against integrin $\beta 1$. These were prepared with the “Quantum Dot Antibody Conjugation Kit” available from Molecular Probes. Briefly, reduced antibodies with free sulfhydryls exposed are attached to PEGylated NCs with terminal maleimide groups. In

the DSC chamber of a VEGF-GFP mouse¹⁸ bearing a human soft tissue sarcoma xenograft, this construct demonstrated labeling of stromal cells colocalized with second harmonic signal generated from collagen (**Figure VII-2**). Further optimization of the NC construct design for size and charge introduces the ability to perform targeted sensing. Further, the narrow emission spectra and broad two-photon excitation spectra would allow for multiplexed phenotyping of cells in the tumor microenvironment¹⁹. It is apparent that luminescent semiconductor nanocrystals possess many possibilities for studying *in vivo* cancer biology as both sensing and imaging agents.

VII.4 Future Directions of OFDI in Cancer Biology

The interaction of light with tissue contains much information about structure and dynamic processes. In Chapter 6, the coherent microscopy technique of optical frequency domain imaging was shown to provide quantitative three-dimensional images of *in vivo* tumor vasculature, lymphatic vessels, tissue viability and microanatomy over wide fields of view. There is much still to be advanced using this technology both in methodology and assessment of additional anatomical and functional parameters of the tumor microenvironment. These include measuring blood flow, vascular permeability, tumor transport properties, edema, and cell metabolism. The application of multiparametric OFDI to a number of *in vivo* tissues was demonstrated in Chapter 6. However, additional aspects of the tumor microenvironment may still be uncovered including *in vivo* staging of tumorigenesis and lymphatic metastasis.

Given the ability to non-invasively determine the morphometry and three-dimensional geometry of tumor vascular networks, the next logical step is to develop methods that probe the function of the vascular network. Others have demonstrated an ability to qualitatively measure blood flow perfusion using Doppler methodologies and OCT²⁰⁻²². Quantitative velocity measurements with OCT require either standard vessel geometries (straight tube)²³ or specially designed probes to measure multiple components of the velocity vector²⁴. At minimum, the angle of the sample beam with the vessel of interest needs to be known to determine the velocity. If the beam is directly perpendicular to

the flow vector, no measurement is possible. With our collaborators at the Wellman Laboratories, we have proposed three methods for *in vivo* quantitation of flow velocities.

- 1.) Calibrate the temporal modulation of the reflectance signature with known flow velocities and apply to *in vivo* measurements.
- 2.) Either incorporate a second sample beam at a different angle of incidence for simultaneous measurements or rotate the subject to obtain measurements from another angle. Additional angles of incidence with the velocity vector will permit direct calculation of velocity magnitude.
- 3.) Use the geometrical information obtained from semi-automated vascular tracing of the three-dimensional tumor microvasculature to determine the incidence angle of the sample beam along a discriminated length of vessel. An average velocity along the vessel length could then be calculated. This is computationally more intensive, but attemptable with the current OFDI systems.

Beyond flow, quantitative assessment of other parameters of vascular function may be accessible by OFDI. Spectroscopic OFDI has been shown to differentiate between scatterers of different sizes based on Mie theory²⁵. Mie theory predicts that particles scatter light with a wavelength around the spherical dimension of the particle. Using angle-resolved OFDI, which removes the speckle (coherent noise)^{26,27} by averaging over different reflectance angles of the backscattered photons, the microarchitecture of tissue in the murine models is better defined²⁸ (**Figure VII-3**). Further, measurements of tissue scattering are found to be more accurate; enabling the discrimination of particles of different size. We hypothesize that angular-resolved OFDI will be able to quantify vascular permeability and interstitial transport in the tumor microenvironment. We theorize that intravascular administration of optical scatterers (gold nanoparticles, carbon nanotubes, etc) on the order of the wavelengths of light used to probe the tissue (1230-1370nm) or possibly smaller will extravasate from the vasculature and be detectable by OFDI.

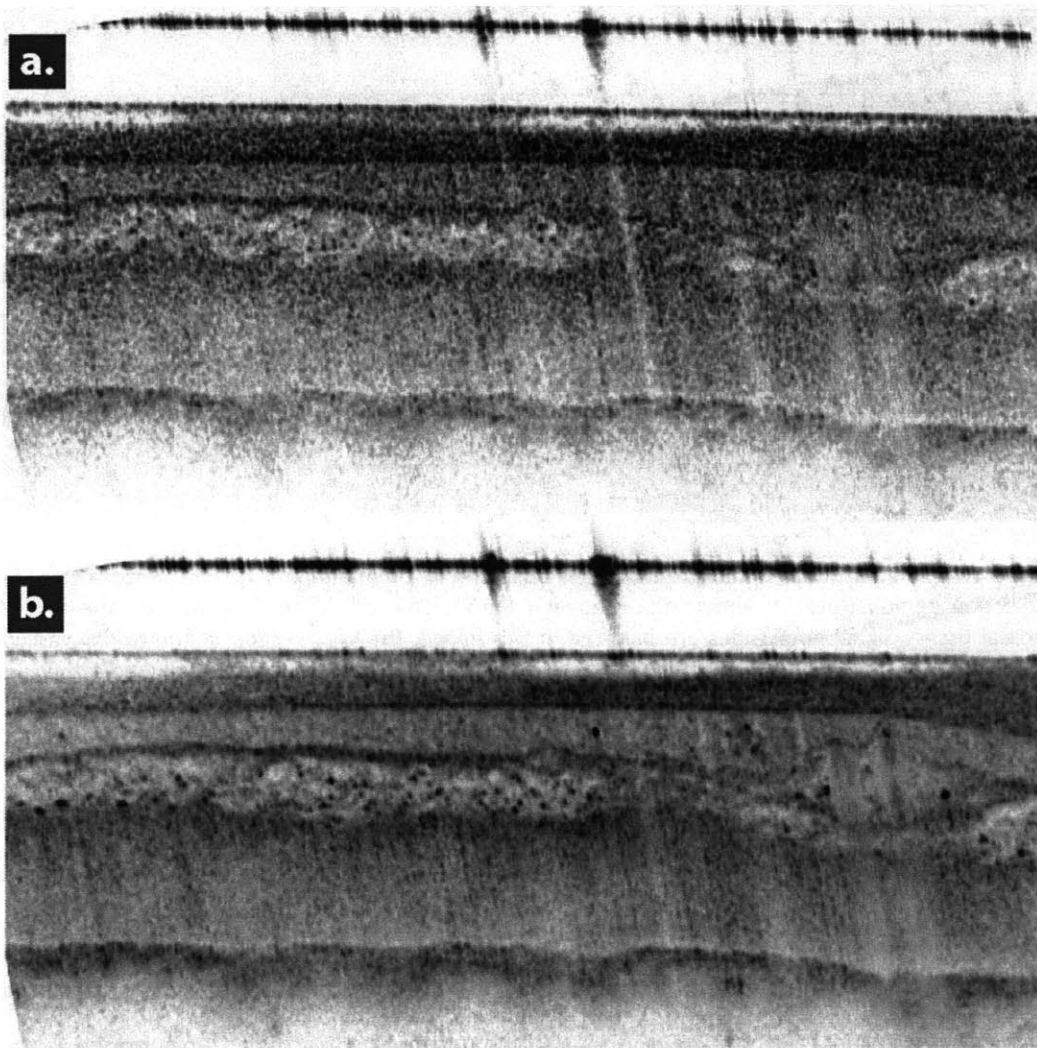


Figure VII-3 Angle-resolved OFDI of normal murine skin in the DSC. (a) Ordinary OFDI with speckle noise apparent. (b) Same tissue with angular averaging reduces speckle and reveals additional microstructure.

Time-resolved measurements of dynamic changes in tissue scattering coupled with Doppler OFDI imaging of the tumor vasculature may provide measurements of single vessel permeabilities as well as diffusion from the intravascular space through the interstitium. A possible secondary effect of intravenous injection of optical scatterers would be enhances sensitivity of vessels with lower perfusion. However, the “shadowing” noise observed with larger vessels and high hematocrit may be enhanced by this technique. Although the effect of rotating the sample frame discussed above (#1 and 2) may reduce the shadowing effect.

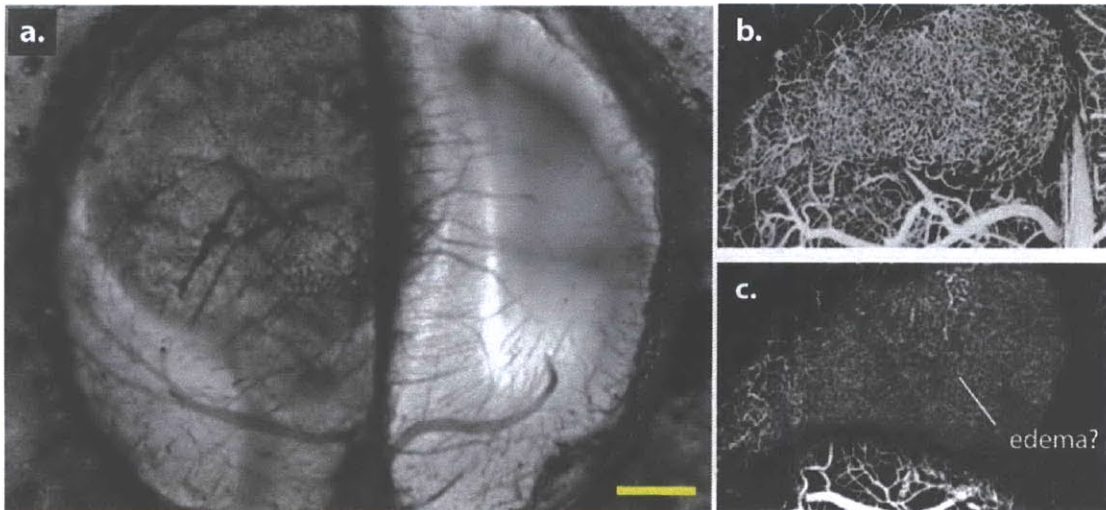


Figure VII-4 Higher Doppler background signal observed in a human glioblastoma xenograft. (a) Enface projection demonstrates a demarcation between the intratumoral Doppler signal and the rest of the cortical tissue. Signal amplitudes are inverted in this image. (b) Axial section of the tumor vasculature from angiographic OFDI. (c) Minimum projection of the Doppler dataset potentially indicating edema. Scale Bar – 1mm.

Doppler OFDI is capable of detecting the movement of scattering interfaces anywhere in the tissue. While the highest sensitivity and signal is obtained from fluid flow in the blood vessels, any other processes that change over time may be observable. When we viewed the minimum intensity projection of the Doppler OFDI datasets, we observed that the tumor tissue exhibited a higher Doppler background than the surrounding tissue (**Figure VII-4**). Others have observed that tumor spheroids²⁹ and individual cells³⁰ modulate the reflectance of light based on metabolic activity in living cells. It is possible that Doppler OFDI is differentiating the tumor based on the higher metabolic activity of the cancer cells. However, preliminary results of Doppler OFDI in formalin-fixed samples from tumors implanted in the DSC reveal similar properties of the tumor to those seen in Figure VII-4.

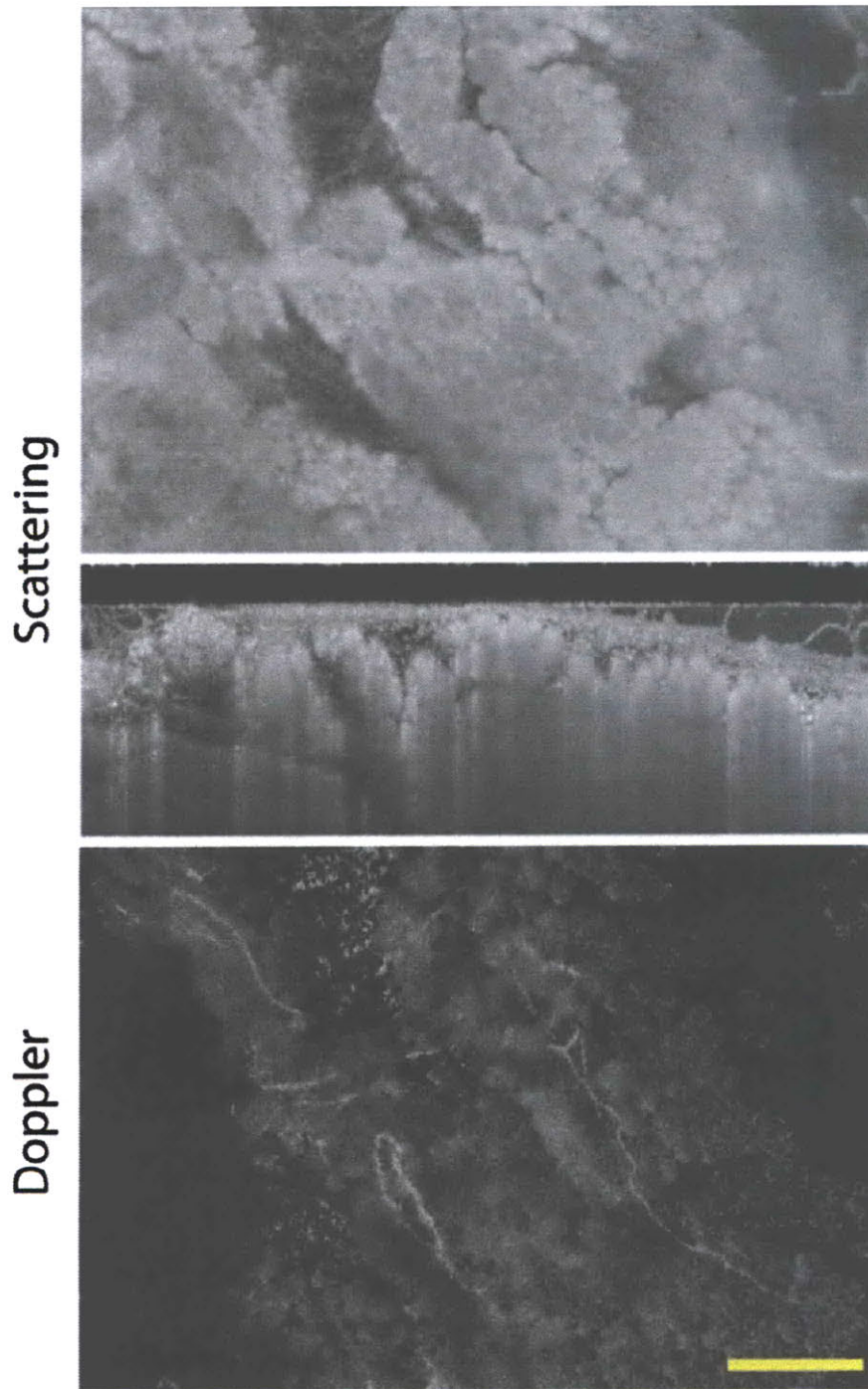


Figure VII-5 *In vivo* microarchitecture and perfusion of murine mammary ducts imaged by OFDI. *Top*: Reflectance signature from the mammary fat pad of a female mouse reveals the normal globular ductal structure. *Bottom*: Doppler OFDI signal showing fluid motion in the globules and within the mammary ducts. Scale Bar - 500 μ m.

It is possible that OFDI is detecting the Brownian motion of particulate matter in the extracellular fluid. In the case of a tumor, the extracellular fluid, particularly at the margins, may be increased due to the high interstitial pressure and absence of lymphatics. In this case, OFDI may be detecting edema in the tumor microenvironment an important pathophysiology found in tumors. Edema can have profound clinical implications particularly for brain tumors where additional pressure on the adjacent normal tissue can induce damage or neurological sequelae. Interestingly, edema is a common finding in the mouse model shown in Figure VII-4, further supporting the possibility that it is edema³¹.

In Chapter 6, we demonstrated the application of OFDI to numerous animal models including neoplastic and normal tissues. These results are only a cursory summary of what is possible with OFDI. We showed that, in some cases, cellular structures are observable in the peritumoral lymphatics. This suggests that OFDI may be used to study lymphatic metastasis in preclinical models. We also demonstrated the ability of OFDI to perform multiparametric assessment of treatment response, but this would also be applicable to studying any facet of tumor biology. One important aspect of cancer biology that has not been well studied in an *in vivo* environment in the same animal is progression of disease from the earliest signs of dysplasia to end-stage metastatic disease. Using spontaneous murine mammary tumor models, such as the MMTV-PyMT mice^{32,33}, it may be possible to non-invasively study tumor progression using all the methods demonstrated in Chapter 6. In a preliminary study, I found that the normal mammary fat pad architecture including mammary ducts is detectable by OFDI (Figure VII-5). With OFDI and these models, we may be able to illuminate the disease process of cancer through progression and treatment.

VII.5 Concluding Statements

My dissertation has focused on the development of new minimally invasive techniques to study the *in vivo* tumor microenvironment during progression and response to treatment. These tools have demonstrated advancements in multiphoton microscopy,

semiconductor nanocrystal technology and coherent microscopy. Utmost has been the development of new methods using these technologies to perform multiparametric analysis of solid tumors. As this final Chapter illustrated many directions in further developing and applying these technologies are possible. Each new step in advancing our understanding of the tumor microenvironment may help develop new methods and drugs for treating cancer.

VII.6 References

1. Milonni, P.W. & Eberly, J.H. *Lasers*, (Wiley, New York, 1988).
2. Lakowicz, J.R. *Topics in fluorescence spectroscopy: Nonlinear and two-photon induced fluorescence.*, (Plenum Press, New York, 1997).
3. Wolleschensky, R., Feurer, T., Sauerbrey, R. & Simon, U. Characterization and optimization of a laser-scanning microscope in the femtosecond regime. *Applied Physics B: Lasers and Optics* **67**, 87-94 (1998).
4. Fork, R.L., Martinez, O.E. & Gordon, J.P. NEGATIVE DISPERSION USING PAIRS OF PRISMS. *Optics Letters* **9**, 150-152 (1984).
5. Treacy, E.B. OPTICAL PULSE COMPRESSION WITH DIFFRACTION GRATINGS. *IEEE Journal of Quantum Electronics* **QE-5**, 454-458 (1969).
6. Yelin, D., Meshulach, D. & Silberberg, Y. Adaptive femtosecond pulse compression. *Optics Letters* **22**, 1793-1793 (1997).
7. Brinas, R.P., Troxler, T., Hochstrasser, R.M. & Vinogradov, S.A. Phosphorescent oxygen sensor with dendritic protection and two-photon absorbing antenna. *J Am Chem Soc* **127**, 11851-11862 (2005).
8. Mik, E.G., van Leeuwen, T.G., Raat, N.J. & Ince, C. Quantitative determination of localized tissue oxygen concentration in vivo by two-photon excitation phosphorescence lifetime measurements. *J Appl Physiol* **97**, 1962-1969 (2004).
9. Finikova, O.S., et al. Oxygen microscopy by two-photon-excited phosphorescence. *Chemphyschem* **9**, 1673-1679 (2008).
10. Baker, G.A.M., C.A.; Bukowski, E.J.; Baker, S.N; Bright, F.V. Assessment of One- and Two-Photon Excited Luminescence for Directly Measuring O₂, pH, Na⁺, Mg²⁺, or Ca²⁺ in Optically Dense and Biologically Relevant Samples. *Appl Spec* **56**, 455-463 (2002).
11. Xing, Y., et al. Bioconjugated quantum dots for multiplexed and quantitative immunohistochemistry. *Nat Protoc* **2**, 1152-1165 (2007).
12. Wu, X., et al. Immunofluorescent labeling of cancer marker Her2 and other cellular targets with semiconductor quantum dots. *Nat Biotechnol* **21**, 41-46 (2003).
13. Prow, T.W., Kotov, N.A., Lvov, Y.M., Rijnbrand, R. & Leary, J.F. Nanoparticles, molecular biosensors, and multispectral confocal microscopy. *J Mol Histol* **35**, 555-564 (2004).
14. Chattopadhyay, P.K., et al. Quantum dot semiconductor nanocrystals for immunophenotyping by polychromatic flow cytometry. *Nat Med* **12**, 972-977 (2006).
15. Gao, X., Cui, Y., Levenson, R.M., Chung, L.W. & Nie, S. In vivo cancer targeting and imaging with semiconductor quantum dots. *Nat Biotechnol* **22**, 969-976 (2004).

16. Smith, B.R., *et al.* Real-time intravital imaging of RGD-quantum dot binding to luminal endothelium in mouse tumor neovasculature. *Nano Lett* **8**, 2599-2606 (2008).
17. Liu, W., *et al.* Compact biocompatible quantum dots functionalized for cellular imaging. *J Am Chem Soc* **130**, 1274-1284 (2008).
18. Fukumura, D., *et al.* Tumor induction of VEGF promoter activity in stromal cells. *Cell* **94**, 715-725 (1998).
19. Chan, P., Yuen, T., Ruf, F., Gonzalez-Maeso, J. & Sealfon, S.C. Method for multiplex cellular detection of mRNAs using quantum dot fluorescent in situ hybridization. *Nucleic Acids Res* **33**, e161 (2005).
20. Aalders, M.C., *et al.* Doppler optical coherence tomography to monitor the effect of photodynamic therapy on tissue morphology and perfusion. *J Biomed Opt* **11**, 044011 (2006).
21. Li, H., *et al.* Feasibility of interstitial Doppler optical coherence tomography for in vivo detection of microvascular changes during photodynamic therapy. *Lasers Surg Med* **38**, 754-761 (2006).
22. Zhao, Y., *et al.* Phase-resolved optical coherence tomography and optical Doppler tomography for imaging blood flow in human skin with fast scanning speed and high velocity sensitivity. *Optics Letters* **25**, 114-116 (2000).
23. Chen, Z.P., Milner, T.E., Dave, D. & Nelson, J.S. Optical Doppler tomographic imaging of fluid flow velocity in highly scattering media. *Optics Letters* **22**, 64-66 (1997).
24. Yeh-Chan, A., Woonggyu, J. & Zhongping, C. Quantification of a three-dimensional velocity vector using spectral-domain Doppler optical coherence tomography. *Optics Letters* **32**, 1587-1589 (2007).
25. Desjardins, A.E., Vakoc, B.J., Tearney, G.J. & Bouma, B.E. Backscattering spectroscopic contrast with angle-resolved optical coherence tomography. *Opt Lett* **32**, 3158-3160 (2007).
26. Briers, J.D. Speckle fluctuations and biomedical optics: implications and applications. *Optical Engineering* **32**, 277-283 (1993).
27. Schmitt, J.M., Xiang, S.H. & Yung, K.M. Speckle in optical coherence tomography. *J Biomed Opt* **4**, 95-105 (1999).
28. Desjardins, A.E., Vakoc, B.J., Bilenca, A., Tearney, G.J. & Bouma, B.E. Estimation of the scattering coefficients of turbid media using angle-resolved optical frequency-domain imaging. *Opt Lett* **32**, 1560-1562 (2007).
29. Yu, P., *et al.* Time-dependent speckle in holographic optical coherence imaging and the health of tumor tissue. *Opt Lett* **29**, 68-70 (2004).
30. Hirakawa, Y., Hasegawa, T. & Masujima, T. Laser speckle microscope for instantaneous determination of condition of single living cell. *Japanese Journal of Applied Physics, Part 2 (Letters)* **44**, 85-87 (2005).
31. Kamoun, W.S., *et al.* Edema control by cediranib, a vascular endothelial growth factor receptor-targeted kinase inhibitor, prolongs survival despite persistent brain tumor growth in mice. *J Clin Oncol* **27**, 2542-2552 (2009).
32. Lin, E.Y., *et al.* Progression to malignancy in the polyoma middle T oncoprotein mouse breast cancer model provides a reliable model for human diseases. *Am J Pathol* **163**, 2113-2126 (2003).
33. Siegel, P.M., Ryan, E.D., Cardiff, R.D. & Muller, W.J. Elevated expression of activated forms of Neu/ErbB-2 and ErbB-3 are involved in the induction of mammary tumors in transgenic mice: implications for human breast cancer. *EMBO J* **18**, 2149-2164 (1999).

Acknowledgements

My dissertation work occurred at the intersection of multiple fields – medicine, biology, chemistry, physics, etc. – and as such I have had the opportunity to interact with so many fantastic people from very diverse fields. First, I must thank my Thesis advisor, Dr. Rakesh Jain who has provided me with almost unfathomable opportunities and resources. What graduate student gets to build their own multiphoton microscope on which to perform their research? His mentorship and guidance have truly fostered my scientific curiosity and opened up new worlds to explore. I have matured scientifically so much while a member of his lab, that it is hard to recognize the fresh and naïve med student who first walked into talk with him. I also cannot thank him enough for the confidence he has shown in me over the years in my own independent research, grant writing, teaching, and mentoring young scientists. Beyond the technical skills I have gained through my work in his lab, I have also discovered how to ask the right questions and coalesce a vast amount of information into a cogent idea – or so I think. I am indebted to him for the scientist I am today.

I would also like to thank the members of my thesis committee. Professor Peter So has been an invaluable resource in all things two-photon and optical. I also greatly appreciate his generosity in the time he has given me to ask so many questions. Professor Mounji Bawendi has been a collaborator on quantum dots and a mentor in the Chemistry department. I cannot thank him enough for giving me the opportunity to enter the program as a PhD student moving across the river from HMS. He has given me so much insight on the application of nanocrystals to biomedicine (Chapter 5) and I have learned so much. Professor Marcos Integlietta has been a mentor from afar – near my home turf at UCSC. He has always been more than willing to answer my questions about the microvasculature, blood substitutes and oxygenation. Also, I must thank him for making the trip out for my defense. Finally, Professor Dai Fukumura, who I have gotten to know well from the Steele Laboratory. Really there is no one I would want to ask more about all things involving mice and tumors. His critical insights into my research have spurred new avenues and more often than not straightened me out onto the correct ones.

My colleagues and friends from the Steele Laboratory have been an invaluable source of information and support. I must highlight so many of them. Dr. Tim Padera, if I had an older brother you would definitely be him, and I mean that in both the good and bad ways – okay actually just good. Your mentorship and guidance have been invaluable to my growth as a scientist. I always look forward to our conversations whether they are about research or baseball. I will carry your mantra with me for the rest of my career: “The data are the data”. No one could have said it better. Oh, and I guess lymphatics are okay. Professor Edward Brown originally took me under his wing to teach me multiphoton microscopy and then unleashed me on the lab after he departed to start his own lab at U. of Rochester. You have been a good friend and mentor, always willing to answer my bone-headed questions. I also gained a mantra from you as well: “If you are not breaking stuff, then you are not trying”. Wise words, just don’t tell Dr. Jain. Also, I will make it out to see your large farmhouse – once you have a baseball field.

ACKNOWLEDGEMENTS

Professor Yves Boucher tried to swing me to the extracellular matrix. I took the bait for awhile because second harmonic imaging is cool. Even though I didn't switch, you have always been willing to answer my questions and give insightful input on my projects. While I am on Yves, I must mention his wife Sylvie Roberge to whom I am indebted for a lot of my animal work. You have always been willing to help and never got frustrated with me, which is quite an accomplishment if you talk to my wife. I also like when you have white chocolate on the white table. Moving from Sylvie and staying with the animals, there is no one who supported my research efforts more than Julia Kahn. Almost at a moment's notice she has prepared me a dozen chamber models without hesitation. Now multiply that by about 50 – 75 and you know how much she has helped me. Dr. Peigen Huang, the commander of the colony, has been so accommodating to my research needs and moving optical equipment into and out of the colony, that I cannot thank him enough. He has also always managed to wrangle up mice when I have needed them. Phyllis McNally, words cannot really describe the support she has offered over the years, especially since she is always working so hard. You never flinched at my many requests, some of which were quite unusual or expensive. I hope you are able to retire someday soon and spend your time between the grandkids and Aruba. Professor Dan Duda has been a good friend and is full of so many ideas for using quantum dots in tumors. I only wish I had the time to help with that. He also has a lot of other ideas for me, but I have to stop the PhD after 6 years – sorry. Professor Lance Munn has been an invaluable resource for computing, modeling, and all things image related, I am just sorry he is a Mac guy. Professor Emmanuelle di Tomaso was always available when I needed help on histology. I only wish we had interacted more, but I preferred to image things non-invasively. Dr. Leo Gerwick, thanks for all your insightful comments on radiation therapy and the effects of pH on chemo. You have been a wealth of information and I have enjoyed our talks over the years. To the other faculty in the lab, Professors Igor Garkavtsev and Lei Xu, thanks for your support over the years.

To the other two HST grad students who entered the lab at the same time, we have had quite an adventure. Dr. Josh Tau I wish you the best of luck in your new scientific endeavors in the Wellman Labs. Dr. Patrick Au, you are one of the smartest and yet most humble person I know - such a wealth of information. It has been great getting to know you over the years and I am sad to see you move on to the FDA, but I know you will be fantastic in that role. Dr. Wilson Mok jumped ship to the corporate consulting world, which he certainly has excelled at. I will miss our conversations about all the things that make grad school difficult, though I do not know how constructive they were. Dr. Ricky Tong, or should I now say Dr. Dr., thanks for showing me the way to close out a research project. Vikash Chauhan, we have had many tangential conversations over the last couple years that hopefully did not prolong my stay, but many times they were quite interesting. I am also glad that we succeeded in finishing the transport project and good luck finishing out your tenure in the Steele lab. Special thanks to Dr. Walid Kamoun and Dr. Alex Tyrell for all your input on Matlab codes and image processing. To Mr. Greek salads have no lettuce, Dr. Fyllos Stylianopoulos, and Prof. Jim Baish thanks for teaching me more than I ever wanted to know about fractals, geometrical analysis and finite volume methods. I would also like to thank all of the other grad students, post-docs and technologists I have interacted with over the years and who have often been very generous with their time and experience: Dr. Mike Booth, Prof. Michelle Dawson, Dr. Kevin Kozak, Dr. Satoshi Kashiwagi, Dr. Yannis Perentes,

ACKNOWLEDGEMENTS

Dr. Johanna Lahdenranta, Eve Smith, Grace Gorospe, Christina Koppel, Dan Nguyen, Dr. Sung-Suk Chae, Carsten Ley, Dr. Delphine Lacorre, Dr. Aaron Mulivor, Dr. Trevor McKee, Ben Diop-Frimpong, Janet Tse, Ming-Zher Poh, Carolyn Smith, A.J., Dr. Gang Cheng, Dr. Euiheon Chung, Dr. Hiroshi Yamashita, Dr. Shan Lao, Dr. Ned Kirkpatrick and Dr. Sachie Hiratsuka- thanks. I would like to also thank the folks in the machine shop: Lenny, Arthur and Jerry, who have always been more than helpful and accommodating over the years in machining the necessary parts for my research projects.

Well deserved thanks must be given to my outside collaborators, without whom much of the work in this dissertation would not be possible. Dr. Becky Somers and I fought the challenges of using quantum dots *in vivo* and succeeded for the most part (Chapter 5). Thanks for your patience and understanding, biology likes to muck up the perfect designs of chemists. Dr. Andrew Greytak and I also worked to bring about the fruition of the NC biosensor model. You answered all of my often quite detailed questions regarding pchem and quantum dots and I learned so much from it. Also, I still do not understand half of what you do in Matlab and I have coded for many hours – if I only had half your genius there. Emily McLaurin was always so generous with her time in helping prepare deoxygenated samples (Chapter 3) and was a significant contribution to my work. I hope to see some oxygen sensors from you in the near future. Prof. Preston Snee was my first collaborator in this project and introduced me to the magic of quantum dots. Finally, Prof. Dan Nocera is one of the coolest Chemistry professors I have met and asks penetrating questions. I know that someday he will solve all of our energy problems.

On the coherent microscopy front, Prof. Ben Vakoc has become a true colleague and friend over the many grueling hours we spent collecting and processing data (Chapter 6). It has been a challenging few years that have led to a successful publication and hopefully many more. I will miss our conversations and time spent pondering OFDI in cancer biology, although I am sure our wives will be happy to have us back. Hopefully, during my final years of med school we can continue our collaborative work. Dr. Adrien Desjardins first introduced me to the wonders of OCT and I enjoyed working with him very much. Prof. Gary Tearney provided much insight on both pathology and pursuing a career as a physician-scientist. Finally, thanks to Prof. Brett Bouma for giving me the opportunity to work in his lab and providing much support to this collaboration. Also, I do not know many other faculty that have his degree of enthusiasm for the multidisciplinary research espoused by HST and needed in the 21st century.

No acknowledgment section would be complete without thanking my family and friends for always being there to support me over the years. To my wife Gina, you have been so understanding and supportive over the challenging times of graduate school and I do not know if I can ever know how difficult it must have been. I love you so much and that has only grown over the years. Now that I am done, I can start doing my chores on a regular basis... My mom, Linda, has always sacrificed to ensure that I received the best education and experiences possible. I would not be where I am today without her love and support. My father and stepmother, Bob and Minuen, have also always been there to support me over the years and ask about my research every step of the way. My brother, Darren, has always been around to make me laugh and remind me of the joys in life. My grandfather, Mayo, is my role model as a

ACKNOWLEDGEMENTS

human being and has always worked to foster my intellectual abilities. My wife's parents, Wayne and Karen, and siblings, Stacie and Jeff, have accepted me as one of their own and provided invaluable support during my graduate years. I would also like to thank Prof. Bruce Tromberg who introduced me to biomedical optics research first-hand. You have served as both a mentor and inspiration during my academic career. Thank you all for your unquestionable support and love.

CURRICULUM VITAE

Ryan M. Lanning

EDUCATION

2003-Present Massachusetts Institute of Technology Cambridge, MA
Degree: Ph.D. Candidate

- Department of Physical Chemistry and Health Sciences and Technology
- Medical Engineering and Medical Physics Program

2001-Present Harvard Medical School Boston, MA
Degree: M.D. Candidate

- Health Sciences and Technology Program

1996 - 2000 University of California Irvine Irvine, CA
Degrees: B.S. in Chemistry and Biology

- Graduated Cum Laude
- Member Campuswide Honors Program

RESEARCH EXPERIENCE

2003 – Present Edwin L. Steele Laboratory in Tumor Biology Boston, MA

Position: Graduate Research Student

Supervisor: Dr. Rakesh Jain

- Use Multiphoton Laser Scanning Microscopy (MPLSM) for imaging tumors *in-vivo*
- Developing novel microscopy method for quantifying oxygen tension and pH *in-vivo* using MPLSM
- Collaborative projects with Bawendi and Nocera Labs at MIT on the use of quantum dots in probing cancer biology
- Collaborative project with MGH Wellman Center for Photomedicine to adapt novel biomedical imaging technologies to study tumor pathophysiology

2000 - 2001 Beckman Laser Institute and Medical Clinic Irvine, CA

Position: Researcher in Photon Migration Lab

1998 – 2000: Undergraduate Student Researcher

Supervisor: Dr. Bruce Tromberg

- Conducted research characterizing tissue physiology/biochemistry in normal and diseased tissue using near-infrared optical spectroscopy.
- Performed non-invasive clinical research measurements.
- Collaborated with surgeons, clinicians, and basic scientists.
- Designed and constructed instruments and probes for optical measurements.
- Developed co-registration methods of optical and MRI measurements.

CURRICULUM VITAE

AWARDS RECEIVED

-
- RESEARCH: Department of Defense Breast Cancer Research Program Pre-doctoral Training Fellowship - 3yr (2005)
- Martinos Research Fellow (2005)
- Office of Enrichment Programs, HMS, Summer Research Fellowship (2002)
- Whitaker Foundation Fellowship (1999)
- ACADMEMIC: UC Regents Scholarship (1996-2000)
- Robert C. Byrd Scholarship (1996-2000)
- OTHER: Honorable mention - NSF Fellowship (2003)
- Finalist in Marshall Scholarship (2000)
- Finalist in Fulbright Scholarship for England (2000)

TEACHING & MENTORING EXPERIENCES

-
- Teaching Assistant for HST.525/Path 209: "Tumor Pathophysiology and Transport Phenomena: A Systems Biology Approach" (Fall 2007)
- Steele Laboratory for Tumor Biology Methods Course - Instructor (2006-2008)
- Mentored 2 Junior Graduate Students (2006 - Present)
- Supervised 2 MIT Undergraduate Research Opportunities Program Students (2007 - 2008)

PUBLICATIONS AND PRESENTATIONS

-
- PUBLICATIONS: Vakoc BJ*, **Lanning RL***, Tyrrell JA, Padera TP, Bartlett L, Stylianopoulos T, Munn LL, Tearney GJ, Fukumura D, Jain RK, Bouma BE. Three-dimensional microscopy of the tumor microenvironment *in vivo* using optical frequency domain imaging. *Nat. Med. In Press* (2009).
- Chauhan VP*, **Lanning RL***, Diop-Frimpong B, Mok W, Brown EB, Padera TP, Boucher Y, Jain RK. Multiscale diffusion measurements uncover the cellular and interstitial contributions to molecular hindrance in vivo. *Biophys J. In Press.* (2009).
- Au P, Daheron LM, Duda DD, Cohen KS, Tyrrell JA, **Lanning R**, Fukumura D, Scadden DT, Jain RK. Differential in vivo potential of endothelial progenitor cells from human umbilical cord blood and adult peripheral blood to form functional long-lasting vessels. *Blood* 111: 1313-1316, (2007).
- Merritt S, Bevilacqua F, Durkin AJ, Cuccia DJ, **Lanning R**, Tromberg BJ, Gulsen

CURRICULUM VITAE

G, Yu H, Wang J, Nalcioglu O. Coregistration of Diffuse Optical Spectroscopy and Magnetic Resonance Imaging in a Rat Tumor Model. *Appl. Optics* **42**: 2951-2959, (2003).

Gulsen G, Yu H, Wang J, Nalcioglu O, Merritt S, Bevilacqua F, Durkin AJ, Cuccia DJ, **Lanning R**, Tromberg BJ. Congruent MRI and near-infrared spectroscopy for functional and structural imaging of tumors. *Technol. Cancer Res. Treat.* **1**: 497-505, (2002).

Jakubowski D, Cerussi AE, Bevilacqua F, Shah N, **Lanning R**, Hsiang D, Butler J, Holcombe RF, Tromberg BJ. Characterizing Breast Tumors Using Broadband Near-Infrared Spectroscopy. *Lasers in Surgery and Medicine* **30**, S14: 1, (2002).

Cerussi AE, Jakubowski D, Shah N, Bevilacqua F, **Lanning R**, Berger AJ, Hsiang D, Butler J, Holcombe RF, Tromberg BJ. Spectroscopy Enhances the Information Content of Optical Mammography. *Journal of Biomedical Optics* **7**: 60-71, (2002).

Cerussi, AE., Bevilacqua, F., Shah, N., Jakubowski, DB., Berger, AJ., **Lanning, RM.**, Tromberg, BJ. The Effects of Water and Lipids on NIR Optical Breast Measurements in *Optical Tomography and Spectroscopy of Tissue IV*, Britton Chance, Robert ER. Alfano, Bruce J. Tromberg, Mamoru Tamura, Eva M. Sevick-Muraca, Editors, Proceedings of SPIE Vol. **4250**, (2001).

Tromberg, BJ, Shah, N, **Lanning, R**, Cerussi, A, Espinoza, J, Pham, T, Svaasand, L, Butler, J. Non-Invasive *In Vivo* Characterization of Breast Tumors Using Photon Migration Spectroscopy. *Neoplasia* **2**: 1-15, (2000).

Lanning, R. Non-Invasive Characterization of Breast Cancer Using Near-Infrared Optical Spectroscopy. *UCI Biological Sciences Undergraduate Research Journal*, (1999).

PRESENTATIONS:

"In vivo dissection of tumor vascular networks, lymphatics, tissue viability and microenvironment using three-dimensional optical frequency domain imaging". **Lanning RL**, Vakoc BJ, Tyrrell JA, Padera TP*, Bartlett L, Stylianopoulos T, Munn LL, Tearney GJ, Fukumura D, Jain RK, Bouma BE. AACR Annual Meeting, Denver, CO 2009.

"Measurement of pO₂ and pH with Three-Dimensional Resolution in Murine Breast Tumor Models by Multiphoton Microscopy during Herceptin Therapy". **Lanning RM**, Fukumura D, Brown EB, Somers R, Greytak AB, Padera TP, Nocera DG, Bawendi MG, Jain RK. Era of Hope, Department of Defense Breast Cancer Research Program Meeting, Baltimore, MD 2008.

"Functional and structural imaging of tumors using near-infrared tissue spectroscopy and MRI co-registration" Bevilacqua F., Durkin AJ., Cuccia D., **Lanning R.**, Merritt S., Gulsen

"In vivo dissection of tumor vascular networks, lymphatics, tissue viability and microenvironment using three-dimensional optical frequency domain imaging". **Lanning RL**, Vakoc BJ, Tyrrell JA, Padera TP*, Bartlett L, Stylianopoulos T, Munn LL, Tearney GJ, Fukumura D, Jain RK, Bouma BE. AACR Annual Meeting, Denver, CO 2009.

"Measurement of pO₂ and pH with Three-Dimensional Resolution in Murine Breast Tumor Models by Multiphoton Microscopy during Herceptin Therapy". **Lanning RM**, Fukumura D, Brown EB, Somers R, Greytak AB, Padera TP, Nocera DG, Bawendi MG, Jain

CURRICULUM VITAE

RK. Era of Hope, Department of Defense Breast Cancer Research Program Meeting, Baltimore, MD 2008.

"Functional and structural imaging of tumors using near-infrared tissue spectroscopy and MRI co-registration" Bevilacqua F., Durkin AJ., Cuccia D., **Lanning R.**, Merritt S., Gulsen G., Wang HYJ., Nalcioglu O., Tromberg BJ., United Engineering Foundation Conference: Advances in Optics for Biotechnology, Medicine and Surgery, Banff, Canada July 2002.

"Non-Invasive Characterization of Breast Cancer Using Near-Infrared Optical Spectroscopy" **Lanning, R.** UCI Biological Sci. Excellence in Research Symposium, May 1999.

PROFFESIONAL ACTIVITIES

Student Member Massachusetts Medical Society

Student Member American Medical Association

Student Member HST MD Admissions Committee (2003-Present)

Invited Reviewer - Journal Biomedical Optics

Invited Reviewer - Cancer Research

REFERENCES

Rakesh K. Jain, Ph.D
Andrew Werk Cook Professor of Tumor Biology
Steele Laboratory for Tumor Biology, Director
Department of Radiation Oncology, Cox 7
Massachusetts General Hospital
Boston, MA 02114
Tel: 617.726.4083 Fax: 617.724.1819
E-mail: jain@steele.mgh.harvard.edu

Moungi G. Bawendi, Ph.D
Lester Wolfe Professor in Chemistry
Department of Chemistry, 6-221
Massachusetts Institute of Technology
Cambridge, MA 02139
Tel: 607.253.9796 Fax: 617.253.7030
E-mail: mgb@mit.edu

Brett E. Bouma, Ph.D
Associate Professor of Dermatology and Health Sciences & Technology,
Harvard Medical School
Wellman Laboratories for Photomedicine
Massachusetts General Hospital
Boston, MA 02114
Tel: 617.726.9007 Fax: 617.726.4103
E-mail: bouma@helix.mgh.harvard.edu